SCUOLA DI DOTTORATO
UNIVERSITÀ DEGLI STUDI DI MILANO-BICOCCA

Department of Physics "Giuseppe Occhialini"

Ph.D. program in Physics and Astronomy, XXXVIII Cycle
Curriculum of Subnuclear Physics

The physics potential of the ENUBET/nuSCOPE neutrino beam at CERN

Candidate: **Bramati Filippo**
Registration number: 813349

Tutor: **Terranova Francesco**
Supervisor: **Branca Antonio**

Coordinator: **Ragazzi Stefano**

ACADEMIC YEAR 2024/2025

To my mom Roberta

Look up at the sky and count the stars, if you can.
Just so shall your descendants be. Gen 15,5

Abstract

The research work presented in this thesis was conducted as part of the NP06/ENUBET and nuSCOPE experimental programs.

The NP06/ENUBET experiment is aimed at designing and experimentally demonstrating the concept of monitored neutrino beams, a novel technology with a superior control of the flux at source. The limited knowledge of neutrino cross-sections at the GeV scale is one of the main systematic uncertainties for the next generation of long-baseline neutrino oscillation experiments (DUNE, HyperK). Neutrino cross-section measurements are limited by the poor knowledge of the initial flux and by uncertainties in the neutrino energy reconstruction. In ENUBET, the neutrino flux is monitored by recording the charged leptons produced in association with neutrinos from meson decay by instrumenting both the decay tunnel and the hadron dump. The use of fast silicon trackers placed along the beamline enables the neutrino tagging technique, which can uniquely associate in time the occurrence of each observed neutrino interaction in the detector with its parent meson and charged lepton, allowing a kinematic reconstruction of neutrino energy on an event-by-event basis.

The nuSCOPE monitored and tagged neutrino beam is designed to eliminate the main sources of systematic uncertainty in cross-section measurements thanks to the flux monitoring at the percent level and the measurement of neutrino energy independent of final state particles reconstruction in the neutrino detector. nuSCOPE aims to deliver measurements of neutrino cross-sections at the GeV scale at the percent level - i.e. improving by one order of magnitude current experimental estimates - and will play a pivotal role in the precision era of oscillation physics.

In my thesis work I contributed to three main aspects: the calorimeter prototype test beam, the neutrino flux systematic assessment, and the physics case of nuSCOPE.

The ENUBET demonstrator, a large-scale prototype of a section of the instrumented decay tunnel, was exposed at the CERN East Experimental Area (PS T9) during dedicated test beam data campaigns. I contributed to the analysis of test beam data to assess the prototype performance, the development of a full and realistic GEANT4 simulation of the demonstrator reproducing test beam conditions, and data/Monte Carlo agreement studies.

A major part of my research work was devoted to the assessment of neutrino flux systematic uncertainties and their mitigation using the charged lepton monitoring technique, with a special focus on the leading systematic contribution: the yields of secondary hadrons produced at target. I developed an algorithm capable of determining the impact of neutrino flux systematic uncertainties before and after using the information provided by the fit to charged lepton observables. I have shown that charged lepton observables can be used to constrain the neutrino flux at the percent level.

Finally, the physics case of the nuSCOPE neutrino beam is presented in terms of cross-section measurements that could be made to reduce uncertainties in neutrino oscillation experiments, summarizing the work I carried out at CERN EP-NU. In particular, I

provided a set of measurements benefiting from neutrino tagging, such as measurements of neutrino energy reconstruction bias and electron-scattering-like measurements with tagged neutrinos, which can provide key insights into electroweak nuclear physics.

Contents

Motivation and outline

The NP06/ENUBET experiment is aimed at designing and experimentally demonstrating the concept of monitored neutrino beams, a novel technology with a superior control of the neutrino flux at source. The limited knowledge of neutrino cross-sections at the GeV scale is one of the main systematic uncertainties for the next generation of long-baseline neutrino oscillation experiments (DUNE, HyperKamiokande) aimed at observing CP violation in the lepton sector and pinning down the neutrino mass ordering. Neutrino cross-section measurements are limited by the poor knowledge of the initial flux and by uncertainties in the neutrino energy reconstruction. In ENUBET, the neutrino flux is monitored by recording the charged leptons produced in association with neutrinos from meson decay by instrumenting both the decay tunnel and the hadron dump. The physics potential of a monitored neutrino beam can be significantly enhanced by the neutrino tagging technique, i.e. correlating in time the occurrence of each observed neutrino interaction in the neutrino detector with its parent meson and charged lepton. The use of fast, radiation-hard silicon trackers placed along the beamline enables to uniquely associate in time the neutrino interaction with the accompanying particles in the transfer line and allows a kinematic reconstruction of neutrino energy on an event-by-event basis. The nuSCOPE monitored and tagged neutrino beam leverages the experience and R&D achievements of the NP06/ENUBET and NuTag Collaborations. The nuSCOPE neutrino beam is designed to eliminate the main sources of systematic uncertainty in cross-section measurements thanks to the flux monitoring at the percent level and the measurement of neutrino energy independent of final state particles reconstruction at the neutrino detector. The nuSCOPE facility aims to deliver measurements of neutrino cross-sections at the GeV scale at the percent level - i.e. improving by one order of magnitude current experimental estimates - and will play a pivotal role in the precision era of oscillation physics to achieve the ultimate sensitivity in the lepton Yukawa sector.

This Ph.D. thesis work presents my contributions to several studies relevant to the ENUBET/nuSCOPE experiment and its future implementation.

The first chapter concerns neutrino physics and describes the status of neutrino cross-section measurements at the GeV scale, with special emphasis on the limitations arising from the uncertainties on the flux and neutrino energy reconstruction.

The second chapter presents the concept of monitored and tagged neutrino beams at accelerators, introducing the rationale of the NP06/ENUBET and nuSCOPE experiments and their beamline design. The detectors instrumenting the decay tunnel to reconstruct charged leptons are described here, as well as the beam and muon spectrometers that enable the tracking of parent mesons and daughter muons.

The third chapter presents the construction, assembly, and characterization of the ENUBET demonstrator, a large-scale prototype of a section of the instrumented decay tunnel exposed at the CERN PS T9 area during dedicated test beam data campaigns, and my contributions to it. They include the development of a full and realistic GEANT4 simulation of the demonstrator reproducing test beam conditions, as well as test beam

data analysis and data/MC comparison of the energy resolution and linearity of response.

The fourth chapter describes the results I obtained on the assessment of neutrino flux systematic uncertainties and their mitigation using the charged lepton monitoring technique, with a special focus on the leading contribution: the yields of secondary hadrons produced at target. I developed an algorithm capable of determining the impact of neutrino flux systematic uncertainties before and after using the information provided by the fit to charged lepton observables. The algorithm is based on a fit model where the parameters of interest are related to the hadron production; additional nuisance parameters are then introduced to parametrize the uncertainties related to detector effects. The information from the GEANT4 simulation of the instrumented tunnel is used to generate a set of pseudo-experiments, including the effects of hadron production and detector uncertainties on the charged lepton observables. These synthetic datasets are then used to perform an extended maximum likelihood fit on the observables to study the feasibility of the monitoring concept; the fit results are used to set a constraint on the hadron production yields and, consequently, on the expected neutrino flux. The observables considered are the distributions of visible energy and impact point of positrons along the decay tunnel. I have shown that these observables can be used to constrain the neutrino flux at the percent level.

The fifth chapter presents the physics prospects and potential of the nuSCOPE monitored and tagged neutrino beam in terms of neutrino cross-section measurements and summarizes the work I carried out at CERN EP-NU. I provided a set of neutrino cross-section measurements that could be made by nuSCOPE to reduce uncertainties in neutrino oscillation experiments, with a focus on their application to supporting DUNE's physics program. I investigated the two methods by which nuSCOPE can measure the neutrino energy without relying on the reconstruction of final state particles in a neutrino interaction: the narrow-band off-axis technique and the neutrino tagging method, which can reach the ultimate precision of $\sim 1\%$. I also investigated the feasibility of a PRISM analysis to create a virtual flux from linear combinations of the narrow-band off-axis fluxes. Finally, I provided a set of measurements benefiting from neutrino tagging: a direct inclusive energy-dependent cross-section measurement, direct measurements of neutrino energy reconstruction bias that can be used to calibrate out nuclear effects in the DUNE far detector, electron-scattering-like measurements with tagged neutrinos, which can provide key insights into electroweak nuclear physics.

1 Neutrino Physics

1.1 Neutrinos in the Standard Model

The Standard Model (SM) of Particle Physics is one of the most successful theories in modern physics and it describes the interactions of the fundamental building blocks of nature, leptons and quarks. The Standard Model is a quantum description of three out of four fundamental interactions[1] mediated by the exchange of gauge bosons: the electromagnetic interaction is mediated by the exchange of photons, the strong interaction by the exchange of gluons and weak interaction by the exchange of massive vector bosons. The *gauge symmetry principle* is one of the pillars of the great success of the SM, since it establishes an unambiguous connection between local (gauge) symmetries and forces mediated by vector bosons [1]. The strong and electroweak interactions are connected to $SU(3)$, $SU(2)$ and $U(1)$ gauge groups, and thus the different characteristics of interactions can be explained by the symmetry they are related to. The way in which particles exert and experience each of the fundamental forces is thus determined by their representation under the corresponding symmetry group. Once the gauge invariance principle is promoted to the level of fundamental physics principle, all terms in the Lagrangian must respect the local symmetry, including the mass terms. This fact has important implications for the neutrino and, in particular, for the question of its mass [2].

1.1.1 Neutrinos in the Standard Model: massless neutrinos

The SM includes three fermion generations and it is based on the gauge group:

$$G_{\mathrm{SM}} = SU(3)_C \times SU(2)_L \times U(1)_Y \tag{1.1}$$

where C stands for colour, L for left-handedness and Y for hypercharge. The model explains all the interactions of the known fermions once they are assigned to well defined representations of the gauge group [1]. Specifically, each fermion generation consists of five different representations of the gauge group:

$$L_L\left(\mathbf{1},\mathbf{2},-\frac{1}{2}\right)\ Q_L\left(\mathbf{3},\mathbf{2},\frac{1}{6}\right)\ E_R\left(\mathbf{1},\mathbf{1},-1\right)\ U_R\left(\mathbf{3},\mathbf{1},\frac{2}{3}\right)\ D_R\left(\mathbf{3},\mathbf{1},-\frac{1}{3}\right) \tag{1.2}$$

The notation used in (1.2) specifies under which representation of the $SU(3)$ and $SU(2)$ gauge groups each matter field transforms and the value of the weak hypercharge for the $U(1)$ group[2]. The matter fields content of the SM is illustrated in Tab. 1.1 and, together with the corresponding gauge boson fields, it constitutes the full list of fields required to describe the observed elementary interactions [2].

[1] The SM does not include gravity.

[2] The notation means that, for instance, a left-handed lepton field L_L is a singlet ($\mathbf{1}$) of the $SU(3)_C$ group, a doublet ($\mathbf{2}$) of the $SU(2)_L$ group and carries hypercharge $-1/2$ under the $U(1)_Y$ group [3].

$L_L(\mathbf{1},\mathbf{2},-\frac{1}{2})$	$Q_L(\mathbf{3},\mathbf{2},\frac{1}{6})$	$E_R(\mathbf{1},\mathbf{1},-1)$	$U_R(\mathbf{3},\mathbf{1},\frac{2}{3})$	$D_R(\mathbf{3},\mathbf{1},-\frac{1}{3})$
$\begin{pmatrix}\nu_e\\ e\end{pmatrix}_L$	$\begin{pmatrix}u\\ d\end{pmatrix}_L$	e_R	u_R	d_R
$\begin{pmatrix}\nu_\mu\\ \mu\end{pmatrix}_L$	$\begin{pmatrix}c\\ s\end{pmatrix}_L$	μ_R	c_R	s_R
$\begin{pmatrix}\nu_\tau\\ \tau\end{pmatrix}_L$	$\begin{pmatrix}t\\ b\end{pmatrix}_L$	τ_R	t_R	b_R

Table 1.1: The matter fields content of the SM.

Moreover, the model contains a single Higgs boson doublet ϕ, with charges $(\mathbf{1},\mathbf{2},1/2)$, whose vacuum expectation value (VEV) partially breaks the gauge symmetry [2]:

$$\langle\phi\rangle = \begin{pmatrix}0\\ \frac{v}{\sqrt{2}}\end{pmatrix} \quad \stackrel{SSB}{\Longrightarrow} \quad G_{\rm SM} \to SU(3)_C \times U(1)_{\rm EM} \tag{1.3}$$

with $U(1)_{\rm EM}$ generated by the unbroken generator $Q = T^3 + Y = \frac{\sigma^3}{2} + Y$, where Y is the weak hypercharge and T^3 the weak isospin, namely the third generator of $SU(2)_L$.

Within the SM, neutrinos are fermions that have neither strong nor electromagnetic interactions, that is, in the group theory language, they are singlets of $SU(3)_C \times U(1)_{\rm EM}$ subgroup. One generally refers as *active* neutrinos to neutrinos residing in the lepton doublet $L_\ell = \begin{pmatrix}\nu_\ell\\ \ell^-\end{pmatrix}_L$, thus having weak interactions. Conversely, *sterile* neutrinos are defined as having none of the SM gauge interactions, that is, they are singlets of the full SM gauge group $G_{\rm SM}$ [2]. Therefore the SM with massless neutrinos, conceived as the gauge theory able to describe all known particle interactions, does not contain sterile neutrinos [1].

In the SM there is one active neutrino for each charged lepton. In particular, the three neutrino interaction eigenstates $\nu_e\,, \nu_\mu$ and ν_τ are defined as the $SU(2)_L$-partners of the charged leptons mass eigenstates $e_L^-\,, \mu_L^-$ and τ_L^- [3]. The $SU(2)_L$ gauge invariance of the Lagrangian dictates the form of weak charged current (CC) interactions between the neutrinos and their corresponding charged leptons to be:

$$-\mathscr{L}_{CC} = \frac{g}{\sqrt{2}} \sum_\ell \overline{\nu}_{L\ell} \gamma^\mu \ell_L^- W_\mu^+ + \text{h.c.} \tag{1.4}$$

and neutral current (NC) interactions among neutrino themselves to be:

$$-\mathscr{L}_{NC} = \frac{g}{2\cos\theta_W} \sum_\ell \overline{\nu}_{L\ell} \gamma^\mu \nu_{L\ell} Z_\mu^0 \tag{1.5}$$

where g is the coupling constant associated to $SU(2)_L$ and θ_W is the Weinberg angle. Therefore, within the SM, Eqs. (1.4) and (1.5) describe all the neutrino interactions. In particular, Eq. (1.5) determines the decay width of the Z^0 boson into light (that is, $m_\nu \lesssim m_{Z^0}/2$) left-handed neutrinos states. Thus one can infer the number N_ν of such states from the measurement of the Z^0 decay width. At present the measurements implies:

$$N_\nu = 2.996 \pm 0.007 \quad \text{(Standard Model fits to LEP-SLC data)} \tag{1.6}$$

$$N_\nu = 2.92 \pm 0.05 \quad \text{(Direct measurment of invisible } Z^0 \text{ width)} \tag{1.7}$$

As a result, any extension of the SM should contain three, and only three, light active neutrinos [1].

Given that fermions reside in chiral representations of the gauge group, no bare mass terms can appear in the Lagrangian. In the Standard Model, fermions masses arise from the Yukawa interaction [4] terms which couple a right-handed fermion with its left-handed doublet and the scalar Higgs doublet ϕ as follows:

$$-\mathscr{L}_{\text{Yukawa}} = Y^d_{ij}\overline{Q}_{Li}\phi D_{Rj} + Y^u_{ij}\overline{Q}_{Li}\widetilde{\phi}U_{Rj} + Y^\ell_{ij}\overline{L}_{Li}\phi E_{Rj} + \text{h.c.} \tag{1.8}$$

where $\widetilde{\phi} = i\sigma^2\phi^*$. After spontaneous symmetry breaking these terms lead to charged fermion masses:

$$m^f_{ij} = Y^f_{ij}\frac{v}{\sqrt{2}} \tag{1.9}$$

where v is the vacuum expectation value of the Higgs field [2]. However, since the model does not contain right-handed neutrinos, no such Yukawa interaction can be built for the neutrinos, which are consequently *massless* at the Lagrangian level [1].

Nevertheless, in principle, a neutrino mass term could be generated at loop level. Within the SM particle content (1.2) the only possible neutrino mass term that could be constructed is the bilinear $\overline{L}_L L^c_L$, where L^c_L is the charge conjugated field $L^c_L = \mathcal{C}\overline{L}^T_L$ and $\mathcal{C}$ is the charge conjugation matrix [1]. However this cannot happen, as can be understood by examining the accidental symmetries of the SM.
The SM respects an *accidental global symmetry* (at the perturbative level) which is not a priori imposed but appears as a consequence of its gauge symmetry (1.1) and of the representations of the matter fields (1.2) required for the gauge interactions:

$$G^{\text{global}}_{\text{SM}} = U(1)_B \times U(1)_{L_e} \times U(1)_{L_\mu} \times U(1)_{L_\tau} \tag{1.10}$$

where $U(1)_B$ is the baryon number symmetry and $U(1)_{L_e,L_\mu,L_\tau}$ are the three lepton flavour symmetries. Thus, the total lepton number $L = L_e + L_\mu + L_\tau$ is an accidental symmetry as well, since it is a subgroup of $G^{\text{global}}_{\text{SM}}$. Consequently, bilinear terms of the form $\overline{L}_L L^c_L$ are forbidden in the SM because they violate the total lepton symmetry by two units; therefore these terms cannot be induced by loop corrections since they break the accidental symmetry of the model. Furthermore, since $U(1)_{B-L}$ is a non-anomalous subgroup of $G^{\text{global}}_{\text{SM}}$, these bilinear terms cannot be induced by non-perturbative corrections either since they would break $B - L$ [1]. Thus, the field content and the gauge symmetries of the SM preclude the existence of neutrino mass.

It follows that the SM predicts that neutrinos are precisely massless and, consequently, there would be neither mixing nor CP violation in the leptonic sector [3]. Actually, experimental evidences for neutrino masses and mixings are in contradiction with the SM predictions and, therefore, one must go beyond the SM in order to add mass to neutrinos [1]. Among all possible extensions of the SM, the simplest one is the *minimally extended SM*, which simply consists in the introduction of three right-handed neutrino fields ν_{eR}, $\nu_{\mu R}$ and $\nu_{\tau R}$, which are singlets under the gauge symmetry of the SM. In such a way, neutrino fields become similar to the other massive fermion fields, having now both left-handed and right-handed components [5].

1.2 Flavour mixing in the lepton sector

Neutrino oscillations are a quantum-mechanical phenomenon that is made possible by the existence of *non-degenerate neutrino masses* and *lepton flavour mixing* [6]. In analogy with what happens in the quark sector, the origin of flavour mixing in the lepton sector lies in a mismatch between the basis of (weak) gauge eigenstates and the basis of mass eigenstates. As a result, when written in the flavour basis[3], the neutrino mass matrix is not diagonal. The flavour and mass eigenstates of left-handed neutrino fields are related by a unitary transformation, the *lepton mixing matrix*, usually known as the PMNS (Pontecorvo-Maki-Nakagawa-Sakata) matrix:

$$\begin{pmatrix} \nu_e(x) \\ \nu_\mu(x) \\ \nu_\tau(x) \end{pmatrix}_L = U \begin{pmatrix} \nu_1(x) \\ \nu_2(x) \\ \nu_3(x) \end{pmatrix}_L = \begin{pmatrix} U_{e1} & U_{e2} & U_{e3} \\ U_{\mu 1} & U_{\mu 2} & U_{\mu 3} \\ U_{\tau 1} & U_{\tau 2} & U_{\tau 3} \end{pmatrix} \begin{pmatrix} \nu_1(x) \\ \nu_2(x) \\ \nu_3(x) \end{pmatrix}_L \tag{1.11}$$

In Eq. (1.11), $\nu_{eL}(x)$, $\nu_{\mu L}(x)$ and $\nu_{\tau L}(x)$ are the fields describing the left-handed *flavour eigenstate* neutrinos, i.e. the neutrinos coupling to charged leptons e, μ and τ via weak charged current processes, and $\nu_{1L}(x)$, $\nu_{2L}(x)$ and $\nu_{3L}(x)$ are the fields describing the left-handed *mass eigenstate* neutrinos with masses m_1, m_2 and m_3. The relation (1.11) can be shortened to:[4]

$$\nu_{\alpha L}(x) = \sum_i U_{\alpha i} \nu_{iL}(x) \tag{1.12}$$

where $\alpha = e, \mu, \tau$ and $i = 1, 2, 3$. As a consequence of flavour mixing, the neutrino that couples to a given flavour charged lepton via charged current is not a mass eigenstate, but a *coherent superposition of mass eigenstates*:

$$\begin{aligned} \mathscr{L}_{CC} &= \frac{g}{\sqrt{2}} W_\mu^- \sum_{\alpha=e,\mu,\tau} \overline{\ell}_{\alpha L} \gamma^\mu \nu_{\alpha L} + \text{h.c.} \\ &= \frac{g}{\sqrt{2}} W_\mu^- \sum_{\alpha=e,\mu,\tau} \overline{\ell}_{\alpha L} \gamma^\mu \sum_{i=1,2,3} U_{\alpha i} \nu_{iL} + \text{h.c.} \end{aligned} \tag{1.13}$$

Since associated with a change of basis, the lepton mixing matrix is unitary. Likewise the CKM (Cabibbo–Kobayashi–Maskawa) matrix for quarks, the PMNS satisfies unitarity relations, derived from $UU^\dagger = U^\dagger U = \mathbf{1}$:

$$\sum_i U_{\alpha i} U_{\beta i}^* = \delta_{\alpha\beta} \qquad \alpha, \beta = e, \mu, \tau \tag{1.14}$$

$$\sum_\alpha U_{\alpha i}^* U_{\alpha j} = \delta_{ij} \qquad i, j = 1, 2, 3 \tag{1.15}$$

Like any 3×3 unitary matrix, U can be parametrized by 3 mixing angles and 6 phases. However, not all of these phases are physical, since lepton fields can be rephased in order to absorb some of them. If one considers neutrinos to be Dirac fermions, then, the charged lepton and the neutrino fields can both be rephased as follows:

$$\ell_\alpha(x) \to e^{i\phi_\alpha} \ell_\alpha(x) \qquad \nu_i(x) \to e^{i\phi_i} \nu_i(x) \tag{1.16}$$

[3]The neutrino flavour basis is defined as the weak eigenstate basis corresponding to the charged lepton mass eigenstates e, μ and τ.

[4]In the following, for the sake of simplicity, the left-handedness subscript L and the x dependence of the fields will be omitted.

where $\ell_\alpha(x)$ and $\nu_i(x)$ denote 4-component Dirac fields[5]. These rephasing transformations leave the CC term (1.13) invariant, provided that the mixing matrix is redefined as follows:

$$U_{\alpha i} \to e^{i(\phi_\alpha - \phi_i)} U_{\alpha i} \tag{1.17}$$

Since there are 5 indipendent phase differences $\phi_\alpha - \phi_i$, it is possible to remove 5 phases from the PMNS matrix, leaving only one physical CP-violating phase, as happens for the CKM matrix. If one assumes neutrinos to be Majorana fermions, conversely, it is not possible to rephase the left-handed neutrino fields, because it would make their masses complex. Indeed, Majorana mass terms are of the form $-\frac{1}{2} m_i \nu_{iL}^T C \nu_{iL} + \text{h.c}$, where the charge conjugation matrix C satisfies the property $C\gamma_\mu C^{-1} = -\gamma_\mu^T$. In such a case, as a result, only the charged lepton fields can be rephased, leading to:

$$U_{\alpha i} \to e^{i\phi_\alpha} U_{\alpha i} \tag{1.18}$$

In the Majorana case, one is left with 3 physical CP-violating phases, instead of a single one as in the Dirac case. The parameter counting can be generalized to an arbitrary number n of lepton flavours. In the Dirac case, the lepton mixing matrix can be parametrized by $n(n-1)/2$ mixing angles and $(n-1)(n-2)/2$ phases, whereas in the Majorana case $n-1$ additional phases would arise. Therefore, in the framework of three active massive neutrinos, the PMNS matrix can be factorized into the product of three rotations through angles θ_{23}, θ_{13} and θ_{12}, where the second (unitary) rotation depends on a phase δ_{CP}, and of a diagonal matrix of phases P:

$$U = \begin{pmatrix} 1 & 0 & 0 \\ 0 & c_{23} & s_{23} \\ 0 & -s_{23} & c_{23} \end{pmatrix} \begin{pmatrix} c_{13} & 0 & s_{13} e^{-i\delta_{\text{CP}}} \\ 0 & 1 & 0 \\ -s_{13} e^{i\delta_{\text{CP}}} & 0 & c_{13} \end{pmatrix} \begin{pmatrix} c_{12} & s_{12} & 0 \\ -s_{12} & c_{12} & 0 \\ 0 & 0 & 1 \end{pmatrix} P \tag{1.19}$$

$$= \begin{pmatrix} c_{12}c_{13} & s_{12}c_{13} & s_{13} e^{-i\delta_{\text{CP}}} \\ -s_{12}c_{23} - c_{12}s_{13}s_{23} e^{i\delta_{\text{CP}}} & c_{12}c_{23} - s_{12}s_{13}s_{23} e^{i\delta_{\text{CP}}} & c_{13}s_{23} \\ s_{12}s_{23} - c_{12}s_{13}c_{23} e^{i\delta_{\text{CP}}} & -c_{12}s_{23} - s_{12}s_{13}c_{23} e^{i\delta_{\text{CP}}} & c_{13}c_{23} \end{pmatrix} P \tag{1.20}$$

where $c_{ij} \equiv \cos\theta_{ij}$, $s_{ij} \equiv \sin\theta_{ij}$ and P is either the unit matrix $\mathbf{1}$ in the Dirac case or a diagonal matrix containing the two additional phases associated with the Majorana nature of neutrinos. Without loss of generality, one can take $\theta_{ij} \in [0, \frac{\pi}{2}]$ and $\delta_{\text{CP}} \in [0, 2\pi)$. Instead, in the Majorana case, the matrix P can be parametrized according to [1, 4]:

$$P_{\text{Majorana}} = \begin{pmatrix} e^{i\alpha_1} & 0 & 0 \\ 0 & e^{i\alpha_2} & 0 \\ 0 & 0 & 1 \end{pmatrix} \tag{1.21}$$

The phase δ_{CP} is generally referred to as the *Dirac phase* of the PMNS matrix, whereas the phases contained in P are the so-called *Majorana phases*. However, since Majorana phases do not enter oscillation probabilities[6], the next sections will not be concerned with them. Conversely, the Dirac phase δ_{CP} is of key importance in neutrino oscillations, since it gives rise to an asymmetry between neutrino and antineutrino oscillations in vacuum.

[5]Note that the phases of the left-handed and right-handed lepton fields are shifted by the same amount, in order not to affect the Dirac mass terms $-\sum_\alpha m_{\ell_\alpha} \bar{\ell}_{\alpha R} \ell_{\alpha L} - \sum_i m_i \bar{\nu}_{iR} \nu_{iL} + \text{h.c}$.

[6]Majorana phases appear instead in lepton number violating processes like *neutrinoless double beta decay*, where the Majorana nature of neutrinos play a crucial role.

1.3 Neutrino oscillations in vacuum

In the standard theory of neutrino oscillations [7], a neutrino flavour eigenstate is a coherent superposition of mass eigenstates determined by the PMNS matrix:[7]

$$|\nu_\alpha\rangle = \sum_k U^*_{\alpha k} |\nu_k\rangle \qquad \alpha = e, \mu, \tau \tag{1.22}$$

In vacuum, the massive neutrino states $|\nu_k\rangle$ are eigenstates of the Hamiltonian:

$$H |\nu_k\rangle = E_k |\nu_k\rangle \tag{1.23}$$

with energy eigenvalues $E_k = \sqrt{|\vec{p}|^2 + m_k^2}$. The solution of the Schrödinger equation:

$$i\frac{\partial}{\partial t} |\nu_k(t)\rangle = H |\nu_k(t)\rangle \tag{1.24}$$

implies that the massive neutrino states evolve in time as plane waves:

$$|\nu_k(t)\rangle = e^{-iE_k t} |\nu_k\rangle \tag{1.25}$$

where $|\nu_k\rangle = |\nu_k(t=0)\rangle$. Let consider now a flavour state $|\nu_\alpha(t)\rangle$ which describes a neutrino created at time $t = 0$ with a definite flavour α. From Eqs. (1.22) and (1.25), the time evolution of this state is given by:

$$|\nu_\alpha(t)\rangle = \sum_k U^*_{\alpha k} e^{-iE_k t} |\nu_k\rangle \tag{1.26}$$

such that $|\nu_\alpha\rangle = |\nu_\alpha(t=0)\rangle$. Using the unitarity relation of Eq. (1.15), it is possible to invert Eq. (1.22) in order to express the massive states in terms of the flavour ones:

$$|\nu_k\rangle = \sum_\alpha U_{\alpha k} |\nu_\alpha\rangle \tag{1.27}$$

Substituting Eq. (1.27) into Eq. (1.26) one obtains:

$$|\nu_\alpha(t)\rangle = \sum_{\beta=e,\mu,\tau} \left(\sum_k U^*_{\alpha k} e^{-iE_k t} U_{\beta k} \right) |\nu_\beta\rangle \tag{1.28}$$

Therefore, the superposition of massive neutrino states $|\nu_\alpha(t)\rangle$, which is a pure flavour state at $t = 0$, becomes a superposition of different flavor states at $t > 0$. The probability amplitude of $\nu_\alpha \to \nu_\beta$ transitions, as a function of time, is given by the coefficient of $|\nu_\beta\rangle$:

$$A_{\nu_\alpha \to \nu_\beta}(t) \equiv \langle \nu_\beta | \nu_\alpha(t) \rangle = \sum_k U^*_{\alpha k} U_{\beta k} e^{-iE_k t} \tag{1.29}$$

The *transition probability* is thus given by:

$$P_{\nu_\alpha \to \nu_\beta}(t) = \left| A_{\nu_\alpha \to \nu_\beta}(t) \right|^2 = \sum_{k,j} U^*_{\alpha k} U_{\beta k} U_{\alpha j} U^*_{\beta j} e^{-i(E_k - E_j)t} \tag{1.30}$$

[7] The relation between the flavour and mass eigenstate neutrino *states* involves the complex conjugate of the PMNS matrix, unlike its definition used in Eq. (1.12) for neutrino *fields*. This is due to the fact that the quantum neutrino field $\nu_\alpha(x)$ annihilates a neutrino of flavour α, whereas the neutrino state $|\nu_\alpha(\vec{p})\rangle$ is obtained by acting with the creation operator $a^\dagger_\alpha(\vec{p})$ on the vacuum. In the case of antineutrinos, in turn, one would have $\overline{\nu}_\alpha(x) = \sum_i U^*_{\alpha i} \overline{\nu}_i(x)$ for fields and $|\overline{\nu}_\alpha\rangle = \sum_i U_{\alpha i} |\overline{\nu}_i\rangle$ for states [6].

Since neutrinos are ultra-relativistic particles in all practical experimental conditions[8], the energy eigenvalues can be approximated according to:[9]

$$E_k = \sqrt{p_k^2 + m_k^2} \simeq E + \frac{m_k^2}{2E} \tag{1.31}$$

That means that, if the neutrino *squared-mass differences* are indicated with $\Delta m^2_{kj} \equiv m_k^2 - m_j^2$, the energy eigenvalues difference can be approximated as $E_k - E_j \simeq \Delta m^2_{kj}/2E$. Moreover, the propagation time t is not measured in neutrino oscillation experiments; instead, what is known, is the distance L between the source and the detector. Since ultra-relativistic neutrinos propagate almost at the speed of light, the distance travelled by a neutrino is approximated as $L \simeq ct$. The transition probability can thus be expressed as:

$$P_{\nu_\alpha \to \nu_\beta}(L, E) = \sum_{k,j} U^*_{\alpha k} U_{\beta k} U_{\alpha j} U^*_{\beta j} \exp\left(-i \frac{\Delta m^2_{kj} L}{2E}\right) \tag{1.32}$$

The amplitude of oscillations is determined only by the elements of the mixing matrix U, whereas the phases depend on the squared mass differences Δm^2_{kj} and the quantities depending on the experiment, i.e. the source-detector distance L (the *baseline*, in jargon) and the neutrino energy E. Although positive measurements of neutrino oscillations imply neutrinos to be massive particles, they yield precise informations only on the values of the squared-mass differences Δm^2_{kj}, but not on the absolute values of neutrino masses, except the obvious constraint that m_k^2 or m_j^2 must be larger than $|\Delta m^2_{kj}|$.
The neutrino oscillation formula (1.32), by using the complex exponential identity $e^{ix} = \cos x + i \sin x = 1 - 2\sin^2(x/2) + i \sin x$, can be rewritten explicitely as:

$$\begin{aligned} P_{\nu_\alpha \to \nu_\beta}(L, E) = &\sum_{k,j} U^*_{\alpha k} U_{\beta k} U_{\alpha j} U^*_{\beta j} - 2 \sum_{k \neq j} U^*_{\alpha k} U_{\beta k} U_{\alpha j} U^*_{\beta j} \sin^2\left(\frac{\Delta m^2_{kj} L}{4E}\right) \\ &- i \sum_{k \neq j} U^*_{\alpha k} U_{\beta k} U_{\alpha j} U^*_{\beta j} \sin\left(\frac{\Delta m^2_{kj} L}{2E}\right) \end{aligned} \tag{1.33}$$

which, in turn, can be simplified, leading to the well-known formula for neutrino transition probability:

$$\begin{aligned} P_{\nu_\alpha \to \nu_\beta}(L, E) = \delta_{\alpha\beta} &- 4 \sum_{k>j} \mathrm{Re}[U^*_{\alpha k} U_{\beta k} U_{\alpha j} U^*_{\beta j}] \sin^2\left(\frac{\Delta m^2_{kj} L}{4E}\right) \\ &+ 2 \sum_{k>j} \mathrm{Im}[U^*_{\alpha k} U_{\beta k} U_{\alpha j} U^*_{\beta j}] \sin\left(\frac{\Delta m^2_{kj} L}{2E}\right) \end{aligned} \tag{1.34}$$

For antineutrino oscillations, it is sufficient to replace U by U^* in Eq. (1.34), leading to a change in the sign of the last term. The formula of transition probability in Eq. (1.34) suggests some straightforward comments which can be made about the properties of neutrino oscillations [6]. Oscillations necessarily require neutrinos to have non-degenerate masses ($\Delta m^2_{kj} \neq 0$) and non-trivial flavour mixing ($U \neq \mathbf{1}$). Moreover, the oscillation

[8] Despite the small values of neutrino masses, assuming neutrinos to be ultra-relativistic particles their mass contribution can be neglected and their energy can be estimated as $E = |\vec{p}|$.

[9] In the standard derivation of oscillation formula, the propagating mass eigenstates are supposed to be described by plane waves with well-defined momenta $\vec{p_k}$, which are assumed to be equal ($\vec{p_k} = \vec{p}$).

probability $P_{\nu_\alpha \to \nu_\beta}$ depends on the three mixing angles θ_{12}, θ_{23} and θ_{13} and on two independent squared-mass differences, which can be chosen to be Δm^2_{21} and Δm^2_{31} (then Δm^2_{32} is determined as $\Delta m^2_{32} = \Delta m^2_{31} - \Delta m^2_{21}$). As previously mentioned, oscillations also depend on the CP-violating Dirac phase $\delta_{\rm CP}$, but not on the Majorana phases. This can be easily explained from the fact that, since the PMNS matrix entries appear in Eq. (1.34) only through the combinations $U_{\alpha k} U^*_{\beta k}$, then, the phases contained in the diagonal matrix P of Eq. (1.19) will not give a contribution in the transition probability. Therefore, Dirac and Majorana neutrinos have the same oscillation probabilities.
In the literature, neutrino oscillation channels where $\alpha \neq \beta$ are called *appearance channels*, whereas the channels where $\alpha = \beta$ are referred to as *disappearance channels*. The oscillation probabilities of the appearance channels are usually called *transition probabilities*, whereas in the disappearance channels they are referred to as *survival probabilities*. Since in the case of the survival probabilities the quartic products of Eq. (1.34) are real and equal to $|U_{\alpha k}|^2 |U_{\alpha j}|^2$, they can be rewritten in a simplest form:

$$P(\nu_\alpha \to \nu_\alpha) = 1 - 4 \sum_{k>j} |U_{\alpha k}|^2 |U_{\alpha j}|^2 \sin^2 \left(\frac{\Delta m^2_{kj} L}{4E} \right) = P(\overline{\nu}_\alpha \to \overline{\nu}_\alpha) \tag{1.35}$$

Therefore, as a consequence of the equality in Eq. (1.35) between the survival probabilities for neutrinos and antineutrinos, CP violation can be observed only in appearance channels and not in the disappearance ones.

1.4 Neutrino oscillations in matter

The propagation of neutrinos in matter is affected by their interactions with electrons, protons and neutrons, leading to a variety of new phenomena, among which [6]:

- oscillations in matter with modified parameters with respect to vacuum oscillations.
- resonant amplification of oscillations in a constant density medium.
- adiabatic flavour conversion in a medium of varying density like the Sun.

Neutrino propagation in matter can be described by a Schrödinger-like equation:

$$i \frac{d}{dt} |\nu_\alpha(t)\rangle = H \, |\nu_\alpha(t)\rangle \tag{1.36}$$

where $|\nu_\alpha(t)\rangle$ is the neutrino state vector at time t with initial flavor α.
The total Hamiltonian in matter H can actually be split into a *kinetic energy* term H_0, describing the free propagation of neutrinos in vacuum, and into an *effective potential* term V, induced by the interactions of neutrinos in the medium:

$$H = H_0 + V \tag{1.37}$$

In the mass eigenstates basis, the vacuum Hamiltonian is diagonal with eigenvalues E_k, i.e. $\langle \nu_k | H | \nu_j \rangle = E_k \delta_{kj}$. The free Hamiltonian H_0 can be expressed in the flavour basis as:

$$H_0 = U \begin{pmatrix} E_1 & 0 & 0 \\ 0 & E_2 & 0 \\ 0 & 0 & E_3 \end{pmatrix} U^\dagger \qquad E_k = \sqrt{p^2 + m_k^2} \tag{1.38}$$

When assuming ultra-relativistic neutrinos, the energy eigenvalues can be expanded as $E_k \simeq p + \frac{m_k^2}{2E}$. Furthermore, with the redefinition $H_0 \to H_0 - p\mathbf{1}$, the vacuum Hamiltonian can be rewritten in a simplest form:

$$H_0 = \frac{1}{2E}\, U \begin{pmatrix} m_1^2 & 0 & 0 \\ 0 & m_2^2 & 0 \\ 0 & 0 & m_3^2 \end{pmatrix} U^\dagger = \frac{M_\nu^\dagger M_\nu}{2E} \tag{1.39}$$

When neutrinos propagate in matter, they are subject to a potential induced by *coherent forward elastic scattering* on the particles in the medium, that is electrons and nucleons [7]. Since the neutrino momentum is left unchanged by the coherent forward scattering, as a result, the scattered neutrino can interfere with the propagation of the unscattered ones. Therefore, the evolution equation of flavor neutrinos propagating in matter is affected by an effective potential V induced by their coherent interactions with the medium itself. The *charged current* (CC) *coherent forward scattering* is mediated by the exchange of a $W^\pm$ boson and is present only for electron neutrinos, since ordinary matter does not contain muons nor tau leptons. On the other hand, the *neutral current* (NC) *coherent forward scattering*, mediated by the exchange of a Z^0 boson, is identical for all neutrino flavours. The Feynman diagrams of CC and NC scattering are shown in Fig. 1.1 [7]. This effective potential is responsible for modification in the mixing of neutrinos, as will be shown hereinafter.

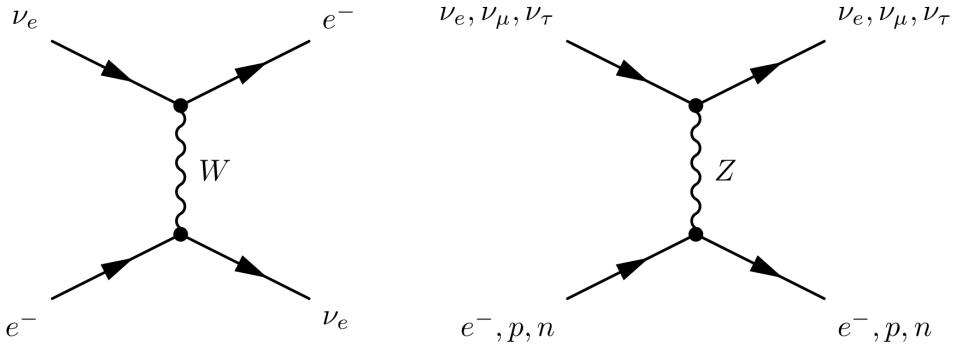

Figure 1.1: Feynman diagrams of the neutrino coherent forward elastic scattering processes inducing the potential V_{CC} through $W^\pm$ boson exchange and the potential V_{NC} through Z^0 boson exchange. Figure from [7].

The matter potential is diagonal in the flavour basis:

$$V_\alpha = V_{CC}\, \delta_{\alpha e} + V_{NC} \tag{1.40}$$

where the CC potential depends on the neutrino flavour α:

$$V_{CC}\, \delta_{\alpha e} = \sqrt{2} G_F n_e(x)\, \delta_{\alpha e} \tag{1.41}$$

while the NC potential is flavour universal:[10]

$$V_{NC} = -\frac{G_F}{\sqrt{2}} n_n(x) \tag{1.42}$$

where n_e and n_n are the electron and neutron densities in the medium, respectively[11]. In matter, the propagation eigenstates are the eigenstates of the matter Hamiltonian $|\nu_i^m\rangle$, and not the mass eigenstates $|\nu_i\rangle$, as happens in vacuum. The *matter eigenstates* $|\nu_i^m\rangle$

[10] For antineutrinos, the matter potential has the opposite sign, i.e. $V_\alpha(\overline{\nu}) = -V_\alpha(\nu)$.

[11] The NC contribution to the matter potential only depends on the neutron density n_n. This is due to the fact that, if one assumes a neutral medium, then $n_p = n_e$ and proton and electron contributions cancel out in V_{NC}.

are related to the flavour eigenstates by the *mixing matrix in matter* U_m:

$$\begin{pmatrix} |\nu_e\rangle \\ |\nu_\mu\rangle \\ |\nu_\tau\rangle \end{pmatrix} = U_m^* \begin{pmatrix} |\nu_1^m\rangle \\ |\nu_2^m\rangle \\ |\nu_3^m\rangle \end{pmatrix} \tag{1.43}$$

diagonalizing H:

$$H = U_m \begin{pmatrix} E_1^m & 0 & 0 \\ 0 & E_2^m & 0 \\ 0 & 0 & E_3^m \end{pmatrix} U_m^\dagger \tag{1.44}$$

The eigenvalues E_i^m of the matter Hamiltonian H are called *energy levels in matter*. Considering the two-flavour framework[12], the matter Hamiltonian can be expressed in the flavour eigenstates basis $\{|\nu_e\rangle, |\nu_\beta\rangle\}$, with $\beta = \mu, \tau$, as follows:

$$H = \begin{pmatrix} -\frac{\Delta m^2}{4E}\cos 2\theta \pm \sqrt{2} G_F n_e & \frac{\Delta m^2}{4E}\sin 2\theta \\ \frac{\Delta m^2}{4E}\sin 2\theta & \frac{\Delta m^2}{4E}\cos 2\theta \end{pmatrix} \tag{1.45}$$

in which Δm^2 and θ are the relevant oscillation parameters in vacuum, whereas the $\pm$ of the V_{CC} potential distinguish neutrinos from antineutrinos, respectively. By means of the effective mixing matrix in matter U_m:

$$U_m = \begin{pmatrix} \cos\theta_m & \sin\theta_m \\ -\sin\theta_m & \cos\theta_m \end{pmatrix} \tag{1.46}$$

it is possible to diagonalize the matter Hamiltonian in Eq. (1.45) as follows:

$$H = U_m \begin{pmatrix} E_1^m & 0 \\ 0 & E_2^m \end{pmatrix} U_m^\dagger \tag{1.47}$$

The difference of energy levels in matter is given by:[13]

$$E_2^m - E_1^m = \frac{\Delta m^2}{2E}\sqrt{\left(1 \mp \frac{n_e}{n_{\text{res}}}\right)^2 \cos^2 2\theta + \sin^2 2\theta} \tag{1.48}$$

while the *effective mixing angle in matter* θ_m can be inferred from the relations:

$$\sin 2\theta_m = \frac{\sin 2\theta}{\sqrt{\left(1 \mp \frac{n_e}{n_{\text{res}}}\right)^2 \cos^2 2\theta + \sin^2 2\theta}} \tag{1.49}$$

$$\cos 2\theta_m = \frac{\left(1 \mp \frac{n_e}{n_{\text{res}}}\right)\cos 2\theta}{\sqrt{\left(1 \mp \frac{n_e}{n_{\text{res}}}\right)^2 \cos^2 2\theta + \sin^2 2\theta}} \tag{1.50}$$

in which we have introduced the *resonance density*:

$$n_{\text{res}} = \frac{\Delta m^2 \cos 2\theta}{2\sqrt{2} G_F E} \tag{1.51}$$

[12] Working in the two-flavour framework is a good approximation in many physical contexts, such as the neutrino propagation in the Sun.

[13] In these relations, the $\mp$ sign distinguish neutrinos from antineutrinos, respectively.

From Eq. (1.48) one can determine the *effective squared-mass difference* Δm^2_m:

$$\Delta m^2_m = \Delta m^2 \sqrt{\left(1 \mp \frac{n_e}{n_{\text{res}}}\right)^2 \cos^2 2\theta + \sin^2 2\theta} \tag{1.52}$$

Moreover, the mixing angle in matter θ_m can be obtained directly from:

$$\tan 2\theta_m = \frac{\tan 2\theta}{1 \mp \frac{n_e}{n_{\text{res}}}} \tag{1.53}$$

simply by means of Eqs. (1.49) and (1.50).
The interesting phenomenon arising is the *resonance* condition occurring when the electron density n_e becomes equal to the resonance density n_{res}, namely when $\Delta m^2 \cos 2\theta = 2\sqrt{2} G_F n_e E$. In particular, when $n_e = n_{\text{res}}$, the mixing angle in matter θ_m becomes maximal, irrespective of the value assumed by the vacuum mixing angle θ. The maximal mixing angle at the resonance condition leads to the possibility of total transitions between the two flavors, if the resonance region is wide enough. This mechanism is the well-known *Mikheev-Smirnov-Wolfenstein* (MSW) *resonance*.
The physics of neutrino flavour transitions in matter depends on whether the matter density is constant or not. In particular, the MSW mechanism predict the possibility to have resonant flavor transitions when neutrinos propagate in a medium with varying density, explaining the flavor conversion of solar neutrinos during their propagation out of the Sun, even in the case of a small vacuum mixing angle.

1.5 Neutrino mass ordering

The ordering of neutrino masses is one of the most compelling questions in the field of neutrino physics. Since the oscillation probability is sensitive to squared mass differences Δm^2_{kj} only, neither their absolute mass scale (equivalently, the absolute value of the lightest mass eigenstate) nor their ordering can be determined by neutrino oscillations. The experimental results obtained from solar and atmospheric neutrino experiments so far indicate the presence of two very distinct mass differences among the neutrino mass eigenstates: $\Delta m^2_{\text{sol}} \sim 7.5 \cdot 10^{-5}$ eV^2 and $\Delta m^2_{\text{atm}} \sim 2.5 \cdot 10^{-3}$ eV^2 [8], such that $\Delta m^2_{\text{sol}} \ll \Delta m^2_{\text{atm}}$. In general, the small solar mass splitting Δm^2_{sol} is identified with the squared mass splitting between ν_1 and ν_2 mass eigenstates, labelled such that $m_2 > m_1$, i.e. $\Delta m^2_{\text{sol}} = \Delta m^2_{21} > 0$ [6]. The large atmospheric mass scale Δm^2_{atm} can thus be identified with $|\Delta m^2_{32}|$ or $|\Delta m^2_{31}|$. Since $\Delta m^2_{\text{sol}} \ll \Delta m^2_{\text{atm}}$, then the following relations among squared mass differences hold:

$$\Delta m^2_{\text{sol}} = \Delta m^2_{21} \ll |\Delta m^2_{31}| \simeq |\Delta m^2_{32}| \simeq \Delta m^2_{\text{atm}} \tag{1.54}$$

Depending on the sign of Δm^2_{31}, there are two different possibilities for the ordering of neutrino masses. The *normal ordering* or *normal hierarchy* is characterized by $\Delta m^2_{31} > 0$ and thus determined by the $m_1 < m_2 < m_3$ mass ordering. The *inverted ordering* or *inverted hierarchy* is instead characterized by $\Delta m^2_{31} < 0$ and thus determined by the $m_3 < m_1 < m_2$ mass ordering. The two neutrino mass hierarchies are shown in Fig. 1.2; for each hierarchy, the neutrino mass eigenstates are illustrated according to their composition in terms of flavor eigenstates. The positive (negative) sign of Δm^2_{31} thus implies that the lightest mass eigenstate ν_1 is the eigenstate having the largest mixing with the electron (tau) neutrino, and thus the smallest mixing with the tau (electron) neutrino [10].

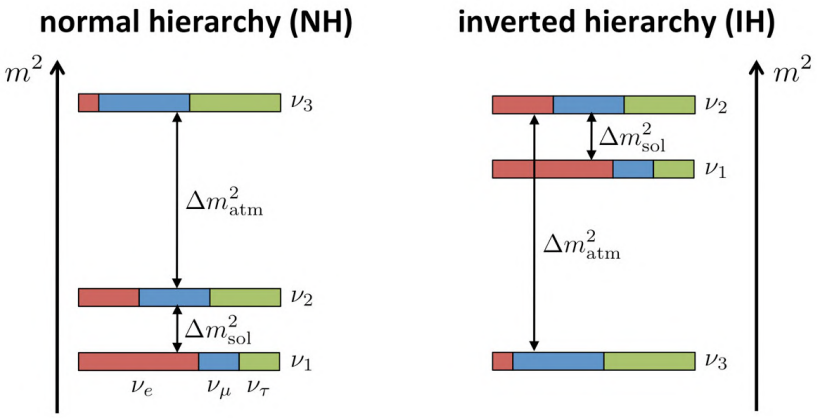

Figure 1.2: Scheme of normal and inverted neutrino mass hierarchies. The colours indicate the flavour composition of each mass eigenstate. Figure from [9].

1.6 CP violation in neutrino oscillations

The violation of the CP symmetry in neutrino oscillations [6] originates from the possibility that neutrinos and antineutrinos oscillate with different probabilities in vacuum. In the minimally extended SM, it arises from the dependence of the oscillation probability on the phase $\delta_{\rm CP}$ of the PMNS matrix. In a more general context, the transformations produced by the different discrete symmetries[14] on neutrino oscillation probabilities can be summarized as:

$$\begin{aligned} P(\nu_\alpha \to \nu_\beta) &\xrightarrow{\rm CP} P(\overline{\nu}_\alpha \to \overline{\nu}_\beta) \\ &\xrightarrow{\rm T} P(\nu_\beta \to \nu_\alpha) \\ &\xrightarrow{\rm CPT} P(\overline{\nu}_\beta \to \overline{\nu}_\alpha) \end{aligned} \tag{1.55}$$

The assumption of CPT conservation $P(\nu_\alpha \to \nu_\beta) = P(\overline{\nu}_\beta \to \overline{\nu}_\alpha)$ implies that the CP and T asymmetries in neutrino oscillations are equal:

$$A^{\rm CP}_{\alpha\beta} \equiv \frac{P(\nu_\alpha \to \nu_\beta) - P(\overline{\nu}_\alpha \to \overline{\nu}_\beta)}{P(\nu_\alpha \to \nu_\beta) + P(\overline{\nu}_\alpha \to \overline{\nu}_\beta)} = \frac{P(\nu_\alpha \to \nu_\beta) - P(\nu_\beta \to \nu_\alpha)}{P(\nu_\alpha \to \nu_\beta) + P(\nu_\beta \to \nu_\alpha)} \equiv A^{\rm T}_{\alpha\beta} \tag{1.56}$$

Moreover, another implication of CPT invariance is $P(\nu_\alpha \to \nu_\alpha) = P(\overline{\nu}_\alpha \to \overline{\nu}_\alpha)$, namely the impossibility to observe CP violation in disappearance channels, as already inferred from the general three-flavour oscillation formula in Eq. (1.35). In order to study the effect of CP violation (CPV) in neutrino oscillations, it can be useful to introduce the quantity $\Delta P_{\alpha\beta} \equiv P(\nu_\alpha \to \nu_\beta) - P(\overline{\nu}_\alpha \to \overline{\nu}_\beta)$, which in turn corresponds to twice the CP-odd part in the three-flavour oscillation probability of Eq. (1.34), namely:

$$\Delta P_{\alpha\beta} = 4 \sum_{k>j} {\rm Im}[U^*_{\alpha k} U_{\beta k} U_{\alpha j} U^*_{\beta j}] \sin\left(\frac{\Delta m^2_{kj} L}{2E}\right) \tag{1.57}$$

which can also be expressed as:

[14] It is important to point out that $P(\overline{\nu}_\alpha \to \overline{\nu}_\beta)$ is $P(\nu_\alpha \to \nu_\beta)$ after a CP transformation, not after a C-only transformation. Indeed, ν_α and ν_β are left-handed neutrinos and their corresponding antiparticles $\overline{\nu}_\alpha$ and $\overline{\nu}_\beta$ are right-handed antineutrinos, namely the CP conjugates of ν_α and ν_β [6].

$$\Delta P_{\alpha\beta} = \pm 16 J \sin\left(\frac{\Delta m^2_{21} L}{4E}\right) \sin\left(\frac{\Delta m^2_{31} L}{4E}\right) \sin\left(\frac{\Delta m^2_{32} L}{4E}\right) \tag{1.58}$$

by defining:

$$J \equiv \mathrm{Im}\left[U^*_{e1} U_{\mu 1} U_{e2} U^*_{\mu 2}\right] \tag{1.59}$$

In Eq. (1.58) one must consider the + sign when (α, β, γ), with $\gamma \neq \alpha, \beta$, is an even permutation of (e, μ, τ) and a - sign when it is an odd permutation[15]. The quantity J defined in Eq. (1.59) is called the *Jarlskog invariant*[16] and it constitutes a measure of CP violation from the Dirac phase δ_{CP}. Using the standard parametrization of the PMNS matrix, the Jarlskog invariant can be written as:

$$J = \frac{1}{8} \cos\theta_{13} \sin 2\theta_{12} \sin 2\theta_{13} \sin 2\theta_{23} \sin\delta_{\mathrm{CP}} \tag{1.60}$$

Therefore, a necessary condition for CP violation in neutrino oscillations is that all three mixing angles θ_{ij} are nonzero and that the phase δ_{CP} is different from 0 and π. In addition, from Eq. (1.58) one can infer that all the squared mass-differences must be non vanishing, that is, all neutrinos masses should be different. The conditions for CPV in neutrino oscillations can thus be summarized as follows:

$$\text{CPV in oscillations} \quad \Longleftrightarrow \quad \delta_{\mathrm{CP}} \neq 0, \pi \ , \ \theta_{ij} \neq 0 \ , \ m_i \neq m_j \quad \forall i \neq j \tag{1.61}$$

1.7 Three-flavour oscillations with matter effects

Since in long-baseline oscillation experiments the neutrino beam propagate through the Earth's crust and mantle, oscillations are thus affected by neutrino interactions in a medium with varying matter density[17]. Unlike solar neutrinos, for which matter perturbations cause a strong change of the oscillation probability, the nearly constant, moderate-size matter density entails a small perturbation for accelerator neutrinos and it can be accounted for by considering a perturbative expansion of the full oscillation formula and retaining only first-order perturbations in $\alpha \equiv \Delta m^2_{21} \,/\, |\Delta m^2_{31}| \simeq 0.03$ [10]. The perturbative expansion of $\nu_\mu \to \nu_e$ oscillation probability at the second order in α is the master formula of long-baseline experiments:

$$\begin{aligned} P(\nu_\mu \to \nu_e) \simeq \quad & \sin^2 2\theta_{13} \sin^2\theta_{23} \frac{\sin^2\left[(1-A)\Delta_{31}\right]}{(1-A)^2} \\ & - \alpha \sin 2\theta_{13}\, \xi \sin\delta_{\mathrm{CP}} \sin\Delta_{31} \frac{\sin\left(A\Delta_{31}\right)}{A} \frac{\sin\left[(1-A)\Delta_{31}\right]}{(1-A)} \\ & + \alpha \sin 2\theta_{13}\, \xi \cos\delta_{\mathrm{CP}} \cos\Delta_{31} \frac{\sin\left(A\Delta_{31}\right)}{A} \frac{\sin\left[(1-A)\Delta_{31}\right]}{(1-A)} \\ & + \alpha^2 \cos^2\theta_{23} \sin^2 2\theta_{12} \frac{\sin^2\left(A\Delta_{31}\right)}{A^2} \end{aligned} \tag{1.62}$$

[15] It should be stressed that the CP-violating term in neutrino oscillations is *universal*, hence, up to a sign, it does not depend on the oscillation channel. This conclusion can be inferred straightforwardly from the unitarity of the PMNS matrix, which implies $\mathrm{Im}[U^*_{e1} U_{\mu 1} U_{e2} U^*_{\mu 2}] = -\,\mathrm{Im}[U^*_{e1} U_{\tau 1} U_{e2} U^*_{\tau 2}] = \mathrm{Im}[U^*_{\mu 1} U_{\tau 1} U_{\mu 2} U^*_{\tau 2}]$. Hence, one would get $\Delta P_{e\mu} = -\Delta P_{e\tau} = \Delta P_{\mu\tau}$ [6].

[16] The name *invariant* refers to the fact that J does not depend on the phase convention used for the PMNS matrix, that is, it is invariant under rephasings of lepton fields [6].

[17] Despite the electron density is not constant in the Earth, a good approximation is to consider it as made of multiple layers of constant density (the crust, the mantle, the outer core and the inner core). The two-layer (mantle-core) approximation is in general sufficient in the study of neutrino oscillations in the Earth [6].

where $\Delta_{31} \equiv \Delta m^2_{31} L/4E$ and the term $\xi = \cos\theta_{13} \sin 2\theta_{12} \sin 2\theta_{23}$ is $\mathcal{O}(1)$. The first term corresponds to the dominant Δm^2_{31}-driven oscillation, the fourth one the Δm^2_{21}-driven oscillation (as the presence of the suppression factor α^2 shows); the second and the third ones are the CP-odd and the CP-even terms. The parameter $A \equiv 2VE/\Delta m^2_{31} = 2\sqrt{2} G_F n_e E/\Delta m^2_{31}$ quantifies the importance of matter effects on Δm^2_{31}-driven oscillations [6]. The electron density n_e in matter is assumed to be constant in the oscillation probability formula[18]. The corresponding probability for $\overline{\nu}_\mu \to \overline{\nu}_e$ oscillations can be obtained by switching the signs of the CP-violating phase $\delta_{\rm CP}$ and of the matter parameter A.
The experimental challenge of long-baseline experiments will be to disentangle matter effects from CP violation, since both of them create an asymmetry between $\nu_\mu \to \nu_e$ and $\overline{\nu}_\mu \to \overline{\nu}_e$ oscillations, depending on the sign of Δm^2_{31} for matter effects and on the value of $\delta_{\rm CP}$ phase for CP violation. Even in the absence of CP violation, neutrino interactions with matter can induce an asymmetry between neutrino and antineutrino oscillations depending on the mass hierarchy: neutrino oscillations are enhanced (suppressed) over antineutrino oscillations for the normal (inverted) ordering. The mass hierarchy enters via the sign of A, depending on the sign of Δm^2_{31}. An experiment with a longer baseline will be more sensitive to the neutrino mass ordering, since in the few-GeV energy range the asymmetry from the matter effect increases with the baseline, as the neutrinos pass through more matter. Fig. 1.3 illustrates how the appearance probability for neutrinos and antineutrinos changes at longer baselines, considering the baseline of T2K [11] (295 km), NOνA [12] (810 km) and DUNE [13] (1300 km). The probabilities are plotted for all possible values of the unknown $\delta_{\rm CP}$ phase, tracing out ellipses in the bi-probability plot. The mass hierarchy discrimination is higher at larger baseline values but its determination is complicated by the lack of knowledge of $\delta_{\rm CP}$ phase; nevertheless at the longest baseline envisaged by the DUNE experiment the hierarchy-dependent matter effects become larger than any $\delta_{\rm CP}$-induced changes in the oscillation probabilities [14].

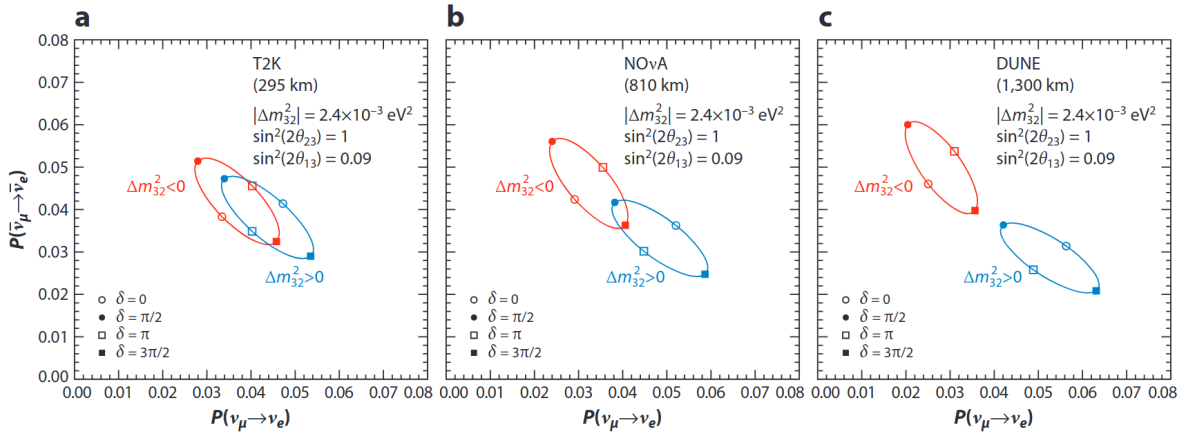

Figure 1.3: Bi-probability plot of $P(\overline{\nu}_\mu \to \overline{\nu}_e)$ versus $P(\nu_\mu \to \nu_e)$ for both mass orderings (red and blue ellipses) and for the full range of true $\delta_{\rm CP}$ (cycling around the ellipses). (a) At the T2K baseline, the neutrino and antineutrino appearance probabilities differ very little between the two hierarchies, thus offering poor hierarchy discrimination. (b) For NOνA, significant splitting of the two orderings occurs. (c) For DUNE, the separation is complete and an unambiguous determination of the hierarchy regardless of $\delta_{\rm CP}$ is possible. The figure is illustrative only, since other oscillation parameters are kept fixed. Figure from [14].

The 1300 km baseline of the DUNE experiment establishes one of its key strengths, enhancing its sensitivity to matter effect and making DUNE able to unambiguously determine the neutrino mass ordering and measure the value of $\delta_{\rm CP}$ [13].

[18] In practice, the assumption of a constant electron density n_e is a good approximation up to very long baselines, since neutrinos travel only through the mantle for $L \lesssim 11\,000$ km [6].

1.8 The current status of PMNS matrix and squared neutrino mass differences

The global picture of three active neutrino mixing parametrized by the PMNS matrix and two independent squared mass differences is supported by a large set of experimental results on neutrino oscillations [6]. In particular, the comprehensive set of neutrino experiments to date has measured five of the oscillation parameters: the three mixing angles θ_{12}, θ_{23}, θ_{13} and the two independent squared mass differences Δm^2_{21} and Δm^2_{32}. The neutrino mass hierarchy (i.e. the sign of Δm^2_{31}) is still unknown. The last unknown mixing angle θ_{13} was measured in 2012 by reactor experiments (Daya Bay [15], RENO [16], Double Chooz [17]) and its value turned out to be quite large. Indeed, the smallest neutrino mixing angle ($\theta_{13} \simeq 8.6^\circ$) has a size comparable with the Cabibbo angle ($\sim 13^\circ$), which is the largest mixing angle in the quark sector. The octant of θ_{23} is still largely undetermined since there is high ambiguity to whether its value is in the first octant ($\theta_{23} < \frac{\pi}{4}$), in the second octant ($\theta_{23} > \frac{\pi}{4}$) or corresponding to the maximal mixing angle ($\theta_{23} = \frac{\pi}{4}$), the latter indicating that ν_μ and ν_τ flavour composition are equal in the third neutrino mass eigenstate ν_3. The value of the CP-violating phase $\delta_{\rm CP}$ is only poorly constrained and its measurement will be one of the main goals of the next generation of long-baseline neutrino oscillation experiments, such as DUNE [13] and HyperKamiokande [18]. In 2020 T2K reported hints of CP violation in neutrino oscillation [19], with their data favoring values of $\delta_{\rm CP}$ near maximal CP violation and by excluding CP conserving values of $\delta_{\rm CP} = 0, \pi$ at the 95% confidence level, but this claim is not supported by the NOνA data to date. The results of a recent global analysis [8] of neutrino oscillation data shows that the parameters θ_{12}, θ_{13}, Δm^2_{21} and $\Delta m^2_{3\ell}$ ($\ell = 1, 2$) are well-determined with relative precision at 3σ of about 13%, 8%, 15%, and 6%, respectively. The atmospheric mixing angle θ_{23} still suffers from the octant ambiguity, thus there is no clear indication of whether it is larger or smaller than $\frac{\pi}{4}$. The determination of $\delta_{\rm CP}$ depends on the neutrino mass ordering: for normal ordering the global fit is consistent with CP conservation within 1σ, whereas for inverted ordering CP-violating values of $\delta_{\rm CP}$ around 270° are favored against CP conservation at more than 3.6σ. The current values of the PMNS parameters and neutrino masses resulting from the global fit [8] are reported in Tab. 1.2, showing the best-fit values as well as 1σ and 3σ confidence intervals for the oscillation parameters in both mass orderings, relative to the local best-fit points in each ordering. Despite the Jarlskog invariant $J = J^{\rm max}_{\rm CP} \sin\delta_{\rm CP}$ cannot be precisely determined to date, its maximum value $J^{\rm max}_{\rm CP}$ is estimated to be:

$$J^{\rm max}_{\rm CP} = 0.0333 \pm 0.0007\ (\pm 0.0017) \tag{1.63}$$

at 1σ (3σ) for both orderings, and it can be compared with the Jarlskog invariant of the CKM matrix $J^{\rm max}_{\rm CP} = \left(3.12^{+0.13}_{-0.12}\right) \cdot 10^{-5}$ [1].

Without SK atmospheric data		Normal Ordering ($\Delta\chi^2 = 0.6$))		Inverted Ordering (best fit)	
		bfp $\pm 1\sigma$	3σ range	bfp $\pm 1\sigma$	3σ range
	$\sin^2\theta_{12}$	$0.307^{+0.012}_{-0.011}$	$0.275 \to 0.345$	$0.308^{+0.012}_{-0.011}$	$0.275 \to 0.345$
	$\theta_{12}/^\circ$	$33.68^{+0.73}_{-0.70}$	$31.63 \to 35.95$	$33.68^{+0.73}_{-0.70}$	$31.63 \to 35.95$
	$\sin^2\theta_{23}$	$0.561^{+0.012}_{-0.015}$	$0.430 \to 0.596$	$0.562^{+0.012}_{-0.015}$	$0.437 \to 0.597$
	$\theta_{23}/^\circ$	$48.5^{+0.7}_{-0.9}$	$41.0 \to 50.5$	$48.6^{+0.7}_{-0.9}$	$41.4 \to 50.6$
	$\sin^2\theta_{13}$	$0.02195^{+0.00054}_{-0.00058}$	$0.02023 \to 0.02376$	$0.02224^{+0.00056}_{-0.00057}$	$0.02053 \to 0.02397$
	$\theta_{13}/^\circ$	$8.52^{+0.11}_{-0.11}$	$8.18 \to 8.87$	$8.58^{+0.11}_{-0.11}$	$8.24 \to 8.91$
	$\delta_{\rm CP}/^\circ$	177^{+19}_{-20}	$96 \to 422$	285^{+25}_{-28}	$201 \to 348$
	$\frac{\Delta m^2_{21}}{10^{-5}\,{\rm eV}^2}$	$7.49^{+0.19}_{-0.19}$	$6.92 \to 8.05$	$7.49^{+0.19}_{-0.19}$	$6.92 \to 8.05$
	$\frac{\Delta m^2_{3\ell}}{10^{-3}\,{\rm eV}^2}$	$+2.534^{+0.025}_{-0.023}$	$+2.463 \to +2.606$	$-2.510^{+0.024}_{-0.025}$	$-2.584 \to -2.438$

Table 1.2: Current values of the PMNS parameters and neutrino masses as extracted by the NuFit collaboration in 2024 [8]. The numbers in the 1st (2nd) column are obtained assuming normal ordering (inverted ordering), i.e. relative to the respective local minimum. It should be noted that $\Delta m^2_{3\ell} \equiv \Delta m^2_{31} > 0$ for normal ordering and $\Delta m^2_{3\ell} \equiv \Delta m^2_{32} < 0$ for inverted ordering; "bfp" stands for "best fit point".

1.9 Neutrino cross-sections

In all neutrino experiments, an accurate knowledge of *neutrino cross-sections* is extremely important [1, 20]. The need for such information in the interpretation of neutrino oscillation data has boosted interest in neutrino scattering measurements, since uncertainties in neutrino-nucleus scattering still remain a dominant source of systematic uncertainty in many current and future neutrino oscillation experiments. Although neutrino scattering results have been collected over many decades using a variety of targets and different detector technologies, nowadays there is a broad consensus in the community about the importance of remeasuring cross-sections with an improved treatment of nuclear effects and the need of accurate neutrino flux estimations. The determination of neutrino cross-sections in the few GeV energy range - relevant for DUNE and Hyper-Kamiokande - presents significant challenges, even theoretically. The complexity in the description of neutrino interactions with nuclei arises from a variety of nuclear effects, such as the Fermi motion of nucleons inside the nucleus, the fact nucleons are not free but bound inside the nucleus, multi-nucleon knock-out and final state interactions of hadrons within the nuclear media. Nuclear effects impacting neutrino scattering on nuclei are particularly relevant nowadays, since modern neutrino experiments make use of moderate to heavy nuclear targets in order to increase their event rates. Therefore, in the precision era of neutrino physics, a better understanding of the neutrino-nucleon and neutrino-nucleus cross-sections is pivotal to achieve a few percent accuracy in the systematic uncertainties of the next generation of long-baseline oscillation experiments. Moreover, such an improved knowledge is important in its own right, since it provides information about the axial-vector part of the nucleons bound inside the nucleus, which is not accessible via photon or electron induced reactions [21].

The total inclusive charged current cross section for muon neutrino ($\nu_\mu N \to \mu^- X$) and antineutrino ($\overline{\nu}_\mu N \to \mu^+ X$) scattering have been measured over the years by many

experiments, covering a broad range of neutrino energies [1]. The inclusive charged current neutrino and antineutrino cross-sections are shown in Fig. 1.4 [22] with some of the existing measurements and predictions for the main neutrino interactions: quasi-elastic, resonant pion production and deep inelastic scattering.

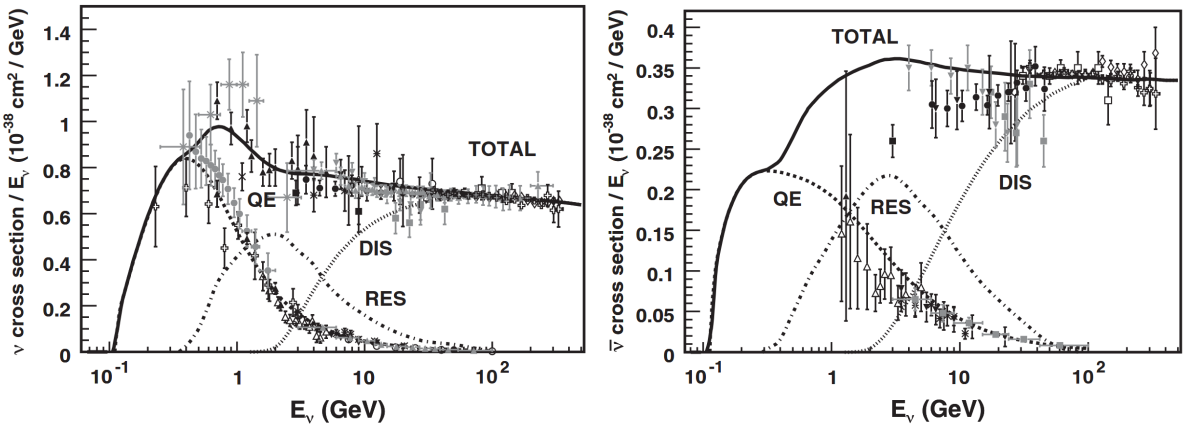

Figure 1.4: Total CC muon neutrino (left) and antineutrino (right) cross-sections per nucleon (for an isoscalar target) divided by neutrino energy, as a function of neutrino energy. The predictions for the dominant types of charged-current interactions are shown: quasi-elastic QE (dashed), resonant pion production RES (dot-dash) and deep inelastic scattering DIS (dotted). Figures from [22].

The total inclusive cross section approaches a linear dependence on neutrino energy, as expected for point-like scattering off quarks (e.g. deep inelastic scattering); such an assumption break down at lower neutrino energies (i.e. lower momentum transfers) [1]. Neutrino cross-sections at lower energies are typically not well-measured as their high energy counterparts, due both to the lack of high statistics data historically available in this energy range and to the complexity of describing the many underlying physical processes that can participate in this region [22]. Due to the presence of many competing interaction processes, the products of neutrino interactions on nuclei include a plethora of final state particles, ranging from the emission of nucleons to more complex final states including pions and kaons. The description of the transition region between resonance excitation and deep inelastic scattering is theoretically challenging. The antineutrino cross-sections are typically less well-measured than their neutrino counterparts, as a result of lower statistics and larger background contamination.

1.10 Neutrino interactions with nucleons and nuclei

1.10.1 Neutrino scattering off free nucleons

In this section the interaction of neutrinos with free nucleons is described and weak nucleon form factors are introduced. In particular, to simplify the discussion, the simplest case of a quasi-elastic interaction is considered. In a charged current quasi-elastic scattering a neutrino (antineutrino) interact with a free neutron (proton):

$$\nu_\ell + n \to \ell^- + p \tag{1.64}$$

$$\overline{\nu}_\ell + p \to \ell^+ + n \tag{1.65}$$

The Feynman diagram of a quasi-elastic scattering is shown in Fig. 1.5.
The charged current quasielastic interaction of a neutrino with a nucleon is thus described by the following reaction:

$$\nu_\ell(k) + n(p) \to \ell^-(k') + p(p') \tag{1.66}$$

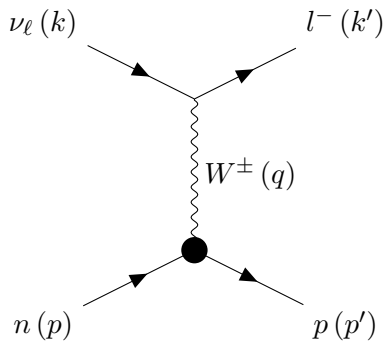

Figure 1.5: Quasielastic neutrino scattering processes on a free nucleon target.

where k and k' are the four momenta of the neutrino and corresponding charged lepton, p and p' are four momenta of the incoming and outgoing nucleons, respectively. The invariant matrix element can be written as:

$$\mathcal{M} = \frac{G_F}{\sqrt{2}}|V_{ud}|\, l_\mu J^\mu \tag{1.67}$$

where l_μ and J^μ are the leptonic and hadronic weak currents. The leptonic weak current l_μ is given by:

$$l_\mu = \overline{u}(k')\gamma_\mu(1 \mp \gamma^5)u(k) \tag{1.68}$$

with the $\mp$ sign referring to reactions induced by neutrinos or antineutrinos, respectively. The hadronic current J^μ is given by:

$$J_\mu = \overline{u}(p')\,(V_\mu - A_\mu)\,u(p) \tag{1.69}$$

The matrix elements of the vector V_μ and axial-vector A_μ currents are given by [20, 21]:

$$\begin{aligned}\langle N'(p')\,|\,V_\mu\,|\,N(p)\rangle =& \overline{u}(p')\left[\gamma_\mu f_1(q^2) + i\sigma_{\mu\nu}\frac{q^\nu}{(M+M')}f_2(q^2)\right.\\ &\left.+\frac{2q_\mu}{(M+M')}f_S(q^2)\right]u(p)\end{aligned} \tag{1.70}$$

$$\begin{aligned}\langle N'(p')\,|\,A_\mu\,|\,N(p)\rangle =& \overline{u}(p')\left[\gamma_\mu\gamma^5 f_A(q^2) + i\sigma_{\mu\nu}\frac{q^\nu}{(M+M')}\gamma^5 f_T(q^2)\right.\\ &\left.+\frac{2q_\mu}{(M+M')}\gamma^5 f_P(q^2)\right]u(p)\end{aligned} \tag{1.71}$$

where N, N' denote the initial and final state nucleon, M and M' are their respective masses and $q^2 = (k-k')^2$ is the four momentum transfer squared. The weak form factors $f_1(q^2)$, $f_2(q^2)$ and $f_S(q^2)$ are denoted as the vector, weak magnetic, and induced scalar form factors whereas $f_A(q^2)$, $f_T(q^2)$ and $f_P(q^2)$ are the axial vector, induced tensor (or weak electric), and induced pseudoscalar form factors, respectively. More details on the form factors are presented in Sec. 1.10.2. Using the leptonic and hadronic currents, the matrix element squared can be expressed as follows:

$$|\mathcal{M}|^2 = \frac{G_F^2}{2}|V_{ud}|^2 L^{\mu\nu}J_{\mu\nu} \tag{1.72}$$

where $L^{\mu\nu}$ and $J_{\mu\nu}$ are the leptonic and hadronic tensors, respectively. In particular, the leptonic tensor $L^{\mu\nu}$ can be computed to be:

$$L^{\mu\nu} = 8\left[k^{\mu}k'^{\nu} + k'^{\mu}k^{\nu} - g^{\mu\nu}k\cdot k' \pm i\epsilon^{\mu\nu\alpha\beta}k'_{\alpha}k_{\beta}\right] \tag{1.73}$$

with $\pm$ sign referring to a neutrino (antineutrino) induced process. The differential scattering cross section in the laboratory reference frame is finally given by:

$$\frac{d\sigma}{dq^2} = \frac{G_F^2|V_{ud}|^2}{8\pi M^2 E^2} L^{\mu\nu}J_{\mu\nu} \tag{1.74}$$

where E is the energy of the incoming neutrino.

1.10.2 Weak nucleon form factors

The weak nucleon form factors $f_{[1,\ 2,\ S,\ A,\ T,\ P]}(q^2)$ introduced in Sec. 1.10.1 correspond to the Dirac, Pauli, scalar, axial-vector, tensor and pseudoscalar weak form factors, respectively. The scalar and tensor form factors are both zero thanks to the invariance of the strong interaction under isospin [22]:

$$f_S(q^2) = f_T(q^2) \equiv 0 \tag{1.75}$$

Moreover, it is possible to relate the form factors probed by weak interactions to those from pure electromagnetic interactions using the Conserved Vector Current (CVC) hypothesis [21]:

$$f_{1,2}(q^2) = F^p_{1,2}(q^2) - F^n_{1,2}(q^2) \tag{1.76}$$

where $F_1^{p,n}$ and $F_2^{p,n}$ are the electromagnetic Dirac and Pauli form factors of the proton and neutron, respectively. In the limit of zero momentum transfer $q \to 0$, the Dirac form factors reduce to the charge of the nucleon, whereas the Pauli form factors reduce to the nucleon's magnetic moments [22]:

$$F_1^N(0) = q_N = \begin{cases} 1 & \text{proton} \\ 0 & \text{neutron} \end{cases} \tag{1.77}$$

$$F_2^N(0) = \begin{cases} \frac{\mu_p}{\mu_N} - 1 & \text{proton} \\ \frac{\mu_n}{\mu_N} & \text{neutron} \end{cases} \tag{1.78}$$

where q_N is the nucleon charge, μ_N is the nuclear magneton, and $\mu_{p,n}$ are the proton and neutron magnetic form factors. The Dirac $F_1(q^2)$ and Pauli $F_2(q^2)$ form factors are expressed in terms of the experimentally determined Sach's $G_E^{p,n}(q^2)$ and magnetic $G_M^{p,n}(q^2)$ form factors of the nucleons as [21]:

$$F_1^{p,n}(q^2) = \left(1 - \frac{q^2}{4M^2}\right)^{-1}\left[G_E^{p,n}(q^2) - \frac{q^2}{4M^2}G_M^{p,n}(q^2)\right] \tag{1.79}$$

$$F_2^{p,n}(q^2) = \left(1 - \frac{q^2}{4M^2}\right)^{-1}\left[G_M^{p,n}(q^2) - G_E^{p,n}(q^2)\right] \tag{1.80}$$

Initially, it was observed that the experimental data for the electromagnetic $e^- p$ scattering may be explained assuming that the Sachs' form factors to have a dipole form, proportional to:

$$G_D(q^2) = \frac{1}{\left(1 - \frac{q^2}{M_V^2}\right)^2} \tag{1.81}$$

where $M_V \simeq 0.84\,\text{GeV}$ was known as the vector dipole mass [20]. However, with the development of electron scattering experiments, it was observed that the Sachs' form factors deviate from the dipole form. In the literature there exist various parameterizations of the Sachs' form factors, such as the one given by Bradford et al. [23] kwown as BBBA-05, Kelly [24], Punjabi et al. [25]. The Goldberger-Treiman relation allows one to also relate the pseudoscalar contribution in terms of the axial term as well:

$$f_P(q^2) = \frac{2M^2}{m_\pi^2 - q^2} f_A(q^2) \tag{1.82}$$

where m_π is the pion mass. The axial-vector form factor $f_A(q^2)$ is often parameterized assuming a dipole-like behavior:

$$f_A(q^2) = \frac{-g_A}{\left(1 - \frac{q^2}{M_A^2}\right)^2} \tag{1.83}$$

where the coupling $g_A = 1.2754 \pm 0.0013$ is determined experimentally from neutron β decay [1]. The M_A parameter is known as the *axial mass* and it is obtained in quasi-elastic scattering measurements. The analysis of quasi-elastic scattering made extensive use of the dipole parameterization [20]; however, a new parameterization based on z-expansion [26, 27] has been proposed and the axial-vector form factor can also be theoretically computed in various lattice QCD models [27]. In recent years, the determination of the numerical value of M_A has been a subject of intense discussion in the neutrino physics community [28]. Before the advent of precision neutrino data on nuclei, the axial mass was extracted from charged current quasi-elastic measurements on deuterium bubble chambers and its value was considered quite stable around $M_A = 1.026 \pm 0.021$ GeV [29] and confirmed by the few-GeV data from NOMAD [30] on carbon. However, modern neutrino scattering data on carbon at lower energies coming from K2K [31], SciBooNE [32] and MiniBooNE [33] suggested larger values of the axial mass in contradiction with the previous one. Indeed, since modern neutrino experiments no longer use deuterium but complex nuclei as their neutrino targets, nuclear effects play a major role and can produce sizable modifications in quasi-elastic cross section. The MiniBooNE data could be reproduced by calculating the nuclear response functions using a relativistic Fermi gas model and increasing the axial mass value to $M_A = 1.35 \pm 0.17$ GeV, revealing a substantial discrepancy. Martini et al. [34] suggested that actually MiniBooNE data was not genuine quasi-elastic and explained the inconsistencies between models and data recorded by MiniBooNE as due to a missing component in the modeling of the cross-sections: the reaction mechanism of multi-nucleon excitations (2p2h) due to short-range nuclear correlations, meson exchange currents and their interference [28].

1.10.3 Quasi-elastic scattering

Neutrinos can elastically scatter off an entire nucleon liberating a nucleon (or multiple nucleons) from the target [22]. Such an interaction mechanism is known as *quasi-elastic scattering* for charged current interactions (QE or CCQE), whereas it is referred to as *elastic scattering* for neutral current interactions. The quasi-elastic neutrino scattering occurs off an entire nucleon, rather than its constituent partons. The neutrino (antineutrino) quasi-elastic scattering off a free nucleon target refers to the process:

$$\nu_\ell + n \to \ell^- + p \tag{1.84}$$

$$\overline{\nu}_\ell + p \to \ell^+ + n \tag{1.85}$$

where a charged lepton and a single nucleon are ejected in the elastic interaction with a nucleon in the target material. The Feynman diagram of a neutrino QE scattering off a free nucleon is shown in Fig. 1.5. In a neutrino QE interaction the target neutron is converted to a proton, whereas in the case of an antineutrino scattering the target proton is converted into a neutron. The final state is traditionally a single nucleon, but can also include multiple nucleons, especially in the case of neutrino-nucleus scattering. The differential cross section of CCQE off free nucleons is predicted by the Llewellyn-Smith model [35]:

$$\frac{d\sigma}{dQ^2} = \frac{G_F^2 M^2 |V_{ud}|^2}{8\pi E_\nu^2} \left[A(Q^2) \pm B(Q^2)\frac{s-u}{M^2} + C(Q^2)\frac{(s-u)^2}{M^4} \right] \tag{1.86}$$

where $\pm$ sign refers to neutrino (antineutrino) scattering, where $M = (m_p + m_n)/2$ is the average nucleon mass, Q^2 is the squared four momentum transfer ($Q^2 = -q^2 > 0$), E_ν is the incident neutrino energy and $s - u = 4ME_\nu - Q^2 - m_l^2$, where m_l is the lepton mass. The factors $A(Q^2)$, $B(Q^2)$ and $C(Q^2)$ are function of the vector $f_{1,2}$, axial-vector f_A and pseudoscalar f_P form factors of the nucleon, according to:

$$\begin{aligned} A(Q^2) = \frac{m_l^2 + Q^2}{4M^2} \Bigg[& \left(4 + \frac{Q^2}{M^2}\right) f_A^2(Q^2) - \left(4 - \frac{Q^2}{M^2}\right) f_1^2(Q^2) \\ & + \frac{Q^2}{M^2}\left(1 - \frac{Q^2}{4M^2}\right) f_2^2(Q^2) + \frac{4Q^2}{M^2} f_1(Q^2) f_2(Q^2) \\ & - \frac{m_l^2}{M^2}\Big(\left[f_1(Q^2) + f_2(Q^2)\right]^2 + \left[f_A(Q^2) + 2f_P(Q^2)\right]^2 \\ & - \left(\frac{Q^2}{M^2} + 4\right) f_P^2(Q^2) \Big) \Bigg] \end{aligned} \tag{1.87}$$

$$B(Q^2) = \frac{Q^2}{M^2} f_A(Q^2) \left[f_1(Q^2) + f_2(Q^2)\right] \tag{1.88}$$

$$C(Q^2) = \frac{1}{4}\left[f_A^2(Q^2) + f_1^2(Q^2) + \frac{Q^2}{4M^2} f_2^2(Q^2) \right] \tag{1.89}$$

The quasi-elastic scattering is the dominant neutrino interaction for neutrino energies less than $\sim 1\,\text{GeV}$ and represents a large fraction of the signal samples in many neutrino oscillation experiments [1]. The early measurements of QE date back to the 1970's, when bubble chamber experiments employed light targets (hydrogen or deuterium) requiring both the detection of a muon and a single nucleon in the final state. For modern neutrino experiments using heavier nuclear targets the situation is much more complicated since nuclear effects impact the size and shape of the cross section as well as the final state kinematics and topology. Therefore, a QE interaction on a nuclear target does not necessarily imply the ejection of a lepton and a single nucleon, since additional particles may be ejected in the final state due to intranuclear hadron rescattering (i.e. final state interactions, FSI) and the effects of correlations between target nucleons (e.g. 2p2h). For nuclear targets heavier than hydrogen or deuterium it is thus important to properly define the meaning of a CCQE scattering and nowadays modern experiments tend to report cross-sections for processes without pions in the final state (referred to as CC0π or QE-like) instead of genuine CCQE reactions.

1.10.4 Resonance production

Given enough energy, neutrinos can excite the struck nucleon to an excited state, producing a baryon resonance (Δ, N^*) which quickly decays, most often to a nucleon and single pion final state [22]:

$$\nu_\mu \; N \to \mu^- \; N^* \tag{1.90}$$

$$N^* \to \pi \; N' \tag{1.91}$$

where $N, N' = n, p$. The baryon resonance can decay through a variety of higher multiplicity decay modes, for instance multi-pion and kaon final states. The *resonant single pion production* is the most common production mechanism, dominated by the $\Delta(1232)$ resonance at the lowest energies. Considering neutrino scattering off free nucleons, there are seven possible resonant single pion reaction channels, three charged current:

$$\nu_\mu \; p \to \mu^- \; p \; \pi^+ \qquad \overline{\nu}_\mu \; p \to \mu^+ \; p \; \pi^- \tag{1.92}$$

$$\nu_\mu \; n \to \mu^- \; p \; \pi^0 \qquad \overline{\nu}_\mu \; p \to \mu^+ \; n \; \pi^0 \tag{1.93}$$

$$\nu_\mu \; n \to \mu^- \; n \; \pi^+ \qquad \overline{\nu}_\mu \; n \to \mu^+ \; n \; \pi^- \tag{1.94}$$

and four neutral current:

$$\nu_\mu \; p \to \nu_\mu \; p \; \pi^0 \qquad \overline{\nu}_\mu \; p \to \overline{\nu}_\mu \; p \; \pi^0 \tag{1.95}$$

$$\nu_\mu \; p \to \nu_\mu \; n \; \pi^+ \qquad \overline{\nu}_\mu \; n \to \overline{\nu}_\mu \; n \; \pi^0 \tag{1.96}$$

$$\nu_\mu \; n \to \nu_\mu \; n \; \pi^0 \qquad \overline{\nu}_\mu \; n \to \overline{\nu}_\mu \; n \; \pi^0 \tag{1.97}$$

$$\nu_\mu \; n \to \nu_\mu \; p \; \pi^- \qquad \overline{\nu}_\mu \; n \to \overline{\nu}_\mu \; p \; \pi^- \tag{1.98}$$

An example of a Feynman diagram for resonant single pion production reaction is shown in Fig. 1.6.

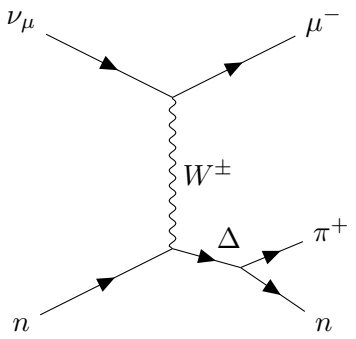

Figure 1.6: Resonant single pion production.

The description used by many neutrino experiments for such resonance production processes is most commonly based on the calculations of the Rein and Sehgal model [36], with the additional inclusion of lepton mass terms. In particular, a proper knowledge of NCπ^0 resonant production process is of great interest for long-baseline oscillation experiments searching for $\nu_\mu \to \nu_e$ oscillations. Indeed, such an interaction is expected to be one of the largest source of background in the far detectors, due to photons which can mimic electron neutrino appearance signals.

1.10.5 Deep inelastic scattering

The neutrino interactions discussed so far involve neutrino scattering off composite entities such as nucleons or nuclei; however, given enough energy, neutrinos can resolve

the internal structure of the target [22]. The neutrino scattering off an individual quark constituent of the nucleon is a process called *deep inelastic scattering* (DIS). The DIS is the dominant neutrino interaction mode for neutrino energies above $\sim 10\,\text{GeV}$ and it breaks apart the nucleon producing a hadronic shower. The neutrino scatters off a quark in the nucleon via the exchange of a virtual W or Z boson, producing a lepton and a hadronic system (X) in the final state:

$$\nu_\mu\, N \to \mu^-\, X \qquad \overline{\nu}_\mu\, N \to \mu^+\, X \tag{1.99}$$

$$\nu_\mu\, N \to \nu_\mu\, X \qquad \overline{\nu}_\mu\, N \to \overline{\nu}_\mu\, X \tag{1.100}$$

Neutrino DIS can be described in terms of three dimensionless kinematic invariants: the inelasticity y, the square of the four-momentum transfer ($Q^2 = -q^2 > 0$) and the Bjorken scaling variable x [37]. Since neutrino DIS has long been used to validate the Standard Model and to probe nucleon structure, several high energy (many GeV) neutrino experimental data are available [22]. However, there are few data at the lower energies relevant to accelerator-based neutrino experiments and it is not clear how to accurately extrapolate DIS models to these energies. Moreover, the treatment of nuclear PDFs (nPDFs), which account for modifications of parton distribution functions (PDFs) within the nuclear medium, is essential for an accurate description of DIS on nuclei and constitutes a major source of theoretical uncertainty in this regime [38].

1.11 Nuclear effects in neutrino-nucleus scattering

The neutrino scattering off free nucleons is an approximation sufficient to describe neutrino interactions on light nuclear targets, such as those employed in old bubble chamber experiments (hydrogen or deuterium). However, modern neutrino experiments make use of moderate to heavy nuclear targets in order to increase their event rates. Therefore, when using heavier targets, it is necessary to account for additional *nuclear effects*, which can alter initial and final state kinematics and topology. The variety of nuclear effects can be broadly classified in *initial state effects* (e.g. Fermi motion, nuclear binding energy and multi-nucleon knock-out) and *final state interactions*.

1.11.1 Fermi motion

Fermi motion describes the initial state momentum distribution of nucleons bound inside the nucleus, prior to any neutrino interaction. The initial state motion of nucleons inside the nuclear medium complicates the description of neutrino scattering with nuclei, since it is responsible for an unknown event-by-event boost in the laboratory frame. Fermi motion can be described by a variety of models based on different assumptions, resulting in different predictions for the kinematics of initial-state nucleons. The models most commonly used to describe the initial nuclear ground state in neutrino interactions at the few-GeV scale are the Relativistic Fermi Gas (RFG), the Local Fermi Gas (LFG) and the Spectral Function (SF) model. In the Relativistic Fermi Gas model [39], nucleons inside the nucleus are treated as non-interacting fermions in a nuclear potential, with all available momentum states filled by nucleons from the ground state upwards. The highest-momentum level causes a sharp cut-off in the range of available energies. Interactions among fermions are not taken into account in this model and the nuclear density is assumed to be flat within the nucleus. The Local Fermi Gas model [40] accounts for local variations in nuclear density, since nucleons are subject to a nuclear potential that varies as a function of the the radial position of the nucleon inside the nucleus. The Local Fermi Gas model can thus be thought as a continuum of many Relativistic Fermi

Gas models, each one with a different Fermi momentum determined by the local nuclear potential. The overall effect of this model is thus to smooth out the initial state momentum distribution of nucleons. The Spectral Function model [41] is a more sophisticated model which takes into account interactions among nucleons and the shell structure of the nucleus.

1.11.2 Multi-nucleon knock-out

In a neutrino-nucleus interaction, the neutrino can scatter off correlated states of two or more nucleons bound inside the nucleus. This multi-nucleon knock-out process is known as n-particles-n-holes (npnh) [34] and the most common occurrence involves the interaction with a correlated pair of nucleons (2p2h) ejected from the nucleus. As mentioned in Secs. 1.10.2 and 1.10.3, multi-nucleon correlations have been proposed to motivate the MiniBooNE axial mass puzzle, explaining the discrepancy observed in the analysis of (non-genuine) CCQE interactions on nuclear targets heavier than deuterium [42]. The multi-nucleon knock-out can be described in terms of nucleon-nucleon short-range correlations (NN), meson exchange currents (MEC) and interference between these processes. The different channels contributing to 2p2h are shown in Fig. 1.7. The 2p2h interactions are described by multiple models [34, 43–45], with varying predictions on the relative amount of NN and MEC interactions.

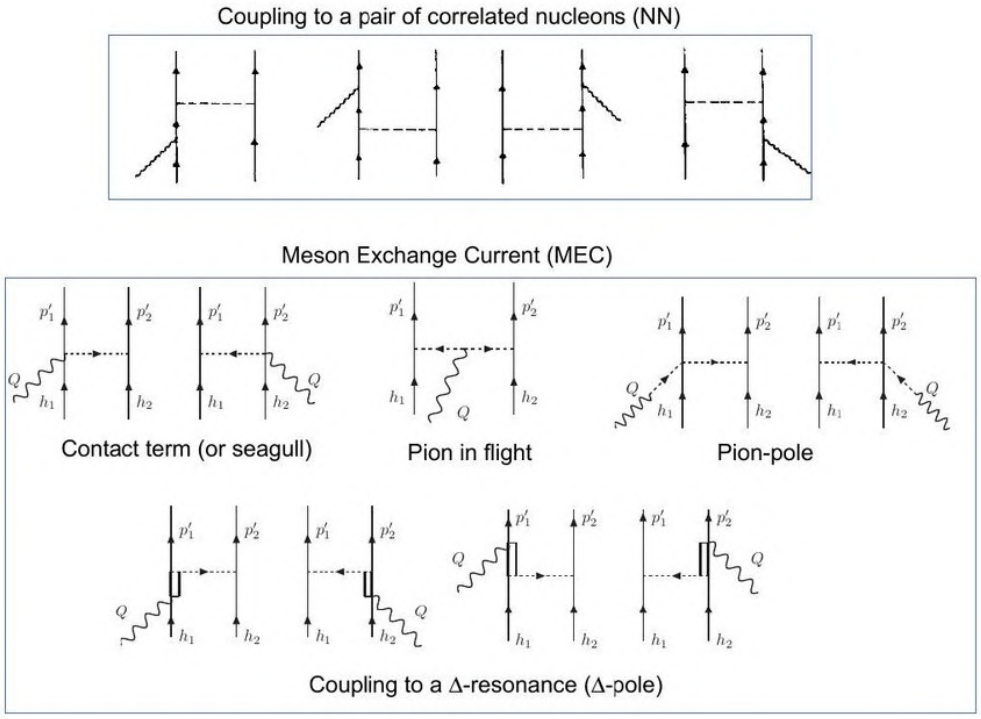

Figure 1.7: Feynman diagrams of NN and MEC interactions, adapted from [43, 46]. Single lines represent nucleons, double lines represent the Δ resonances, dashed lines represent pions, and curly lines represent the W boson. Figure from [47].

1.11.3 Final state interactions

The final state particles produced in a neutrino-nucleus scattering can undergo subsequent interactions with the nuclear medium, further complicating the description of neutrino interactions. Once created in the initial neutrino interaction, the final state hadrons - in

order to be detected - must escape the nucleus. Anyway, along their journey, the hadrons can rescatter, get absorbed, charge-exchange or stimulate additional nuclear emission, thus altering the kinematics and final state topology. These re-interactions are known as final state interactions (FSI). A schematic representation of different types of FSI affecting, for instance, resonant pion production is shown in Fig. 1.8. FSI are difficult to model or constrain with experimental data. Neutrino event generators such as GENIE [48], NEUT [49], and NuWro [50] model FSI using intranuclear cascade models, whereas GiBUU [51] solves coupled hadronic transport equations to propagate all interaction products through the nuclear medium together.

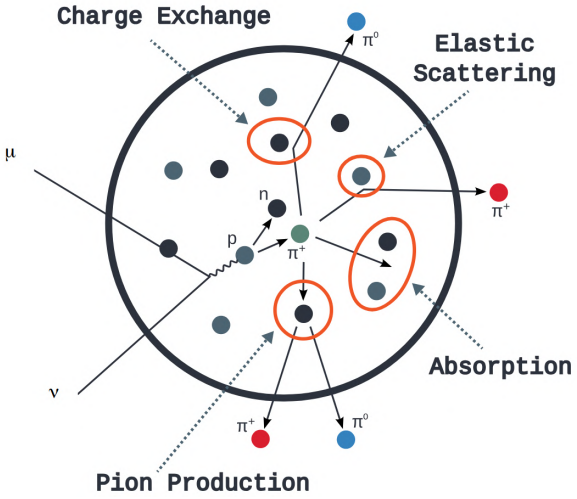

Figure 1.8: Schematic representation of different types of FSI affecting resonant pion production. Figure from [52].

1.12 Status of neutrino cross-section measurements

A wide range of neutrino cross-section measurements on different targets have been measured by past and current experiments such as MiniBooNE, T2K, MicroBooNE, NOνA and MINERνA, with a primary focus on quasi-elastic-like interactions and in the ~ 1 GeV regime. Despite in recent years a considerable progress in neutrino scattering measurements has been achieved by such experiments, they also highlighted some limitations in the modeling of neutrino-nucleus interactions. Furthermore, the precision of current measurements still remains insufficient for the demands of the precision era of neutrino oscillation physics. The QE-like (i.e. CC0π) cross-sections are nowadays reported by many modern experiments as a function of the observed final state particle kinematics [1]. Despite such double differential cross-section measurements make more difficult a direct comparison among different experiments, they have the advantage of being much less model-dependent than the historical cross-sections reported as a function of derived quantities such as neutrino energy E_ν or the square of the 4-momentum transfer $Q^2 = -q^2$, where $q = (q_0, \vec{q}_3)$ is the 4-momentum transfer in a neutrino scatter. Therefore, double differential cross-sections as a function of final state particle kinematics reduce the model-dependence of the measured data, thus providing a more robust set of measurements which allow a rigorous two-dimensional test of the underlying nuclear physics [1]. For instance, the ν_μ CC0π double differential cross-sections measured by T2K [53] as a function of lepton kinematics (i.e. $p_\mu, \cos\theta_\mu$) is shown in Fig. 1.9.

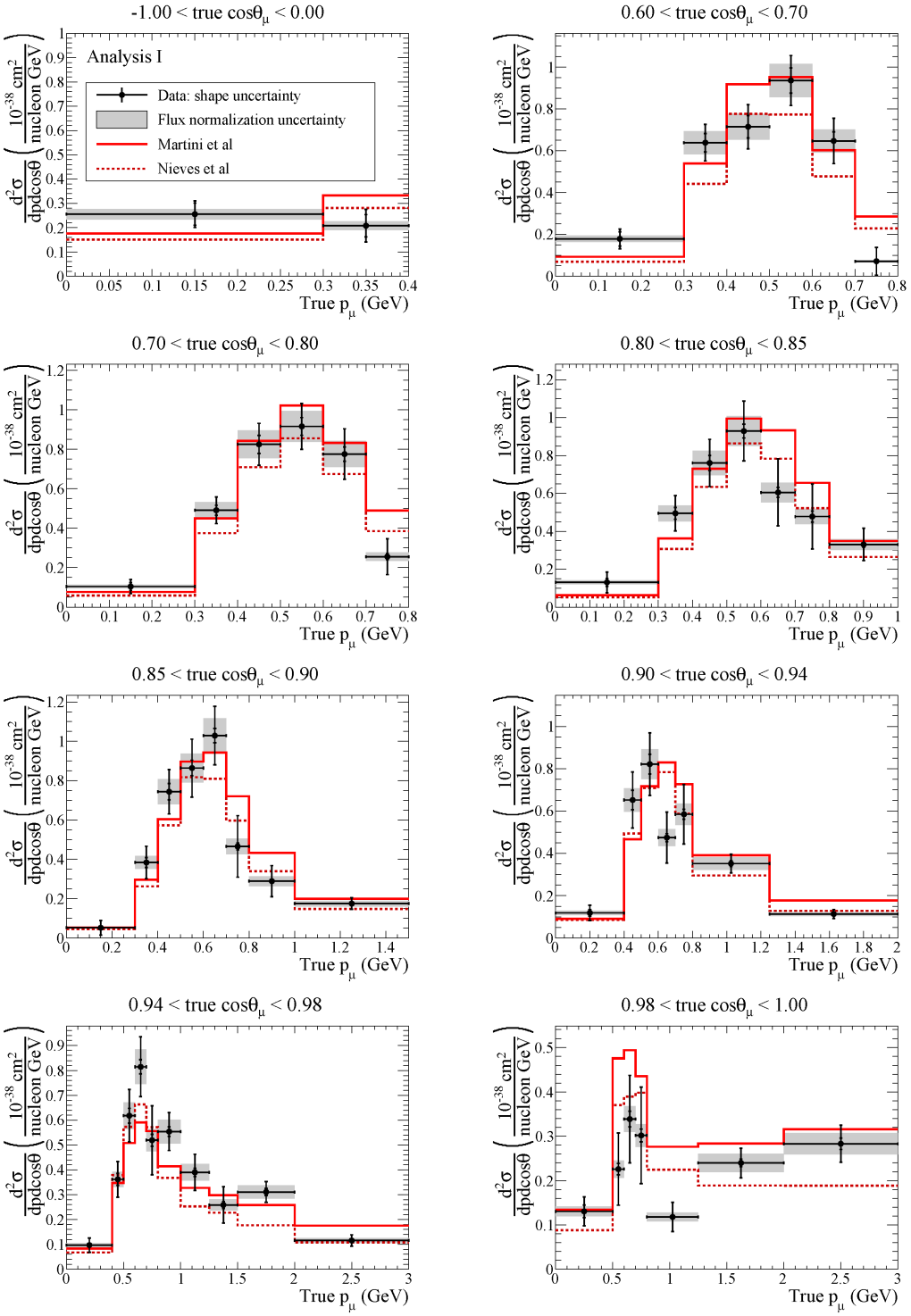

Figure 1.9: The T2K CC0π double differential cross-sections measured in 2016. The flux uncertainty is shown in the gray area and the distributions are compared with the models of Martini et al. [34, 54] (red solid line) and Nieves et al. [42, 55] (red dotted line). Figure from [53].

Since the incident neutrino energy is not known on an event-by-event basis, most modern neutrino cross-section measurements are reported as flux-averaged cross-sections. The total ν_μ flux-averaged cross-section obtained by T2K is shown in Fig. 1.10, together with CC inclusive measurements from other experiments.

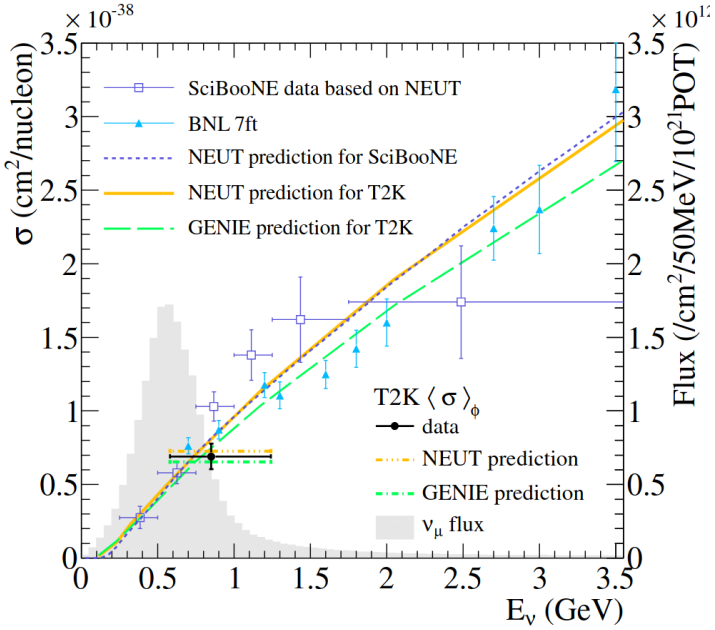

Figure 1.10: The T2K ν_μ total flux-averaged cross-section with the NEUT and the GENIE predictions for T2K and SciBooNE. The T2K data point is placed at the flux mean energy. The vertical error represents the total (statistical and systematic) uncertainty, and the horizontal bar represent 68% of the flux at each side of the mean energy. The T2K ν_μ flux distribution is shown in grey. Figure from [56].

Since current and future long-baseline neutrino oscillation measurements mostly rely on the ν_e appearance at the far detector, an accurate knowledge of ν_e cross-section is essential to properly extract the oscillation probability from event rate spectra at the far detector. However, the conventional intense accelerator-based neutrino beams are sources of ν_μ with a percent contamination of ν_e. Therefore, the near detector constraints are derived from measurements of ν_μ interactions and thus need to be theoretically corrected for ν_e. The main difference in electron and muon neutrino charged current cross-sections is due to terms depending explicitly on the square of the lepton mass [57]. Such lepton mass terms are in general negligible for ν_e at accelerator energies, but they may provide non-negligible corrections for ν_μ at low neutrino energies or energy transfers. In addition, momentum and energy transfer limits for ν_e and ν_μ interactions are different because the kinematic limits in momentum and energy transfer are function of the lepton mass [57]. The energy transfer q_0 in a neutrino scatter cannot be directly measured in a wide band neutrino beam, however it can be inferred from the visible recoil products in the detector [57]. The available, or recoil, energy E_{avail} is the calorimetric sum of the outgoing hadronic state, defined as:

$$E_{\text{avail}} = \sum_{i=\pi^\pm,p} T_i + \sum_{i=\pi^0,\gamma} E_i, \tag{1.101}$$

where $\sum_{i=\pi^\pm,p} T_i$ is the sum of proton and charged pion kinetic energies, and $\sum_{i=\pi^0,\gamma} E_i$ is the sum of total energies deposited by neutral pions and photons. This variable has been used by the MINERνA experiment as a proxy for the energy transfer q_0 in a neutrino

interaction. However, such a quantity differs from q_0 in that it does not have the kinetic energy of final-state neutrons nor the rest mass of charged pions, and then it ignores the nucleons removal energy. MINERνA also reconstructed q_3 using lepton kinematics and the inferred energy transfer $q_0 \sim E_{\text{avail}}$, according to:

$$q_3 = \sqrt{Q^2 + q_0^2} \tag{1.102}$$

$$Q^2 = 2(E_l + q_0)\,(E_l - |\vec{p}_l|\cos\theta_l) - m_l^2 \tag{1.103}$$

The ν_e double differential cross-section measurements as a function of calorimetric observables E_{avail} and q_3 measured by the MINERνA experiment [57] is shown in Fig. 1.11.

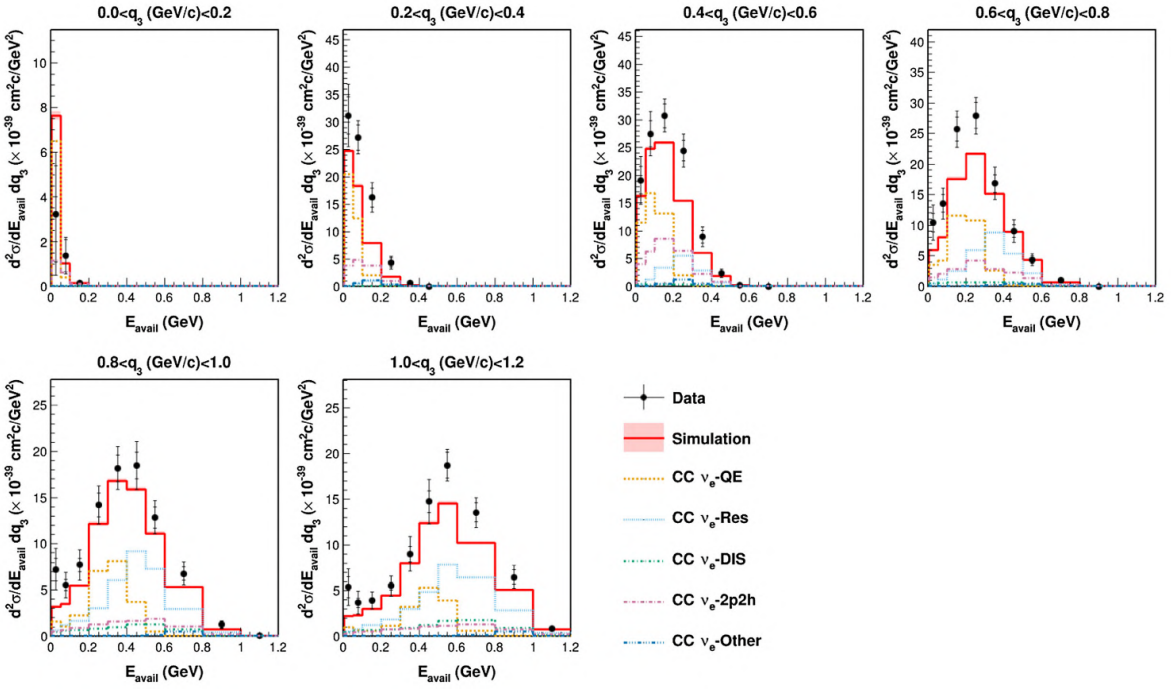

Figure 1.11: The MINERνA ν_e double differential cross-section $d^2\sigma/dE_{\text{avail}}dq_3$ in six regions of q_3. Figure from [57].

1.13 Systematic uncertainties in long-baseline neutrino oscillation experiments

The physics of neutrino oscillations at accelerators [58] has entered a new precision era with the approval of DUNE and HyperKamiokande - ambitious experiments with an extraordinary level of complexity, cost and timescale [28]. These oscillation experiments, for the first time in the history of neutrino physics, will be no more limited by the event statistics – thanks to their unprecedented detector mass and beam power – but by a large set of systematic uncertainties that must be controlled and kept at the per-cent level [59]. Neutrino cross-section systematic uncertainties already represent the largest source of systematic error in current long-baseline experiments such as T2K and NOνA, where statistical errors still contribute significantly, and will become the dominant factor limiting the physics reach of DUNE and HyperKamiokande, where statistical uncertainties will be pushed far below the systematic budget. Therefore, the ambitious goals of

the next generation of long-baseline oscillation experiments can be critically hindered by the limited understanding of neutrino interactions and the poor knowledge of neutrino cross-sections, still at $\mathcal{O}(10-30\%)$ level at the few-GeV scale [28]. Indeed, an accurate knowledge of neutrino cross-sections is essential to extract the oscillation probabilities $P_{\nu_\alpha \to \nu_\beta}(E_\nu, L)$ as a function of the neutrino energy E_ν and source-to-detector distance, apart from being interesting in its own right as a probe of nuclear media via pure weak interactions.

In long-baseline neutrino oscillation experiments, the near detector is the smaller detector located in the proximity of the source and the far detector is larger and located at an optimal baseline to study neutrino oscillations. The near detector should be identical to the far detector but located in a position where oscillation effects are negligible, thus providing a measurement of ν_μ unoscillated beam and its ν_e contamination. At the near detector, the measurement of neutrino rate as a function of energy is the convolution of neutrino flux produced at the accelerator and the neutrino cross-section. At the far detector, those are further convoluted with the neutrino oscillation probability. The extrapolation of the near detector constraints to the far detector is challenging since it is affected by differences in detector acceptances, and - most critically - by the different energy distribution before and after oscillation (i.e. as measured at the near and far detectors, respectively) and by the fact that the near detector measures the convolution of flux and cross-section, while those must be disentangled in order to be propagated separately to the far detector [60]. Therefore, the extrapolation of the near detector constraints to the far detector generally relies on assumptions from nuclear models for flux production and neutrino-nucleus cross-section. In long-baseline oscillation experiments, systematic uncertainties can be mitigated using the near-far detector cancellation technique, consisting in a direct cancellation of errors common to both near and far detectors [61]. The use of identical near and far detectors cancels out systematic differences in the detection efficiency between the near and far detector and this is the technique of choice for moderate-precision disappearance experiments [28]. However, such a time-honored and elegant solution does not work at $< 5\%$ level and is therefore inadequate for the forthcoming precision neutrino oscillation programme. Indeed, the near and far detectors are not perfectly identical and their efficiencies are different both for ν_e and ν_μ detection. Moreover, the neutrino fluxes at the near and far locations are different beyond the expected geometrical reduction ($\Phi \sim L^{-2}$) because the near detector integrates the flux in a much larger neutrino phase-space. Therefore, since the solid angle seen by the near detector is much bigger than the far detector one, such a phase-space mismatch requires additional corrections both on flux normalization and energy spectrum, thus increasing the systematic uncertainty.

1.13.1 Neutrino energy systematic uncertainties

Since the oscillation parameters are extracted from the energy distribution of collected events, their determination requires an accurate reconstruction of the neutrino energy [62]. Nuclear effects and detector response are responsible for smearing and bias in neutrino energy reconstruction, impacting both the calorimetric and kinematic reconstruction approaches. In particular, the use of nuclear targets in modern experiments makes the description and modeling of nuclear effects one of the largest sources of systematic uncertainties in neutrino energy reconstruction. For instance, neutrino energy can be reconstructed calorimetrically as the sum of the visible energy deposited by final state particles in the detector. However, such a reconstructed neutrino energy is generally bi-

ased by the missing energy due to the removal energy of nucleons inside the nucleus, by the rest mass of charged pions and, more importantly, by the invisible fraction of energy carried away by undetected neutrons. Therefore, an accurate neutrino energy reconstruction still remains one of the biggest challenges for the ambitious physics reach of the next generation of long-baseline oscillation experiments.

1.13.2 Neutrino flux systematic uncertainties

Despite the complexity of the reconstruction of neutrino interactions, the leading source of systematics on neutrino cross-sections is the limited knowledge of the neutrino flux, generally known with a precision worse than $\mathcal{O}(10\%)$ [59]. An accurate determination of the neutrino flux - its flavor composition and energy spectrum - is currently a challenging task for accelerator-based neutrino experiments. Conventional neutrino beams are created by high energy protons impinging onto a target (usually made of carbon or beryllium) in order to produce π and K secondary mesons. Then, secondary mesons are magnetically focused into a long tunnel in which they can decay, producing neutrinos. In principle, a precise knowledge of π and K production cross-sections on the target material - as well as an accurate knowledge of the focusing properties of the beamline - should translate in a well known neutrino flux [63]. In practice the situation is more complicated, since multiple interactions occurs within the target and in the materials downstream of it.

The dominant source of systematic uncertainty in the neutrino flux is the *yield of secondary hadrons* produced at the target, currently used by many neutrino experiments to extrapolate and determine the flux of neutrinos [59]. Indeed, since hadron production processes are governed by non-perturbative QCD and occur inside a nucleus, accurate theoretical predictions are not available. Over the years, the neutrino flux predictions of many experiments have relied on detailed simulations of the beamline materials and geometry, coupled with phenomenological models of hadronic cascades [63], such as those in `GEANT4` [64] and `FLUKA` [65]. Those models are not particularly accurate, but can be tuned or benchmarked by comparing their predictions to existing hadron production measurements. The differential distributions from fragmentation models can be used by Monte Carlo generators in order to compute the hadron production yield; nevertheless, they are usually not able to reproduce the kinematic distribution of secondaries, even if the models are tuned with external data. Unfortunately, mastering the hadron production mechanisms at a level sufficient to predict the accepted flux before the focusing and decay volume in high-precision neutrino experiments is still outside the reach of these models [59]. Hadron production measurements on various target materials are currently used by many experiments in order to constrain their neutrino beamline simulation.
Even after having incorporated the hadron production information in the neutrino beamline simulation, the neutrino flux at the detector site is not yet predicted with a sufficient precision. There are a large number of geometric and magnetic details - such as alignment tolerances on the primary proton beam direction, target and horns - that can affect the neutrino energy distribution, and those detail must be precisely measured and then incorporated in the beamline simulation [63]. Furthermore, variations in the current flowing through magnetic horns and permanent deformations of the conductor can generate systematic biases in the beam focusing, which ultimately affects the neutrino flux [59]. Indeed, since the magnetic field of a horn is proportional to the injected current, pulsed currents of hundreds of kA are tipically used, inducing a strong Joule heating on the device. Moreover, the high magnetic fields can generate strong forces which might distort the horn shape; these deformations can change the beam optics from the designed one, reducing the flux directed toward the neutrino detector and increasing the pro-

duction of background tertiaries[19]. The magnetic horn currents are typically measured with a precision of 1%, and give a very small contribution to the flux systematic budget [59]. The systematic uncertainties on the beamline geometry and the horn current are in general negligible with respect to the leading hadron production one. For instance, for MINERνA [63] in low energy NuMI beam configuration the hadron production systematic uncertainty amounts to $\sim 7\%$ around the flux peak and $\sim 9\%$ at high energy ($E_\nu \gtrsim 7\,\text{GeV}$); the flux precision can be improved ($\sim 4\%$) using the constraint from ν_μ e^- scattering. For T2K, instead, the ν_μ flux uncertainty can be reduced to below 4% for energies up to 7 GeV [66] using the constraints from the NA61/SHINE replica target datasets [67]. After the hadron production, the main contributions come from the beamline geometry and focusing systematics. For MINERνA it amounts to $\sim 6\%$ in the region among $4 - 5\,\text{GeV}$, where the flux tends to decrease, while for T2K, it is comparable to hadron production around the flux peak [68, 69].
In this scenario, neutrino cross-section systematic uncertainties can jeopardize the physics reach of such ambitious long-baseline oscillation experiments. Given the unprecedented complexity and cost of such facilities, strategic investment in reducing their final systematic budget is essential. The construction of high-precision neutrino cross-section experiments, operating concurrently with DUNE and Hyper-Kamiokande, offers the most robust and cost-effective pathway to achieve the ultimate sensitivity to the lepton Yukawa sector. One of the most promising candidate is the novel technology of *monitored and tagged neutrino beam*: the monitored neutrino sample can be used to provide high-precision neutrino cross-section measurements thanks to the reduction of the main neutrino flux systematics at per-cent level and, moreover, a tagged neutrino sample can be used to reconstruct kinematically the neutrino energy on an event-by-event basis, making possible to measure neutrino-nucleus cross-section with a precision comparable to electron-scattering experiments. These new technologies will be discussed extensively in Chapter 2.

[19]This background originates in unfocused particles hitting the downstream beamline elements.

2 Monitored and tagged neutrino beam

Over the years, accelerator neutrino beams have played a pivotal role in the discovery of neutrino oscillations. Unlike natural neutrino sources, accelerator neutrino beams can offer a superior degree of control on momentum, direction, flux and flavour of neutrinos produced at the source [59]. Therefore, they are considered as the ideal facilities for the forthcoming precision era of neutrino oscillation physics, opened up in 2012 by the discovery of the non-zero value of the θ_{13} mixing angle. Although it is well established that these facilities will be the optimal tools to investigate lepton mixing with unprecedented precision, the neutrino precision physics program will pose major requirements to the level of control and diagnostics of neutrino beams. Therefore, in the next future, accelerator neutrino beams will inevitably have to face and overcome unprecedented challenges in terms of precision. For instance, since long-baseline oscillation experiments such as DUNE and HyperKamiokande aim to probe CP violation in the lepton sector measuring the oscillation of $\nu_\mu \to \nu_e$ and its CP conjugate $\overline{\nu}_\mu \to \overline{\nu}_e$, an accurate knowledge of neutrino interaction cross-section at the GeV scale is essential. The need to cope with these requirements motivates the design of a new generation of neutrino beams with an improved knowledge of neutrino flux, thus tailored for high precision neutrino cross-section measurements. *Monitored neutrino beams* are a novel technology aimed at determine the flux and flavour of neutrinos produced at the source at the per-cent level. The core concept of a monitored neutrino beam is that the neutrino flux can be derived by measuring the charged leptons associated to neutrinos produced in meson decays occurring along the decay volume, which are thus proportional to the number of neutrinos created at the source. The most advanced design for monitored neutrino beams, to date, has been developed by NP06/ENUBET, whose goal is to monitor the neutrino flux in a direct manner by recording large angle charged leptons in an instrumented decay tunnel, in order to provide measurements of electron and muon neutrino cross-sections with a precision of $\mathcal{O}(1\%)$. Furthermore, thanks to recent and future advancements in fast silicon tracking technologies, the capabilities of such a facility can be further enhanced by the use of fast ($<$100 ps) and radiation-hard silicon trackers placed along the beamline, in order to track both the parent meson and its daughter leptons. Given a sufficient timing resolution ($<$1 ns) of the neutrino detector [70], it is possible to uniquely correlate each observed neutrino interaction with its parent meson and associated charged lepton, making possible a direct measurement of neutrino energy on an event-by-event basis exploiting the two-body kinematics of the parent meson decay. This is the core concept of the *tagged neutrino beam* proposed by the NuTag Collaboration, which is a long-standing goal in accelerator neutrino physics historically unattainable due to technological limitations [71–73]. The ENUBET and NuTag Collaborations recently joined forces to combine their approaches and to explore the feasibility of implementing a monitored and tagged neutrino beam at CERN for high precision neutrino cross-section measurements.

2.1 Accelerator neutrino beams

In conventional neutrino beams, the neutrinos are created from the decay of pions or kaons produced by the interaction of a high-energy proton beam impinging on a fixed target [59]. A system of magnets allows the focusing and momentum selection, in the energy region of interest, of the meson beam before entering the decay tunnel. Once the selected mesons pass through the decay volume, they eventually decay producing neutrinos. Conventional beams are in general sources of ν_μ and $\overline{\nu}_\mu$, produced mainly from the decay of charged pions ($\pi^+ \to \mu^+ \nu_\mu$) and kaons ($K^+ \to \mu^+ \nu_\mu$), with a relatively small contamination of ν_e and $\overline{\nu}_e$ created either in the three body semileptonic decay of kaons ($K^+ \to e^+ \pi^0 \nu_e$) or by the decay in flight of muons ($\mu^+ \to e^+ \nu_e \overline{\nu}_\mu$). The relative weight of ν_e from kaons and muons depends on the hadron energy, the length of the secondary hadron beamline and the length of the decay volume.
Conventional neutrino beams are generally classified in wide and narrow band beams [59]. Specifically, the term "band" refers to the width of the momentum spectrum of the hadrons and, as a consequence, produced neutrinos. *Wide band beams* are optimized to ensure the largest neutrino flux in a broad energy range. They constitute the vast majority of neutrino beams designed in the past and those currently in operation, since their significant flux compensates the tiny neutrino cross-section at the GeV scale ($\sigma \simeq 10^{-38}$ cm^2). In a wide band beam the focusing mechanism is provided by magnetic horns, which allow to produce a large acceptance beam. Then, focused pions and kaons subsequently decay producing neutrinos over a broad energy range. The focusing of secondary mesons produced at the target is fundamental to increase the neutrino flux to the detector located on axis with the beamline. The typical layout for a wide band beam is shown in the bottom of Fig. 2.1, where the focusing and momentum selection is performed by a set of horns.

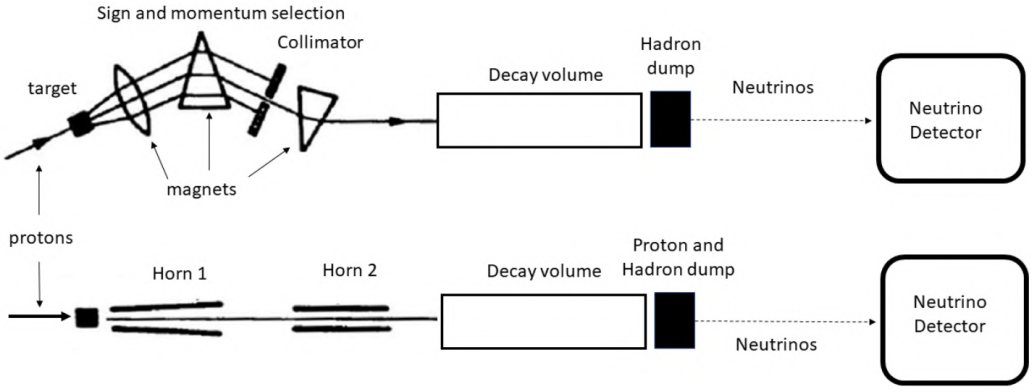

Figure 2.1: A typical layout for a narrow band beam (top) and a wide band beam (bottom). Figure from [59].

Narrow band beams can offer a higher degree of precision at the expenses of a strong reduction of the flux. In this case, the momentum and charge of the hadrons (and, in turn, the produced neutrinos) are selected employing magnetic dipoles and slits. A typical layout for a narrow band beam is shown in the top of Fig. 2.1, where a set of quadrupoles, dipoles and collimators (slits) is placed after the target and used to select the sign and momentum of the secondaries and, finally, to steer them towards the decay volume. In particular, both for wide and narrow band beams, all charged particles but neutrinos are stopped at the hadron dump, located before the neutrino detector. The typical ν_μ spectrum for a narrow band beam is dichromatic since two distinct peaks can

be recognised, namely the peak of neutrinos coming from the selected pions and the peak of neutrinos from the selected kaons. If the accepted momentum range (momentum bite) is very small, the width of the peak is actually dominated by the two-body decay of either pions or kaons.
A narrower neutrino flux can also be achieved using the off-axis technique. *Off-axis neutrino beams* are a special configuration of wide band beams that operate with a detector located off the beam axis. The idea for an off-axis neutrino beam was first proposed by the BNL experiment E889 [74] to solve the issue of neutrino energy estimation, caused by the wide energy range of focused mesons, by simply detecting neutrinos at a given angle with respect to the beam direction. The off-axis technique is motivated by the two-body decay kinematics of secondary pions or kaons, resulting in neutrinos with energy given by [75]:

$$E_{\nu_\mu} = \frac{\left(1 - m_\mu^2/m_{\pi/K}^2\right) E_{\pi/K}}{(1 + \gamma^2 \tan^2 \theta)} \tag{2.1}$$

where θ is the angle between the neutrino and meson direction and $\gamma = E_{\pi/K}/m_{\pi/K}$. For decays occurring on-axis ($\theta = 0°$), the neutrino and meson energies are linearly related, whereas for neutrinos observed at a certain angle with respect to the beam axis the relation becomes weaker [75]. The neutrino energy as a function of pion energy for different decay angles between the neutrino and meson direction is shown in Fig. 2.2, left. For large off-axis angles, mesons of any energy contribute to producing neutrinos with almost the same energy in their decays. T2K was the first long-baseline oscillation experiment to employ the off-axis method to generate a narrow-band neutrino beam [68], selecting a neutrino flux with a peak energy near the oscillation maximum at the SuperKamiokande far detector. The T2K near and far detectors are located 2.5° off-axis from the center of the neutrino beam to select a peak energy of $\sim 600\,\text{MeV}$. The T2K neutrino flux as a function of neutrino energy at different off-axis locations is shown in Fig. 2.2, right.

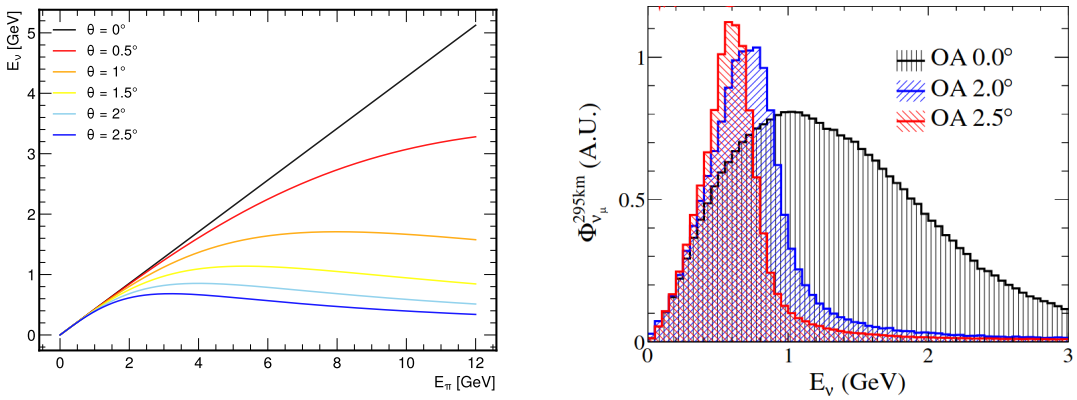

Figure 2.2: (left) Neutrino energy as a function of pion energy for different decay angle values between the ν_μ and π directions. (right) T2K flux as a function of neutrino energy, for different off-axis angles with respect to the neutrino beam direction. Figure from [68].

In particular, not only at larger off-axis angles the energy spectrum becomes lower and narrower, but at certain energies, the flux at the peak actually exceeds the flux at that same energy in the on-axis case [75], as shown in Fig. 2.2, right.
In conclusion, high-intensity beams are in most cases wide band beams and the determination of the neutrino energy must rely either on the reconstruction of the final state

particles in a neutrino interaction or by the off-axis location of the detector. Instead, a narrow band beam turns out to be an optimal choice for cross-section measurements since it can reduce the intrinsic uncertainty on the neutrino energy and, therefore, to obtain an improved accuracy for dedicated measurements of neutrino cross-sections.

2.2 The ENUBET monitored neutrino beam

Neutrino cross-sections at the GeV scale are currently known with limited precision despite their prominent role in the present and future long-baseline neutrino oscillation experiments [76]. These measurements are currently limited by systematic uncertainties in the flux and energy of initial-state neutrinos and the precision that can be achieved is generally larger than 10% [52]. There is a broad consensus on the fact that "to extract the most physics from DUNE and Hyper-Kamiokande a complementary programme of experimentation to determine neutrino cross-sections and fluxes is required" [77]. The design of modern neutrino beams with unprecedented control of flux, flavor and energy of neutrinos is therefore instrumental to tackle this challenge.

Monitored neutrino beams [78] are a novel technology aimed at determine the flux and the flavour of neutrinos produced at the source at the per-cent level. The core concept of a monitored neutrino beam is that the neutrino flux can be obtained by measuring the rate of charged leptons associated to neutrinos produced in the decay volume. Since every neutrino created by the decay of a charged meson produces one charged lepton, counting charged leptons in the decay tunnel provides a direct measurement of the flux because the ν_μ ($\overline{\nu}_\mu$) yield is proportional to the μ^+ (μ^-) yield in the tunnel and the ν_e ($\overline{\nu}_e$) yield is proportional to the e^+ (e^-) yield in the tunnel [76]. Therefore, thanks to the one-to-one correspondence between the charged lepton in the decay tunnel and the corresponding neutrino, this method provides a direct handle on neutrino flux normalization. Unlike conventional beams, the decay tunnel of a monitored neutrino beam [78] is instrumented with radiation-hard detectors for diagnostics, capable to record the charged leptons produced in association with neutrinos and thus to provide a direct measurement of the neutrino flux and flavor at the source. These facilities are thus the ideal tool for high-precision neutrino cross-section measurements at the GeV scale since they offer superior control of beam systematics with respect to existing facilities.

The ENUBET (Enhanced NeUtrino BEam with kaon Tagging) project is aimed at designing and experimentally demonstrating the concept of monitored neutrino beams [76]. The ERC ENUBET project [79] focused on the identification of positrons from the three-body semileptonic decay of kaons ($K_{e3} \equiv K^+ \to e^+\pi^0\nu_e$). More recently, the CERN NP06/ENUBET experiment [80–85] extended the original project reach to monitor muons from the two-body decay of kaons ($K_{\mu\nu} \equiv K^+ \to \mu^+\nu_\mu$) and pions ($\pi_{\mu\nu} \equiv \pi^+ \to \mu^+\nu_\mu$). Therefore, the ENUBET transfer line can be used to monitor both electron and muon neutrinos produced in the instrumented decay tunnel. A simplified scheme of the entire ENUBET facility is shown in Fig. 2.3, where the instrumented decay tunnel is depicted in the right inset.

The ENUBET Collaboration delivered the first end-to-end design [76] of a monitored neutrino beam capable of monitoring lepton production at single particle level using a focusing system without magnetic horns, a 20 m normal-conducting transfer line for charge and momentum selection and a 40 m tunnel instrumented with cost-effective particle detectors. The final design of the ENUBET beamline is shown in Fig. 2.4.

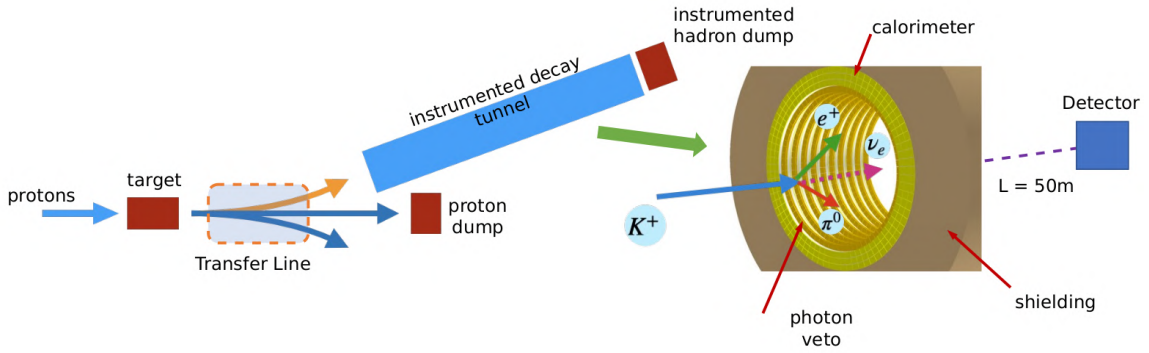

Figure 2.3: Scheme of the ENUBET facility. The decay volume instrumentation is shown in the right inset.

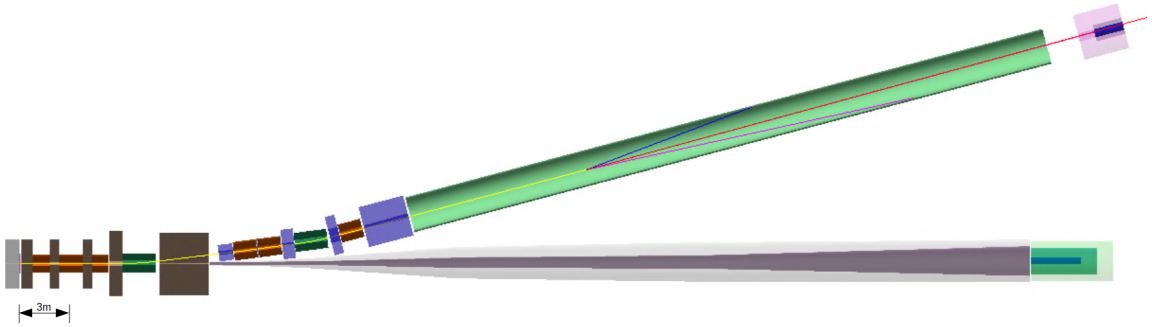

Figure 2.4: The final design of the ENUBET beamline. The primary protons impinge on the target producing secondaries which are are sign- and momentum-selected by the transfer line and transported at the entrance of the instrumented decay tunnel (light green). From left to right: the quadrupole triplet (orange) and copper collimators (brown), double-bend momentum selector section composed of two dipoles (green), two quadrupoles, one momentum copper collimator (brown) and the last quadrupole surrounded by two Inermet180 collimators (blue). The hadron dump is located at the tunnel exit stopping all particles but neutrinos. The non-interacting protons travel inside the proton pipe (gray) and are stopped by the proton dump (dark green). The neutrino detector is located 50 m far from the decay tunnel exit, not shown in the figure. Figure from [76].

The fast-extraction scheme of primary protons, where protons from the accelerator are extracted in short bunches, is employed by the vast majority of accelerator neutrino beams but cannot be employed for a successful operation of the ENUBET monitored neutrino beam. Indeed, in a fast-extraction scheme the full primary proton beam is extracted onto the target in tens of microseconds or less; this would generate a pile-up rate not sustainable in the tunnel instrumentation, making a direct neutrino flux estimation impossible [76]. To guarantee a successful lepton monitoring operation, the detector technology instrumenting the decay tunnel can only withstand a particle rate $\lesssim 100\text{kHz/cm}^2$[1]. Therefore, the ideal extraction method for a monitored neutrino beam is the slow resonant ("multi-turn") extraction of primary protons, where the full intensity is continuously extracted in a time interval of a few seconds [59]. The slow extraction of primary protons reduces the particle rate at a sustainable level for detectors, but sets important design constraints for the beamline, which cannot employ a magnetic horn and relies only on static focusing magnetic elements, i.e. dipoles and quadrupoles [76]. Indeed, magnetic horns are difficult to be operated with a proton extraction longer than a few ms due to Joule heating of the conductors [59]. A pulsed version of the slow

[1]If conventional, low cost, scintillator based calorimeters are employed, this limit comes from the detector granularity ($3\times3\,\text{cm}^2$), the intrinsic time resolution ($\sim 400\,\text{ps}$) and the front-end electronics and digitizer sampling rate ($\sim 1\,\text{Gs/s}$) [76].

extraction (burst-mode slow extraction, e.g. with 10 ms bursts repeated at 10 Hz) has been designed and successfully tested at the CERN SPS, with the goal of pairing it with stronger focusing devices such as magnetic horns [86, 87]. The use of a magnetic horn in a monitored neutrino beam is therefore possible but non-trivial, in particular for the hardware-side R&D required to pulse a conventional horn for several ms. The design of a purely static transfer line with adequate intensity without employing a pulsed magnetic focusing horn has been a breakthrough achievement in the ENUBET R&D, since it allows low pile-up levels, removes the operational complexity of a magnetic horn and turns out to be cost-effective [76]. The beamline optics were simulated using `TRANSPORT` [88] and validated with `MAD-X` [89]. The beamline was then implemented both in `G4Beamline` [90] and `GEANT4` [64], in order to have full control of the particle history for the neutrino flux systematics studies.

The primary protons are slowly extracted from the CERN SPS proton driver with a 400 GeV/c momentum and steered to a graphite target (70 cm length, 3 cm radius). The primary proton interactions with the target produce secondary mesons, mainly pions and kaons. The secondary pions and kaons are then sign- and momentum-selected by a static focusing system made entirely of normal-conducting elements: six quadrupoles and two bending dipoles. The beamline consists of a quadrupole triplet followed by a bending dipole, a pair of quadrupoles, another bending dipole and a final quadrupole [76]. The two dipoles are based on existing CERN magnets that can be operated up to 1.8 T and each dipole provides a bending angle of 7.4°, for a total bending of the beam with respect to the primary proton line of 14.8°. The transfer line details are shown in Fig. 2.5. Unlike magnetic horns, dipoles and quadrupoles are DC powered and there is no constraint on the duration of the proton extraction: in the case of ENUBET protons are slowly steered to the target in ~ 2 s. Absorbers and collimators are placed between magnetic elements, and a 5 cm thick tungsten foil ($\sim 14.3X_0$, $0.5\lambda_0$) is located after the target to screen positrons that otherwise would reach the tunnel entrance contributing to the background [76].

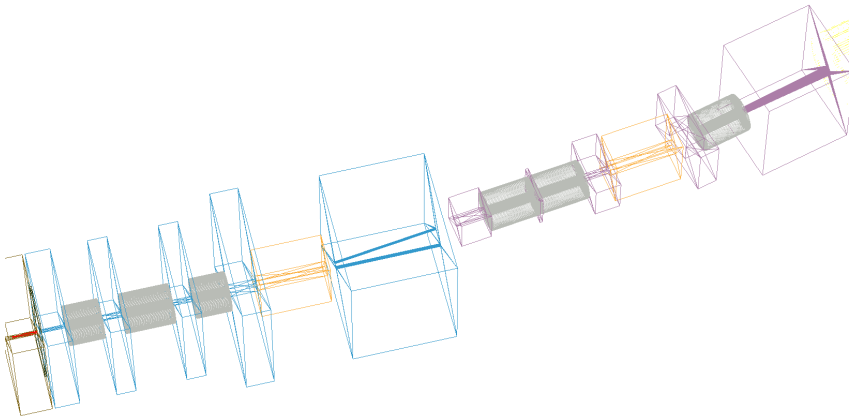

Figure 2.5: Details of the transfer line: graphite target (red cylinder) surrounded by concrete shielding, quadrupoles (gray) and dipoles (orange), copper collimators (blue) and Inermet180 collimators (purple). Figure from [76].

The ENUBET narrow-band beamline aims at producing secondary kaons and pions with a central momentum of 8.5 GeV/c and with a momentum bite $\Delta p/p = 10\%$. The length

of the transfer line needs to be short enough ($\sim$ 26.7 m up to the tunnel entrance) to minimize kaon decays before the entrance of the decay tunnel. Since kaons must decay inside the tunnel volume but muons must reach the hadron dump, the 40 m length of the instrumented decay tunnel is shorter than in a conventional beamline, with the advantage of a decrease in the cost of the tunnel instrumentation. The non-interacting primary protons and high-momentum secondaries are then stopped in the proton dump and only a small fraction of their neutrinos are in the geometrical acceptance of the detector, which is located off-axis with respect to the proton dump.
Since the kaon mass is much larger than pions, charged leptons emitted in kaon decays are produced at a larger angle with respect to muons produced in pion decays. In particular, positrons are emitted with an average angle of $\sim$ 88 mrad [78], whereas muons from kaon decays have an average emission angle of about 60 mrad [76], both inside the geometrical acceptance of the decay tunnel. Therefore, the instrumented decay tunnel can be used to record large-angle charged leptons emitted in kaon decays, thus determining the ν_e flux and the high-energy component of the ν_μ flux from $K_{\mu\nu}$ decay. However, the highly boosted pions emit muons almost collinear and thus outside the acceptance region of the calorimeters. The monitoring of the low energy ν_μ component from $\pi_{\mu\nu}$ decays can anyway be achieved by instrumenting the hadron dump, placed after the tunnel end, with muon stations to measure the range-out of muons from pions [76]. The hadron dump instrumentation must be capable to withstand a muon rate of $\sim 2\,\mathrm{MHz/cm^2}$ and a neutron fluence of about $\sim 10^{12}$ $1\,\mathrm{MeV\text{-}n_{eq}/cm^2}$ in the upstream layer closer to the tunnel end. The suitable detector technology is object of R&D studies in the framework of the PIMENT (Picosecond Micromegas for ENUBET) project [91]. The hadron dump is placed 2 m after the tunnel exit and it is designed to reduce the background due to backscattering particles reaching the decay volume instrumentation. A preliminary configuration of the muon detection instrumentation has already been studied. The hadron dump is made of a 2 m long iron slab and the first muon station is placed after the dump, followed by another iron absorber of the same length. Seven additional muon stations follow the first one, interspersed with 0.5 m long iron absorbers. The muon spectrum can be measured by exploiting their range out through the absorbers.

The particles within the momentum bite entering the decay volume are mainly protons, K^+, and π^+ ($\overline{p}$, K^-, and π^- in an antineutrino run). In particular, the flux at the tunnel entrance is $0.4 \cdot 10^{-3}$/pot for K^+ and $4.6 \cdot 10^{-3}$/pot for π^+. Other than protons, other background particles are transported at the entrance of the tunnel, such as tertiaries ($e^\pm$, γ, muons, $\pi^\pm$), off-momentum mesons and halo muons. The momentum spectra of particles at the tunnel obtained from the `GEANT4` simulation of the beamline is shown in Fig. 2.6.

The neutrino detector considered to compute the expected event rate spectra is a 500-ton LAr detector, with a $6 \times 6\,\mathrm{m^2}$ front-face area, namely with dimensions comparable to ProtoDUNE-SP [92] at CERN, and located at 50 m from the tunnel end. The neutrinos reaching the detector are mostly due to kaon and pion decays, plus contamination originating from early decays of off-momentum particles and also low-energy neutrinos from the proton and hadron dumps. The design of the beamline has been optimized to produce neutrinos in the energy range of interest for the DUNE experiment ($1 - 4\,\mathrm{GeV}$) [76]. In particular, in ENUBET the neutrino energy can be determined a priori using the *narrow-band off-axis* technique, without relying on the reconstruction of final-state particles. Such a technique enables to provide the muon neutrino energy on an event-by-event basis exploiting both the narrow momentum width of the parent beam at $\mathcal{O}(10\%)$

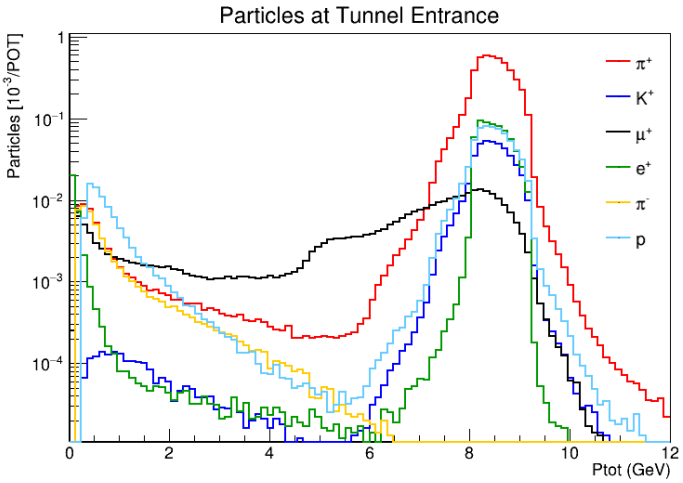

Figure 2.6: Momentum distribution of particles at the tunnel entrance as obtained from `GEANT4`. Figure from [76].

and the tight correlation existing between neutrino energy and the radial off-axis position of the interaction vertex due to two-body meson decay kinematics [76], i.e. the off-axis technique described in Sec. 2.1.

2.3 Decay tunnel instrumentation

In a monitored neutrino beam the cylindrical walls of the decay tunnel are equipped with low-cost detectors that act as beam diagnostics [76]. One of the major challenges of ENUBET R&D was to design a compact, radiation-hard, efficient and cost-effective instrumentation for the decay volume. The optimal tunnel instrumentation is made of a set of longitudinal iron-scintillator sampling calorimeter modules, with front readout for scintillation light, complemented by a photon veto ("t_0-layer") made of plastic scintillator tiles positioned in the innermost part of the calorimeter, to be used for timing and photon discrimination. The instrumentation of the decay tunnel aims to record large-angle charged leptons, perform event reconstruction and particle identification. The use of iron-scintillator calorimeter modules is a solution that keeps the cost of diagnostics well below the overall cost of the neutrino beamline. A schematic of the ENUBET instrumented decay tunnel in shown in Fig. 2.7, left.

The calorimeter is employed to achieve $e^+/\pi^+/\mu^+$ separation and it is segmented in the longitudinal, azimuthal and radial directions. The basic unit is called Lateral Compact Module (LCM), made of five slabs of iron interleaved with plastic scintillator tiles (Eljen EJ-200). The transverse size of the iron and scintillator tiles is $3 \times 3\,\mathrm{cm}^2$ and their thicknesses are 1.5 cm and 0.7 cm, respectively, for a total LCM thickness of 11 cm, corresponding to $4.3X_0$. The dimension of the LCM is a compromise between the need for high-granularity modules for pile-up reduction and particle identification and the total cost of the tunnel instrumentation. The LCMs are arranged in three radial layers; every module covers an azimuthal angle of 31 mrad for a total of 200 LCMs per layer at a fixed longitudinal position along the tunnel, for a total number of $2.2 \cdot 10^5$ LCMs, considering the decay tunnel to be fully instrumented [76]. The scintillation light is routed by a couple of WLS fibers, placed on the front face of each scintillator tile of both calorimeter and t_0-layer modules, towards Silicon Photomultipliers (SiPMs) placed above a 30 cm thick

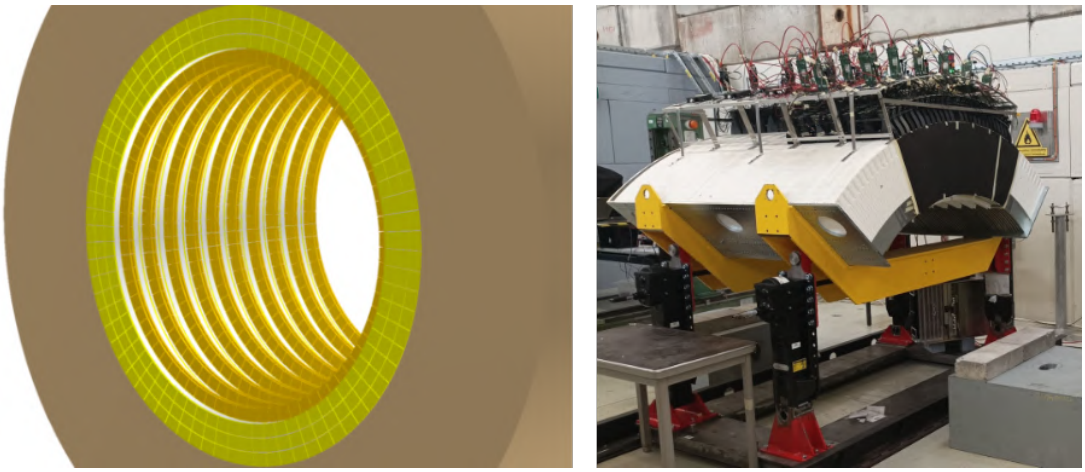

Figure 2.7: (left) Schematic of the ENUBET instrumented decay tunnel. The three layers of modules of the calorimeter (light green) constitute the inner wall of the tunnel. The rings of the scintillator tiles (doublets) of the photon veto (yellow) are located just below the modules. The optical fibers (not shown) bring the light to the outer part of the tunnel in the radial direction. They cross the neutron shielding (light brown) where the SiPMs (not shown) are positioned. (right) Prototype of a section of the instrumented decay tunnel during a test-beam at CERN-PS T9 beamline.

borated polyethylene (BPE, 5% Boron concentration) shielding that protects against neutron radiation damage of the sensors. The neutron reduction induced by adding the BPE layer amounts to a factor of ~ 18, averaging over the expected energy spectrum and it settles at about $7 \cdot 10^{-11}$ $n/\text{pot}/\text{cm}^2$ in the middle region of the tagger ($7 \cdot 10^9$ n/cm^2 for 10^{20} pot) [76]. The 10 fibers of each LCM are read out together, whereas each t_0-layer tile is read out individually by digitizers connected to the respective SiPM that sample the resulting waveforms [83].

The separation of charged pions from positrons can be accomplished by exploiting the different energy deposition topologies in hadronic and electromagnetic showers, namely by means of the different patterns of energy clusters in the longitudinal modules of the calorimeter. Positron-induced electromagnetic showers are more localized and fully contained within a few modules, whereas the more penetrating pion-induced hadronic showers cross many more modules than the electromagnetic ones. Fig. 2.8 shows the different energy deposition topologies due to electromagnetic showers initiated either by signal positrons (left), background photons from $\pi^0 \to \gamma\gamma$ (center) or due to hadronic shower initiated by charged pions (right). Other than π and e^+ PID, the calorimeter can perform μ identification. As muons are mip-like particles, they produce energy deposits compatible with that of a mip in the LCMs, with peculiar long track topologies. Complementing the calorimeter with a photon veto system is an essential task to accomplish separation between positrons and photons[2], since their signals in the calorimeter have the same topology.

The t_0-layer is composed of rings of plastic scintillator tiles placed in the innermost part of the tunnel, in correspondence of the first two tiles of each LCM, to distinguish γ-initiated electromagnetic showers from those induced by positrons and to provide the absolute time of each charged particle impinging on the tunnel walls. Since each tile of the doublet is read out separately, the t_0-layer is used to veto photons (no signal in any

[2]Background photons stem from other K^+ decay modes producing neutral pions (for instance the $K^+ \to \pi^0\pi^+$ decay), as well as to electromagnetic showers originated by particle interactions with the passive elements of the transfer line.

tile of the doublet) and converted photons (two mip-like signals in one or two tiles of the doublet) against charged particles (one mip-like signal per tile) [76]. A schematic of the layout of the t_0-layer, together with its working principle, is shown in Fig. 2.9.

Figure 2.8: Energy deposition topologies for electromagnetic and hadronic showers in the longitudinally segmented calorimeter.

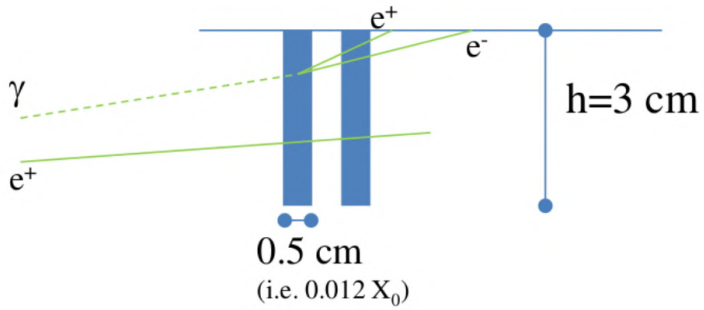

Figure 2.9: Schematic of the working principle of the t_0-layer.

The scintillation light produced by charged particles energy deposition is trapped inside the tiles by a diffusive coating (Eljen EJ-510) deposited on the tile surfaces [76]. A pair of grooves in one of the tile faces are not covered by the diffuser, and are used to readout the scintillation light by means of WLS fibers. Two WLS optical fibers (Y11, Kuraray) are glued to the grooves using an Eljen optical glue (EJ-500) with a refraction index similar to the plastic scintillator. As a consequence, part of the light impinges on the WLS fibers and is re-emitted at $\lambda \sim 440\,\text{nm}$ inside the fiber, transported outside the calorimetric layers and finally recorded by a $4 \times 4\,\text{mm}^2$ SiPM. All (ten) fibers belonging to the same LCM are grouped and optically connected to the same SiPM. Each calorimeter module corresponds to one electronic channel. The SiPM output signal is connected to a digitizer that samples the waveform and sends them to the DAQ. The light produced in the photon veto doublets is transported by Y11 Kuraray WLS fibers running through the first two LCM tiles of each layer by means of additional grooves. Each t_0-layer tile is read out by two WLS fibers and one $3 \times 3\,\text{mm}^2$ SiPM. Since each doublet is positioned below the first tile of each LCM of the innermost calorimetric layer, the photon veto can be used to measure the absolute time when a charged particle (a candidate positron or muon) impinges on the tunnel wall [76]. Test-beam data collected at CERN in 2018 and 2022 show a time resolution of 400 ps when the waveform is sampled by a 1 Gs/s digitizer [93]. The algorithms developed for the reconstruction and classification of positron events from energy deposition in the calorimeter modules are described in Chapter 4.
The detector technology to be used for the instrumentation of the decay tunnel was investigated by the ENUBET collaboration from 2016 to 2022 [93–98] and culminated with the construction of a large-scale prototype ("demonstrator") of a section of the instrumented decay tunnel (1.65 m length, 90° azimuthal coverage), which is shown in Fig. 2.7, right. The demonstrator was exposed to charged-particle beams in the T9 secondary line of the CERN-PS for validation in 2022-24. The demonstrator performances measured in dedicated test-beams are described in Chapter 3.

2.4 The nuSCOPE monitored and tagged neutrino beam

In a monitored neutrino beam, the charged leptons produced in association with neutrinos are recorded by the detectors instrumenting the decay tunnel and provide a direct measurement of the neutrino flux and flavour. The physics potential of a monitored neutrino beam can be significantly enhanced by correlating in time the occurrence of the charged lepton measured in the tunnel with the corresponding neutrino interaction in the neutrino detector. If the neutrino detector possesses a sufficient time resolution ($< 1\,\text{ns}$), each observed neutrino interaction can be uniquely associated with its parent meson and charged lepton [76]. The measurement of the lepton energy combined with a high-precision measurement of the parent meson momentum can be used to kinematically reconstruct the neutrino energy on an event-by-event basis. Such a bold technique is called *neutrino tagging* and it was proposed in the past by several authors [72, 99]. The first pioneering attempts of creating a *tagged neutrino beam* were developed in USSR in the 1980s, but because of the enormous charged particle rate in the decay volume and the limited 4D (i.e. time and space) precision of trackers they never achieved their physics goals [73]. Neutrino tagging has been a long-standing goal in accelerator neutrino physics, but historically unattainable due to technological limitations [71, 72]. The implementation of a tagged neutrino beam would thus constitute a major advance in experimental physics, enabling for the first time a direct measurement of neutrino energy on an event-by-event basis using the two-body kinematics of the parent meson decay.

The introduction of long proton extractions in accelerator neutrino beams to reduce the instantaneous particle rate has unlocked new possibilities, capitalized upon by the NuTag Collaboration starting in 2022 [100, 101]. The core of the tagged neutrino beam proposed by NuTag builds upon recent advancements in fast silicon tracking technologies, which have been successfully demonstrated in kaon physics by the NA62 Gigatracker and further enhanced by the technological innovations driven by LHC upgrade programs [102, 103]. Therefore, the historical technological limitations in neutrino tagging are currently being lifted, and just recently NA62 reported the detection of the first tagged neutrino candidate [104]. In particular, the use of a slow proton extraction scheme in a purely static transfer line such as the one designed by NP06/ENUBET represents a great opportunity to implement a tagged neutrino beam. The use of fast ($< 100\,\text{ps}$), radiation-hard silicon trackers placed along the beamline to track both the parent meson and its daughter leptons constitute a remarkable extension of the ENUBET's capabilities. Indeed, lepton monitoring with advanced tracking significantly improves the neutrino flux determination, eliminating the dependencies on Monte Carlo simulations of the beamline and finally offering a direct and precise initial flux measurement. Furthermore, the capability to uniquely associate in time the neutrino interaction with accompanying particles in the transfer line by means of fast silicon trackers would be definetely a game changer in the field, enabling a kinematic reconstruction of neutrino energy on an event-by-event basis with sub-percent energy resolution. The ENUBET and NuTag Collaborations recently recognized the possibility to integrate in synergy their approaches and thus joined forces to explore the feasibility of implementing a monitored and tagged neutrino beam at CERN within the framework of Physics Beyond Colliders (PBC) at CERN [105]. The outcome of these joint efforts resulted in the concept study for a short-baseline neutrino beam at CERN for high-precision cross-section measurements submitted as an input document [70, 106] for the European Strategy for Particle Physics 2026 Update. The convergence of the ENUBET and NuTag approaches revealed the potential to deliver neutrino-nucleus cross-section measurements at the few GeV scale with unprecedented precision and cul-

minated in the birth of a new collaboration named nuSCOPE (NeUtrino SPS COmplex for Precision Experiments).

The nuSCOPE beamline [70] aims at producing secondary kaons and pions with a 8.5 GeV/c central momentum. The transfer line has been optimized to generate a narrow band meson beam that remains parallel throughout the 40 m long decay tunnel. The schematic design of the nuSCOPE transfer line is shown in Fig. 2.10. The initial quadrupole triplet downstream of the target provide the necessary transverse acceptance and transport towards the momentum-selection section of the beamline, made of bending dipoles with small vertical gaps that deflect the secondary beam by 18° and remove particles with momenta outside the desired ±10 % momentum range. The last quadrupole triplet is instead used to produce a meson beam parallel to the decay tunnel axis.

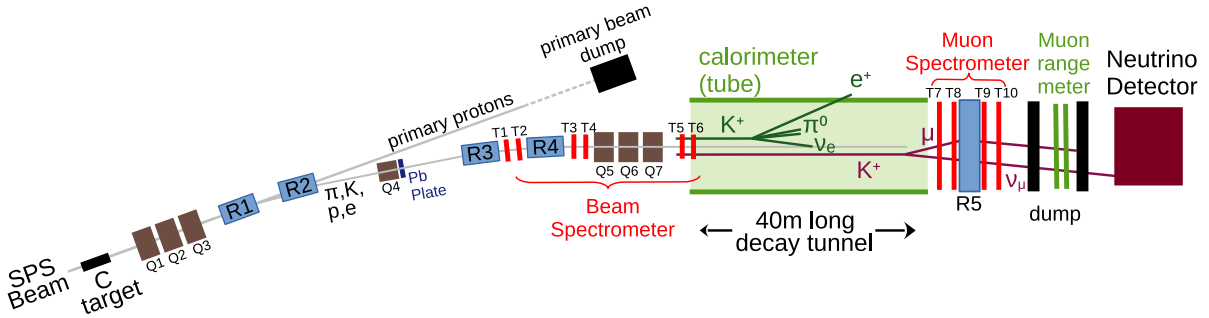

Figure 2.10: Layout of the nuSCOPE beamline. The beamline (not to scale) combines both the ENUBET (in green) and the NuTag (in red) beam instrumentation. The first part of the beamline contains the beamline magnets (blue: rectangular bending magnets; brown: quadrupole magnets). Figure from [70].

The nuSCOPE beam instrumentation is non-conventional and benefits from the installation of the NP06/ENUBET and NuTag detectors, providing an unprecedented control of the neutrino flux and energy at source. The charged lepton production monitoring is performed using the NP06/ENUBET technique, based on a modular calorimeter instrumenting the decay tunnel and a hadron dump instrumented as a muon range-meter, enabling an accurate measurement of the ν_e and ν_μ fluxes. The parent meson reconstruction and neutrino tagging are carried out using the methods and devices developed by NuTag. A pair of silicon pixel detectors (NuTag trackers) is positioned on each side of the fourth bending magnet (R4) to track the parent meson and measure its momentum; two additional trackers are then located just upstream of the decay tunnel to determine the particle trajectory. A pair of trackers is also placed on each side of an additional bending magnet (R5) downstream of the decay tunnel, aiming to measure the momentum of the daughter muon. The beamline is driven by 400 GeV/c protons that are slowly extracted from the CERN SPS. The neutrino detector is located 25 m downstream of the end of the decay tunnel and based on a 500-ton fiducial mass LAr detector with $4 \times 4\,\mathrm{m}^2$ front-face area, 22.3 m length.

The design of the nuSCOPE beamline [70] is inspired by the NP06/ENUBET multi-momentum beamline [107], which was designed to allow for runs at different secondary momenta (4, 6 and 8.5 GeV/c) with the aim of improving the statistical sample in the $\sim$ 1 GeV region to deliver neutrino cross-section measurement of relevance for Hyper-Kamiokande [84]. The nuSCOPE beamline is the result of an optimisation process and its design differs from the previous ones [76, 107] in several aspects. For instance, in order to ensure the proper operation of the silicon trackers installed along the transfer line it is necessary to reduce the pile-up and the detector throughput at a sustainable

level by these devices, with particle rates of $\mathcal{O}(10\,\mathrm{MHz/mm^2})$. For this reason, the large number of positrons produced in the graphite target needs to be mitigated, otherwise their particle flux would compromise momentum measurement on a particle-by-particle basis. To counter these, a thin Pb plate has been inserted into the transfer line right after the Q4 quadrupole, to degrade their energy outside the beamline acceptance[3]. The beamline has been optimised using a multi-objective genetic algorithm (MOGA) and validated with an end-to-end BDSIM simulation [109]. The beamline optimization has been performed within the PBC framework and it significantly enhanced the original ENUBET design [76], increasing the pion and kaon yield per proton-on-target (pot) by factors of 4.8 and 3.5, respectively. The BDSIM beamline results are listed in Tab. 2.1, showing a distinct improvement of the nuSCOPE beamline performance in comparison to the ENUBET baseline design.

Particle yield	**ENUBET design**	**nuSCOPE design**
K^+/pot [10^{-4}]	3.6	12.6
π^+/pot [10^{-2}]	0.4	1.9

Table 2.1: Comparison of the optimised nuSCOPE beamline design with the initial ENUBET baseline design [76] at $p = 8.5\,\mathrm{GeV/c}$ in the $\Delta p/p \in [-10\%, 10\%]$ momentum selection. Table reproduced from [70].

The increase of K^+/π^+ yield at tunnel entrance allows for a reduction in the number of protons-on-target needed to accumulate the desired neutrino statistics. This significant reduction in the protons-on-target requirement has been a key advancement that enables the implementation of nuSCOPE without significant impact on CERN's fixed-target program, including the operation of BDF/SHiP [110] experiment. The nuSCOPE beam parameters are summarized in Tab. 2.2.

Parameter	**Value**
Primary proton momentum [GeV/c]	400
Beamline meson momentum [GeV/c]	max. 8.5
Proton-beam spill duration	slow (4.8 s to 9.6 s)
Spill intensity [protons/spill]	1.0×10^{13}
Event rate [THz]	1 – 2
Instantaneous power on target [W]	170 – 340
(K^+, π^+) yield per proton	(1.3×10^{-3}, 1.9×10^{-2})
(K^+, π^+) rate [GHz]	max. (2.7, 40)
Annual proton intensity [protons/year]	2.1–3.2×10^{18}
Total proton requirement [protons]	1.4×10^{19}

Table 2.2: Beamline parameters and specifications of the optimized nuSCOPE beamline at SPS energies. Meson yields and rates refer to the decay tunnel entrance. The total proton requirement targets a 1 % statistical uncertainty on the inclusive ν_e cross-section. The annual proton intensity assumes a spill duration of 4.8 s. Table reproduced from [70].

A critical parameter in the beamline optimisation and design is the particle rate at the silicon trackers used for meson momentum reconstruction at the R4 bending magnet. In the current design, the particle flux on the first pixel detector upstream of the R4 bending magnet (spill intensity 1×10^{13} pot, spill duration 4.8 s) is in the range of $10 - 40\,\mathrm{MHz/mm^2}$, that is a fully acceptable flux for the NuTag technology. In order to further

[3] As done for K12/NA62 in the CERN North Area [108], it is possible to adjust the thickness of the positron-absorbing Pb plate (e.g. using a motorized wedge with variable thickness) to effectively tune the flux on the pixel detectors.

reduce the instantaneous rates, a longer spill duration of 9.6 s has also been considered. The spectrum of particles transported at the tunnel entrance is shown in Fig. 2.11.

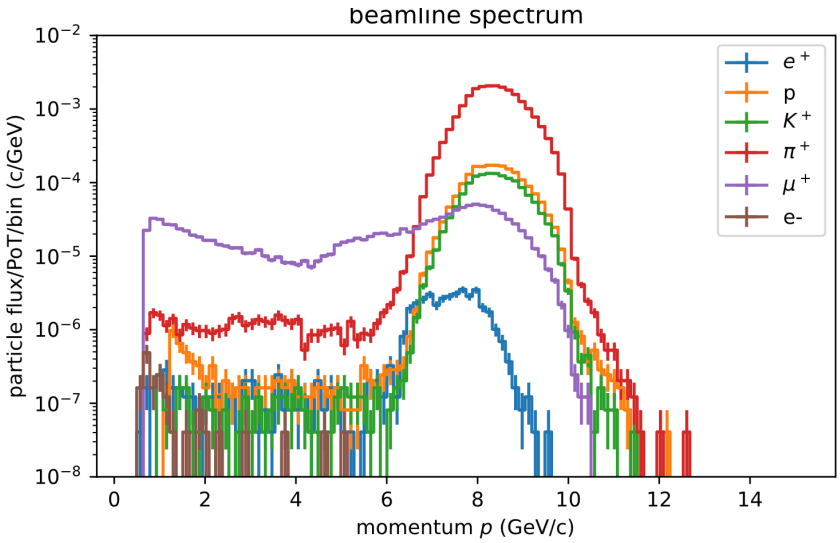

Figure 2.11: Spectrum of particles transported at the tunnel entrance with the optimised transfer line. The positron transmission is suppressed due to the Pb plate followed by two bending magnets. Figure from [70].

Several locations have been investigated for the nuSCOPE beamline implementation at CERN before LHC Run 5 to ensure that its construction and operation do not interfere with the CERN LHC and fixed target programme. The top view of the CERN SPS map is shown in Fig. 2.12, reporting the three experimental areas at SPS located at the three long straight sections LSS2, LSS4 and LSS6. The most promising locations for nuSCOPE beamline are in a new experimental Hall (ECN4) in the Prevessin campus and in an extension of existing tunnels near the SPS Long Straight Section 6 (LSS6), close to HighRadMat in the Meyrin campus. Details concerning potential locations of nuSCOPE beamline at CERN are extensively discussed in [70].

2.5 Silicon tracking devices

The innovative aspect of the nuSCOPE beamline is the fact it is instrumented with three sets of detectors for beam diagnostics, as schematically shown in Fig. 2.10. The neutrino flux originating from kaon decays can be monitored by means of the instrumentation in the tunnel walls, whereas the ν_μ flux from pion decays is monitored by means of the instrumented hadron dump. The detector technologies instrumenting the decay tunnel and the hadron dump are fully inherited from the NP06/ENUBET design, as extensively described in Secs. 2.2 and 2.3. In addition to the NP06/ENUBET detectors for charged lepton monitoring, the NuTag silicon detectors can also be used to track the parent mesons and daughter muons, allowing for neutrino tagging at single-particle level. The nuSCOPE beamline is instrumented with two spectrometers measuring the momentum, direction, time and position of charged beam particles and their decay products. Each spectrometer consists of a dipole magnet installed between two pairs of silicon pixel tracking planes [70]. The *beam* and *muon spectrometers* are located upstream and downstream of the decay tunnel, respectively, and are used to kinematically reconstruct the neutrinos produced in $\pi^+ \to \mu^+\nu_\mu$ and $K^+ \to \mu^+\nu_\mu$ decays. In particular, the beam spectrometer makes use of the last dipole magnet (R4) of the front-end beamline, in order to minimize

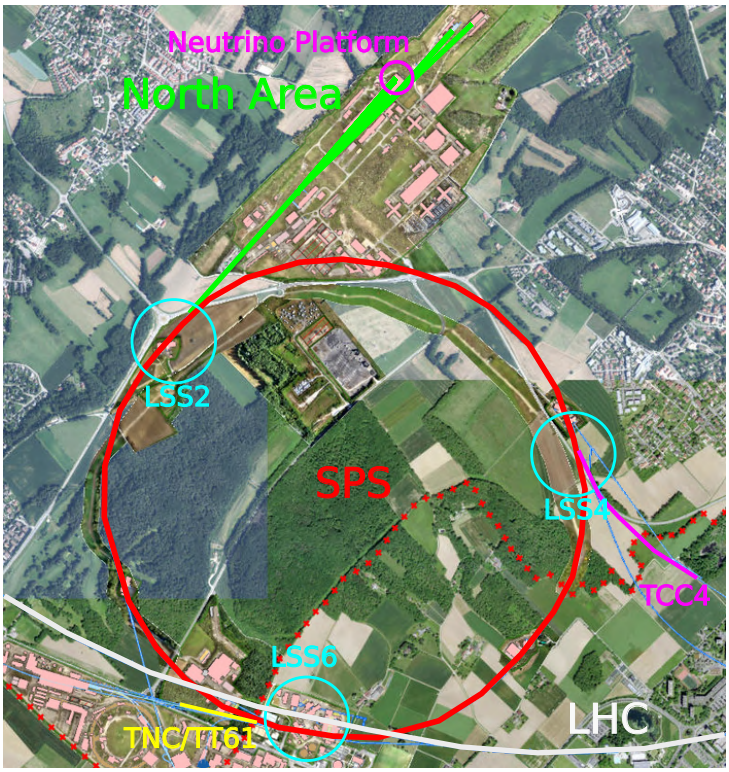

Figure 2.12: Top view of the CERN SPS. The three experimental areas at the SPS are located at the three long straight sections LSS2, LSS4 and LSS6 of the SPS. The Neutrino Platform that houses the ProtoDUNEs are located at the ends of the H2 and H4 beamlines in the North Area. Figure from [70].

the length of the region upstream of the tunnel where π^+ and K^+ decays cannot be reconstructed. Moreover, since the field map of the quadrupole triplet (Q5-7) downstream of R4 may vary, the beam spectrometer also includes two additional tracking planes (T5-6) positioned at the entrance of the tunnel, enabling an accurate measurement of the beam particle direction. The layouts of the beam and muon spectrometers are schematically shown in 2.13.

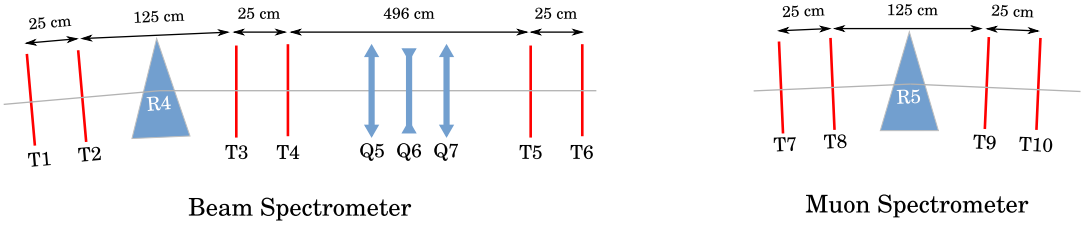

Figure 2.13: Layout of the beam (left) and muon (right) spectrometers.

The momentum and angular resolutions of spectrometers are essential for the tagging technique, as they allow for the correct association of a neutrino interaction with its parent decay. A material budget per plane of $\sim 1\,\%$ of a radiation length is sufficient to meet the requirements of the tagging technique. The simulations and studies for the optimization of the beamline assume a material budget of $0.5\,\%$ of a radiation length. The dimensions of the tracking planes were chosen to provide the largest ratio between the number of reconstructed $\pi_{\mu\nu}$ and $K_{\mu\nu}$ decays and the total tracking plane surface. The spatial distribution of the charged particle flux in the transverse plane to the beam axis is shown in Fig. 2.14 for T1, T5, and T7 silicon trackers, respectively. The tracking

plane surfaces are $12 \times 10\,\mathrm{cm}^2$ in T1-4 trackers, $20 \times 16\,\mathrm{cm}^2$ in T5-6 and $80 \times 100\,\mathrm{cm}^2$ in T7-10. The tracking planes for the muon spectrometer are thus larger than for the beam spectrometer ones, due to beam divergence and the muon emission angle. The particle flux at T1 is the highest and reaches $20\,\mathrm{MHz/mm}^2$ at the center of the tracking plane, with 9.6 s spills of 10^{13} pots. In the muon spectrometer the expected flux is significantly lower with a peak flux of $0.6\,\mathrm{MHz/mm}^2$ [70].

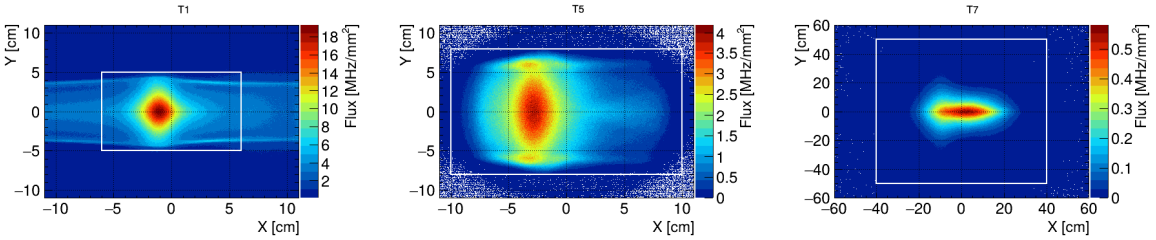

Figure 2.14: Spatial distributions of charged particles in the plane transverse to the beamline at T1, T5, and T7 silicon trackers, respectively, overlaid with the tracking plane acceptances (white line). Figure from [70].

The track reconstruction will be performed in 4D, exploiting an accurate measurement of particle position and time at the tracking planes. The integrated particle rate on the beam spectrometer planes reaches up to 45 GHz and 20 GHz on the muon spectrometer ones. Time resolutions of ~ 40 ps for the beam spectrometer tracking planes and ~ 100 ps for the muon spectrometer ones should allow for the track and decay reconstructions. The list of all trackers specifications for nuSCOPE is reported in Tab. 2.3, compared to present and future devices discussed in the following.

Specifications [units]	**Beam Spectro.**	**Muon Spectro.**	**LHCb-VELO** (2028)	**NA62-GTK** (since 2014)
Peak Dose [Mrad]	700	60	$> 10^3$	16
Peak Fluence [1MeV n_{eq}/cm^2]	1×10^{16}	6×10^{14}	5×10^{16}	4.5×10^{14}
Peak Rate [MHz/mm^2]	20	0.6	$10 - 100$	2
Time Resolution [ps]	< 40	< 100	< 50	< 130
Pixel Pitch [μm]	300		45	300
Material Budget [X_0]	$< 1\%$		0.8%	0.5%

Table 2.3: Silicon tracker specifications of the beam and muon spectrometers, compared to the present NA62 Gigatracker and the future upgraded LHCb VELO. A material budget of 0.5 % of a radiation length and a spill duration of 9.6 s is assumed in neutrino tagging simulations and studies discussed in [70]. Table reproduced from [70].

The 4D tracking approach has been successfully pioneered by the NA62 Collaboration, which has developed $3 \times 6\,\mathrm{cm}^2$ silicon pixel detectors with a pitch of $300\,\mu$m and a time resolution of 130 ps [102]. The NA62 Gigatrackers (GTK) are capable of operating at a peak flux of $2\,\mathrm{MHz/mm}^2$. Such a technology can be used for the tracking planes of the muon spectrometer either in a fully silicon-based configuration or in a hybrid approach, where silicon is used for the most illuminated region while more scalable technologies – such as Micromegas, straw tubes, or scintillating fibers – are employed for the outer regions. The main challenge for neutrino tagging is represented by the beam spectrometer technology, which need to withstand a high particle rate up to $20\,\mathrm{MHz/mm}^2$ at the center of the first tracking plane, namely an order of magnitude greater than what current NA62

Gigatrackers are capable to cope with [102]. Therefore, new silicon technologies are required to match the flux in the core of the beam spectrometer and they are currently in an advanced R&D stage. In the context of the LHC experiment upgrades for the High Luminosity phase – particularly the second upgrade of the LHCb Vertex Locator (VELO) [111] – R&D programs for high-intensity 4D trackers were initiated by INFN and CERN, and later joined by the NuTag Collaboration. Technological solutions on pixel sensors and integrated electronics, capable of standing the challenge in terms of time resolution and radiation hardness, have been developed and are currently under study by the INFN TimeSPOT (2018-2021 and follow-ups) [112, 113] and IGNITE (2023, ongoing) [103] projects. A parallel development named LA-Picopix, with similar characteristics, is presently ongoing at CERN. Both the IGNITE and the LA-Picopix developments aim to deliver their ASICs in 2026. Therefore, a suitable technological solution for the beam spectrometers is still in a R&D phase and requires completion in a timescale compatible with the LHC Run 5. The physics prospects and potential of the nuSCOPE monitored and tagged neutrino beam in terms of neutrino cross-section measurements is discussed in Chapter 5.

3 The ENUBET demonstrator

The ENUBET demonstrator is a large-scale prototype of a section of the instrumented decay tunnel (1.65 m length, 90° azimuthal coverage). The ENUBET demonstrator was exposed at the CERN PS T9 area during dedicated test beam data campaigns in 2022, 2023 and 2024. During my Ph.D. I joined the test beam data campaigns and I contributed to different activities, such as the development of software to monitor the quality of acquired data, hardware interventions performed to setup the prototype for different tests and beam conditions, shifts during data taking and decommissioning of the prototype. In particular, I contributed to the development of a full and realistic `GEANT4` simulation of the demonstrator reproducing test beam conditions, shifts during the demonstrator construction and assembling at INFN-LNL[1], test beam data analysis and data/MC agreement studies. The test beam of August 2023 is the main focus of this Chapter, in terms of simulation, data analysis and data/MC comparison.

3.1 The demonstrator layout

The ENUBET demonstrator is a large-scale prototype of a section of the instrumented decay tunnel. The aim of the demonstrator is to assess the cost-effectiveness and scalability of the chosen detector technology, and to ensure that it meets the design performance requirements in terms of uniformity of response, efficiency and particle identification (PID) capabilities in a high-flux and irradiation environment [82–85]. The detector technology is based on a sampling calorimeter for $e^+/\pi^+/\mu^+$ PID and energy measurement. The calorimeter is coupled to a photon veto system (t_0-layer) placed in the innermost region to perform $e^\pm/\pi^0$ separation and timing measurements. The demonstrator layout, shown in Fig. 3.1, features cylindrical symmetry, matching the geometry of the decay tunnel. The detector extends for 1.65 m in the longitudinal direction with a 90° azimuthal coverage. It consists of 75 zinc-coated iron arcs, each extending 1.5 cm longitudinally and 11 cm radially; the corresponding scintillator layers are 0.7 cm thick. The demonstrator radial span ranges from 97 cm to about 150 cm, excluding the electronics. The prototype structure is designed to be extendable to a full 2π object by joining four similar detectors with minimal dead regions. The detector mechanics consists of a crawl sitting on four extensible legs that are designed to allow tilting the calorimeter-beam angle in the vertical plane and adjusting the horizontal position by means of a wheel-rail mechanism. The total weight is about 3.5 ton[2]. The mechanics allows to modify the tilt angle by up to 200 mrad and the horizontal position with a range of variation of about 1 m. The demonstrator implements a 30 cm thick shielding of borated polyethylene slabs with 5% Boron (BPE) to protect the photo-sensors from excessive neutron irradiation. Each BPE slab is 2.2 cm thick and hosts the WLS fibers collecting the light from the scintillator

[1] National Laboratories of Legnaro of the Italian Institute for Nuclear Physics.

[2] Before carrying the detector at CERN, the system was loaded with 2 additional tons at INFN-LNL and held for 15 min on a crane to experimentally test the reliability of the holding system.

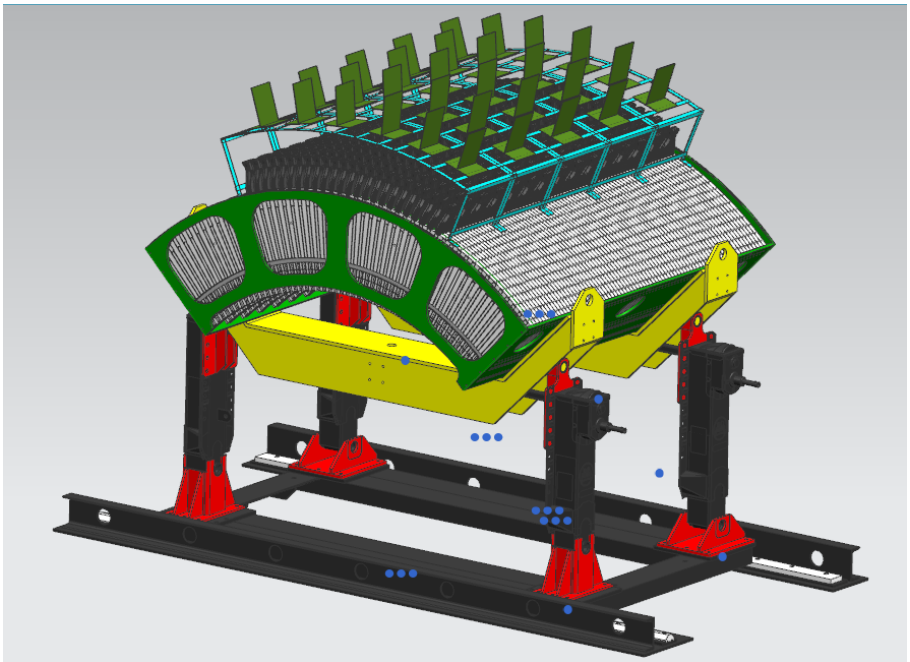

Figure 3.1: A 3D rendering of the ENUBET demonstrator. Figure from [84].

tiles in a dedicated system of grooves. A rendering of a section of the demonstrator is shown in Fig. 3.2, left. The plastic scintillator tiles are trapezoidal in shape to minimize dead regions, with a transverse dimension of $\sim 3 \times 3\,\mathrm{cm}^2$. They are arranged radially in two configurations: quadruplets, consisting of a t_0-layer tile and three calorimetric tiles; and triplets, consisting of three calorimetric tiles only. The layout is shown in Fig. 3.2, right, which also illustrates the frontal grooves readout scheme. The grooves are 1 mm deep such that the diameter of WLS fibers is fully enclosed in the scintillator. In the quadruplet, the t_0-layer tile is located at the innermost radial position and holds two grooves. These two grooves are meant for light collection (*readout* grooves) and they are propagated to the other three outer tiles, where they only have the function of letting space to host the WLS fibers preventing the scintillation light to enter (*transit* grooves). The tile located radially after the t_0-layer tile has readout grooves on the other side of the transit grooves, and this pattern repeats as in Fig. 3.2, right. In order to accommodate the readout grooves with the transit ones in the same tile, the readout grooves of tiles 2 and 3 are slightly offset with respect to those of tiles 0 and 1. A similar configuration for the grooves is used in the triplet.
The ten WLS fibers belonging to the same module (LCM) are routed by passing through grooves milled in the BPE slab and bundled to a $4 \times 4\,\mathrm{mm}^2$ SiPM. The t_0-layer fibers are instead read by two independent $3 \times 3\,\mathrm{mm}^2$ SiPMs. The process of fibers bundling is eased by the adoption of fiber *concentrators*, developed using 3D-printing techniques. The coupling of WLS fibers to the SiPM is therefore accomplished in a neat and reproducible way, allowing a good and homogeneous optical contact. After fiber polishing a $7 \times 4\,\mathrm{cm}^2$ PCB (Front-end, FE board), hosting the five SiPMs (three $4 \times 4\,\mathrm{mm}^2$ for calorimeter module and two $3 \times 3\,\mathrm{mm}^2$ for the t_0-layer), is fixed to the top of each fiber concentrator with screws, allowing for optimal optical matching.

The ENUBET demonstrator was exposed at the CERN-PS T9 area during dedicated test beam data campaigns in 2022, 2023 and 2024. Due to difficulties in the procurement and machining of the scintillators (see Sec. 3.2 below), the instrumented fraction of the

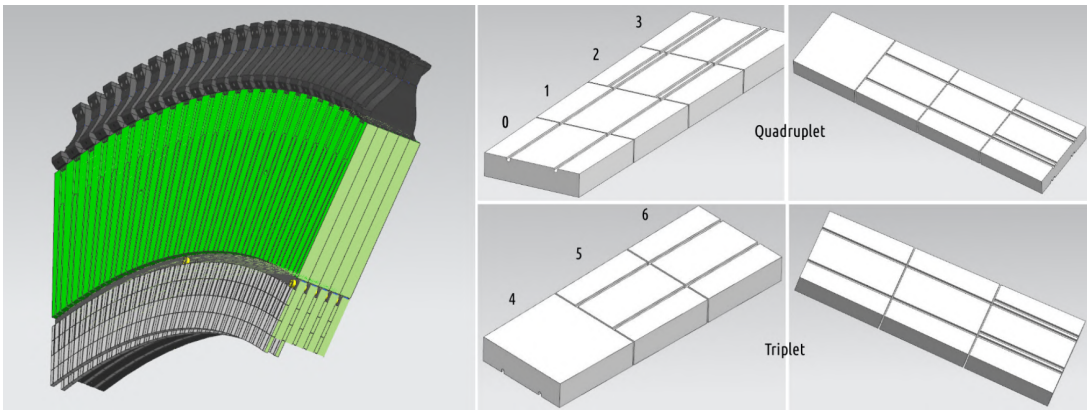

Figure 3.2: (left) Rendering of a section of the demonstrator corresponding to the extension along the beam axis of a single module (LCM). The scintillators are shown in gray, BPE shielding in green and fiber concentrators in black. (right) Layout of the frontal grooves readout scheme used in the scintillator tiles. The quadruplet consists of a t_0-layer tile (0) and three calorimetric tiles (1-2-3), while the triplet consists of three calorimetric tiles (4-5-6), mounted along the radial direction. Figure from [83].

prototype was reduced with respect to the original plans [82, 83] and a first portion of the demonstrator was built and tested in 2022. For the October 2022 test beam, the central region was instrumented with 10ϕ sectors, corresponding to 18°, and $8z$ layers[3], while the rest was kept passive and used to test the mechanical requirements. The coverage of the active region was $8z \times 3r \times 10\phi$ (= 240) calorimeter channels and $8z \times 2\text{layers} \times 10\phi$ (= 160) t_0-layer channels, for a total of 400 channels. For the August 2023 test beam, the fraction of instrumented channels was significantly extended, enlarging the azimuthal coverage to 25ϕ sectors, corresponding to 45°, for the 7 downstream z layers[4]. Since each ϕ sector consists of 5 channels (three calorimeter cells at different radii and two t_0-layer scintillator tiles), the final number of channels amounts to $5\times(10\phi\times8z+25\phi\times7z) = 1275$. The portion of the demonstrator instrumented in 2023 is shown in Fig. 3.3. A summary of the configurations used in the 2022 and 2023 test beams is reported in Tab. 3.1. The 2023 configuration was also used for an additional test beam conducted in August 2024.

Parameter	**2022**	**2023**
Scintillator tiles (7 shapes)	1360	4335
WLS fibers	$\sim 1.5\,\text{km}$	$\sim 4.5\,\text{km}$
Channels (SiPM)	400	1275
Hamamatsu (50 μm cell) $4 \times 4\,\text{mm}^2$ calo and $3 \times 3\,\text{mm}^2$ t_0	240 calo + 160 t_0	765 calo + 510 t_0
Fiber concentrators (FE boards)	80	255
Interface boards	8	22
Read-out boards (A5202)	8	22
CAEN digitizers channels	45	/
Horizontal movement	$\sim 1\,\text{m}$	
Vertical tilt	up to $\sim 200\,\text{mrad}$	

Table 3.1: Demonstrator parameters for the 2022 and 2023 test beams at CERN PS T9 area. Table reproduced from [85].

[3]The (r, ϕ, z) coordinates are the radial, azimuthal and longitudinal coordinates, respectively.

[4]The extension of the azimuthal coverage of the already instrumented $8z$ planes was not possible due to technical limitations.

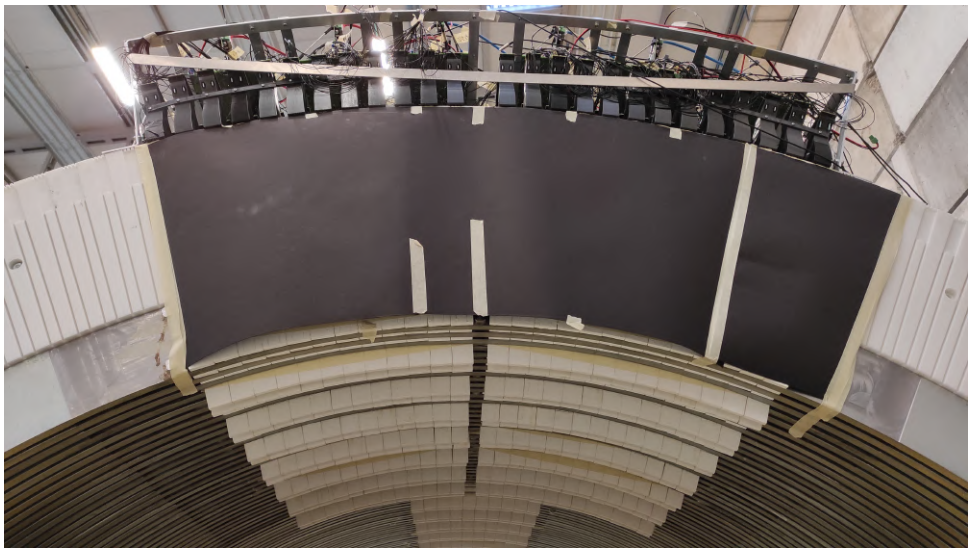

Figure 3.3: The instrumented portion of the demonstrator in August 2023 test beam, bottom view.

3.2 The demonstrator construction

The assembling of the ENUBET demonstrator took place at INFN-LNL. The first instrumented portion of the demonstrator was built and tested in 2022, while in 2023 the prototype coverage was extended with the construction of a second instrumented portion. The construction process involved several operations and steps related to the structures that make up the demonstrator.

Scintillators
The production and machining of the scintillators tiles was the most challenging and critical task. Scintillators had initially been produced by UNIPLAST (Moscow) in collaboration with the INR group using injection molding. Unfortunately, due to the war outbreak in 2022, it was not possible to finalize the procurement from Russia. The total number of needed tiles, 6375, in seven different shapes were produced by an Italian company (STYLPLEX) in a short time and with critical deadlines. The machining was achieved using cutting and milling with numerical control machines in place of injection molding, starting from large scintillator sheets procured by SCIONIX. A view of one of the squared grooves is visible in Fig. 3.4 (center). The preparation of scintillators was managed internally and without relying on the expertise and methods of INR/UNIPLAST.

WLS fibers
The wavelength shifting (WLS) fibers employed are the Y-11 double clad 1 mm diameter from Kuraray (JP). The fibers were cut in four different lenghts to account for the three calorimeter radial layers and the t_0 layer and then their ends were sandpapered/polished using some tools developed on purpose (see Fig. 3.4).

Fiber concentrators
The fibers concentrators (FC) were developed with a batch of five commercial 3D printers using PLA filaments. The use of printed fibers concentrators proved to be a successful and elegant solution to the problem of routing the fibers in a tidy and reproducible manner: 34 WLS fibers, emerging from a channel area of about $3 \times 11\,\mathrm{cm}^2$, are collected into

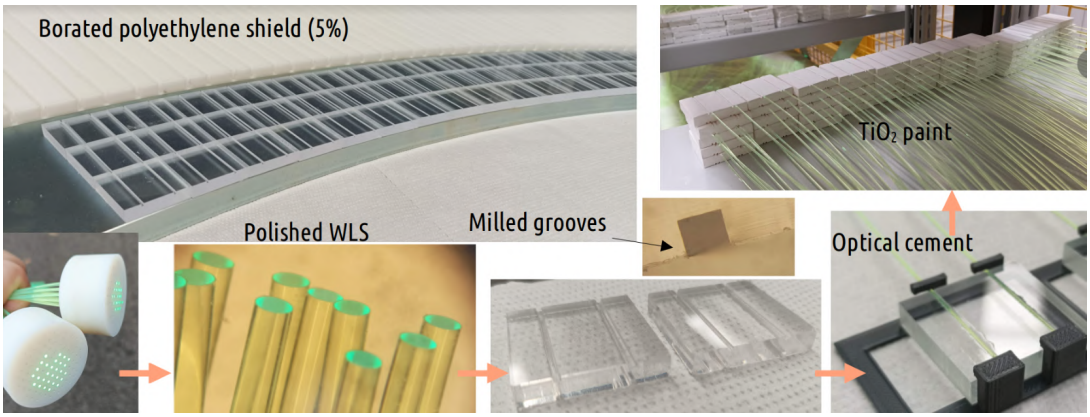

Figure 3.4: Preparation and pre-assembly phase of the demonstrator. (top left) The iron and BPE arcs are visible with scintillators (not yet painted nor glued to WLS). The thickness of the BPE (22.5 mm) is within tolerances equal to the sum of scintillators' (7 mm) and iron thicknesses (15 mm). The grooves on the BPE layers host the WLS fibers. (top center) Microscope view of a milled groove with a squared cross section. (bottom left) WLS fibers inserted into a tool for sandpapering in a plane orthogonal to the fibers' axis. (bottom middle left) Polished WLS fibers seen at the optical microscope. (bottom center right) Scintillator tiles before sandpapering, WLS gluing and painting. (bottom right) WLS gluing with an ad hoc support to keep the WLS fibers horizontal. (top right) A batch of scintillator tiles after WLS gluing and painting with TiO_2, ready for mounting on the iron arcs.

3 bundles of 10 fibers (calorimeter modules) and 2 couples of 2 fibers (t_0-layer) over an area of about $5 \times 3\,\mathrm{cm}^2$ [81].

Photo-sensors
The silicon photomultipliers (SiPMs) employed are the Hamamatsu models S14160-4050HS ($4 \times 4\,\mathrm{mm}^2$) for calorimeter layers and S14160-3050HS ($3 \times 3\,\mathrm{mm}^2$) for t_0-layer. The SiPMs and related electronic components are soldered on a PCB, as shown in Fig. 3.7, right.

Front-end boards
The front-end boards are mounted and screwed on the fiber concentrators, each one hosting five SiPMs, as shown in Fig. 3.8. The large and small SiPMs can be powered with separate bias lines.

Interface boards
The signals are sent from the front-end boards to interface boards with host receptacles for many very thin coaxial cables by HIROSE which are used both for providing the HV to the SiPM and reading out the signals (see Fig. 3.8).

Readout boards
The readout boards are 64-channels boards by CAEN (FERS[5], A5202) based on the WeeROC CitiROC-1A ASICs. They readout the amplitudes and time of signals for a total of 1280 channels (see Fig. 3.8).

DAQ
The data acquisition chain consists of several CAEN A5202 boards (8 during test beam in 2022, 9 during test beam in 2023) controlled via ethernet connection by a customized version of the open source Janus software provided by CAEN.

[5]Front End Readout System.

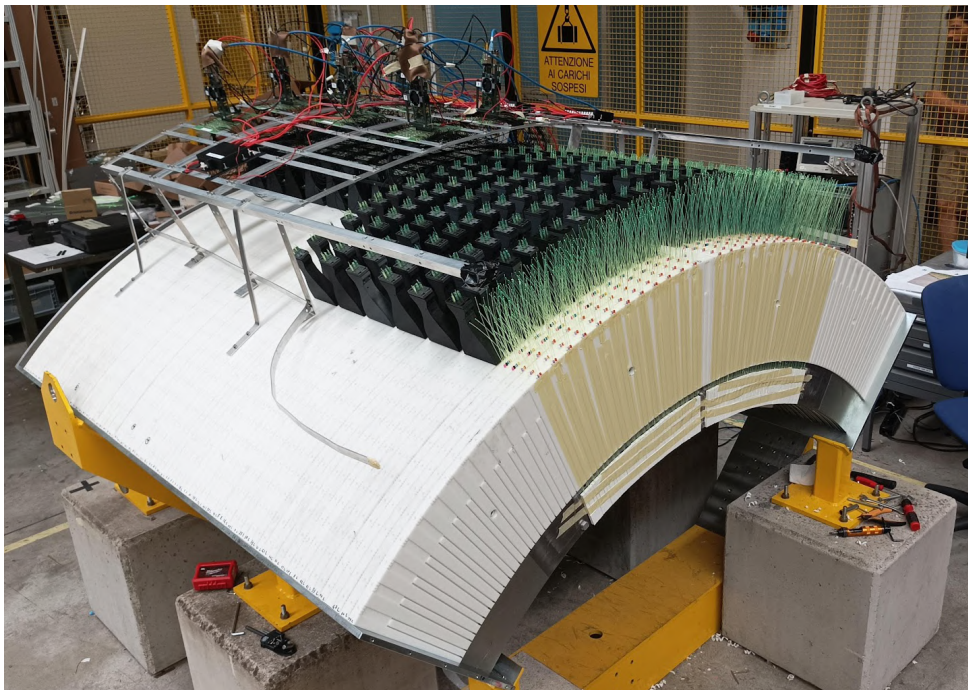

Figure 3.5: Demonstrator assembly at INFN-LNL: the instrumented iron (grey) and BPE (white) arc pairs are installed on the detector holding structure, partially shown in yellow. The WLS fibers (green) exiting from the BPE are inserted into the fibers concentrators (black boxes).

The operations performed during the assembly of the prototype can be summarized as follows:

1. Scintillators sand-papering for TiO_2 paint adhesion
2. Measurement of scintillators individual thickness with a caliper.
3. WLS fibers cutting, polishing and glueing to scintillators (Fig. 3.4).
4. Scintillators painting with TiO_2 paint (Fig. 3.4).
5. Assembly of scintillators with glued fibers onto the iron and BPE arc pairs, by routing WLS fibers through the transit grooves of the tiles and the grooves in the BPE.
6. Mounting of the instrumented iron and BPE arc pairs on the detector holding structure (Fig. 3.5).
7. Bundling of the WLS fibers inside concentrators (Fig. 3.6).
8. Cutting and polishing WLS fibers bundles in situ on top of fiber concentrators (Fig. 3.7).
9. Installation and cabling of front-end boards, interconnection boards and readout boards (Fig. 3.8).

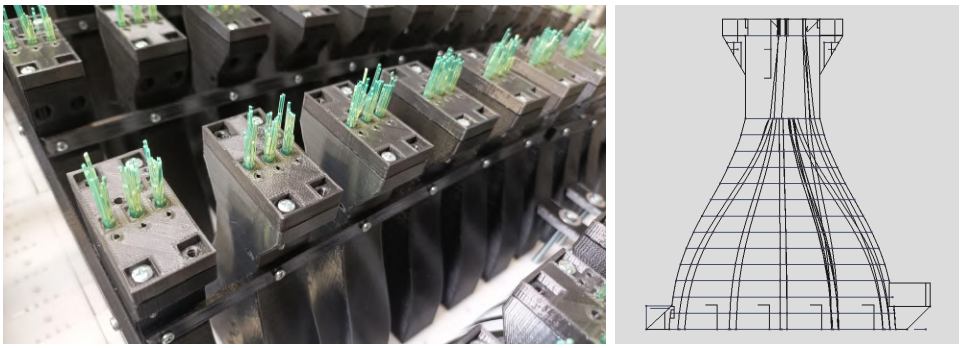

Figure 3.6: Demonstrator assembly at INFN-LNL. (left) Detailed view of WLS fibers bundles (green) exiting from the top of the fiber concentrators (black boxes). An additional plastic collimator was added on top of the concentrator to keep the fiber bundles tightly packed. At the stage shown here, the fiber ends had not yet been cut and polished. The fibers were glued among themselves and to the fiber concentrators using EJ510 bi-component optical cement by BICRON. (right) Internal layout of a fiber concentrator.

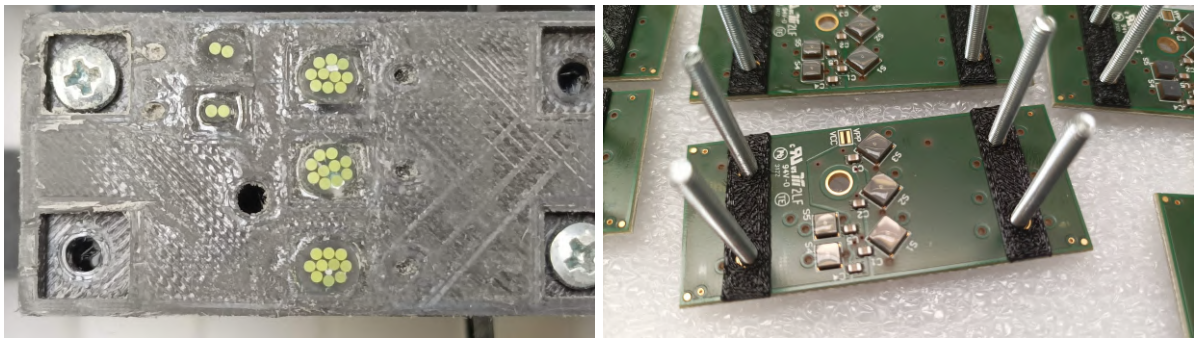

Figure 3.7: Demonstrator assembly at INFN-LNL. (left) The fiber bundles were cut with a hot filament (usually employed to cut polystyrene foam) and sandpapered in situ with a dedicated tool. (right) Demonstrator front-end electronics. The front-end board is fixed to the fiber concentrator with 5 screws. The three larger SiPMs ($4 \times 4\,\mathrm{mm}^2$) readout three 10 WLS fiber bundles from the three radial calorimeter modules which are present in each ϕ module, while the two smaller SiPMs ($3 \times 3\,\mathrm{mm}^2$) read a pair of WLS fibers each, from the two t_0 channels. The black plastic rectangles are spacer needed to prevent the PCB from buckling under the pressure of screws.

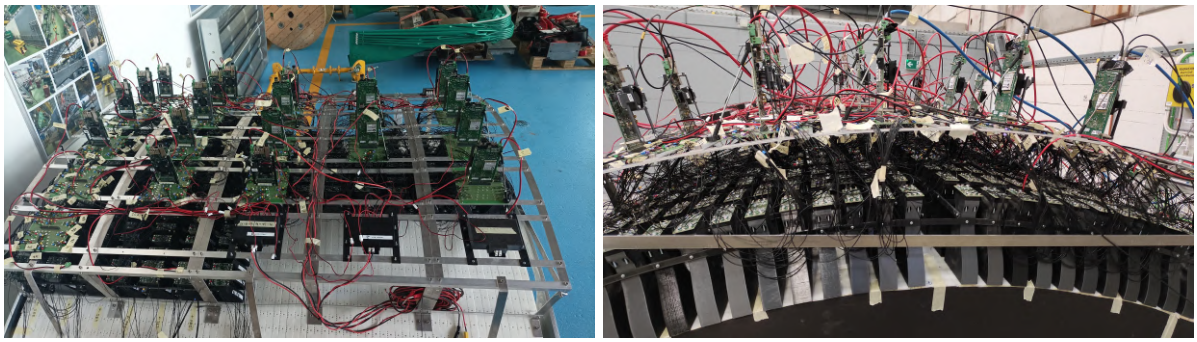

Figure 3.8: Two views of the installed front-end boards (above the fiber concentrators), interconnecting boards and read-out boards (mounted on the grey aluminum frame). Each CAEN A5202 readout board (vertical) is plugged on top of an interconnection board (horizontal) and cabled together with HIROSE micro-coaxial cables. The readout boards are cooled with fans mounted in a 3D printed support.

3.3 The test beam of August 2023 at CERN PS T9

The ENUBET demonstrator was exposed at the CERN PS T9 area during dedicated test beam data campaigns in 2022, 2023 and 2024. This section, and the remainder of the Chapter, is focused on the test beam of August 2023, for which data analysis and simulation development are presented. The T9 secondary beamline in the CERN East Area is obtained from the interaction of 24 GeV/c primary protons from the PS impinging on a fixed target, with secondaries momenta up to 15 GeV/c [114].
Data have been collected with the detector prototype exposed to beams of electrons, hadrons and muons with momenta spanning from 0.5 to 10 GeV/c. The August 2023 test beam setup at CERN PS T9 experimental area is shown in Fig. 3.9. A schematic representation of the 2023 test beam setup is shown in Fig. 3.10.

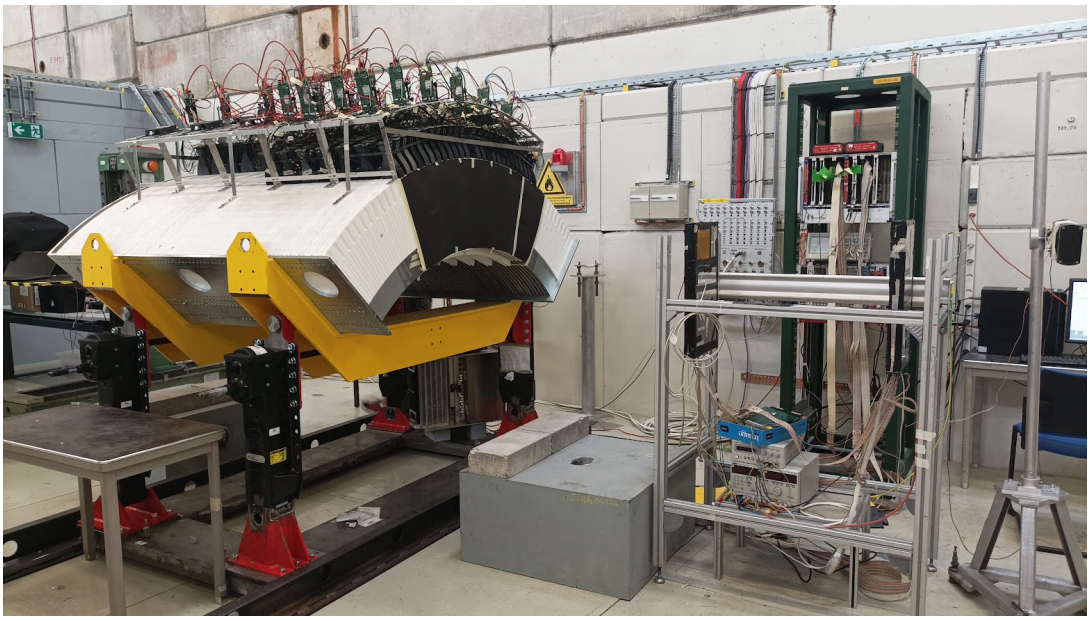

Figure 3.9: The ENUBET demonstrator in the CERN PS T9 experimental area, with silicon chambers and a trigger scintillator plane installed. The Cherenkov counters are not shown since positioned further upstream.

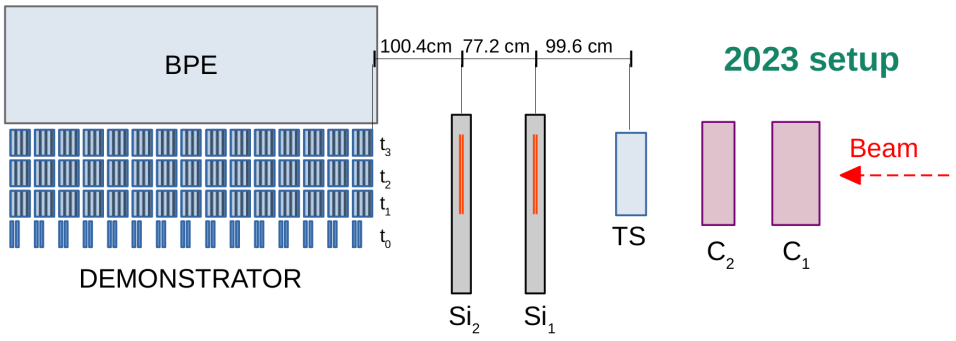

Figure 3.10: Schematic representation of the August 2023 test beam setup. The Cherenkov counters (C_1, C_2), the trigger scintillator (TS), the silicon trackers (Si_1, Si_2) and the demonstrator are shown. Drawing not to scale.

The demonstrator, mounted on its mechanical structure, was positioned on the beam line downstream of two silicon microstrip trackers and a plastic scintillator used as a trigger. Each silicon tracker consists of two sets of single-side silicon microstrip sensors [115], each one with an active area of $9.3 \times 9.3\,\mathrm{cm}^2$ and arranged in a x-y configuration. Each silicon

tracker provides the hit position of a particle on its plane, which is orthogonal to the incoming beam direction. The combined information of the two silicon trackers are used to reconstruct the direction of beam particles, namely extrapolating their impact point on the front face of the detector. The trigger scintillator is a $10 \times 10\,\mathrm{cm}^2$ plastic scintillator readout by a photomultiplier tube; it is positioned on the beam, upstream of the first silicon tracker. Further upstream in the T9 beamline are positioned two Cherenkov counters (XCET044 and XCET048 in [116]) which are set to different pressures to perform particle identification. In the case of a gaseous medium, the Cherenkov radiation threshold can be tuned by controlling the gas pressure. Since beam particles are momentum selected, different velocities are due to different mass of particles. The detection of Cherenkov radiation is thus well suited for particle identification purposes. The Cherenkov counters were both filled with CO_2 and, depending on the beam momentum, their operating pressures were set in order to have one counter with both muons and electrons above threshold[6] and the other one with only electrons above threshold.
The demonstrator was moved horizontally by means of the wheel-rail mechanism to calibrate the response of all modules to particle beam. Furthermore, the demonstrator was tilted at different inclinations in order to measure the calorimeter response to incoming particle beam at different angles (0, 50, 100, 200 mrad). These tilted runs are essential to reproduce experimentally the expected ENUBET particle flow in realistic conditions, where positrons from K_{e3} kaon decay are emitted with an average angle of $\sim 88\,\mathrm{mrad}$.
The DAQ system used in the test beam consisted of two main acquisition chains synchronized with each other: one for the trigger scintillator, silicon trackers and Cherenkov counters, readout by a CAEN V1730 digitizer, and another one for the demonstrator front-end boards (FEBs), readout by several CAEN A5202 boards. In addition to the trigger scintillator signal, the DAQ system also receives the $\sim 400\,\mathrm{ms}$ beam spill signal, acting as an "enable" signal for the data acquisition.
The layout of the instrumented portions of the demonstrator changed from 2022 to 2023, whereas during the test beam in 2024 the same layout as in 2023 was used. The demonstrator layout used during the 2023 test beam is shown in Fig. 3.11, consisting of 15 z-layers and 26 ϕ-layers. In the 2022 test beam only $z \in [0, 7]$ layers were instrumented, whereas the other layers were instrumented during 2023. The test beams in 2023 and 2024 focused mainly on the $\phi \in [5, 17]$ and $z \in [8, 14]$. It should be noted that in the 2022 test beam, the beam spot was on the calorimetric side corresponding to the $z = 0$ layer, whereas in both 2023 and 2024 test beams, it was on the opposite calorimetric side, corresponding to the $z = 14$ layer.

3.4 The demonstrator simulation

The simulation of the demonstrator and test beam experimental setup is essential to compare the expected detector performance with those obtained from experimental data. A full `GEANT4` [64] simulation of the demonstrator was developed, reproducing realistically the experimental conditions. The starting point for the development of the demonstrator simulation was the implementation of ENUBINO [83], a small pre-demonstrator prototype corresponding to one azimuthal unit (i.e. three radial LCMs) built to test the frontal light readout scheme. The demonstrator simulation was initially developed for the small instrumented section used in 2022, and later updated to the extended design implemented in 2023, as presented in the following of this Chapter. The simulation development of the

[6] For the runs at 0.5 GeV/c, the operating pressure range of the Cherenkov detector only allowed for electron detection.

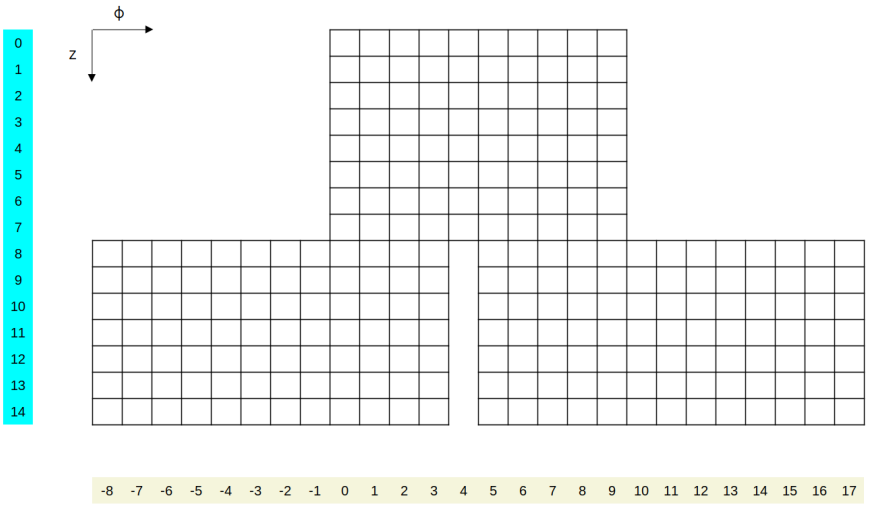

Figure 3.11: Layout of the instrumented azimuthal (ϕ) sectors of the demonstrator, shown schematically from above, with the corresponding (r, ϕ) coordinates used by convention in the analysis.

final demonstrator presents several differences compared to the ENUBINO early-stage implementation. For instance, the scintillator tiles are trapezoidal rather than squared, and the cylindrical WLS fibers are embedded inside rectangular grooves instead of cylindrical ones. In addition, the implementation of the detector geometry takes into account the possibility to randomize or fix to a default value the thickness of plastic scintillator tiles. Indeed, as a consequence of the mechanical process of cutting and drilling the tiles from scintillator slabs, minor differences among tiles are present. Moreover, two distinct batches of scintillator sheets were used, one produced by SCIONIX and another one provided by CERN in 2022. If the scintillator tiles had been produced with the planned technique based on the injection molding, such small non-uniformities observed among different tiles would have been avoided. The average thickness of scintillator tiles observed during the 2022 demonstrator construction was 6.7 mm with a standard deviation of 0.12 mm. Although such differences were accounted for in the simulation by randomizing the tile thickness in the geometry implementation of each tile, no significant impact on the visible energy was observed. Therefore, in the analysis presented here, the simulation was performed using scintillator tiles with average thickness.
The geometry of the frontal grooves readout scheme for the quadruplet and triplet stack of scintillator tiles (illustrated in Fig. 3.2, right) is implemented in the simulation, as shown in Fig. 3.12. Each demonstrator azimuthal unit is made of two quadruplets and three triplets. The dimensions of a scintillator tile in the plane orthogonal to the beam direction are defined according to their radial position. In particular, due to their trapezoidal shape, the vertical placement of quadruplets and triplets in front of the iron arcs is performed computing the major and minor basis from geometrical considerations, moving upwards along the radial direction. Specifically, it is considered that each tile in an azimuthal sector spans an angle of $\phi = 1.77°$ and has a height of 3 cm. Within a scintillator tile. The implementation of WLS fibers into the demonstrator geometry enables a more realistic simulation by accounting for the detailed geometry of the scintillator material. Moreover, it allows for detailed analysis of light collection efficiency through a full optical simulation in future studies. Currently, the scintillation process and light propagation are not simulated; however, these effects can be easily included, as they have already been implemented in the code at an early stage. The full geometry of the demonstrator was implemented positioning 75 layers of iron and BPE arcs instrumented with

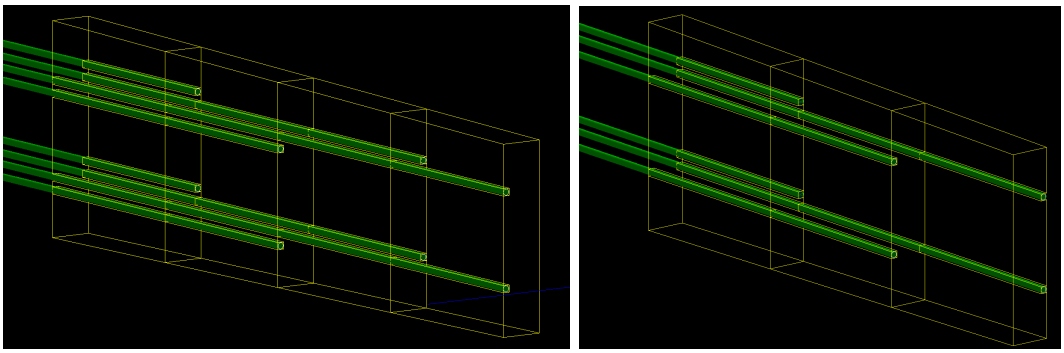

Figure 3.12: Geometry of the frontal grooves readout scheme for the quadruplet (left) and triplet (right) stack of scintillator tiles, with the WLS fibers positioned inside the rectangular grooves.

the corresponding scintillator tiles. The geometry development followed a layer-by-layer placement approach. First, all the ϕ sectors of a layer are instrumented with tiles and corresponding WLS fibers. Next, the upstream iron and BPE arcs, with same thickness and stacked radially, are added. To reproduce the real configuration - where WLS fibers are accommodated in holes in the BPE arcs and then routed to the concentrators - additional BPE material is inserted in between and on the outer sides of fiber pairs in each ϕ sector, thus filling the gaps left by the outgoing fibers (see Fig. 3.13, right). As an example, a single z-layer of the 2022 test beam configuration ($3r \times 10\phi \times 8z$ LCMS) is shown in Fig. 3.13, left. The full geometry of the demonstrator in 2023 test beam is shown in Fig. 3.14.

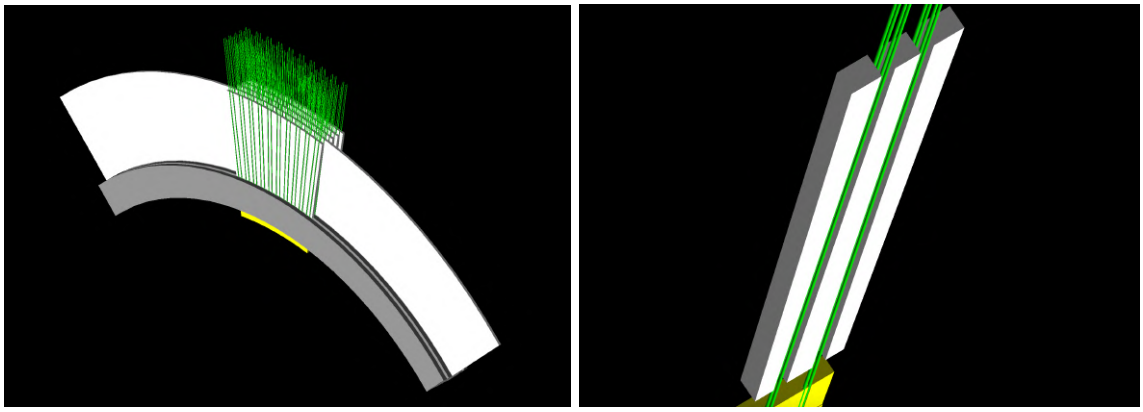

Figure 3.13: (left) A single z-layer of the demonstrator made by two layers of quadruplets and three layers of triplets, covering 10 ϕ central sectors (2022 test beam configuration). In the planes containing the scintillator tiles, each BPE arc (white) is made of three parts: two external sections of arc, on top of the non instrumented part of the demonstrator, and a central BPE module, on top of instrumented part, defined to simulate the holes hosting the outgoing fibers in the BPE (shown on the right). Above each iron arc the BPE forms an arc of the same thickness. (right) Detail of a single BPE module for a ϕ sector of tiles, made of three section of arcs to fill the middle and external gaps between fibers and adjacent ϕ sectors.

Once the demonstrator geometry is implemented, simulated data are produced in conditions as close as possible to those of the test beam. In particular, the beam particles hitting the demonstrator are generated sampling the transverse beam profile[7] and beam angular divergence obtained experimentally during different test beam runs. The detector response is at hit-level and signal in each demonstrator channel is measured as the visible energy deposited in the scintillator tiles. Since at present scintillation light is not

[7]The transverse beam profile is measured as the $x-y$ distributions of hit positions on the microstrips of silicon trackers.

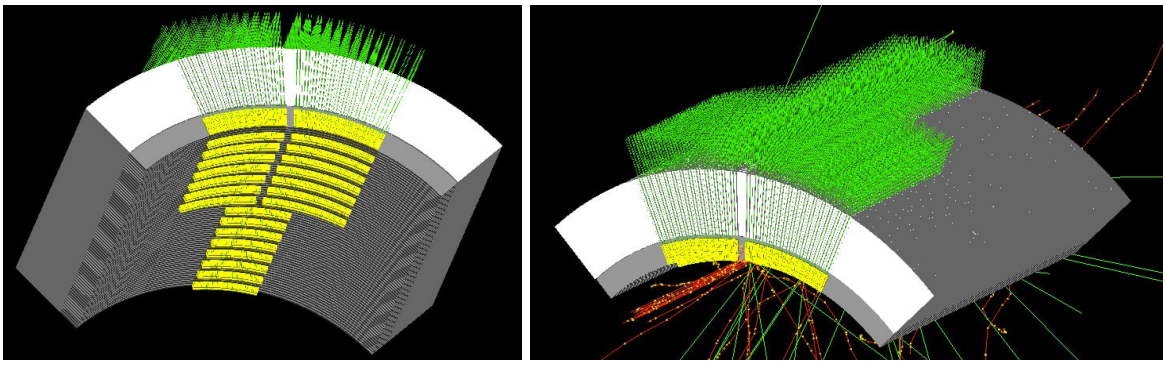

Figure 3.14: (left) Full geometry of the demonstrator in 2023 test beam, bottom view. The incoming beam direction is orthogonal to the front face. (right) Visualization example of simulated interactions of 3 GeV muons, hitting the front face of the detector, sampled from a squared $10 \times 10\,\mathrm{cm}^2$ area.

simulated, potential inefficiencies due to conversion of energy deposition to scintillation light, wavelength shifting and detection by the SiPMs are not taken into account. The comparison of experimental data with the Monte Carlo (MC) prediction is of great importance for a final validation of the detector performance and as a proof of principle of the ENUBET technique. The data/MC comparison for the energy resolution and linearity of the prototype tested at CERN in 2023 is discussed in Sec. 3.7.

3.5 Calibration and channel response equalization

The inter-calibration of the demonstrator channels and the equalization of their response are essential for the test beam data analysis, since different calorimeter channels might have different responses to the same energy deposition. Such differences in channel response are due to a variety of factors: mechanical variations in the scintillator tiles, intrinsic differences among the SiPMs, imperfections in the coupling between optical fibers and photosensors, and potential inefficiencies in the transport and collection of light from the scintillators to the SiPMs. In order to equalize the channels response, two dedicated calibration runs were performed during the test beam data campaigns, acquiring the data necessary to estimate such response. The first calibration run covered the right side of the demonstrator ($\phi \in [5, 17]$, see Fig. 3.11) and was performed with a 10 GeV/c beam containing pions and muons. The second calibration run was performed on the left side of the demonstrator ($\phi \in [-8, 3]$, see Fig. 3.11) using a 10 GeV/c muon enriched beam. The energy deposit of minimum ionizing particles (mips) is used as a reference for the equalization of calorimeter channels response. Indeed, mips are particularly well-suited for calibration purposes because, for a given material and a fixed path length, they deposit a nearly constant amount of energy. The inter-calibration of demonstrator channels is performed applying fiducial cuts to ensure that particles deposit the same energy amount in each module by traveling approximately the same distance. The tracking of particles crossing the calorimeter channels is carried out using the two silicon microstrip chambers. The primary tracks are reconstructed only for single-cluster events, i.e. events that left a single track in the silicon chambers. The tracks are extrapolated to the halfway point of each channel and used to reconstruct the impact point on calorimeter modules, obtaining a projection of the particle hit position (x, y) in the transverse plane to the beam direction. The distribution of impact points of primary tracks extrapolated on the most upstream part of the demonstrator is shown in Fig. 3.15. Since the right side of the demonstrator was illuminated mainly with focused pion beams, their beam spots are spatially concentrated; conversely, the left side was illuminated with muon beams and

their beam spots are much more spatially spread out, since muons are tertiary particles and thus not well focused (see Fig. 3.15). In addition, the farther right side of the demonstrator was also illuminated with a muon run, and its beam spot is much larger with respect to the pion ones.

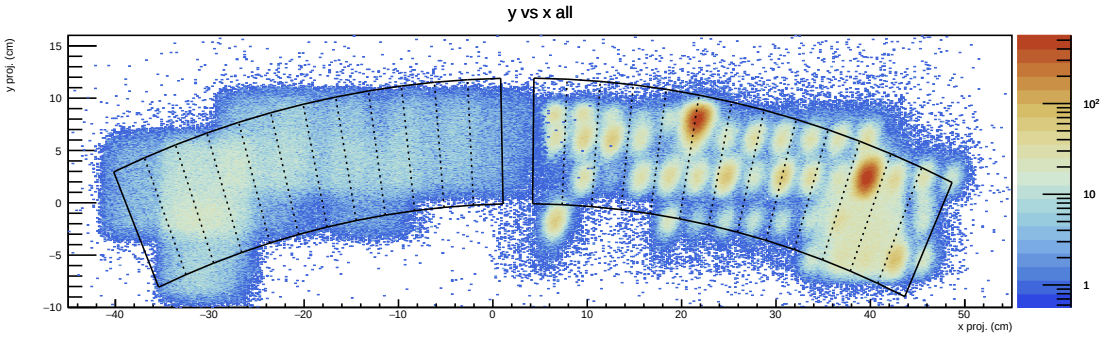

Figure 3.15: Distribution of the impact points of primary tracks extrapolated on the most upstream part of the demonstrator. The instrumented sectors are highlighted by the black line frame. The left-side channels ($x < 4\,\text{cm}$) are hit by muons, while the right-side channels ($x > 4\,\text{cm}$) are hit by pions. A muon run was performed in the region around $(x, y) = (40, -3)$ cm instead of using pions.

Then, for each channel, efficiency maps are computed by considering the projections $(x_{\text{proj}},\ y_{\text{proj}})$ of particles producing a signal with a pulse height above a given threshold. Therefore, the efficiency map of a given channel corresponds to the fraction of events with a primary track crossing the channel and producing a non-negligible signal. An example of an efficiency map for a channel of the first calorimeter layer is shown in Fig. 3.16.

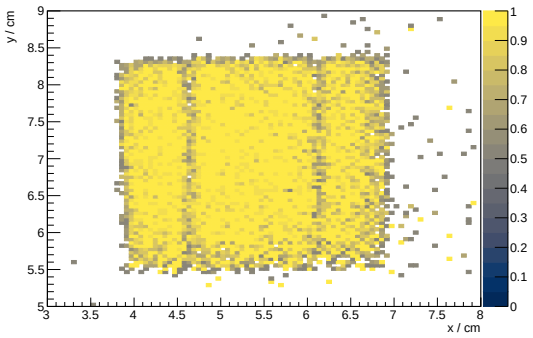

Figure 3.16: Example of an efficiency map for a channel in the first calorimeter layer. The efficiency is well above 95%, with lower values only at the channel edges due to border effects, and at the positions corresponding to the grooves hosting the fibers ($x \sim 4.6\,\text{cm}$ and $x \sim 6.2\,\text{cm}$), where the amount of scintillator material is reduced.

The efficiency maps can be used as a good proxy for estimating the channel position: the center coordinates $(x_0,\ y_0)$ of each channel are calculated using the weighted average $x_0 = \sum x_b \cdot n_b / \sum n_b$ and $y_0 = \sum y_b \cdot n_b / \sum n_b$, where $(x_b,\ y_b)$ are the bin coordinates from the efficiency map and n_b is the bin content of the projection map with a threshold cut. In particular, center coordinates (x_0, y_0) are estimated applying an efficiency filter to remove bins with efficiency less than 50%. The center coordinates of each channel are then used to define a fiducial area. During the 2023 test beam, the fiducial area was defined as a $1.1 \times 1.1\,\text{cm}^2$ square centered in (x_0, y_0) for the first four z-layers of the demonstrator, then up to the eighth z-layer the fiducial area was $1.5 \times 1.5\,\text{cm}^2$, whereas for all farther z-layers it was set to $2 \times 2\,\text{cm}^2$. Indeed, different fiducial areas for different z-layers have been implemented to combat the reduced statistics in the farther demonstrator channels as well as to account for Coulomb scattering of mips within the demonstrator material.

The events with an impact point falling within such a fiducial area are selected as a subsample for the estimation of the energy deposit distribution of minimum ionizing particles. For each channel, the pulse height distribution for events satisfying the fiducial cut is computed. The channel response histograms are then fitted with a Landau function growing on a linear background, and the most probable value (MPV) of the Landau function is estimated and used as a reference for the mip energy deposition. Due to the large number of channels to be calibrated, a custom fitting routine was implemented to fit the mip peak for all calorimeter channels. In case the fitting procedure failed for some channels, the contingency was to estimate the MPV from the most populated bin. As an example, the Landau fit of the mip peak for some channels is shown in Fig. 3.17. The presence of a baseline (or pedestal) is also evident, and it is shifted from zero by an electronic offset. The pulse heights and mip response of each channel need to be corrected for this effect by subtracting the baseline value. The baseline estimation and subtraction are discussed in Sec. 3.6.

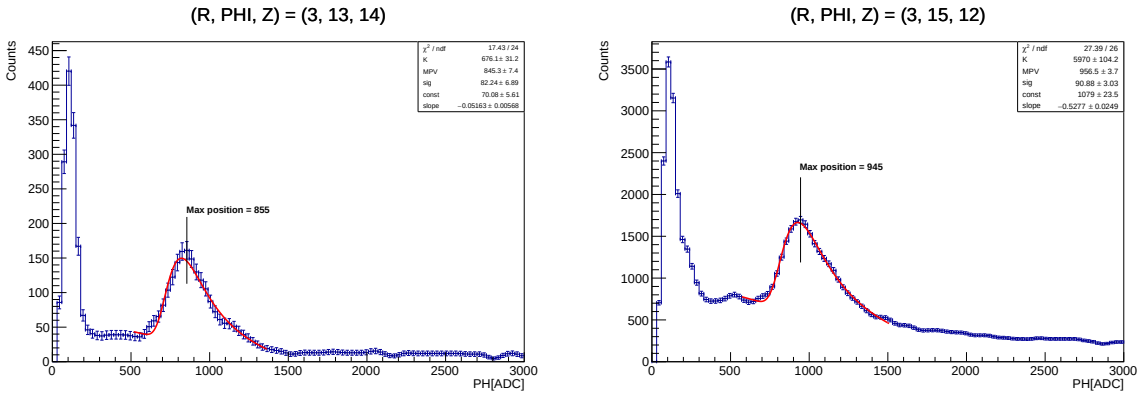

Figure 3.17: Examples of energy deposition distributions from mips for channels of the demonstrator prototype during the 2023 test beam.

The calibration procedure described above was applied to most of the demonstrator channels, with a few exceptions. Indeed, a few channels showed no signal, probably due to a failure in the SiPM or the connection to the frontend electronics; these channels were thus excluded from the analysis. In addition, due to mechanical constraints, it was not possible to completely cover all of the demonstrator channels during the calibration runs, therefore, some channels were only partially illuminated, as shown in Fig. 3.15. Nevertheless, this does not impact the analysis, as the dead channels account for less than 1% of the total, and the uncovered ones are at the calorimeter borders.
Similar calibration studies were also performed on simulated data, considering the right side of the demonstrator. The calibration runs for the right side were experimentally made both of pions and muons at 10 GeV, as discussed above. In the MC simulation, the primary pion or muon beams are generated from their beam profiles and angular divergences measured by the silicon chambers; the muon composition of the beam spot is $\sim$ 14% whereas the pion composition is $\sim$ 86%. The fiducial cuts are defined as a $1.5 \times 1.5\,\mathrm{cm}^2$ square centered on the center of each module and are performed to the front and back of each module to select only mip-like particles travelling straight. The spectrum of the total energy deposited in each calorimeter module can be computed and the mip peak is then fitted with a Landau function. According to these simulation studies, the energy released by a mip in a module has a most probable value of ~ 6.12 MeV, obtained averaging the MPVs of all calorimeter channels.
The pulse heights of each channel can be equalized to the response of a mip in that

channel, according to:

$$\mathrm{PH}^{\mathrm{ch}}_{eq} \propto \frac{\mathrm{PH}^{\mathrm{ch}} - bl^{\mathrm{ch}}}{\mathrm{MPV}^{\mathrm{ch}}_{mip} - bl^{\mathrm{ch}}} \tag{3.1}$$

where $\mathrm{PH}^{\mathrm{ch}}$ is the raw signal from the channel (in ADC counts), bl^{ch} is the baseline (mean of the gaussian fit, see following Sec. 3.6) and $\mathrm{MPV}^{\mathrm{ch}}_{mip}$ is the MPV of the Landau fit of the mip energy deposit.

3.6 Baseline estimation and subtraction

The baseline estimation and subtraction are crucial for the equalization of the channels response and to estimate the energy resolution and linearity of the calorimeter prototype. For the left side of the demonstrator, the baseline of each channel was directly measured using dark runs[8], i.e. pedestal data. The baseline distribution of each channel was fitted with a gaussian function and its mean μ_{bl} and standard deviation σ_{bl} were estimated. The baseline of a given left side channel, measured from dark runs, is shown in Fig. 3.18, left. However, due to test beam time constraints, no dark runs data were acquired for the right side of the demonstrator. Nonetheless, the baseline for the right side channels can be estimated using the calibration runs according to the following procedure. The baseline histogram of a given channel is filled with the measured pulse height $\mathrm{PH}^{\mathrm{ch}}$ only if the particle does not cross the channel itself. Specifically, the requirement is that the impact point (x_{calo}, y_{calo}) of the track, extrapolated onto the same z-layer as the channel, is at least one nuclear interaction length λ_I away from its center of gravity (anti-fiducial cut). Therefore, the anti-fiducial cut allows the exclusion of events with spurious energy deposits from hadrons crossing nearby channels. In such a way, the measured signal is expected to originate from electronic noise only.
The nuclear interaction length λ_I of a LCM channel can be computed easily. Indeed, for compounds and mixtures, Bragg addition (mass fraction weighted sum) is used to calculate the reciprocal of nuclear interaction length [117]. Each LCM calorimeter module is made of five slabs of iron interleaved with tiles of plastic scintillator (Eljen EJ-200). The cross section of both the iron slabs and scintillator tiles is approximately 3×3 cm^2, and their respective thicknesses are $\Delta x_{\mathrm{Fe}} = 1.5\,\mathrm{cm}$ and $\Delta x_{\mathrm{scinti}} = 0.7\,\mathrm{cm}$. The LCM nuclear interaction length can be estimated as follows [117]:

$$\lambda_I = \frac{\rho_{\mathrm{Fe}} \cdot \Delta x_{\mathrm{Fe}} + \rho_{\mathrm{scinti}} \cdot \Delta x_{\mathrm{scinti}}}{\rho_{\mathrm{Fe}} \cdot \frac{\Delta x_{\mathrm{Fe}}}{\lambda_{\mathrm{Fe}}} + \rho_{\mathrm{scinti}} \cdot \frac{\Delta x_{\mathrm{scinti}}}{\lambda_{\mathrm{scinti}}}} = 17.567\,\mathrm{cm} \tag{3.2}$$

where $\lambda_{\mathrm{Fe}} = 16.77\,\mathrm{cm}$ and $\lambda_{\mathrm{scinti}} = 78.79\,\mathrm{cm}$ are the iron and polyvinyltoluene nuclear interaction lengths, and $\rho_{\mathrm{Fe}} = 7.874\,\mathrm{g/cm^{-3}}$ and $\rho_{\mathrm{scinti}} = 1.032\,\mathrm{g/cm^{-3}}$ their corresponding densities [1]. The baseline of a channel of the right side estimated from calibration runs with an anti-fiducial cut is shown in Fig. 3.18, right. The baseline distributions of all channels are fitted with a gaussian function to estimate the baseline means μ_{bl} and standard deviations σ_{bl}. In the analysis discussed in Sec. 3.7, the baseline subtraction is performed according to Eq. 3.1, where both the raw pulse height and the mip MPV are corrected for the mean baseline value. Moreover, signals induced by baseline fluctuations are removed by considering only pulse heights that are at least 5σ above the baseline mean:

$$\mathrm{PH}^{\mathrm{ch}} \geq \mu^{\mathrm{ch}}_{bl} + 5 \cdot \sigma^{\mathrm{ch}}_{bl} \tag{3.3}$$

[8] A dark run is a run with no beam.

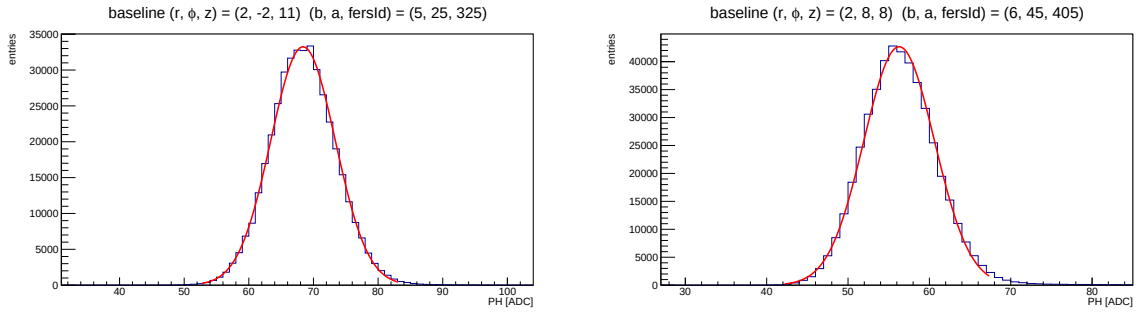

Figure 3.18: (left) Baseline of a left side channel measured from dark runs, i.e. pedestal data. (right) Baseline of a right side channel estimated from calibration data with anti-fiducial cut. The gaussian fit performed to estimate baseline mean and standard deviation is also shown (red curve).

3.7 Data analysis of electron runs for energy resolution and linearity assessment

In order to assess the energy resolution of the calorimeter prototype, dedicated electron runs at different beam momenta (p = 0.5, 1, 2, 3, 4 and 5 GeV) were performed. The electron content of the beam was enhanced employing an electron enriched target (electron enriched runs). In this section the data analysis of electron runs is discussed, aiming to assess the energy resolution and linearity of the calorimeter and their data/MC comparison.

3.7.1 Particle identification with Cherenkov counters

The separation of electrons from heavier beam particles is achieved using the signals collected from two Cherenkov detectors, hereafter referred to as Cher1 and Cher2. Indeed, given the fixed momentum of the beam particles and the pressures set in the two Cherenkov detectors, discrimination between electrons, muons and pions can be achieved. During the test beam, the pressure of Cher2 was set to be above threshold for electrons and below threshold for muons. In particular, for all beam energies considered in the test beam, electrons in a CO_2 gas always emit Cherenkov radiation. Therefore, electrons produce a signal in both Cherenkov counters, whereas events with no signal in Cher2 are due to the passage of muons or heavier particles that do not emit Cherenkov radiation. The pressure of Cher1 detector, on the other hand, was set to be above threshold for muons, so both muons and electrons produce a light signal in the detector. The signals recorded by Cherenkov counters are thus exploited to perform beam particle identification: pions do not produce a signal in either detector, electrons produce a signal in both detectors, whereas muons produce a signal in Cher1 but not in Cher2.
In the data analysis of electron runs, the Cherenkov counter signals were used to select only electron events, ensuring that the selected particle sample was not contaminated by spurious muons or heavier particles. The pulse heights of both Cherenkov detectors were considered. Since electrons are in time coincidence with the trigger scintillator, a preliminary timing selection can be applied in the analysis to improve the purity of the selected electron sample. The distributions of the pulse heights in the two Cherenkov detectors are shown in Fig. 3.19, before and after selecting particles to be in time coincidence with the trigger scintillator. The scatter plot of the pulse heights from the two Cherenkov detectors is shown in Fig. 3.20, left. Since electrons produce a high signal in both detectors, while muons produce a lower signal in Cher1 and no signal in Cher2, it is possible to select a pure electron sample by requiring that both Cherenkov detector

recorded a signal above a pulse height threshold. Specifically, a rectangular cut is defined, as shown in Fig. 3.20, right, on the particle sample in time coincidence with the trigger scintillator.

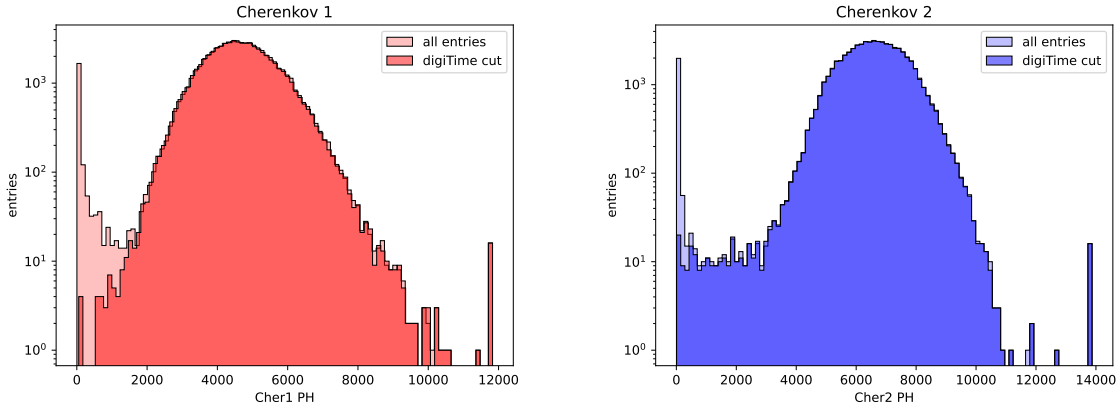

Figure 3.19: Pulse heights in the two Cherenkov detectors for the electron run at 2 GeV, before (light color) and after (dark color) selecting particles to be in time coincidence with the trigger scintillator.

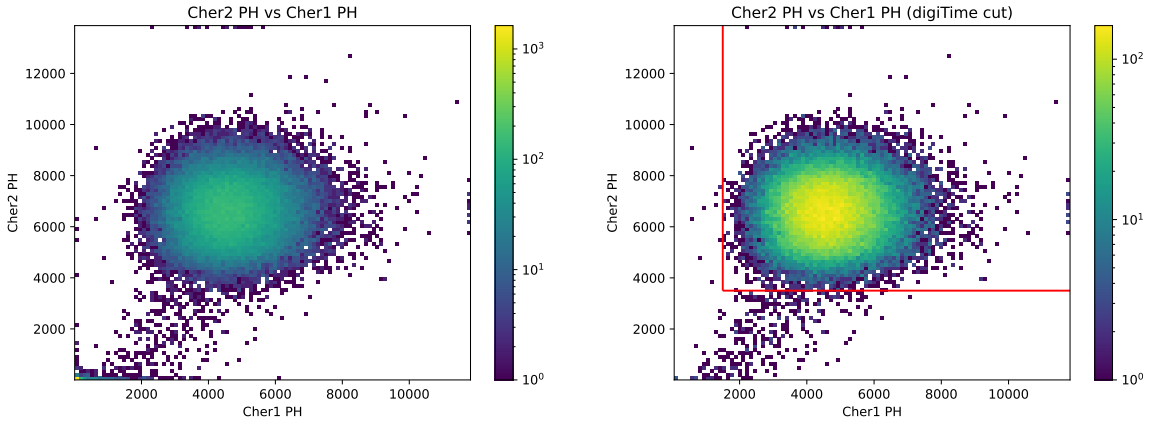

Figure 3.20: Scatter plot of the pulse heights from the two Cherenkov detectors, before (left) and after (right) selecting particles to be in time coincidence with the trigger scintillator. (right) Rectangular pulse height cut for electron selection.

3.7.2 Efficiency maps for electron runs

The knowledge of front channels center coordinates (x_0, y_0) is crucial to perform a fiducial cut to ensure electromagnetic shower containment, as discussed in Sec. 3.7.3. Since the reference coordinate system of silicon chambers during electron and calibration runs was different, the center coordinates of front channels estimated from calibration data (see Sec. 3.5) cannot be used for the analysis of electron runs. Therefore, the computation of efficiency maps for electron runs is necessary to determine the center coordinates of the demonstrator front channels in these runs. The channel efficiency is computed using a pulse height cut to select signals larger than the response of a mip, i.e. $\mathrm{PH}^{\mathrm{ch}} \geq 1.5 \cdot \mathrm{MPV}^{\mathrm{ch}}_{mip}$. The channel efficiency map obtained in this manner is a good proxy for the estimation of the channel position in electron runs, as shown in Fig. 3.21, left. Due to the transverse development of electromagnetic showers induced by electrons, the efficiency maps obtained in electron runs are less sharp than those obtained with mips in

calibration runs, making the estimation of center coordinates of channels less accurate. In order to estimate the center coordinates $(x_0,\ y_0)$ of front channels, an efficiency filter is applied to remove bins with efficiency less than 50%, as shown in Fig. 3.21, center. The center coordinates $(x_0,\ y_0)$ of each channel are then estimated using the weighted average of the bins position, as discussed for the calibration runs (see Sec. 3.5). Nevertheless, a refinement of the channel position estimation is required, using an iterative approach. The weighted mean provides an initial estimate of the channel's center of gravity; however, since not all halo bins around the channel area are suppressed by the efficiency filter (compare the left and center plots in Fig. 3.21), a systematic shift of the estimated channel position toward the beam spot center is introduced, as seen in the center plot of Fig. 3.21. To correct for this, a radial cut is applied to effectively remove the halo from the efficiency map, selecting only the bins within a radial distance $R = 3\,\text{cm}$ from the initial center of gravity estimate. The center of gravity is finally estimated using the means along x/y of the refined efficiency histogram, as shown in Fig. 3.21, right. The final efficiency maps of the front channels hit by electrons are shown in Fig. 3.22 for the left and right side of the demonstrator, respectively. Also shown are the estimated coordinates of each channel's center of gravity and the projection of tracks on the calorimeter front face.

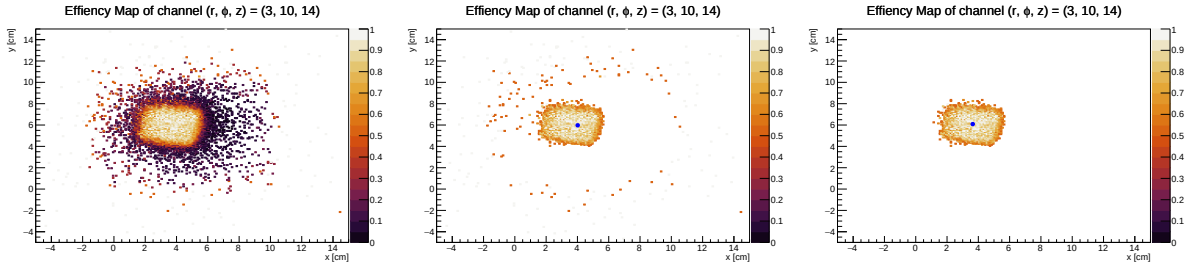

Figure 3.21: (left) Efficiency map of a right side front channel. (center) Efficiency map of a right side front channel with a 50% efficiency filter to estimate the center coordinates using the weighted mean approach. The center of gravity estimate is systematically shifted towards the center of the beam spot. (right) Efficiency map of a right side front channel with a 50% efficiency filter and a $R = 3\,\text{cm}$ radial filter for the final estimation of the center coordinates using the mean along x/y directions. See text for details.

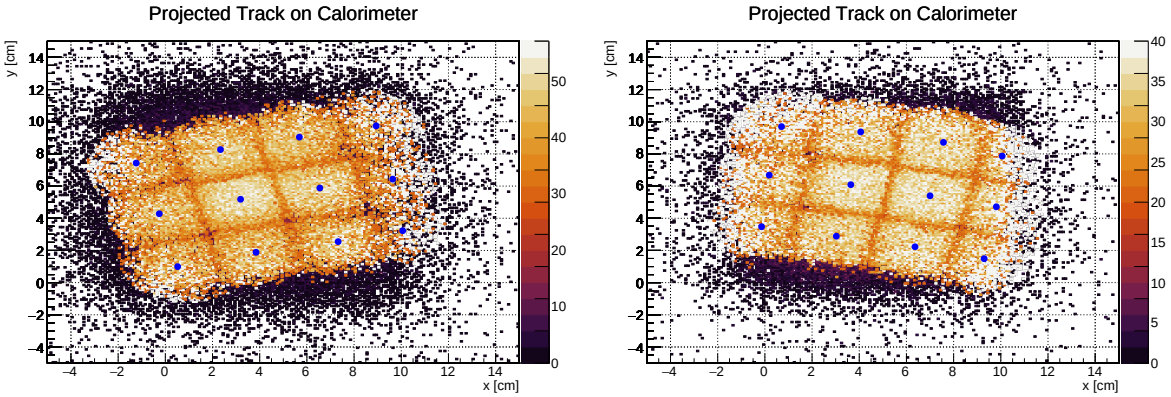

Figure 3.22: Final efficiency maps of front channels for the left and right side of the demonstrator, respectively, together with their estimated center of gravity coordinates and superimposed to the projection of tracks on the calorimeter front face.

3.7.3 Total energy deposited and shower containment

The total energy deposited in the calorimeter is estimated on an event basis as the sum of equalized pulse heights of each channel, as follows:

$$E_{tot} = \sum_{\text{ch}} \text{PH}^{\text{ch}}_{eq}$$

The pulse heights are equalized to the response of a mip in that channel and scaled to the average response of a mip over all the channels. Both signal pulse height and mip response are corrected by subtracting the baseline. Thus, for each channel, the pulse heights are equalized as follows:

$$\text{PH}^{\text{ch}}_{eq} = \frac{\text{PH}^{\text{ch}} - bl^{\text{ch}}}{\text{MPV}^{\text{ch}}_{mip} - bl^{\text{ch}}} \cdot \langle \text{MPV}^{\text{ch}}_{mip} - bl^{\text{ch}} \rangle \tag{3.4}$$

The equalized pulse heights are thus expressed in ADC counts. However, the pulse heights summation is not done for all the calorimeter channels, but only for those which were calibrated. Indeed, as mentioned, some channels were dead or difficult to calibrate due to low statistics, as they were only partially illuminated. The layouts of the left and right side of the demonstrator are shown in Fig. 3.23, respectively. The non-calibrated channels are shown in gray, whereas the yellow channels represent the ϕ sector illuminated by the beam spot during electron runs. In addition, to exclude contributions from residual baseline fluctuations above the cut in Eq. 3.3, channels farthest from those illuminated by the beam are excluded, and only the channels in $\phi \in [8, 13]$ for the right side and $\phi \in [-5, 0]$ for the left side are considered for the total energy estimation.

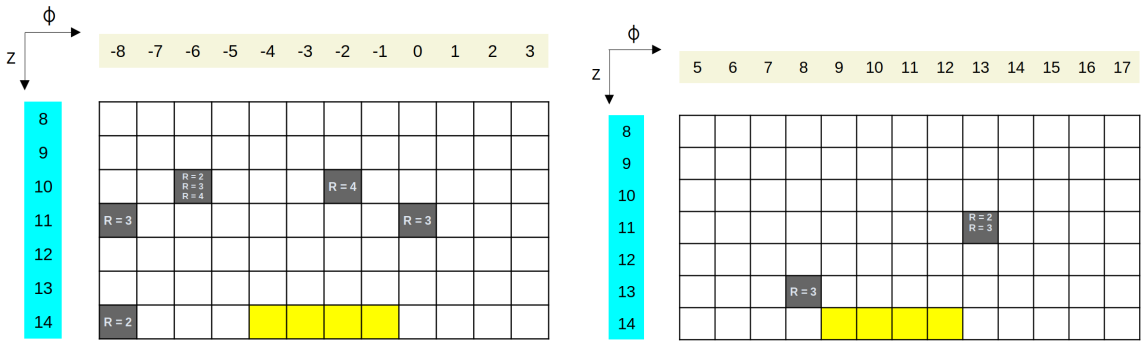

Figure 3.23: Schematics of the left and right side of the demonstrator, respectively. The non-calibrated channels are shown in gray, whereas the yellow channels represent the ϕ sector illuminated by the beam spot during electron runs.

In order to ensure a 95% containment of the electromagnetic shower induced by electrons, a fiducial cut is applied to select electrons whose impact point on the calorimeter front face is at least two Moliere radii from the calorimeter edges [118]. Since the Moliere radius in iron is $R_M = 1.72\,\text{cm}$ [1], the fiducial cut can be applied by selecting electrons impinging onto the central radial calorimeter layer. The efficiency maps of central channels illuminated by the beam spot are used to locate the central radial calorimeter layer using trapezoidal fiducial cut, as shown in Fig. 3.24.
The equalized pulse heights can also be converted from ADC counts to visible energy in MeV. The conversion factor is obtained from the ratio of the energy linearity slopes between simulation and data, using the following procedure. The equalized pulse heights in ADC counts are used to compute the total energy deposited and thus to estimate

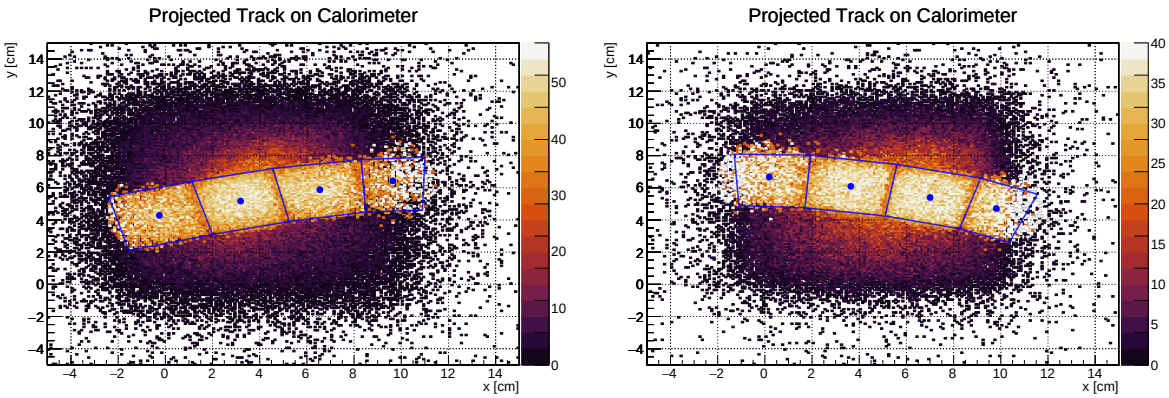

Figure 3.24: The fiducial cut for shower containment is applied by selecting electrons impinging onto the central radial calorimeter layer, for the left and right side of demonstrator respectively. The central radial calorimeter layer is located using trapezoidal cuts from the efficiency maps and positions of the central channels illuminated by the beam spot.

the energy linearity from electron runs in data. The energy linearity is assessed by plotting the relationship between the mean of the distribution from the total energy deposited E_{dep} and the beam energy E_{beam}, and fitting it with a first-degree polynomial $E_{\text{dep}} = m \cdot E_{\text{beam}} + q$. The slope m_{data}[ADC/GeV] obtained from the energy linearity from data, and the corresponding slope m_{MC}[MeV/GeV] from simulation (see Fig. 3.29), can thus be used to provide a conversion from ADC to visible energy in MeV. Therefore, data are corrected using MC prediction instead of relying on an absolute energy scale calibration based on mips. The linearity fit, shown in Fig. 3.25, is performed excluding points at 4 and 5 GeV, which are affected by saturation effects in SiPMs (see following analysis). This is not done for the simulation, where these effects are not included.

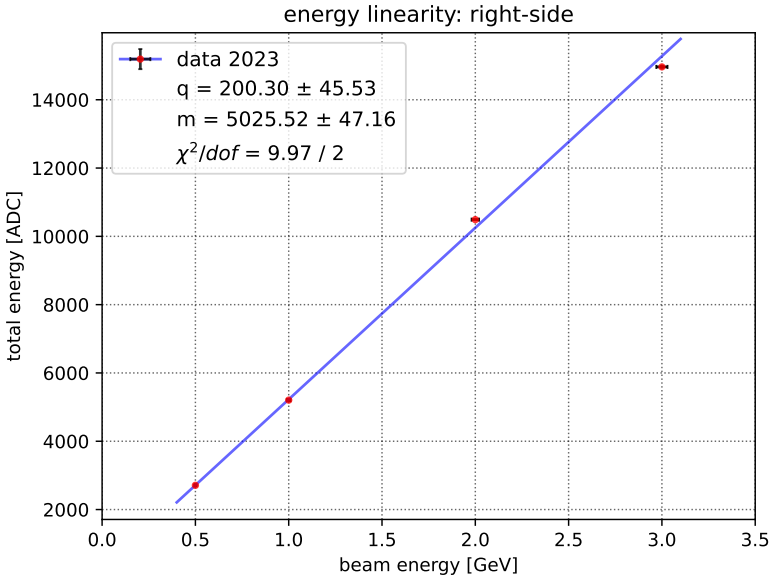

Figure 3.25: Energy linearity fit for the demonstrator right side excluding 4 and 5 GeV data points affected by saturation effects in SiPMs.

Finally, the equalized pulse heights expressed in MeV can be computed rescaling the average response of mip in ADC counts to the ratio of slopes $m_{\text{MC}}/m_{\text{data}}$ obtained from

MC simulation and data, as follows:

$$\mathrm{PH}^{\mathrm{ch}}_{eq} = \frac{\mathrm{PH}^{\mathrm{ch}} - bl^{\mathrm{ch}}}{\mathrm{MPV}^{\mathrm{ch}}_{mip} - bl^{\mathrm{ch}}} \cdot \frac{m_{\mathrm{MC}}}{m_{\mathrm{data}}} \cdot \langle \mathrm{MPV}^{\mathrm{ch}}_{mip} - bl^{\mathrm{ch}} \rangle \tag{3.5}$$

The conversion of equalized pulse heights from ADC counts to MeV implies a scaling factor only, therefore it does not affect the energy resolution estimation and allows for a better agreement between the data/MC linearity, highlighting potential discrepancies due to saturation effects of SiPMs at high energies.
The distributions of total energy deposited in the calorimeter by electrons at different energies are shown in Fig. 3.26. The total energy deposited distributions are shown before (red) and after (blue) applying the fiducial cut for shower containment. Therefore, the fiducial cut allows to discard those events with an electromagnetic shower not fully contained in the calorimeter, responsible for an energy tail at lower energies.

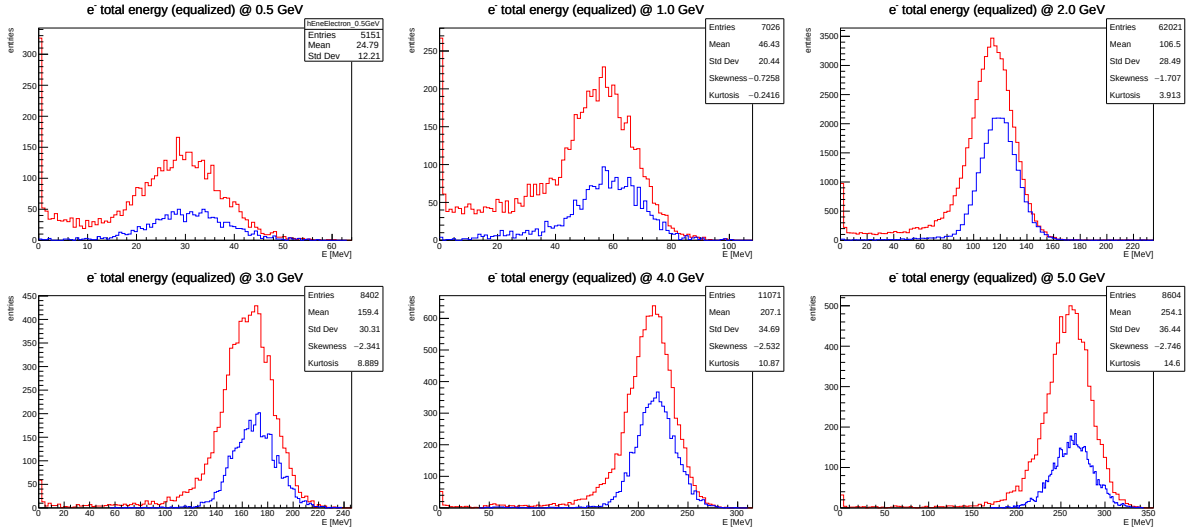

Figure 3.26: Total energy deposited in the calorimeter before (red) and after (blue) fiducial cut for shower containment for electron beam energies of 0.5, 1, 2, 3, 4 and 5 GeV.

3.7.4 Energy resolution and linearity

The study of the calorimeter response to electromagnetic showers is important for its characterization and performance assessment. The measurement of energy with an electromagnetic calorimeter is based on the principle that the energy deposited in the detector by the charged particles of the shower, mainly through ionization and excitation, is proportional to the energy of the incident particle [119]. The intrinsic energy resolution of an ideal calorimeter, i.e. a calorimeter with an infinite size and no response deterioration due to instrumental effects, is mainly due to fluctuations of the track length T_0. The track length T_0 is defined as the sum of all ionization tracks due to charged particles in the cascade. Since T_0 is proportional to the number of track segments in the shower, and the shower development is a stochastic process, from purely statistical arguments the intrinsic energy resolution is given by:

$$\sigma(E) \propto \sqrt{T_0} \tag{3.6}$$

from which the energy dependence of the fractional energy resolution is obtained:

$$\frac{\sigma(E)}{E} \propto \frac{1}{\sqrt{T_0}} \propto \frac{1}{\sqrt{E_0}} \tag{3.7}$$

In a realistic calorimeter, the actual energy resolution is deteriorated by other contributions and it is expressed more generally according to:

$$\frac{\sigma_E(E)}{E} = \frac{a}{\sqrt{E}} \oplus \frac{b}{E} \oplus c \tag{3.8}$$

where the symbol $\oplus$ indicates a quadratic sum. The a term is the stochastic term that includes the shower intrinsic fluctuations, the b term is the noise term, whereas the c term is the constant term [118].
In order to assess the energy resolution and linearity, the distributions of the total energy deposited in the calorimeter for fully contained events at the different beam energies are fitted with a gaussian function, as shown in Fig. 3.27.

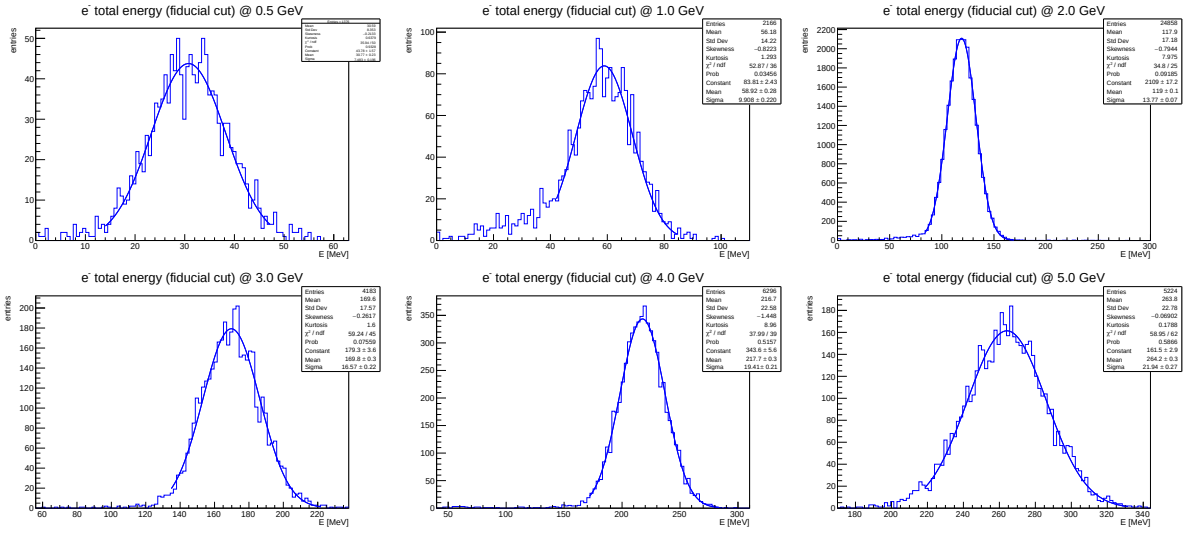

Figure 3.27: Gaussian fit of the total energy distributions in the calorimeter, after applying a fiducial cut for shower containment, for electron beam energies of 0.5, 1, 2, 3, 4 and 5 GeV.

The fitted mean μ and standard deviation σ of the gaussian function are used to estimate the energy resolution and linearity. The relative energy resolution is computed as the ratio of the standard deviation σ and the mean μ, both estimated from the gaussian fit, and is shown in Fig. 3.28 for the right side of the demonstrator at each beam energy. In general, if the noise term b is included in the fit as a free parameter, since it is highly correlated with the other parameters, non realistic high values for this term are obtained. Therefore, the b term is considered as a fix parameter in the fit, and an independent estimate of its value is obtained according to the discussion detailed in Sec. 3.7.5. The data/MC comparison for the energy resolution, shown in Fig. 3.28, highlights a discrepancy between the data and the simulation; this can be explained introducing in the MC simulation potential factors that contribute to the degradation of the energy resolution, as discussed in Sec. 3.8.

The energy linearity of the calorimeter is assessed by plotting the relationship between the fitted mean μ of total energy deposited and the beam energy E_{beam}, and fitting it with a first-degree polynomial $\mu = m \cdot E_{\text{beam}} + q$. The energy linearity obtained in electron runs for different beam energies is shown in Fig. 3.29, for the right side of the demonstrator. The energy linearity points obtained from data at 4 and 5 GeV show a discrepancy from the expected linear trend due to saturation effects of SiPMs.

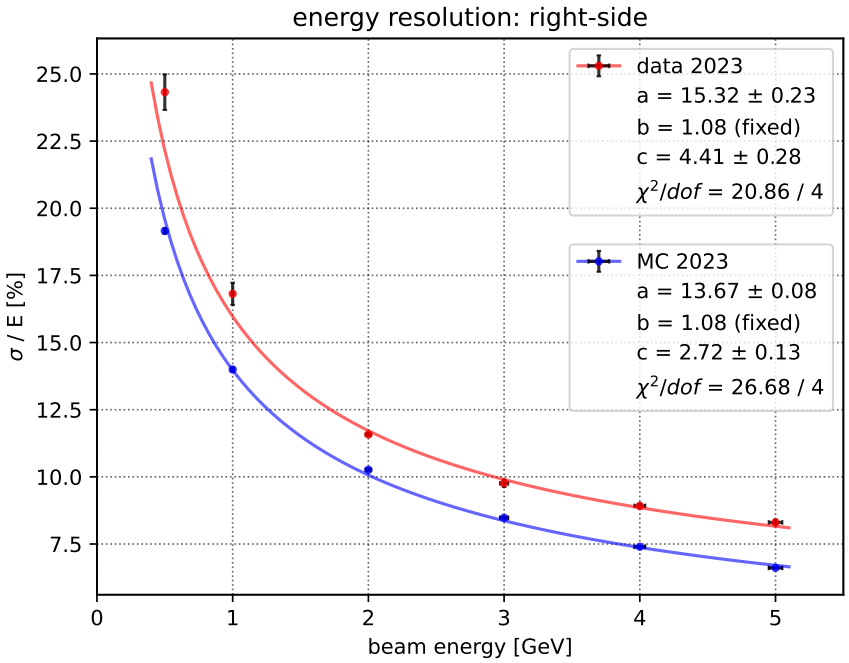

Figure 3.28: Energy resolution of the right side of the demonstrator. Data (red points) are compared with the simulation prediction (blue points). Fits using Eq. 3.8 are also shown as solid lines.

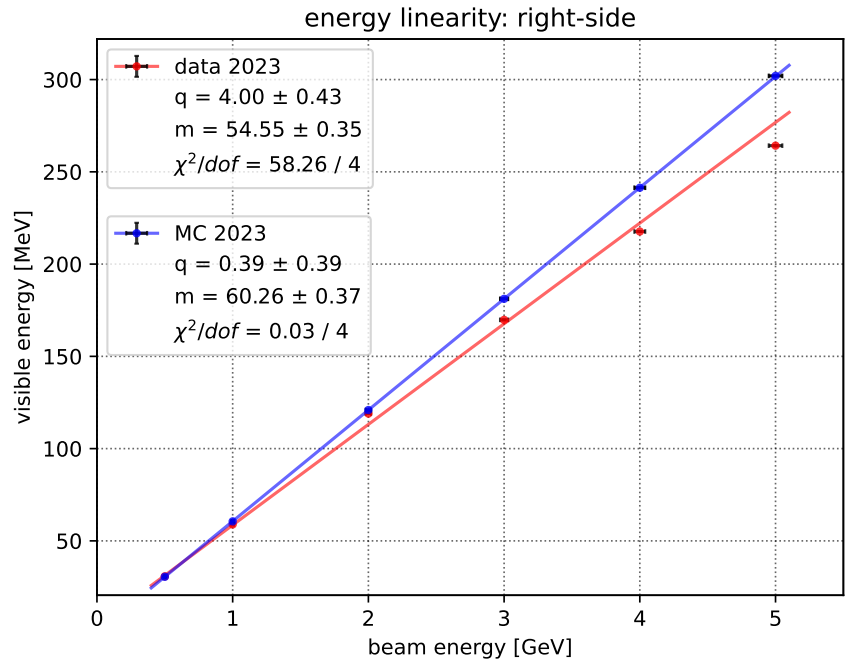

Figure 3.29: Energy linearity of the right side of the demonstrator. Data (red points) are compared with the simulation prediction (blue points). Linear fits are also shown as solid lines.

3.7.5 Independent estimate of the noise term in the energy resolution

The noise term b in the energy resolution fit is pinned down using an independent estimate based on measurements of the channels baseline. Indeed, the estimate of the total energy deposited is affected by the baseline fluctuations from electronics. The total energy deposited is estimated as the sum of the channels pulse heights and it can be expressed isolating the pulse height contribution due to the baseline, according to:

$$E_{\text{dep}} = \sum \text{PH}_i = \sum (\text{PH}_{\text{meas},i} + \text{PH}_{bl,i}) = \sum \text{PH}_{\text{meas},i} + \sum \text{PH}_{bl,i} \tag{3.9}$$

The baseline of all channels can be assumed to be distributed according to a gaussian with known mean and variance $\sigma^2_{bl,i}$. Therefore, according to the central limit theorem[9] [120], the term $\sum \text{PH}_{bl,i}$ is a sum of random variables following gaussian distributions and its variance can be estimated as:

$$V\left[\sum \text{PH}_{bl,i}\right] = \sum V[\text{PH}_{bl,i}] = \sum \sigma^2_{bl,i} \tag{3.10}$$

The total energy uncertainty due to baseline is thus given by:

$$\sigma^2_{\text{tot}} = \sum \sigma^2_{bl,i} \tag{3.11}$$

This sum is done over all the calorimeter channels used for computing the total energy. Since this number could be higher than the number of channels recording an actual energy deposition in an event, this sum is actually an overestimate of the baseline effect. The distribution of the σ_{bl} used in the sum of Eq. 3.11, expressed in raw ADC counts, is shown in Fig. 3.30, left. The same σ_{bl} distribution but equalized to the response of a mip in a channel and scaled to the average response of a mip is shown in Fig. 3.30, right.

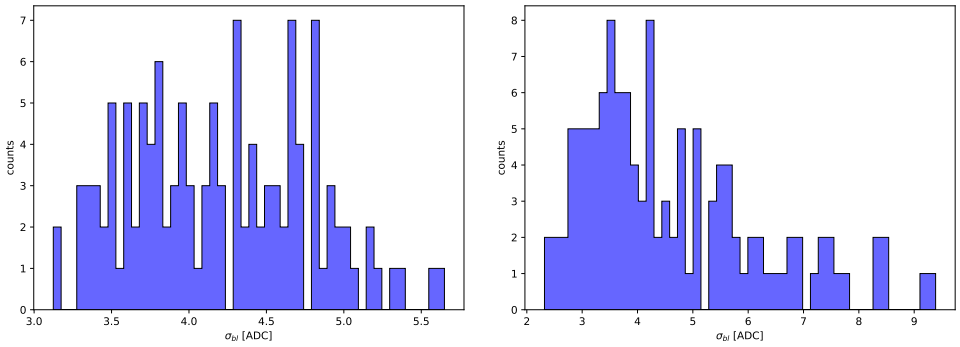

Figure 3.30: (left) Distribution of σ_{bl} of fiducial channels expressed in raw ADC counts. (right) Distribution of σ_{bl} equalized to the response of a mip in a channel and scaled to the average response of a mip.

The b term in the energy resolution fit is expressed in units of beam energy (GeV). The linearity formula is thus used to convert from ADC to beam energy units, namely using $E_{\text{beam}} = (E_{\text{dep}} - q)/m$. Since σ_{tot} represents a width, the intercept q does not affect the result, as $\Delta E_{\text{beam}} = \Delta(E_{\text{dep}} - q)/m = \Delta E_{\text{dep}}/m$. Therefore, σ_{tot} is expressed in GeV according to $\sigma_{\text{tot,beam}}[\text{GeV}] = \sigma_{\text{tot}}[\text{ADC}]/m$ and, finally, the b term can be (over)estimated as:

$$b = \sigma_{\text{tot,beam}} \tag{3.12}$$

[9]The central limit theorem states that, given n independent variables x_i, distributed according to p.d.f.s f_i, having mean μ_i and variance $V_i = \sigma_i^2$, then the p.d.f. for the sum of the x_i, $S \equiv \sum x_i$, has expectation (mean) $E[S] = \sum \mu_i$ and variance $V[S] = \sum V_i = \sum \sigma_i^2$ and approaches the normal p.d.f. $N(S; \sum \mu_i, \sum \sigma_i^2)$ as $n \to \infty$ [120].

The noise term for the right side of the demonstrator is estimated as $b = 0.0108\,\text{GeV}$ and it is used as a fixed parameter in the energy resolution fit, as discussed in Sec. 3.7.4.

3.8 Accounting for detector effects in the MC simulation

In order to explain the discrepancies observed between energy resolution measurements and simulation predictions, potential factors contributing to a degradation of energy resolution were investigated and introduced in the MC simulation, such as the effect of photostatistics, baseline effects and possible geometrical misalignments.

3.8.1 Photo-electron statistics

The number of optical photons produced in the scintillator tiles by an energy deposition is subject to statistical fluctuations, leading eventually to a fluctuations in the number of photo-electrons (p.e.) detected by SiPMs. The *photo-electron statistics* can affect the energy resolution estimate: a given amount of energy deposited can produce different readout signals in the SiPMs due to statistical fluctuations in the number of detected photo-electrons. The photo-electron statistical fluctuation can be described according to a Poisson distribution:

$$P(n) = e^{-\mu} \cdot \frac{\mu^n}{n!} \tag{3.13}$$

where n is the number of photo-electrons and μ the mean number of photo-electrons produced by an energy deposition E_{dep}. The scintillation light is not simulated and the detector response is at hit-level. The effect of *p.e. statistics fluctuations* on visible energy depositions can be introduced in the simulation output according to the following steps:

1. The average number of photo-electrons $\langle N_{p.e.} \rangle$ produced by an energy deposition is estimated according to:

$$\mu \equiv \langle N_{p.e.} \rangle = E_{\text{hit}} \cdot \varepsilon^{-1} \tag{3.14}$$

   where E_{hit} is the hit level energy deposition and ε^{-1} is the mean number of photo-electrons produced per unit of deposited energy [p.e./MeV]. This parameter can be estimated from dark runs. In the following a value $\varepsilon^{-1} = 15\,\text{p.e./MeV}$ is considered, according to past test beams and cosmic ray measurements [76].

2. The differences in mip response among channels are taken into account by means of a correction factor:

$$\mathcal{C}_{\text{ch}} = \frac{\text{MPV}_{\text{ch}} - bl_{\text{ch}}}{\langle \text{MPV}_{\text{ch}} - bl_{\text{ch}} \rangle} \tag{3.15}$$

   defined as the ratio between the MPV of a channel and the average MPV over all channels. The mip MPVs are obtained from data using a Landau fit in calibration runs and then baseline subtracted.

3. The actual number of p.e. in a channel is obtained scaling the average number of p.e. with the correction factor, namely:

$$\mu' = \mathcal{C}_{\text{ch}} \cdot \mu \tag{3.16}$$

thus taking into account differences in mip response observed in data among channels.

4. The corresponding number of p.e. $n_{p.e.}$ is sampled from a Poisson distribution with mean μ', namely:

$$n_{p.e.} \in \text{Poiss}(\mu') \tag{3.17}$$

5. The deposited energy E_{dep} smeared for p.e. statistic fluctuations is finally estimated according to:

$$E_{\text{dep}} = \frac{n_{p.e.}}{\mathcal{C}_{\text{ch}} \cdot \varepsilon^{-1}} \tag{3.18}$$

Since the mean number of p.e. per 1 MeV energy deposition is high, the p.e. statistical fluctuations should not affect significantly the energy resolution estimate.

3.8.2 Baseline effect

The baseline fluctuations can affect the estimate of the total energy deposited in the calorimeter modules. The effect of baseline fluctuations, for each channel, is thus introduced in the MC simulation. The standard deviation of the baseline distribution of a given channel is converted from ADC counts to visible energy in MeV according to[10]:

$$\sigma_{bl}^{\text{ch}}[\text{MeV}] = \sigma_{bl}^{\text{ch}}[\text{ADC}] \cdot \frac{6.12\,\text{MeV}}{\text{MPV}_{mip}^{\text{ch}} - bl^{\text{ch}}[\text{ADC}]}$$

The baseline contribution to deposited energy in a given channel is thus sampled from a gaussian with mean zero and $\sigma = \sigma_{bl}^{\text{ch}}$, according to:

$$E_{bl}^{\text{ch}} \in \text{Gauss}(0, \sigma_{bl}^{\text{ch}}) \tag{3.19}$$

The baseline fluctuations are thus introduced in the simulation as follows:

$$E_{\text{dep}}^{\text{ch}} \rightarrow E_{\text{dep}}^{\text{ch}} + E_{bl}^{\text{ch}} \tag{3.20}$$

and their contribution to total energy deposited is expected to be negligible.

3.8.3 Scintillator tiles interspaces due to geometric misalignment

The geometry implemented in the MC simulation is perfect, with all tiles aligned and without gaps. However, geometric misalignment among scintillator tiles are expected as a result of the handmade construction and assembling of the calorimeter prototype. The effect of interspaces among scintillator tiles has been taken into account in the demonstrator geometry, introducing both azimuthal and radial gaps for several values. Fig. 3.31 shows the implementation in the demonstrator geometry of 1 mm gaps, both azimuthally and radially. The residual interspaces between scintillator tiles may explain the discrepancy between data and MC energy resolution, as dead-regions and non-uniformities in the calorimeter coverage contribute to increased energy fluctuations.

[10] The weighted mean of MPVs in the calorimeter layers obtained for the demonstrator right side simulation is ~ 6.12 MeV.

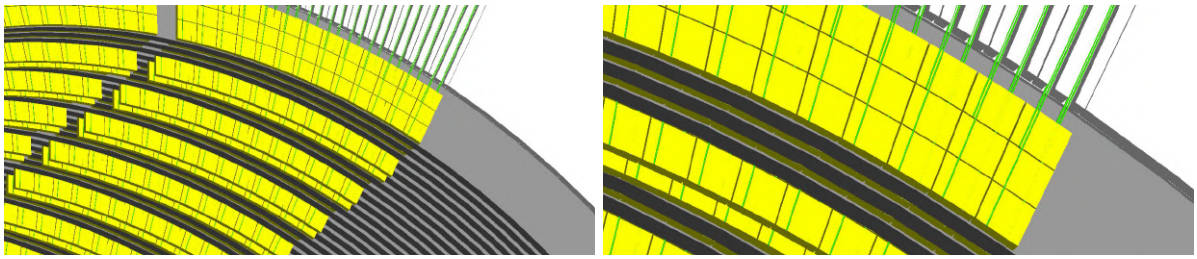

Figure 3.31: Implementation of 1 mm azimuthal and radial interspace among scintillator tiles in the demonstrator geometry.

3.9 Data/MC comparison of energy response after including detector effects

The data/MC comparison of the energy resolution and linearity of the demonstrator is discussed in this section, after including in the simulation the detector effects discussed in Sec. 3.8. The discrepancies in the data/MC agreement on energy resolution observed in Sec. 3.7.4 are addressed by the inclusion of these effects in the MC simulation. Specifically, the 1 mm azimuthal and radial gaps between the scintillator tiles turned out to be the dominant factor in explaining the data/MC discrepancy shown in Fig. 3.28. The data/MC comparison of the energy resolution and linearity for the right side of the demonstrator is shown in Figs. 3.32 and 3.33, respectively. The MC simulation includes the effects of photo-electron statistics, baseline fluctuations and 1 mm azimuthal and radial dead regions between the scintillator tiles.

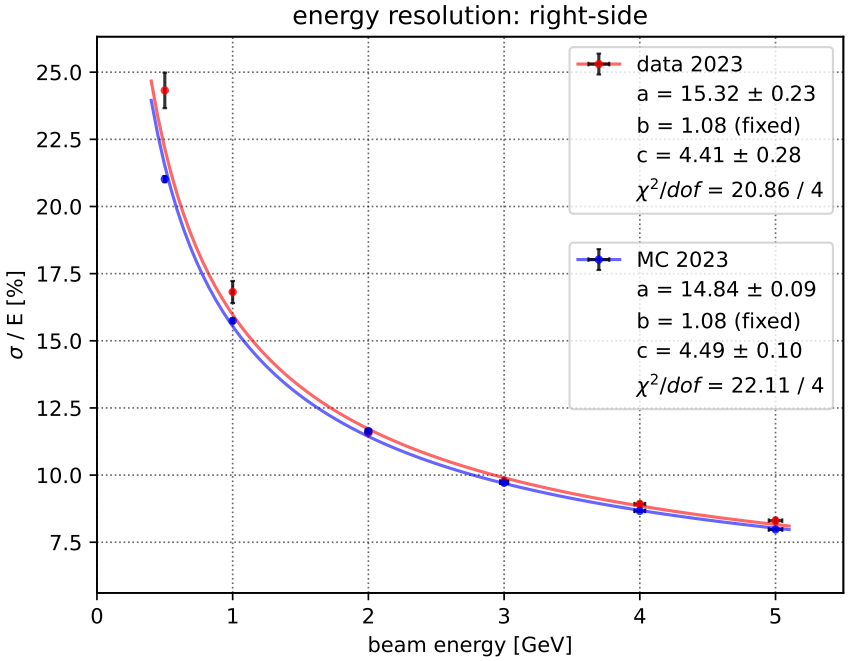

Figure 3.32: Data/MC comparison of the energy resolution of the right side of the demonstrator. The photo-electron statistic, baseline effects and a 1 mm azimuthal and radial dead regions among scintillator tiles are considered in the MC simulation. Data (red points) are compared with the simulation prediction (blue points). Fits using Eq. 3.8 are also shown as solid lines.

The presence of dead regions among scintillator tiles also improves the agreement in the slope between data and MC in the energy linearity, shifting the deposited energy in the calorimeter to lower values (compare the MC points between Fig. 3.29 and Fig. 3.33). The energy linearity points at 4 and 5 GeV in the data show a deviation from the expected linear trend due to SiPM saturation effects, which were investigated in [93] and whose study is beyond the aim of the present work.

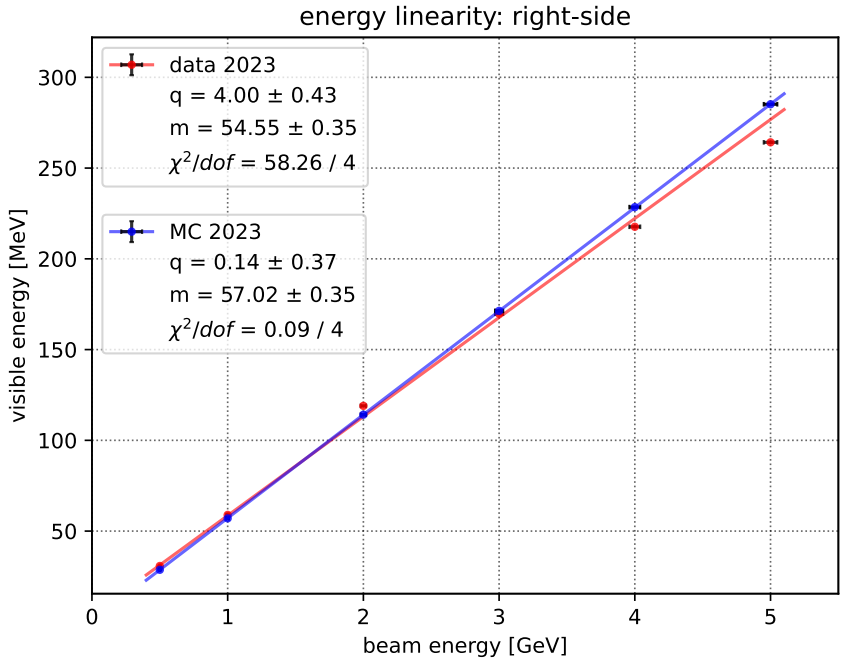

Figure 3.33: Data/MC comparison of the energy linearity of the right side of the demonstrator. The photo-electron statistic, baseline effects and a 1 mm angular and radial dead regions among scintillator tiles are considered in the MC simulation. Data (red points) are compared with the simulation prediction (blue points). Linear fits are also shown as solid lines.

In conclusion, the performance of the demonstrator is well within the ENUBET requirements. The achieved energy resolution is $\sim 15\%/\sqrt{E[\mathrm{GeV}]}$, with good energy linearity up to 5 GeV, and deviations of only few % due to SiPM saturation effects. The data analysis results are in agreement with those obtained from the `GEANT4` simulation of the demonstrator, thus validating the ENUBET simulation. The simulated geometry needs to be slightly modified by introducing 1 mm gaps between tiles to account for data/MC discrepancies, which arise when assuming an ideal geometry with perfectly aligned scintillators and no dead regions. The presence of small dead regions are ascribable to limitations in the construction procedure used to build the prototype, which can be overcome by adopting standardized, high-precision manufacturing processes rather than manual assembly.

4 The assessment of neutrino flux systematic uncertainties in NP06/ENUBET

The most important source of systematic uncertainty on neutrino flux is represented by the *yields of secondary hadrons* produced at the target. Indeed, an accurate knowledge of cross-sections and yields is crucial for a correct normalization of the number of secondary mesons produced at target and, therefore, of the number of neutrinos reaching the detector. The fragmentation models implemented in Monte Carlo event generators make possible to predict differential distributions that can be used to compute the *hadron production yields*. Nonetheless, even if these models can be tuned with external data, they usually are not able to reproduce the kinematic distribution of secondaries [59]. The leading *hadroproduction systematic uncertainty* can be included in the simulation of the facility by reweighting on hadron production data both the charged lepton observables measured at the instrumented decay tunnel and the neutrino flux at detector. A realistic hadroproduction model [121] has been fitted to data from NA56/SPY [122] and NA20 [123] experiments that used 450 and 400 GeV/c protons on target, respectively. The ENUBET charged lepton monitoring technique in the instrumented decay tunnel is exploited to constrain the neutrino flux at detector, finally enhancing its precision. Indeed, the fit to charged lepton observables measured in the tunnel walls is used to set a constraint on the hadroproduction weights used to reweight the neutrino flux at detector. In addition to the conventional systematics of a neutrino beam, subdominant detector-related systematics due to the instrumentation of the decay tunnel are also expected, and their contribution is assessed. In this Chapter, the positrons emitted from K_{e3} decay and recorded in the tunnel walls are exploited to constrain the ν_e flux systematic uncertainties, providing the first end-to-end assessment of hadroproduction and detector-related systematics in a monitored neutrino beam.

4.1 Event simulation and reconstruction in the tagger

A full `GEANT4` simulation of the 40 m long instrumented decay tunnel (`G4TAG` simulation) has been developed, tracking all the particles at the tunnel entrance derived from the transfer line simulation output and recording in each detector module the energy deposition from the particles impinging the tunnel walls [76]. The detector response is simulated at hit level. A protons-on-target (pot) intensity of 4.5×10^{13} pot in a 2 s slow extraction scheme is assumed hereafter. The `G4TAG` simulation framework has been used to develop and assess the performance of charged lepton identification algorithms in the decay tunnel. The pile-up effects are handled by the `Middlelayer` algorithm by adding the energy and averaging the time of neighboring hits with a time difference below 1 ns [76]. The first step of the reconstruction chain is the `Event Builder` algorithm, aiming to reconstruct an event by correlating in space and time hits in different LCMs and t_0-layer tiles in order

to select those belonging to the same particle. Signal events are preselected at the event building level with specific cuts that were optimized to suppress the background arising from beam-halo particles and from other mesons decay modes. The reconstructed events are then processed with a multivariate analysis based on a Multilayer Perceptron Neural Network (`NN`) provided by the TMVA toolkit [124], in order to discriminate the signal from the background.
Two different event reconstruction and analysis chains - employing specific cuts, ANN training samples and discriminating variables - are used for positrons and muons from kaon decays, respectively. The algorithms developed for the reconstruction and classification of positron events from K_{e3} decay are described in the following, as they are essential for the charged lepton monitoring technique used to reduce the main systematic uncertainties.

4.1.1 Reconstruction and selection of positron events

The `Event Builder` algorithm for K_{e3} aims to preselect positron candidates through the identification of a visible energy deposit in the LCMs of the innermost layer exceeding 28 MeV[1] as a *seed* for the event reconstruction [76]. In particular, the seed value was chosen maximising the signal times purity figure of merit of reconstructed events. The signals in the LCMs and t_0-layer tiles correlated to the seed are then clustered taking into account their position and timing. In the event building, all the LCMs in ± 5 azimuthal ϕ sectors with respect to the seed and in longitudinal planes in the interval $[-3, 10]$ around the seed plane are taken into account. The nine upstream t_0-layer tiles in the same ϕ sector as the seed are also sought for compatible hits. After correcting the time of each hit for its distance from the seed, those in a time window of ± 1 ns with respect to the seed are considered. If at least 10 hits are clustered, the reconstructed event is then considered for subsequent analysis. This procedure is iterated over all the recorded signals, discarding those already clustered[2] [76].
The request of at least one calorimeter module - the event seed - with an energy deposit largely exceeding the typical mip signal determines a relevant reduction of halo muons and non-interacting hadrons background, that can be further suppressed by exploiting their single-track topology. The t_0-layer is exploited to suppress the residual photon background originated from π^0 produced in kaon decays and from interactions of stray particles with the elements of the beamline. Moreover, the longitudinal, transverse and radial segmentation of the calorimeter can be exploited to reject the hadronic background due to off-momentum particles and to pions generated in most of kaon decay modes, since electromagnetic showers develop inside a few LCMs whereas the energy deposit pattern of hadronic showers encompasses tens of LCMs [76]. A set of discriminating variables that exploit differences in the energy deposition pattern in calorimeter modules is implemented in a multivariate analysis, based on a Multilayer Perceptron Neural Network. For instance, some of the variables that feed the input layer of the Neural Network (`NN`) are the fraction of energy in the LCM of the first calorimeter layer with the largest energy deposition, the fraction of energy of the LCMs in the same ϕ sector as the seed, the total number of LCM hits clustered in the event, the energy deposition in the most upstream t_0-layer tile. The event position in the transverse and longitudinal direction are also included, since positrons from kaon decays impact mostly the downstream part of the tunnel with a uniform distribution in ϕ, whereas off-momentum particles lay mostly on the bending plane intercepting the initial part of the tunnel.

[1] The Landau fit of the energy released by a mip in a LCM has a most probable value of ~ 6.5 MeV.
[2] On average $\sim 95\%$ of the clustered hits belongs to the same event as the seed.

The NN selection efficiency is defined as the ratio of the number of reconstructed signal events $N_{\rm sgn}^{\rm reco}$ over the total number of signal events $N_{\rm sgn}^{\rm tot}$ in the MC simulation:

$$\epsilon = \frac{N_{\rm sgn}^{\rm reco}}{N_{\rm sgn}^{\rm tot}} \tag{4.1}$$

whereas the purity of the selected sample can be computed as:

$$p = \frac{N_{\rm sgn}^{\rm reco}}{N_{\rm sgn}^{\rm reco} + N_{\rm bkg}^{\rm reco}} \tag{4.2}$$

where $N_{\rm bkg}^{\rm reco}$ is the number of misidentified background events. The selection efficiency ϵ and purity p of the selected sample as a function of a given NN cut value are shown in Fig. 4.1, left and center. The best value for the NN cut has been found by maximizing the product of selection efficiency and purity figure of merit, as shown in Fig. 4.1, right.

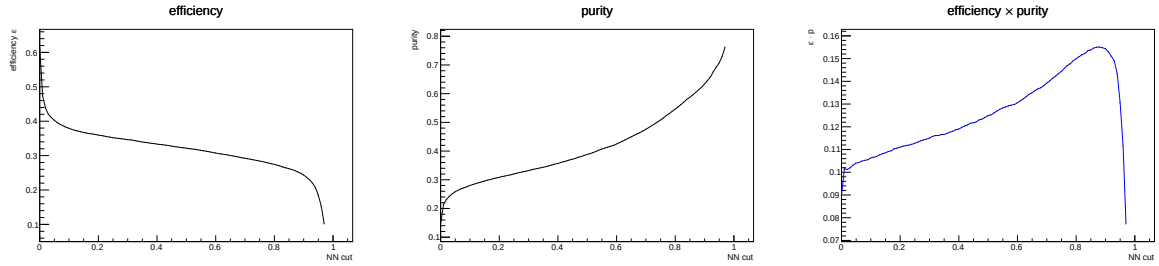

Figure 4.1: Signal selection efficiency ϵ (left), purity p of the selected sample (center) and efficiency $\times$ purity figure of merit (right) as a function of a given NN cut value.

The optimal cut for the NN classifier has been found to be:

$$\text{NN classifier cut} = 0.88 \tag{4.3}$$

providing the following values:

$$\epsilon = 25.26\% \tag{4.4}$$

$$p = 61.38\% \tag{4.5}$$

$$S/N = 1.59 \tag{4.6}$$

for the signal selection effiency ϵ, sample purity p and signal-to-noise ratio S/N, respectively. Therefore, a positron selection efficiency of $\sim 25.3\%$ (including the $\sim 53\%$ geometrical acceptance) and a $S/N \sim 1.6$ are achieved by applying a cut on the NN classifier that maximizes their product. The selection efficiency as a function of signal-to-noise ratio curve for the K_{e3} event selection is shown in Fig. 4.2, showing the optimal working point. Figs. 4.3 and 4.4 show, respectively, the total visible energy and the longitudinal position z of the impact point along the decay tunnel of the reconstructed events before and after the NN cut. In particular, these two observables play a special role since used as priors to reduce the systematic uncertainty in the ν_e flux, as will be described in the following.

The dominant background sources at the event building level are due to hadronic decays of kaons (yellow), non-collimated pions coming directly from the target or from early decays in the transfer line (green) and photons from the beamline (orange). The dominant backgrounds can be efficiently suppressed by the NN classifier, as shown in Figs. 4.3 and 4.4; however, halo positrons produced in the beamline and transported to the walls of the tunnel (black) are left as the main background component [76].

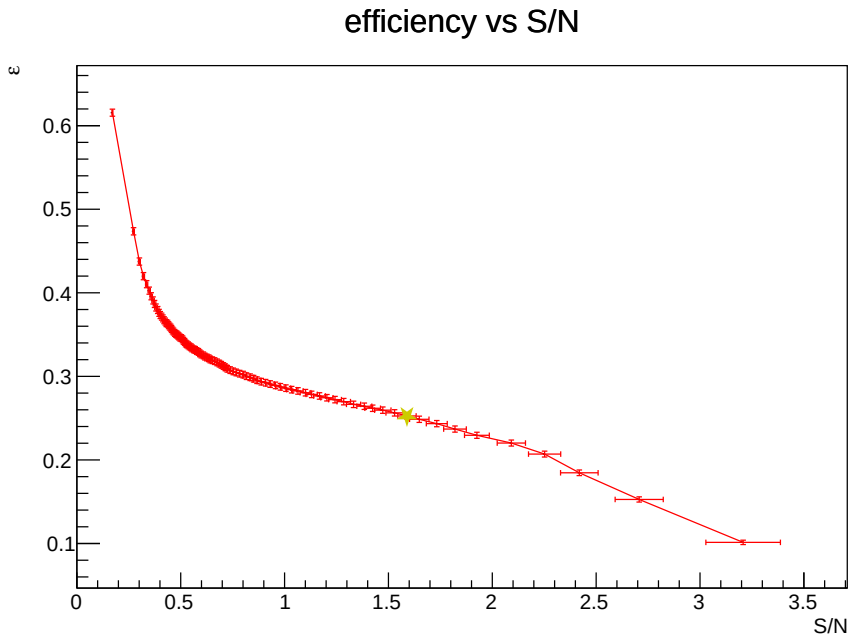

Figure 4.2: Signal efficiency ϵ as a function of the signal-to-noise ratio S/N for the K_{e3} event selection. The yellow star corresponds to the working point for signal selection, i.e. the point in the curve maximizing the product between signal efficiency and purity.

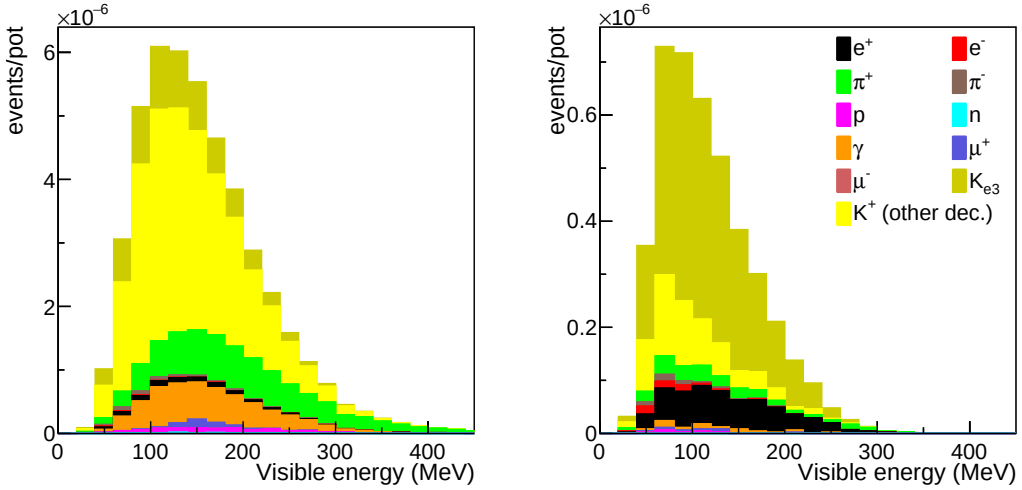

Figure 4.3: Visible energy of reconstructed events, before (left) and after (right) the cut on the NN classifier. Figure from [76].

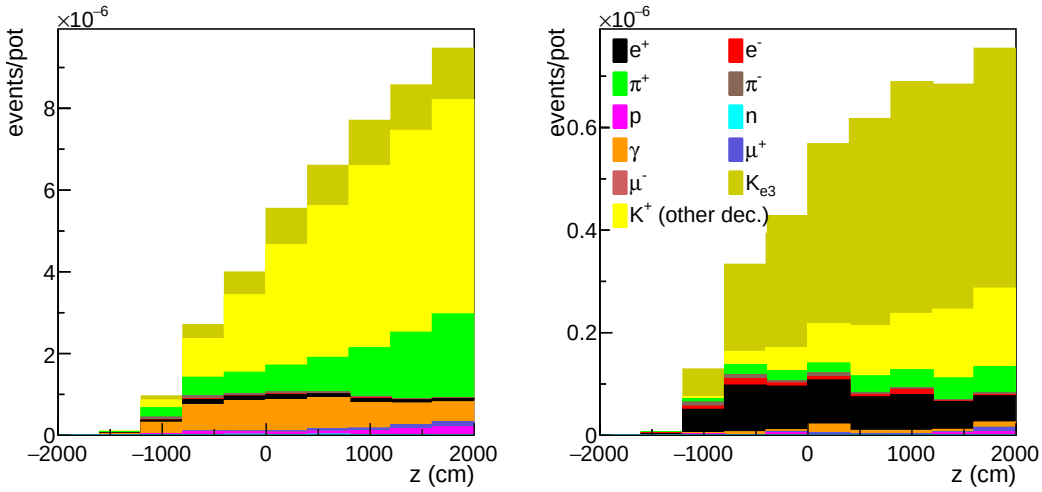

Figure 4.4: Longitudinal position of reconstructed events, before (left) and after (right) the cut on the NN classifier. Figure from [76].

4.2 NA56/SPY hadron yields data

The NA20 [123] and NA56/SPY [122] experiments performed a consistent set of measurements of particle yields on beryllium targets of different lengths, using 400 GeV/c and 450 GeV/c incident protons, respectively. Secondary particles (π^+, π^-, K^+, K^-, p, $\overline{p}$) were measured in a transverse momentum range up to 600 MeV/c, with the NA20 measurements in the high momentum range (60 GeV/c $< p <$ 300 GeV/c) and with NA56/SPY extending to the low momentum region (7 GeV/c $< p <$ 135 GeV/c). Since the available experimental data on particle yields from high energy proton interactions on light nuclei targets are not extensive, hadron yields needs in general to be extrapolated to different target materials, shapes and to different incident proton energies. Some useful analytical formulae for the calculation of secondary particle yields in p-A interactions, based on the NA20 and NA56/SPY measurements of particle yields, have been provided by M. Bonesini, A. Marchionni, F. Pietropaolo and T. Tabarelli de Fatis in [121].
In particular, in order to make NA20 and NA56/SPY measurements of general applicability, the measured single-particle yields on beryllium were converted to single-particle invariant cross-sections, correcting for target efficiency and tertiary particle production. Therefore, the authors in [121] provided a convenient parameterization of the inclusive invariant cross-sections for secondary particle production[3]. Although the cross-section parameterization was based on the measured yields from data collected by NA20 and NA56/SPY for protons impinging onto a beryllium target, in [121] were provided useful prescriptions to extrapolate such a parameterization to targets of different materials and geometry. The idea behind this work was to use a simple empirical parameterization of particle yields to predict the neutrino flux in neutrino beam facilities. This approach has the advantage of providing more transparent physical input to the calculations than the standard method of using complex Monte Carlo simulations based on hadronic cascade codes [121]. In the analysis discussed hereafter, these formulae turned out to be of great practical importance for reweighting on hadroproduction data both charged lepton observables measured in the tunnel and neutrino flux at detector.

[3]The obtained empirical formulae were found to reproduce experimental data within a 10% accuracy.

4.2.1 Particle production yields

The *secondary particle production yields* Y, as a function both of the momentum p and emission angle θ of secondary hadrons produced at target, can be computed as follows [122]:

$$Y(p,\theta) = \frac{N(p,\theta)}{I \cdot \Delta p/p \cdot \Delta\Omega} \tag{4.7}$$

where $N(p,\theta)$ is the measured number of events at momentum p and angle θ, $\Delta p/p$ is the momentum bite of the beamline, $\Delta\Omega$ is the angular acceptance and I is the total number of protons-on-target (POT).
The *inclusive invariant particle production cross-section* can be related to the measured yields from targets of finite length as follows:

$$E \times \frac{d^3\sigma}{dp^3} = \frac{E}{p^3}\frac{A}{N_0 \rho \lambda_p F(L)} Y \tag{4.8}$$

where Y is the particle yield per unit steradian and unit momentum bite $\Delta p/p$ normalized to the number of incident protons, A, ρ, L are the atomic mass number, density and length of the target, N_0 the Avogadro's number, λ_p is the nuclear interaction length for protons, E and p are the energy and momentum of the secondary particles, respectively. The target efficiency $F(L)$ can be computed analytically from the interaction probability of a particle crossing the target material. The simplest case is that of a particle normally incident on a homogeneous target material and subject to an interaction process characterized by a mean free path λ between collisions. The probability that a particle has an interaction along the target axis at a depth between z and $z + dz$ is given by:

$$p(z)dz = \frac{dz}{\lambda} e^{-z/\lambda} \tag{4.9}$$

The cumulative interaction probability

$$P(z) = \int_0^z p(z')dz' = 1 - e^{-z/\lambda} \tag{4.10}$$

accounts for the probability that a particle interacts in the medium before reaching a path length z. Hence, the non-interaction (survival) probability after a path length z is given by:

$$1 - P(z) = e^{-z/\lambda} \tag{4.11}$$

The target efficiency $F(L)$ can be estimated using a naive reabsorption model, namely assuming that the produced secondary particles - if absorbed in the target - do not generate additional particles. Under this approximation and considering forward production, by means of Eq. (4.9) for primaries and Eq. (4.11) for secondaries, the target efficiency can be computed as:

$$F(L) = \int_0^L f(z)dz = \int_0^L \frac{dz}{\lambda_p} e^{-z/\lambda_p} \cdot e^{-(L-z)/\lambda_s} \tag{4.12}$$

where λ_p and λ_s are the effective mean free paths of primary and secondary particles, respectively[4]. In particular, the target efficiency in Eq. (4.12) represents the convolution of the probability that the primary proton interacts between z and $z + dz$ in the target

[4]The nuclear interaction lengths for pions, kaons and protons in a graphite target, computed according to [125], are $\lambda_\pi = 51.81\,\text{cm}$, $\lambda_K = 59.05\,\text{cm}$ and $\lambda_p = 39.25\,\text{cm}$, respectively.

and the probability that the produced secondary particle escapes from the target without being reabsorbed. In a more general case, $f(z)$ in Eq. (4.12) will also depend on the production angle θ of the secondary particle, hence, Eq. (4.12) can be rewritten in a more general form as:

$$f(z,\theta) = \frac{1}{\lambda_p} e^{-z/\lambda_p} e^{-z'(z,\theta)/\lambda_s} \tag{4.13}$$

with $z'(z,\theta)$ representing the target length that the produced hadron has to cross in order to escape from the target ($z' = L - z$ for forward production).

4.2.2 Inclusive invariant cross-sections parameterization

An empirical functional form for inclusive particle production is provided in [121], which is appropriate for extrapolation to different center of mass energies and/or secondary particle momenta. The single-particle inclusive invariant cross-section has been empirically parameterized as a function of the transverse momentum p_T and the scaling variable $x_R = E^*/E^*_{max}$, defined as the ratio of the energy of the detected particle in the centre-of-momentum frame and the maximum energy kinematically available to the detected particle. The inclusive invariant cross-sections for the production of positively charged secondary mesons (π^+, K^+) in p-Be interactions has been parameterized, giving a suitable description of data, as follows:

$$\left(E \times \frac{d^3\sigma}{dp^3}\right) = A\,(1 - x_R)^{\alpha}\,(1 + Bx_R)\,x_R^{-\beta}\left[1 + a'(x_R)p_T + b'(x_R)p_T^2\right] e^{-a'(x_R)p_T} \tag{4.14}$$

where $a'(x_R) = a/x_R^{\gamma}$ and $b'(x_R) = a^2/2x_R^{\delta}$.
The ratio r of positive to negative particle data (π^+/π^- or K^+/K^-) has been parameterized with the empirical formulae:

$$r(\pi) = r_0 \cdot (1 + x_R)^{r_1} \tag{4.15}$$

$$r(K) = r_0 \cdot (1 - x_R)^{r_1} \tag{4.16}$$

It should be stressed that, in order to keep the number of free parameters limited, [121] assumed positive and negative mesons to have the same p_T distributions. Furthermore, some of the parameters have been fixed in the fitting procedure, since they appeared to be redundant. For instance, in the $K^{\pm}$ fit, $\delta = 2\gamma$ was chosen and B was set to zero, since its fitted value was found to be consistent with zero within errors.
Proton and anti-proton data, despite being of less direct interest for neutrino beams, have been parameterized with the following empirical formulae:

$$\left(E \times \frac{d^3\sigma}{dp^3}\right)_{p\,\mathrm{Be}\to p\,X} = A\,(1 + Bx_R)\,(1 - x_R)^{bp_T^2}\left(1 + ap_T + \frac{a^2}{2}p_T^2\right) e^{-ap_T} \tag{4.17}$$

$$\left(E \times \frac{d^3\sigma}{dp^3}\right)_{p\,\mathrm{Be}\to \overline{p}\,X} = A\,(1 - x_R)^{\alpha}\,x_R^{-\beta}\left(1 + ap_T + \frac{a^2}{2}p_T^2\right) e^{-ap_T} \tag{4.18}$$

For anti-protons a functional form similar to the one given in Eq. (4.14) has been adopted, except that an exact factorization in x_R and p_T has been assumed, since this was sufficient to give a reasonable fit to data. For protons, instead, the leading particle effect had to be taken into account. In particular, the parameter a, controlling the shape of the p_T distribution for non-leading particle production, has been assumed to be the same for

protons and anti-protons.

The data yields of K^0_S and K^0_L exiting the target can be estimated from hadron production measurements as follows. The yields of neutral kaons can be related to the production rate of charged kaons using the Gatignon - Wachsmuth formula, derived assuming isospin symmetry in a $p+p$ collision [121]:

$$N_{K^0_L} = N_{K^0_S} = \frac{N_{K^+} + 3N_{K^-}}{4} \tag{4.19}$$

The relation between neutral and charged kaons yields is derived using a model based on the parton structure (valence and sea quarks) of different kaons and initial hadrons and assuming the conservation of isospin symmetry [126]. The neutral kaons yields for proton–proton, neutron–neutron and proton-neutron collisions are given by:

$$N_{K^0_L} = N_{K^0_S} = \frac{1}{4}(N_{K^+} + 3N_{K^-}) \qquad p+p \text{ collision} \tag{4.20}$$

$$N_{K^0_L} = N_{K^0_S} = N_{K^+} \qquad n+n \text{ collision} \tag{4.21}$$

$$N_{K^0_L} = N_{K^0_S} = \frac{1}{2}(N_{K^+} + N_{K^-}) \qquad p+n \text{ collision} \tag{4.22}$$

Since in the case of NP06/ENUBET the SPS proton beam impinges on a graphite target we have a *proton-carbon collision*. Therefore, the formula of Eq. (4.19) should be adapted for p-C collision. Considering the collision between a proton and a carbon target[5], the incoming proton is equally likely to interact with a proton as it is with a neutron [127]. Therefore Eqs. (4.20) and (4.22) can be averaged. The yields of neutral kaons for a proton-carbon collision is thus given by:

$$N_{K^0_L} = N_{K^0_S} = \frac{3N_{K^+} + 5N_{K^-}}{8} \qquad p+\text{C collision} \tag{4.23}$$

4.2.3 Scaling to targets of different materials

Despite beryllium targets have been used to measure particle yields and to parameterize inclusive cross-sections, in practice, the NP06/ENUBET experiment will consider graphite as a more promising candidate material for the realization of the target. Anyway, inclusive invariant cross-sections can be rescaled to different target materials as described in the following.
The invariant cross-sections $E\frac{d^3\sigma^{hA}}{dp^3}$ for hadron-nucleus interactions ($hA \to h'X$) depend on the mass number A of the target nucleus via parameterizations of the type [121]:

$$E\frac{d^3\sigma^{hA_1}}{dp^3} = \left(\frac{A_1}{A_2}\right)^{\alpha} \cdot E\frac{d^3\sigma^{hA_2}}{dp^3} \tag{4.24}$$

In particular, α has been found to be weakly dependent on the incident beam momentum. Furthermore, it depends on the incident hadron type h and it is a smooth function of p_T and x_F of the produced hadron. Considering the Feynman longitudinal variable $x_F = 2p^*_L/\sqrt{s}$, where p^*_L and $\sqrt{s}$ are the longitudinal momentum of the detected particle and the total energy in the centre-of-momentum frame, it is possible to obtain a suitable representation of the whole set of data with the the following parameterization of α as a function of x_F [121]:

$$\alpha(x_F) = (0.74 - 0.55x_F + 0.26x_F^2) \cdot (0.98 + 0.21p_T^2) \tag{4.25}$$

[5]One can assume that the carbon target is entirely ^{12}C.

4.2.4 Yields from finite length targets

With reference to Eq. (4.8), the differential particle production along the target can be parameterized as [121]:

$$\frac{dY(E,p_T,z)}{dz} = \frac{N_0\rho\lambda_p}{A}\frac{p^3}{E}\left(E\times\frac{d^3\sigma}{dp^3}\right)f(z) \tag{4.26}$$

where $f(z)dz$ is the probability that the outgoing particle is produced at a depth from z to $z+dz$ inside the target. The naive reabsorption model used in Eqs. (4.12) and (4.13) is only adequate to give a first order description of particle production from relatively thin targets or at large x, nonetheless, particles produced in cascade processes cannot be neglected. In the collinear approximation and assuming that leading (i.e. fast forward-going) particles in p-A interactions are mostly protons - thus characterized by an effective mean free path equal to that of primary protons λ_p - the naive reabsorption model of (4.13) can be improved by the following expansion [121]:

$$f(z) = \frac{1}{\lambda_p}e^{-z/\lambda_p}\left[1+A_h(x)\frac{z}{\lambda_p}\right]e^{-z'(z,\theta)/\lambda_s} \tag{4.27}$$

where the second term in brackets accounts for tertiary particle production, namely particle production by reinteractions of secondary particles. In Eq. (4.27), the term $A_h(x)$ weights the probability that reinteractions of secondary particles will result in a produced hadron h of fractional longitudinal momentum x. In the short target approximation - valid until the target length satisfy the condition $L \ll \lambda_p\lambda_s/(\lambda_s-\lambda_p)$ - when integrating Eq. (4.27) in the forward direction (i.e. $z' = L - z$) the target efficiency turns out to be given by [121]:

$$F(L) = \int_0^L f(z)dz = \frac{L}{\lambda_p}e^{-L/\lambda_s}\left[1+A_h(x)\frac{L}{2\lambda_p}\right] \tag{4.28}$$

Furthermore, under the above-mentioned assumptions, it is possible to predict the fraction $t(L)$ of tertiary particle production to be approximately a linear function of the target length L given by:

$$t(L) \simeq A_h(x)\frac{L}{2\lambda_p} \tag{4.29}$$

A possible parameterization of $A_h(x)$ as function of the fractional longitudinal momentum $x_{\rm Lab} = p_{\rm Lab}/p_{\rm inc}$ has been proposed [121]:

$$A_h(x_{\rm Lab}) = A_h^{\rm ter}(1-x_{\rm Lab})^{b_h^{\rm ter}} \tag{4.30}$$

choosing a common value of $A_h^{\rm ter}$ and $b_h^{\rm ter}$ for positive and negative particles.

4.3 Reweighting simulated events on hadron production data

The *hadroproduction uncertainty* is the largest source of systematic uncertainty on the neutrino flux, due to a limited knowledge of the *secondary particle production yields* at target, as discussed in Sec. 1.13.2. The yields of secondary hadrons produced at target are generally used by many neutrino experiments to extrapolate and determine the flux of neutrinos. Indeed, hadron production directly affect the normalization of the number of secondary mesons produced at target, implicating large systematic uncertainties

both in the number of charged leptons measured in the instrumented decay tunnel and neutrinos reaching the detector. Therefore, correcting the Monte Carlo simulation of the facility with measured hadron production yields is mandatory. The hadron production data measured by NA20 [123] and NA56/SPY [122] are extrapolated to the case of 400 GeV/c primary protons impinging onto a cylindrical graphite target (70 cm length, 3 cm radius). The full `GEANT4` simulation of the facility provides all the necessary information for reweighting the kinematic distributions of both charged leptons measured in the tunnel walls and neutrinos reaching the detector. Indeed, the events producing a detectable signal in the calorimeter and/or neutrinos reaching the detector can be directly linked to the corresponding parent hadrons produced at target level. The MC simulation can thus be reweighted on hadron production data, providing reweighted templates for the charged lepton observables and neutrino flux at detector. However, when reweighting such kinematic distributions, the uncertainties on the data must be propagated as well. The propagation of systematic uncertainties affecting the hadroproduction parameters, i.e. the parameters on which depends the hadroproduction model under investigation, can be accomplished by means of the multi-universe method described in Sec. 4.4.

4.3.1 Reweighting positron events

The *hadroproduction weights* (data/MC hadron yields ratios) are used to reweight reconstructed charged lepton observables and to compute the corresponding covariance matrices. The *hadroproduction weights maps* in the *target phase-space* (p, θ), i.e. the phase space defined by the momentum p and emission angle θ of secondary particles produced at target, can be computed from the data/MC yields ratio:

$$w(p,\theta) = \frac{Y_{\text{data}}(p,\theta)}{Y_{\text{MC}}(p,\theta)} \tag{4.31}$$

where Y_{data} is the particle yield on data computed with the cross-section parameterization in [121], and Y_{MC} stands for the particle yield predicted by `FLUKA` simulation[6]. In the final design of the ENUBET beamline [76] a 5 cm thick tungsten foil was placed just after the target to filter out excess positrons produced by proton interactions with graphite. Two `FLUKA` simulations of the proton beam interactions with the target have been produced: one where the target is the graphite rod (`FLUKA` C-only) and another one where the target consists of the graphite rod and the tungsten foil (`FLUKA` C + W_{foil}). In [76] the `FLUKA` C-only was used as input file for the transfer line simulation (`G4TL` simulation), where the tungsten foil was implemented in the `G4TL` simulation itself. However, if the fact that the tungsten foil acts as a second target is not taken into account in the reweight process, this causes issues when constraining the neutrino flux. For this reason the tungsten foil was moved to the `FLUKA` simulation and the output of the `FLUKA` C+W_{foil} is then used as input of the `G4TL` simulation. Since the available hadron production data are computed for a graphite target, then the data/MC ratio used to reweight the observables and neutrino flux needs to be corrected as follows:

$$w = \frac{Y^{\text{C+W}_{\text{foil}}}_{\text{data, corr}}}{Y^{\text{C+W}_{\text{foil}}}_{\text{MC}}} \tag{4.32}$$

where the correction to the yields in the data due to the tungsten foil is computed as follows:

$$Y^{\text{C+W}_{\text{foil}}}_{\text{data, corr}} = Y^{\text{C}}_{\text{data}} + \Delta Y_{\text{MC}} = Y^{\text{C}}_{\text{data}} + (Y^{\text{C+W}_{\text{foil}}}_{\text{MC}} - Y^{\text{C}}_{\text{MC}}) \tag{4.33}$$

[6]The interactions of primary protons onto a graphite target are simulated with `FLUKA`, and its output is used to determine the hadron yields to reweight the MC simulation.

Therefore, the yields from graphite data ($Y^{\mathrm{C}}_{\mathrm{data}}$) are corrected with the difference of yields computed from FLUKA $\mathrm{C} + \mathrm{W}_{\mathrm{foil}}$ and FLUKA C-only (ΔY_{MC}), relying on the MC to account for the difference in yields due to the tungsten foil. This means that the yields for both FLUKA productions are needed for computing the weights used to reweight simulated events.

The target phase space (p, θ) under consideration corresponds to the region covered by NA20 and NA56/SPY data points, thus defined by $(p, \theta) \in [0, 350\mathrm{GeV}] \times [0, 45\mathrm{mrad}]$. The yields computed on data for kaons, pions and protons in such target phase space are shown in Fig. 4.5, together with the phase space coverage by NA20 and NA56/SPY data points, displayed with black triangles and red stars, respectively. In particular, an angular acceptance cut ($\Omega < 110\,\mathrm{msr}$) has been applied, corresponding to the aperture of the first quadrupole.

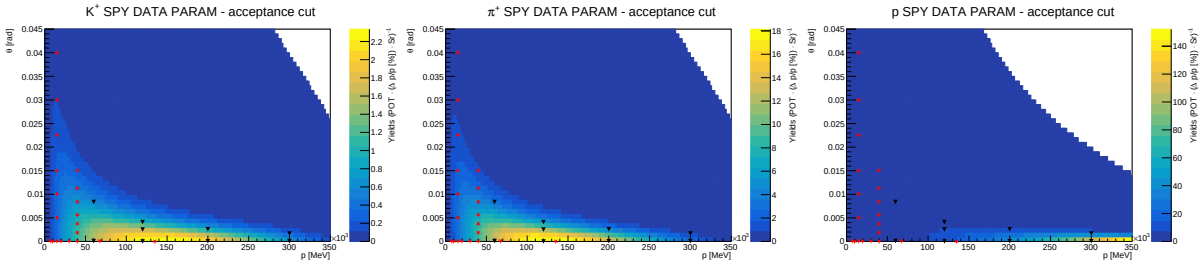

Figure 4.5: Yields computed on data in the target phase-space for kaons (left), pions (center) and protons (right). The target phase space coverage by NA20 and NA56/SPY data points is displayed with black triangles and red stars, respectively. An angular acceptance cut $\Omega < 110\,\mathrm{msr}$ has been applied.

The NA20 and NA56/SPY hadron production measurements have been fitted in order to get the nominal values of hadroproduction parameters and their covariance matrix, with the aim to implement the multi-universes method. The fit describes the data with a good accuracy, with a reduced $\chi^2 \sim 1$. Highly correlated parameters have been fixed and an extra systematic error of 10% on the normalization parameter of the cross section (A in Eqs. (4.14), (4.17), (4.18)) has been assumed, corresponding to the typical $\mathcal{O}(10\%)$ pre-fit error on the neutrino flux normalization. The nominal hadroproduction parameters obtained fitting the parameterized inclusive invariant cross-section on NA20 and NA56/SPY data are used to compute the *nominal hadroproduction weight maps*, which can be used to reweight the kinematic distributions. The nominal hadroproduction weight maps for kaons, pions and protons are shown in Fig. 4.6, respectively[7].
For kaons and pions, in the phase-space probed by experimental data, values for the data/MC ratio around 1 are observed, typically within 20-30%. These are usual discrepancies observed in hadroproduction data/MC comparisons. Outside the region probed by experiments, the data/MC ratio significantly deviates from one, as can be expected. Instead hadroproduction weights computed for protons show values much less than the unity. This could be due to the fact that the data yields for protons do not include the corrections for tertiary production. In order to recover this discrepancy the tertiary particle production has been evaluated from data and taken into account also for protons, other than kaons and pions. Therefore, the fraction of tertiaries have been determined

[7]The yields correction due to the tungsten foil causes halos in regions of the weight maps where the MC statistics is low, as can be noticed in particular for the case of protons. However, the hadron production weights corresponding to these regions of the target phase space are expected to have a negligible impact for the ENUBET case, since most of the target particles producing reconstructed events are expected to populate a target phase space within a 10% momentum bite around the central momentum $p = 8.5\,\mathrm{GeV/c}$ and within the tagger angular acceptance (see Sec. 4.6.1).

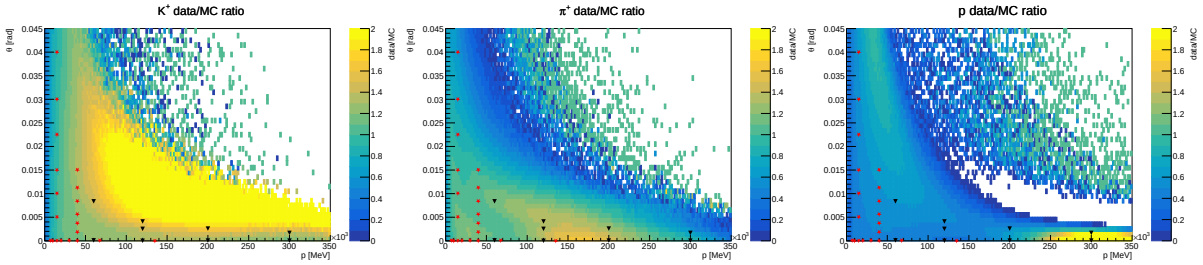

Figure 4.6: Nominal hadroproduction weight maps for kaons (left), pions (center) and protons (right) in the target phase space.

from yields measured by NA20 and NA56/SPY and then fitted in order to estimate the parameters of the $A_h(x)$ term in Eq. (4.30), i.e. the probability that reinteractions of secondaries will result in a produced hadron h. In such a way the target efficiency has been corrected for tertiary particle production, as accounted for in Eq. (4.28). In Fig. 4.7 are shown the fitted tertiary fractions for kaons, pions and protons, respectively.

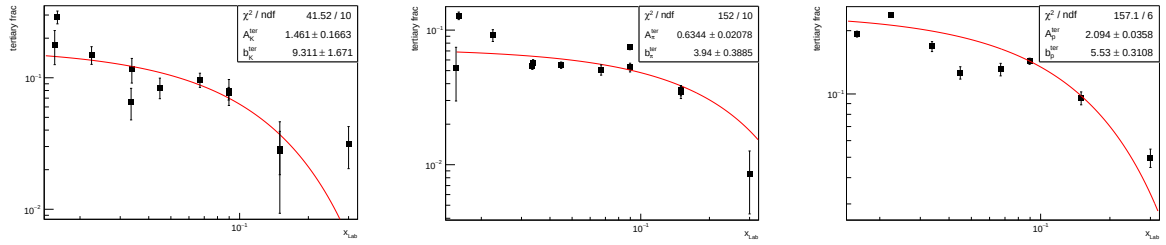

Figure 4.7: Fit of the tertiary fractions for kaons (left), pions (center) and protons (right) as a function of the fractional longitudinal momentum $x_{\mathrm{Lab}} = p_{\mathrm{Lab}}/p_{\mathrm{inc}}$.

Nonetheless, even after accounting for the production of tertiaries, the hadroproduction weights for protons remain much smaller than the unity and it should be cautious to investigate further. Anyway, when reweighting positron observables the contribution coming from protons is negligible.

4.4 Error bands from the many universes method

The *multi-universes method* [128–130] consists in varying model parameters with a known covariance matrix in order to produce an error band representing the effect of model uncertainties on any distribution influenced by the model. The kinematic distributions of positrons and the neutrino flux are both influenced by the number of secondary particles produced at target, which in principle could be predicted a priori from an accurate knowledge of hadron production yields and inclusive cross-section. However, the model employed for cross-sections has uncertain parameters which are correlated. The multi-universes method can be applied to vary the hadroproduction parameters according to their covariance matrix, namely simulating many realizations of the possible values that the hadroproduction parameters can assume (i.e. many universes). Therefore, new *varied hadroproduction weight maps* are obtained and used to reweight the Monte Carlo predictions. In such a way, for each generated universe varied kinematic distributions are obtained (this is the reason why this numerical method is dubbed multi-universes).

4.4.1 Computation of the error band

Using the multi-universes technique the error band and covariance matrix can be computed as follows [128]:

1. Many universes are randomly generated, each with different values for the model parameters. In particular, N different realizations of the hadroproduction model are produced, i.e. randomly generating several different values that the correlated hadroproduction parameters can assume. For the sake of notational simplicity, one can consider the vector $\vec{v}$ of the hadroproduction parameters, denoting as $\vec{v}_0$ the vector of nominal parameters. If hadroproduction parameters were uncorrelated with uncertainties, in that case, a random set of parameters $\vec{v}$ could be computed from the nominal parameters vector $\vec{v}_0$ simply as:

$$\vec{v} = \vec{v}_0 + \Sigma \cdot \vec{r} \tag{4.34}$$

   where Σ is the covariance matrix and $\vec{r}$ is a vector of random numbers distributed according to a gaussian p.d.f. with unit variance and centered at zero. Indeed, if parameters were uncorrelated, Σ would be a diagonal matrix with uncertainties σ along the diagonal. In the case in which the hadroproduction parameters are correlated, as it is in our case, the appropriate equation is given by:

$$\vec{v} = \vec{v}_0 + L \cdot \vec{r} \tag{4.35}$$

   where L is the *Cholesky decomposition* of the covariance matrix Σ[8]. There is a quite general way to construct a vector deviate $\vec{x}$ with a specified covariance Σ and mean $\vec{\mu}$, starting from a vector $\vec{y}$ of independent random deviates of zero mean and unit variance [131]. To this scope, the Cholesky decomposition is used in order to factorize Σ into a left triangular matrix L times its transpose, namely[9]:

$$\Sigma = L \cdot L^T \tag{4.36}$$

   Therefore, whenever one wants to generate a new deviate $\vec{x}$ it is sufficient to fill $\vec{y}$ with independent deviates of unit variance and then construct:

$$\vec{x} = L \cdot \vec{y} + \vec{\mu} \tag{4.37}$$

   As a matter of fact, the so constructed deviate $\vec{x}$ will be distributed according to a multivariate normal gaussian p.d.f. with mean $\vec{\mu}$ and covariance Σ, namely:

$$G(\vec{x} \,|\, \vec{\mu}, \Sigma) = \frac{1}{(2\pi)^{n/2}|\Sigma|^{1/2}} \exp\left(-\frac{1}{2}(\vec{x}-\vec{\mu})^T \Sigma^{-1} (\vec{x}-\vec{\mu})\right)$$

2. For each generated universe u, the *varied hadroproduction weights* in the target phase-space (p, θ) can be computed as:

$$w_u(p,\theta) = \frac{Y^u_{\text{data}}(p,\theta)}{Y_{\text{MC}}(p,\theta)} \tag{4.38}$$

   where Y^u_{data} is the yields on data for the generated universe u, namely for a given realization of the hadroproduction parameters. For each simulated event, the kinematic

[8] Note that the covariance matrix is symmetrical and positive-definite.

[9] This decomposition is always possible because Σ is positive-definite, and one need do it only once for each distinct Σ of interest.

variable of interest (the positron visible energy or impact point along the calorimeter, the neutrino energy distribution etc.) obtained from the simulation can be reweighted with the varied hadroproduction weights in Eq. (4.38), thus realizing N varied histograms for the kinematic variable of interest, namely one histogram for each generated universe u.

3. Finally, the systematic uncertainty for the histogram of the kinematic variable of interest ν must be computed. The bin-by-bin error can be easily computed from the standard deviation. In fact, the error band in bin j is given by:

$$\sigma_j = \sqrt{\frac{1}{N}\sum_{u=1}^{N}(\nu_j - n_{uj})^2} \tag{4.39}$$

where N is the number of universes, ν_j is the nominal bin content of bin j, and n_{uj} is the content of bin j in histogram corresponding to universe u. The covariance can also be computed:

$$\mathrm{cov}(j,k) = \frac{1}{N}\sum_{u=1}^{N}(\nu_j - n_{uj})(\nu_k - n_{uk}) \tag{4.40}$$

where j, k label the bins. The correlation matrix can be easily derived computing $\mathrm{corr}(j,k) = \mathrm{cov}(j,k)/\sigma_j\sigma_k$.

4.5 Exploiting positron monitoring for hadroproduction systematic assessment

In this section are discussed the basic tools used to perform the positron monitoring and exploited to assess the dominant hadron production systematic uncertainty. These tools consist of the positron observables templates, the fit model and likelihood, synthetic datasets generation and fitting algorithms. The fit performance as a function of increasing protons-on-target statistics is also discussed.

4.5.1 Positron observables templates

Templates from the observables measured in the calorimeter are built and used in the analysis for the assessment of systematic effects. These are obtained from the MC simulation output of the facility. The positron analysis presented hereafter refers to the most recent transfer line [76] based on a `FLUKA` simulation with the 5 cm thick tungsten foil integrated as target ($\mathrm{C} + \mathrm{W_{foil}}$ production). The MC statistics corresponds to 1 GPOT, namely to a total of 10^9 protons-on-target in the `FLUKA` simulation. However, the low number of events in the 2-dim observables distributions obtained with 1 GPOT, used for events generation and fitting, limits the systematics analysis for K_{e3} positrons, and therefore is essential to increase the available MC statistics. In principle, the MC statistics could be increased using a brute force method, namely producing more target files with `FLUKA` and then running `G4TL` and `G4TAG` simulations. This approach has the advantage that all the particles are fully simulated, although this comes at the expense of storage disk space needed and longer production time. Therefore, in order to artificially enhance the available MC statistics an alternative method is used, based on the sampling of the phase space of particles at both the target exit and the tunnel entrance. Using such an approach, the correlation among variables at tunnel entrance (y, z, p_x, p_y, p_z, t)

and variables at target exit (p_x, p_y, p_z) needs to be taken into account, resulting in a multi-dimensional problem due to the high dimension of the phase-space (9-dim). To this aim, the universal algorithms contained in the `UNU.RAN C` library [132] can be used to generate random numbers from large classes of continuous or discrete distributions. In particular, the VEMPK[10] method [133] is exploited to sample a multi-dimensional empirical distribution, i.e. a distribution defined only by its dimensions and points. The sampling method is effective in reproducing the original MC data, as summarized by the distributions of the original and sampled momentum of particles at tunnel entrance shown in Fig. 4.8, respectively. An extensive validation study, performed comparing the sampled and original distributions for a large number of variables, allowed to demonstrate the reliability of the sampling method. The sampling of the phase space of particles at the tunnel entrance is thus used to artificially enhance the MC statistic, obtaining a 100 GPOT production.

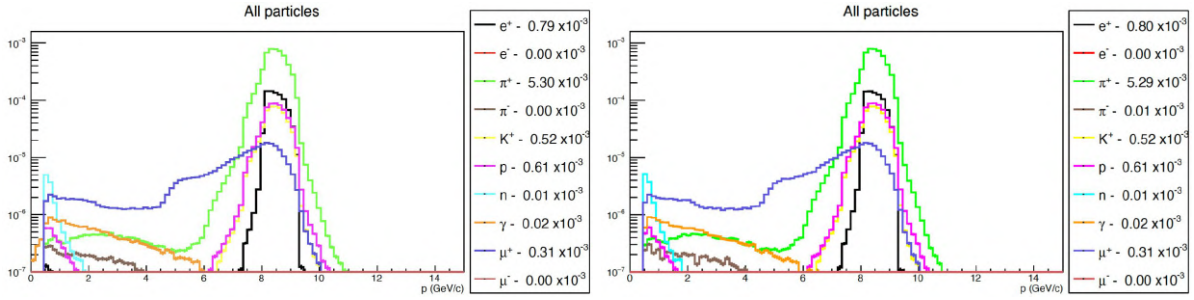

Figure 4.8: Original (left) and sampled (right) momentum distribution of particles at tunnel entrance.

4.5.2 Building the templates

The observables templates are computed from reconstructed events identified as positrons. The reconstructed positrons from K_{e3} decay (signal) are discriminated from the misidentified ones (background) by means of the NN classifier cut. The positron observables are the visible energy and the impact point along the tunnel axis, and the 2-dim distribution of these two variables defines the *positron observables templates*. These templates are computed for both signal and background events. The observables templates obtained from bare MC prediction are shown in Fig. 4.9 for signal and background, respectively.
The actual observables templates used to assess systematic effects are computed from simulated events reweighted on hadroproduction data. The multi-universes method is used to reweight the observables templates varying the hadroproduction parameters, thus obtaining an ensemble of $N = 1000$ different realizations of the observables templates. The *mean observables templates* are computed as the mean of the ensemble of N templates and are shown in Fig. 4.10 for signal and background, respectively. The global effect of the hadroproduction reweighting is to lower the MC prediction for observables.
Due to the enhancement of MC statistics obtained sampling the phase space of particles at tunnel entrance, observables templates with a fine binning can be defined to enhance potential differences in shape between signal and background, differences to which the fit model described in Sec. 4.5.3 might be sensitive. In Figs. 4.11 and 4.12 are shown 3-dim representations of mean observables templates using a front and back view respectively, pointing out shape differences between signal and background templates.

[10](Vector) EMPirical distribution with Kernel smoothing.

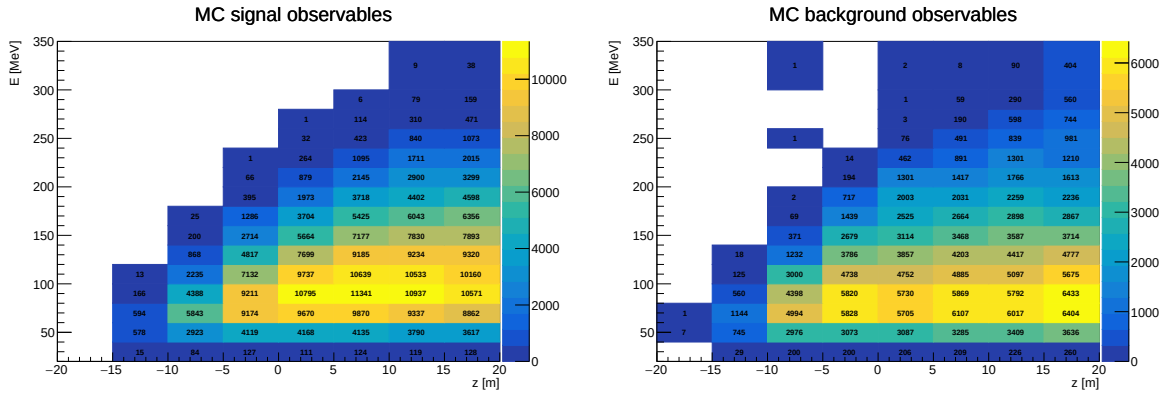

Figure 4.9: MC observables templates for signal (left) and background (right) events.

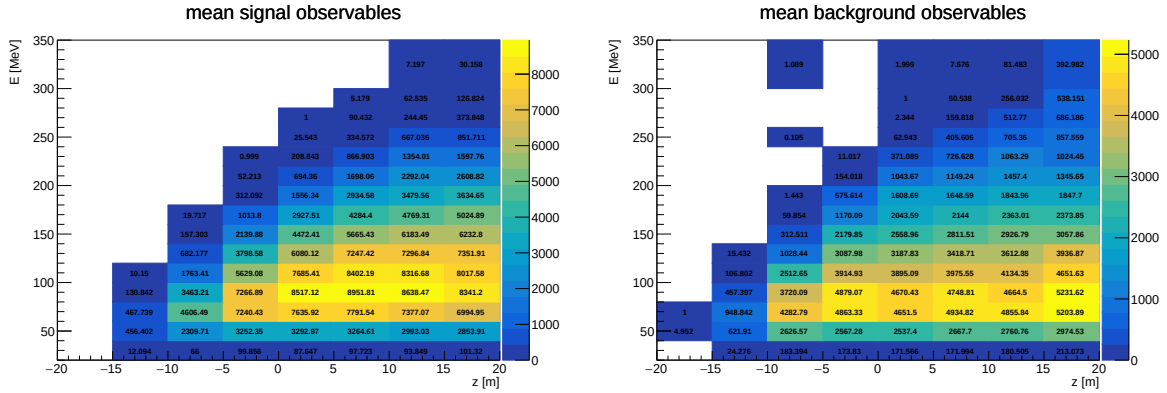

Figure 4.10: Mean observables templates for signal (left) and background (right) events.

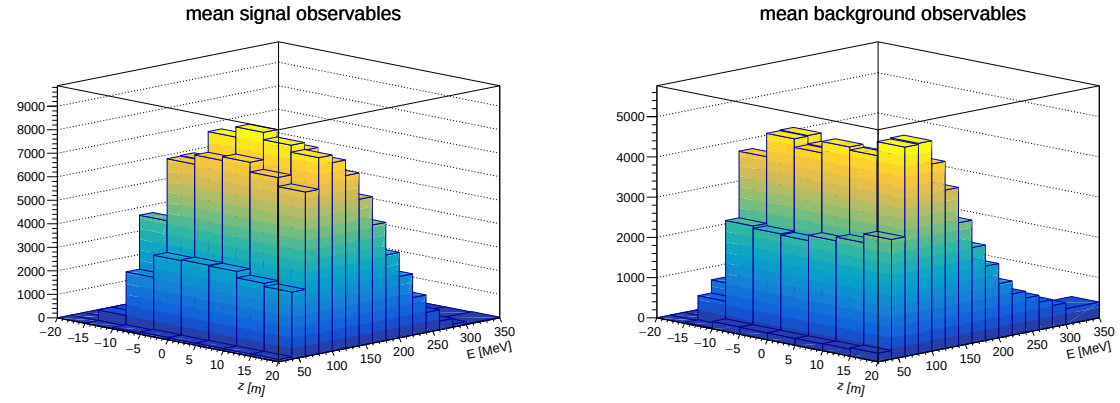

Figure 4.11: Mean observables templates for signal (left) and background (right) events, front view.

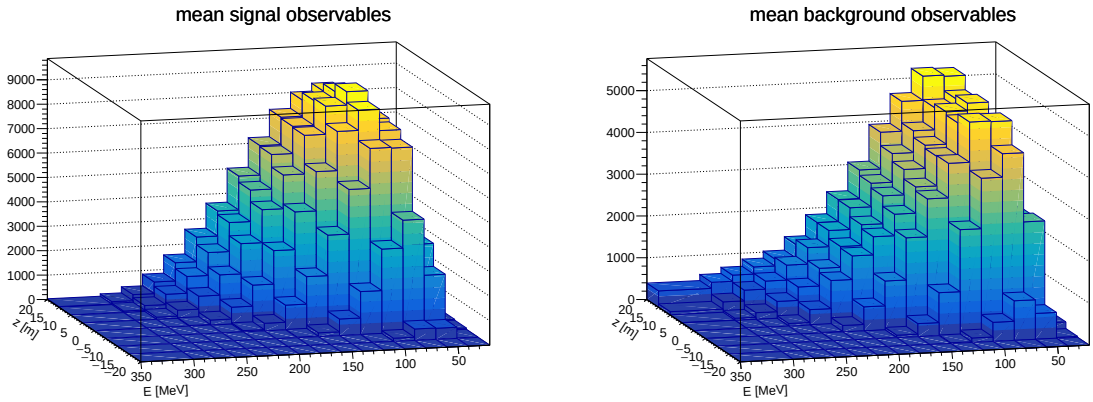

Figure 4.12: Mean observables templates for signal (left) and background (right) events, back view.

The covariance and correlation matrices for signal and background observables templates are computed by means of the multi-universes method. The covariance and correlation matrices obtained for signal observables templates are shown in Fig. 4.13; the same matrices are shown for background in Fig. 4.14 respectively. It can be noticed that a high correlation is observed for all bins of observables templates, both for signal and background events.

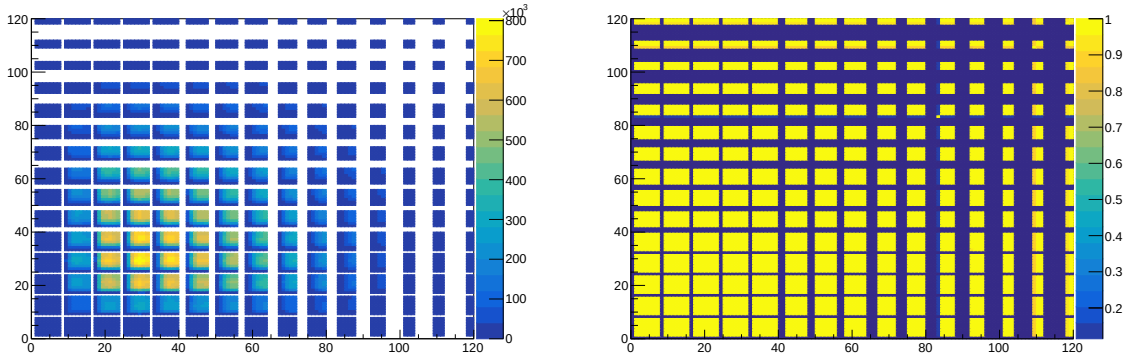

Figure 4.13: Covariance (left) and correlation (right) matrices for signal observables templates.

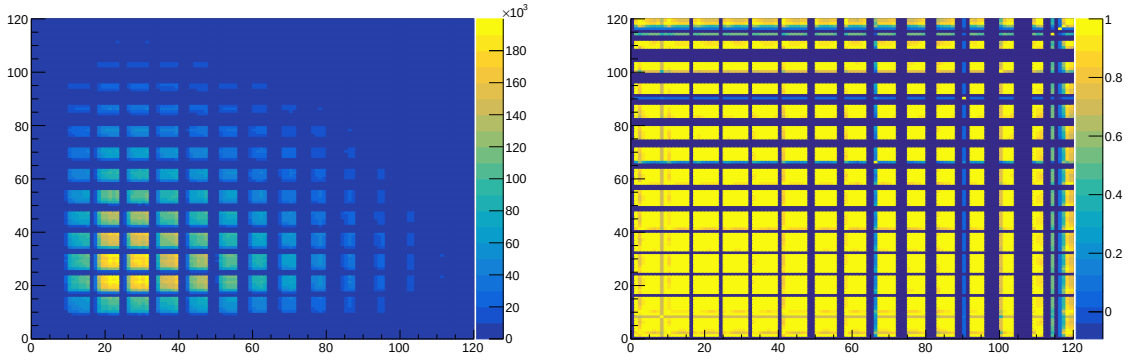

Figure 4.14: Covariance (left) and correlation (right) matrices for background observables templates.

4.5.3 The fit model

The *fit model* is defined to predict the expected number of events in each bin of the 2-dim distribution of the positron observables. For each bin i of observables templates, one parameter α_i for signal and one parameter β_i for background are defined. The total number of fit parameters is thus twice the number of bins. The set of α and β parameters are the *parameters of interest*, since they are introduced to parameterize hadroproduction uncertainties affecting both the normalization and shape of signal and background templates. For clarity's sake, these parameters are gathered in a single vector $\vec{p}$ defined as:

$$\vec{p} = (\vec{\alpha}, \vec{\beta}) \tag{4.41}$$

The number of events predicted by the model in each bin i is given by:

$$N_i^{\mathrm{p}}(\vec{p}) = (1 + \alpha_i)T_{S_i} + (1 + \beta_i)T_{B_i} \tag{4.42}$$

where T_S and T_B are the signal and background observables templates, respectively. The $N_i(\vec{p})$ prediction is a function of the set of α and β fit parameters. By varying the α and β fit parameters for each bin, the predicted bin occupancies can be fit to the observed bin contents in pseudo-data. These parameters are constrained in the likelihood by the corresponding covariance matrix V induced by hadron production uncertainties from data. The templates T_S and T_B used in the fit model are computed from the mean of many distributions as discussed in Sec. 4.5.2. This implementation of the fit model is dubbed *full parameters*.

4.5.4 Binned extended maximum likelihood

The set of $\vec{\alpha}$ and $\vec{\beta}$ parameters of interest are determined using a *binned extended maximum likelihood fit*. The likelihood is constructed assuming n independent bins, each with a Poisson probability of observing N_i events given the expected number of events N_i^{p} in a certain bin i. The systematic uncertainties can be included in the likelihood using a Bayesian approach, namely assuming a prior probability density function (p.d.f.) for the parameter sets [134]. The binned likelihood is thus given by:

$$\mathcal{L}(\vec{p}) = \pi_{\mathrm{hp}}(\vec{p}) \cdot \prod_i^n P(N_i | N_i^{\mathrm{p}}(\vec{p})) \tag{4.43}$$

which can be written explicitly as follows:

$$\mathcal{L}(\vec{p}) = \pi_{\mathrm{hp}}(\vec{p}) \cdot \prod_i^n \frac{(N_i^{\mathrm{p}}(\vec{p}))^{N_i}}{N_i!} e^{-N_i^{\mathrm{p}}(\vec{p})} \tag{4.44}$$

The π_{hp} is the prior p.d.f. for hadroproduction systematic uncertainties and it is assumed to be a multivariate normal distribution, defined as:

$$\pi_{\mathrm{hp}}(\vec{p}) = \frac{1}{(2\pi)^{\frac{m}{2}} \cdot |V|^{\frac{1}{2}}} \cdot e^{-\frac{1}{2}\Delta\vec{p}V^{-1}\Delta\vec{p}^T} \tag{4.45}$$

where m is the dimension of the parameter vector $\vec{p}$[11], V is a constant covariance matrix whose elements $V_{i,j}$ are defined as the covariance between the i-th and j-th element of

[11] In the full parameters fit implementation case, the dimension m of the parameter vector $\vec{p}$ is simply twice the number of bins, that is $2n$.

the $\vec{p}$ vector and $\Delta\vec{p} = \vec{p} - \vec{p}_0$ is the deviation of the $\vec{p}$ parameters from their nominal values $\vec{p}_0$. The *likelihood ratio* λ is defined as:

$$\lambda(\vec{p}) = \frac{\mathcal{L}(\vec{p})}{\mathcal{L}(\vec{p}_0)} \tag{4.46}$$

The likelihood ratio can thus be explicitly expressed as follows:

$$\lambda(\vec{p}) = \frac{\pi_{\rm hp}(\vec{p}) \cdot \prod_i^n \frac{\left(N_i^{\rm p}(\vec{p})\right)^{N_i}}{N_i!} e^{-N_i^{\rm p}(\vec{p})}}{\pi_{\rm hp}(\vec{p}_0) \cdot \prod_i^n \frac{(N_i)^{N_i}}{N_i!} e^{-N_i}} \tag{4.47}$$

where the denominator is simply the numerator evaluated at $N_i^{\rm p} = N_i$ and with the parameters equal to their nominal values. Substituting in the expression for $\pi_{\rm hp}$ and simplifying, the likelihood ratio can be written as:

$$\lambda(\vec{p}) = e^{-\frac{1}{2}\Delta\vec{p}V^{-1}\Delta\vec{p}^T} \cdot \prod_i^n \left(\frac{N_i^{\rm p}(\vec{p})}{N_i}\right)^{N_i} e^{N_i - N_i^{\rm p}(\vec{p})} \tag{4.48}$$

The benefit of computing the likelihood ratio is that it can be used to convert the likelihood function into a χ^2 statistic. Indeed, the Wilks' theorem states that the negative log-likelihood ratio $-2\ln\lambda$ follows a χ^2 distribution for a sufficiently large dataset [135]. This theorem has important implications since it means that the $-2\ln\lambda$ quantity can be used not only for parameters estimation but also to determine the goodness-of-fit and for confidence level estimation. The negative log-likelihood ratio can thus be computed as:

$$\begin{aligned}\chi^2(\vec{p}_i) = -2\ln\lambda(\vec{p}_i) = 2\sum_i^n \left[N_i^{\rm p}(\vec{p}_i) - N_i + N_i \ln\left(\frac{N_i}{N_i^{\rm p}(\vec{p}_i)}\right)\right] \\ + \sum_{j,k}^m \Delta p_j V_{j,k}^{-1} \Delta p_k\end{aligned} \tag{4.49}$$

and it approaches a χ^2 distribution in the limit where the data sample is very large. The last term in Eq. (4.49) is the *penalty term* on the parameters.

The covariance and correlation matrices due to variations induced by hadroproduction are computed using the many universe technique. The covariance and correlation matrices of *bin contents of signal and background observables templates*, namely bins $= \{n^i_{sgn}, n^j_{bkg}\}_{i,j=1,\dots,n}$, are shown in Fig. 4.15. This is the V covariance matrix used to constrain the $\vec{\alpha}$, $\vec{\beta}$ parameters in the likelihood with the full parameter fitting approach.

4.5.5 Pseudo-datasets generation and fitting

Pseudo-data, reproducing the outcome from the data-taking of the real experiment, are generated from the observables templates computed from MC events reweighted on hadroproduction data. As pointed out in Sec. 4.5.1, the fit performance are in general limited by the available MC statistics. This limitation is more problematic in the positron sample because of the small branching ratio of the K_{e3} decay. Moreover, the NP06/ENUBET experiment will not be limited by statistics since in a single proton beam extraction $4.5 \cdot 10^{13}$ pot are expected; the MC statistics is just a tiny amount if compared

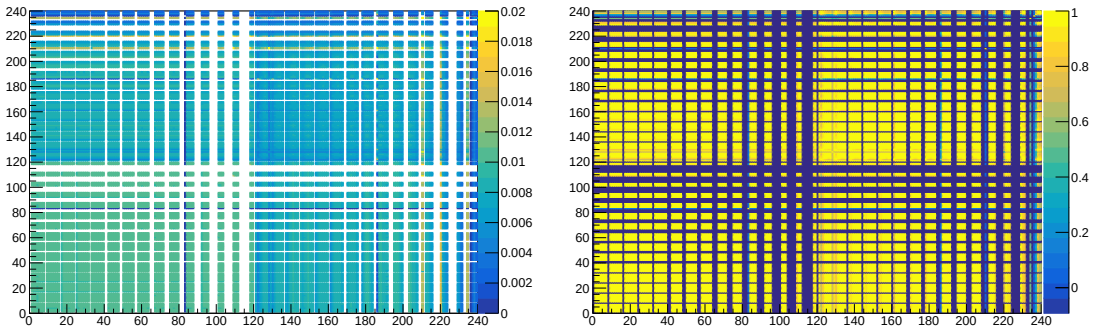

Figure 4.15: Covariance (left) and correlation (right) matrices of bin contents of signal and background observables templates induced by hadroproduction uncertainties.

to it. To counter this limitation, the original 1 GPOT MC statistics of `G4TL` simulation was artificially increased by sampling the phase space of particles both at the target exit and at the tunnel entrance, obtaining a 100 GPOT MC statistic.
Moreover, the pseudo-data statistics can be further artificially increased producing many *pseudo-datasets with statistical fluctuations*. This kind of approach is somehow similar to what a real experiment does in practice: the data-taking is split in N datasets, each with a fixed statistics, which are then combined in the fit.
The operating procedure to generate pseudo-datasets can be outlined as follows:

1. Consider a hadroproduction universe u generated from hadron production variation of the MC (*hp-universe* for short).

2. Sum the signal and background distributions (observables templates for the hp-universe).

3. Obtain a new distribution by varying the bin contents according to a Poissonian p.d.f. with mean $\mu = N_{bin}$ and $\sigma = \sqrt{N_{bin}}$. A dataset with statistical fluctuations corresponding to the MC statistics is thus obtained.

$$(T_S + T_B) + \text{Poisson fluctuations} \;\rightarrow\; \text{dataset}_i$$

4. Repeat point (3) N times to generate a larger statistics (N $\times$ MC-statistics).

$$\text{dataset (N} \times \text{MC-statistics)} = \text{dataset}_1 + \text{dataset}_2 + \ldots + \text{dataset}_\text{N}$$

5. Perform a combined fit of the N datasets.

The negative log-likelihood ratio in Eq. (4.49) can be extended to perform a combined fit on D pseudo datasets as follows:

$$\chi^2(\vec{p}_i) = -2\ln\lambda(\vec{p}_i) = 2\sum_{d}^{D}\sum_{i}^{n}\left[N_i^{\text{p}}(\vec{p}_i) - N_i + N_i\ln\left(\frac{N_i}{N_i^{\text{p}}(\vec{p}_i)}\right)\right] + \sum_{j,k}^{m}\Delta p_j V_{j,k}^{-1}\Delta p_k \tag{4.50}$$

Of course, even enhancing MC statistics there are still regions of the observables templates where bins are poorly populated, due to the very low probability of events falling in that

regions[12] (see Fig. 4.10). As a result fit convergence problems can be encountered because of these bins with limited statistics. In order to prevent such problems, a threshold of 10 events in the content of poorly populated bins is used to fix the corresponding $\vec{\alpha}$ and $\vec{\beta}$ fit parameters. As an example of the fitting procedure outcome, Fig. 4.16 shows the result from fitting 100 pseudo-datasets, corresponding to 10^{13} pot. The projections of positron observables templates on visible energy and z impact point are shown in Fig. 4.16, respectively. The red and blue stacked components correspond to the signal and background components predicted by the fit model, respectively. The 2-dim and 1-dim fit residuals are shown in Fig. 4.17, respectively.

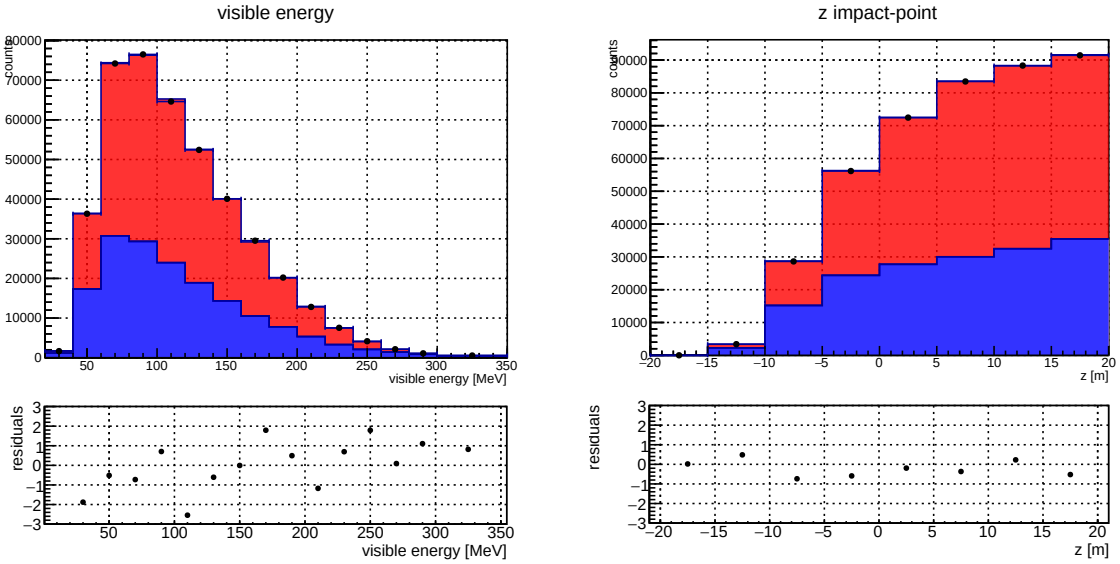

Figure 4.16: Projections of positron observables templates on visible energy (left) and z impact point along the tunnel axis (right) as an outcome of fitting 100 pseudo-datasets. The red and blue stacked components correspond to the signal and background components predicted by the model.

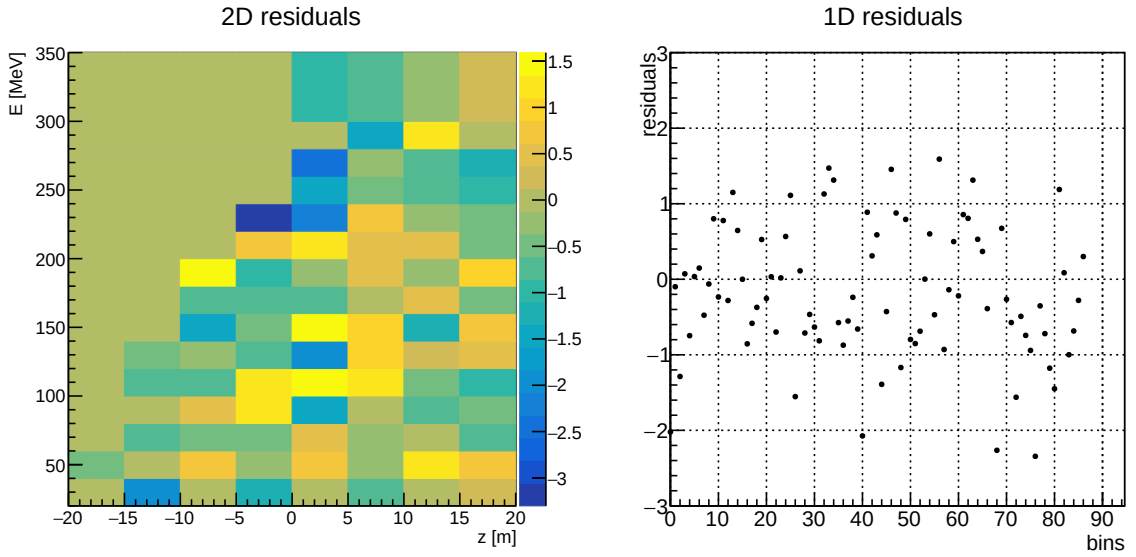

Figure 4.17: 2-dim and 1-dim fit residuals, respectively, as an outcome of fitting 100 pseudo-datasets.

[12]This behaviour is related to the kinematics of the signal and background events, and not to the total available statistics itself.

4.5.6 Fit performance with increasing statistics

In this section the fit performance with increasing protons-on-target (pot) statistics is discussed. Increasing values of pot statistics are simulated by generating many pseudo-datasets, with statistics ranging from 10^{11} to 10^{15} pot. In the following sections, the fit of positron observables will be performed considering a total statistic of $5 \cdot 10^{12}$ pot, i.e. obtained performing a combined fit on 50 datasets. Considering a larger number of datasets, fit convergence problems may arise, due to difficulties of an automated initialization of $\vec{\alpha}, \vec{\beta}$ fit parameters for a large number of bins and many datasets. The χ^2 distributions are obtained fitting pseudo-experiments for multiple pseudo-datasets, according to Eq. (4.50). Fig.4.18 shows the χ^2 distribution obtained fitting pseudo-experiments for the $5 \cdot 10^{12}$ pot statistic of interest.

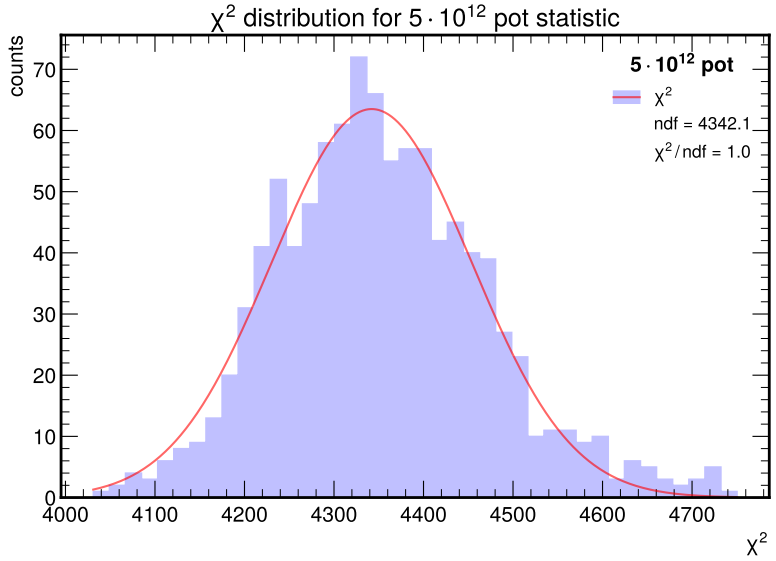

Figure 4.18: χ^2 distribution obtained fitting pseudo-experiments for a total $5 \cdot 10^{12}$ pot statistic.

Possible fit biasses are evaluated from signal and background pulls, defined as follows:

$$\text{pull}_{\text{sgn}} = \frac{N_{\text{sgn}}^{\text{fit}} - N_{\text{sgn}}^{\text{true}}}{N_{\text{sgn}}^{\text{err}}} \tag{4.51}$$

$$\text{pull}_{\text{bkg}} = \frac{N_{\text{bkg}}^{\text{fit}} - N_{\text{bkg}}^{\text{true}}}{N_{\text{bkg}}^{\text{err}}} \tag{4.52}$$

The pull distributions of signal and background fitted events obtained fitting many pseudo-experiments and corresponding to a total statistic of $5 \cdot 10^{12}$ pot are shown in Fig. 4.19, in red for signal and in blue for background fitted events.
The mean, μ_{pull}, and standard deviation, σ_{pull}, of the pulls are evaluated from a gaussian fit to their distributions. The trends of μ_{pull} and σ_{pull} with increasing pot statistic are shown in Figs. 4.20 and 4.21 for signal and background fitted events, respectively.
The trend of the pulls mean suggests that the fit is not biased (or slightly biased) within the uncertainties, while the trend of the pulls standard deviation shows values systematically greater than 1 by about 10%, suggesting an underestimation of the fit error. Nevertheless, being the relative fit error smaller than $\sim 0.1\%$ (see Fig. 4.23) the bias is negligible for practical purposes.

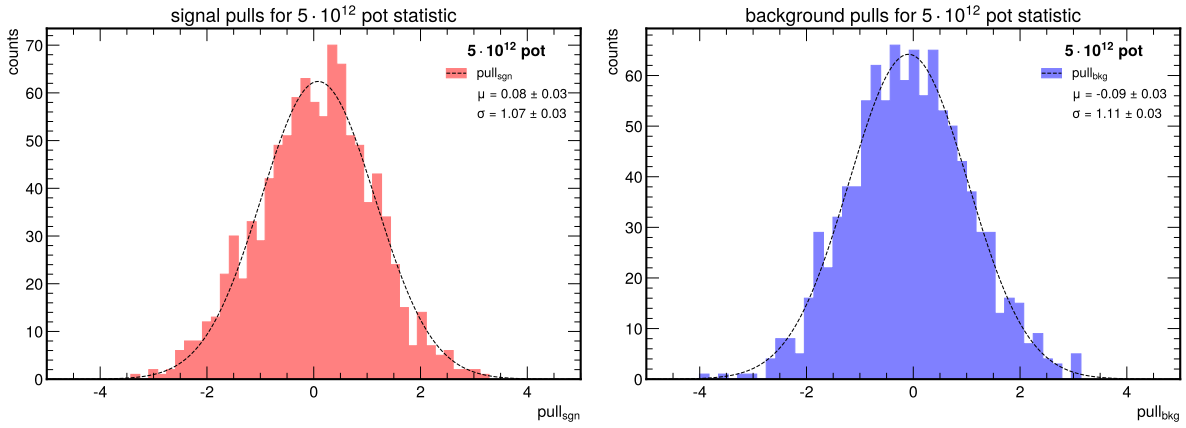

Figure 4.19: Pulls of signal (left) and background (right) fitted events for a total $5 \cdot 10^{12}$ pot statistic.

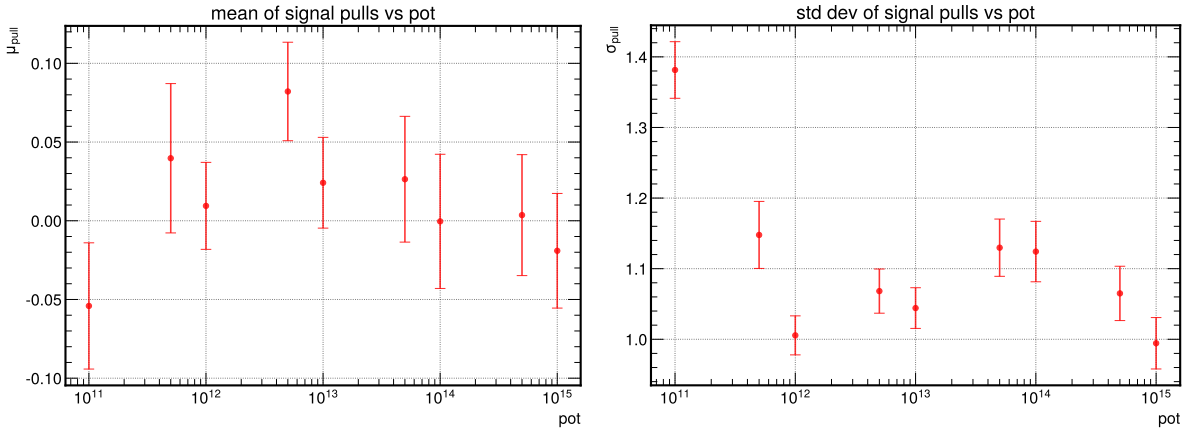

Figure 4.20: Trend of mean (left) and standard deviation (right) of signal pulls with increasing pot statistic.

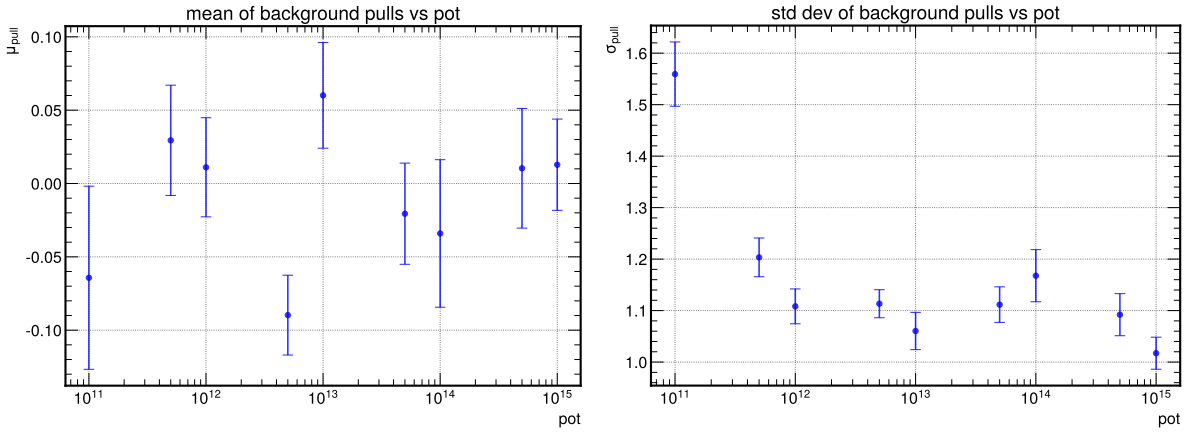

Figure 4.21: Trend of mean (left) and standard deviation (right) of background pulls with increasing pot statistic.

The *relative fit error* of signal and background fitted events can be estimated from the standard deviation of the the following distributions:

$$\frac{\delta N^{\text{fit}}_{\text{sgn}}}{N^{\text{fit}}_{\text{sgn}}} = \frac{N^{\text{fit}}_{\text{sgn}} - N^{\text{gen}}_{\text{sgn}}}{N^{\text{gen}}_{\text{sgn}}} \tag{4.53}$$

$$\frac{\delta N^{\text{fit}}_{\text{bkg}}}{N^{\text{fit}}_{\text{bkg}}} = \frac{N^{\text{fit}}_{\text{bkg}} - N^{\text{gen}}_{\text{bkg}}}{N^{\text{gen}}_{\text{bkg}}} \tag{4.54}$$

Fig. 4.22 shows these distributions as obtained fitting a large sample of pseudo-experiments, each one corresponding to the total statistics of $5 \cdot 10^{12}$ pot. A gaussian fit of these distributions allows to evaluate their standard deviation and mean, where the former is used as estimator of the relative fit error $\delta N^{\text{fit}}/N^{\text{fit}}$ and the product of standard deviation and mean as estimator of the fit error δN^{fit}.

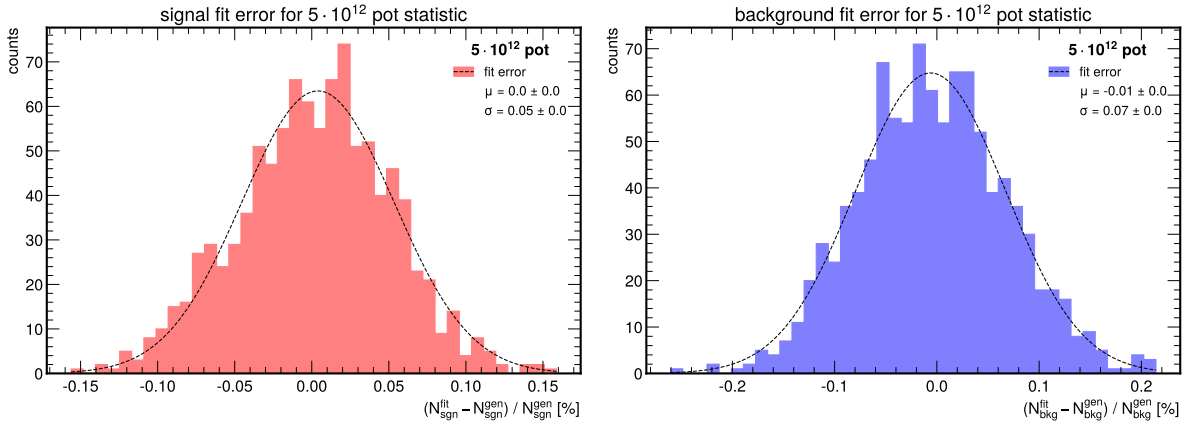

Figure 4.22: Relative fit error distributions for signal (left) and background (right) fitted events for a total $5 \cdot 10^{12}$ pot statistic.

The trend of the *relative fit error* $\delta N^{\text{fit}}/N^{\text{fit}}$ with increasing pot statistic for signal and background fitted events is shown in Fig 4.23, compared to expected relative statistical error. The expected relative statistical error - for a given pot statistic - is $\sim \sqrt{\langle N^{\text{gen}} \rangle}/\langle N^{\text{gen}} \rangle$, where $\langle N^{\text{gen}} \rangle$ is the mean of N^{gen} distribution.

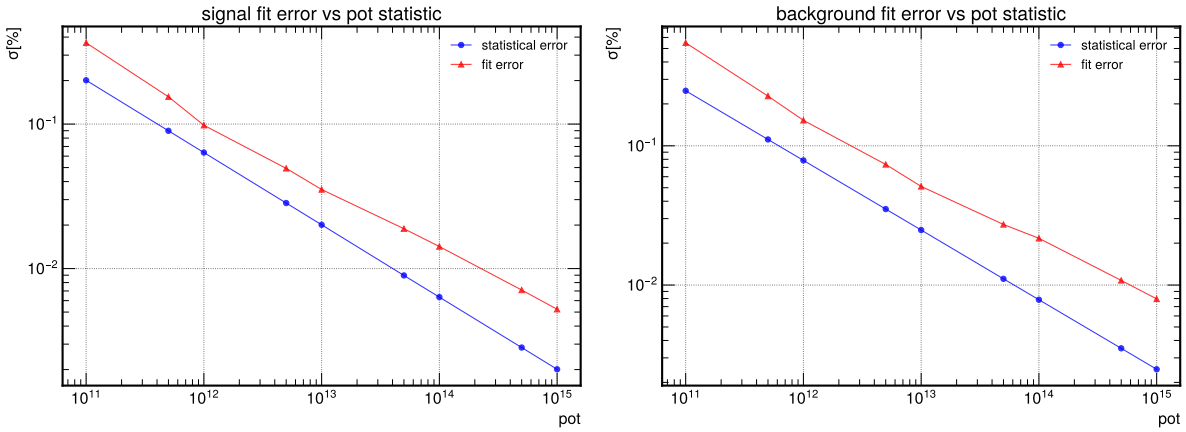

Figure 4.23: Trend of fit relative errors (red) and statistical relative errors (blue) with increasing pot statistic for signal (left) and background (right) fitted events.

The fit relative errors for the chosen total $5 \cdot 10^{12}$ pot statistic is $\lesssim 0.1\%$ for both signal and background fitted events.

4.5.7 Pseudo-experiments fit results

In this section the fit to positron observables for hadron production systematic assessment is discussed. Many pseudo-experiments, with hadroproduction-induced variations, are generated with the technique discussed in Sec. 4.5.5. Each pseudo-experiment consists of a sample of pseudo data split in different datasets. The hadroproduction-induced variations are drawn from a specific universe, which will be referred to as the *fixed hadroproduction universe*. Indeed, of all the hadroproduction universes generated by the multi-universes technique, it is possible to choose one and assume that its hadroproduction parameter values are those that the Nature has chosen as the true ones.
As a matter of fact, the assessment of hadroproduction systematic is independent of the choice of a specific universe, and conventionally one of them is chosen as representative of the true hadroproduction parameter values. The analysis workflow has been tested in this respect by considering different choices for the hadroproduction universe, each one affecting the normalization of the neutrino flux differently. The tests have been performed by choosing the hadroproduction universe to match the mean μ_{I_w} and $\mu_{I_w} \pm \sigma_{I_w}/2$ of the distribution of the weights map integral, I_w, for kaons. In the following, results are presented for the hadroproduction universe fixed to the one corresponding to μ_{I_w}. Fig. 4.24 shows the distributions of fitted signal and background events across 1000 pseudo-experiments, each generated with a total statistics of $5 \cdot 10^{12}$ pot. The corresponding distributions of the relative fit error are reported in Fig. 4.25. A gaussian fit is used to extract the values of means and standard deviations of these distributions. Specifically, the evaluated means of the distributions in Fig. 4.24, namely $N^{\text{fit}}_{\text{sgn}}$ and $N^{\text{fit}}_{\text{bkg}}$, and the evaluated standard deviations of the distributions in Fig. 4.25, namely $\sigma^{\text{fit}}_{\text{sgn}}$ and $\sigma^{\text{fit}}_{\text{bkg}}$, will be used as a prior to set a constraint on the hadroproduction weights, as will be discussed in Sec. 4.6.2.

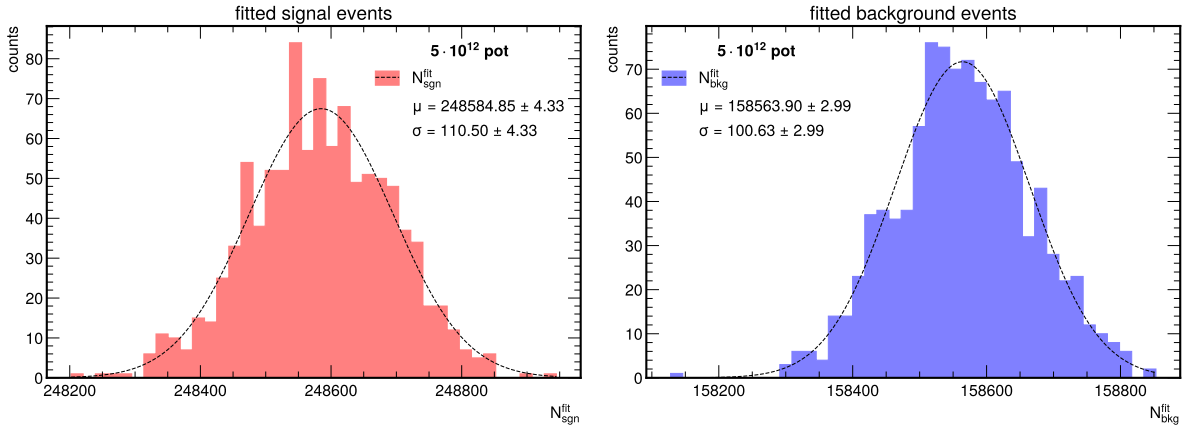

Figure 4.24: Fitted signal (left) and background (right) events distribution across 1000 pseudo-experiments for a total $5 \cdot 10^{12}$ pot statistic. These fitted events distributions are then fitted with a gaussian function to estimate their means, namely $N^{\text{fit}}_{\text{sgn}}$ and $N^{\text{fit}}_{\text{bkg}}$.

4.6 Constraint on hadron production weights

The NP06/ENUBET charged lepton monitoring technique can be exploited to constrain the hadron production systematic uncertainties affecting the neutrino flux at detector.

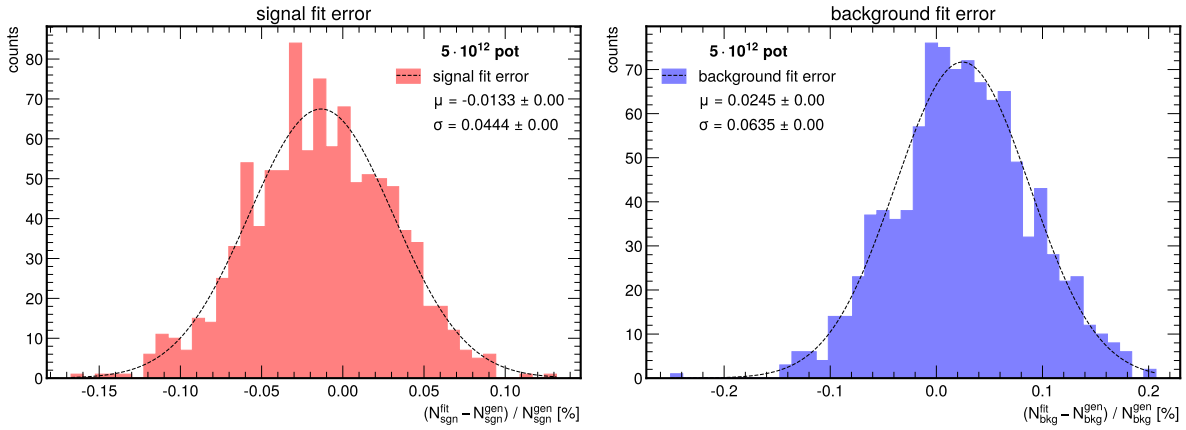

Figure 4.25: Relative fit errors for signal (left) and background (right) events across 1000 pseudo-experiments for a total $5 \cdot 10^{12}$ pot statistic. These fitted events distributions are then fitted with a gaussian function to estimate their standard deviations, namely $\sigma^{\text{fit}}_{\text{sgn}}$ and $\sigma^{\text{fit}}_{\text{bkg}}$.

Indeed, the fit to charged lepton observables measured at the instrumented decay tunnel can be used to constrain the hadroproduction weight maps which will be used to reweight the Monte Carlo simulation, finally achieving a higher precision on the neutrino flux. It is worth to remark that the final constraint we are interested in is the one on the neutrino flux at detector. Other methods could be envisaged and studied to directly link the observables to the neutrino flux at detector, like studying the correlation between observed leptons and neutrino flux. Nonetheless, we think that the chosen solution is cleaner and more robust: we set a constraint directly on the cause of the flux uncertainties. This way, we are also able to pin down the component of the neutrino flux that is not directly taggable (for instance, neutrinos produced by kaon decays happening before the decay tunnel). Another approach would not allow such a potentiality, at least not as much as the one adopted here. In this section, the strategy used to constrain the hadron production weight maps from the fit to the positron observables is discussed in detail.

4.6.1 Correlations between hadroproduction weights and monitored positrons

The strategy used to set the constraint is based on the correlation existing between the number of monitored positrons and some quantity influenced by the uncertainties on the hadron production parameters. Basically, exploiting such a correlation, a constraint on the hadroproduction can be set from the fit to the measured observables. A possibility is to consider the correlation existing among the number of measured positrons and each one of the bins values w_K in the hadroproduction weights maps in Fig. 4.6, by varying the weights based on the uncertainties. The number of signal events N_{sig} and the hadroproduction weights w_K for kaons are expected to be strongly correlated. Indeed, if the weight w_K for K increases (decreases) one expects that the number of kaons produced at target increases (decreases) as well. Furthermore, one should also expect a correlation between the background events N_{bkg} and w_K, although less pronounced than for the signal, since a considerable fraction of the background events actually originates from other K decay modes. Nevertheless, studying the correlation between the number of measured positrons and each w_K weight is excessive and adds little value to the analysis, due to the large number of bins in the hadroproduction weight maps (see Fig. 4.6). A better approach is to study the correlation between the number of events and the integral I_w of the hadroproduction weight map. If the full phase space of the weight map is considered, the sought-after correlation is actually lost. This is explained by the

fact that the full phase space includes many w_K values that do not contribute to the measured signal (see below). However, instead of computing the integral I_w over the full phase-space, one can evaluate it in a tighter region around the beamline *momentum bite*, where the w_K weights directly contribute to the observed positrons. Indeed, the majority of the reconstructed events come from particles which are produced in a narrow region of the target phase-space (p, θ), around the design central momentum, $p = 8.5\,\mathrm{GeV/c}$, and momentum bite, $\Delta p/p = 10\%$, of the beamline. This can be seen in Fig. 4.26, which shows the phase-space of kaons produced at target that give rise to reconstructed K_{e3} signal events at the tagger, superimposed on the nominal hadroproduction weight map for kaons.

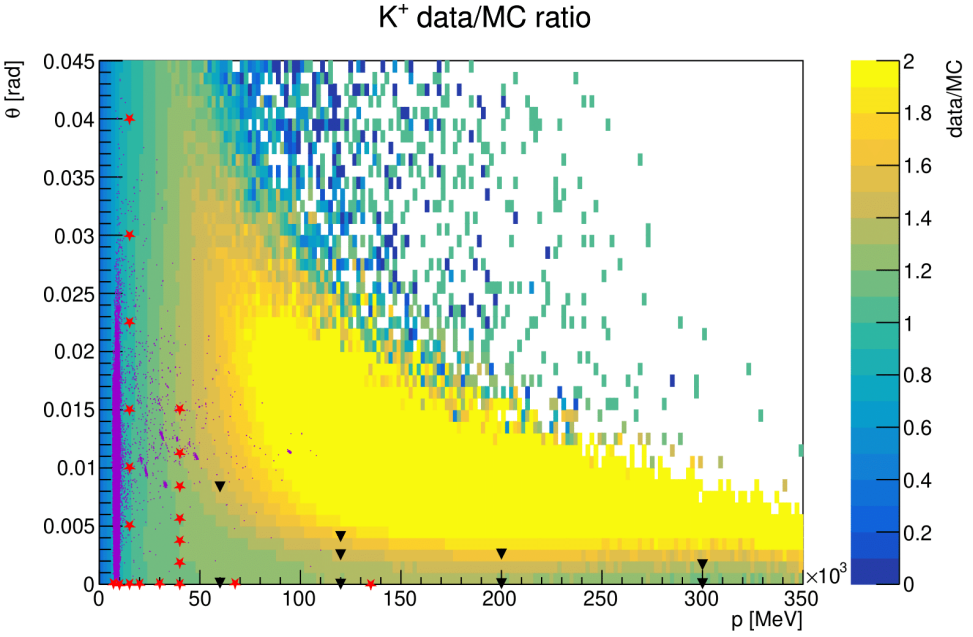

Figure 4.26: The phase-space of kaons produced at target giving origin to reconstructed K_{e3} signal events (purple dots), superimposed on the nominal hadroproduction weight map for kaons.

Fig. 4.26 also shows that the integral I_w can be computed up to $\theta_{max} = 25\,\mathrm{mrad}$. For larger angles, the contribution to the reconstructed K_{e3} signal events is negligible. The region of the target phase space chosen for the computation of the I_w integral, defined by $(p, \theta) \in [7.65\,\mathrm{GeV/c}, 9.35\,\mathrm{GeV/c}] \times [0, 25\,\mathrm{mrad}]$, will be referred to as the *ENUBET phase space*. Almost all kaons corresponding to K_{e3} signal events measured at tagger are produced in this region of the phase space. Therefore, the weights in this tighter region provide the most significant contribution when reweighting the reconstructed events. Consequently, the integral I_w of the hadroproduction weight map restricted to the ENUBET phase space will be considered in the following analysis.
By means of the multi-universes method, namely varying the hadroproduction parameters within their uncertainties, it is possible to create a scatter plot of the number of signal N_{sig} and background N_{bkg} events against the corresponding integral I_w in the ENUBET phase space of the hadroproduction weight maps for kaons, as shown in Fig. 4.27. As expected, these scatter plots show a strong correlation between the reconstructed signal or background and I_w, which is exploited to set the constraint on the hadroproduction weights.

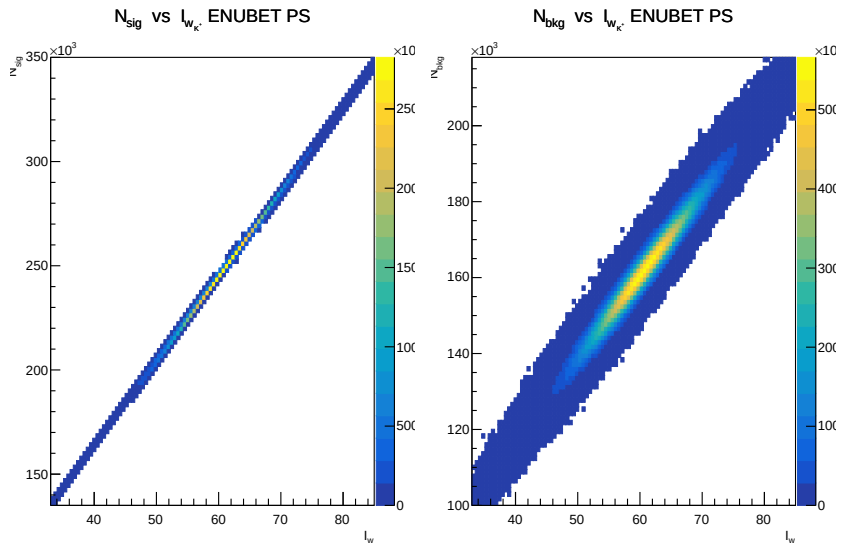

Figure 4.27: Scatter plot of N_{sig} and N_{bkg} versus the integral of weights I_w in the ENUBET phase space for kaons.

4.6.2 Procedure to set hadroproduction constraint

In this section it is discussed how to exploit the fit to positron observables in order to constrain the hadroproduction weight maps for kaons. The constrained hadroproduction weight map will be used to build a neutrino flux at the detector with higher precision. The constraint procedure is based on reducing the variance of the I_w distribution, following the workflow described below:

1. A 3-dim scatter plot of N_{sig}, N_{bkg} and I_w is built.

2. Before using the fit information, the integral of weights I_w is distributed according to a gaussian p.d.f. (pre-fit distribution), with a given mean $I_{w,0}$ and standard deviation σ_{I_w}.

3. A new distribution for I_w (post-fit distribution) can be computed by using the fitted values of N_{sig} and N_{bkg} with their uncertainties and the 3-dim scatter plot mentioned before. A slicing and projection procedure is used to retain only the I_w values matching the actual N_{sig} and N_{bkg} values from the fit to data. The details of this procedure are discussed later in this section.

4. The new distribution of I_w will have a central value $I'_w \neq I_{w,0}$ and standard deviation $\sigma_{I'_w} < \sigma_{I_w}$. In other words, after including the fit information, the integral of weights I_w is distributed according to a gaussian p.d.f. with a smaller variance.

5. From the knowledge of the post-fit gaussian p.d.f. Gauss$(I'_w, \sigma_{I'_w})$, having mean value I'_w and standard deviation $\sigma_{I'_w}$, one can generate - by means of a *rejection sampling method* - a new set of hadroproduction weight maps with reduced uncertainties.

The 3-dim scatter plot of N_{sig}, N_{bkg} and I_w is shown in Fig. 4.28, left. The projection on the (N_{sig}, N_{bkg}) space is also reported in Fig. 4.28, right, highlighting the values of $N_{\text{sig}}^{\text{fit}}$ and $N_{\text{bkg}}^{\text{fit}}$ and their errors from the fit to the positron observables. The joint p.d.f. $f(I_w, N_{\text{sig}}, N_{\text{bkg}})$ can be build from the 3-dim scatter plot above. The pre-fit I_w p.d.f. can be computed from the marginal p.d.f. of the joint p.d.f. $f(I_w, N_{\text{sig}}, N_{\text{bkg}})$, as follows:

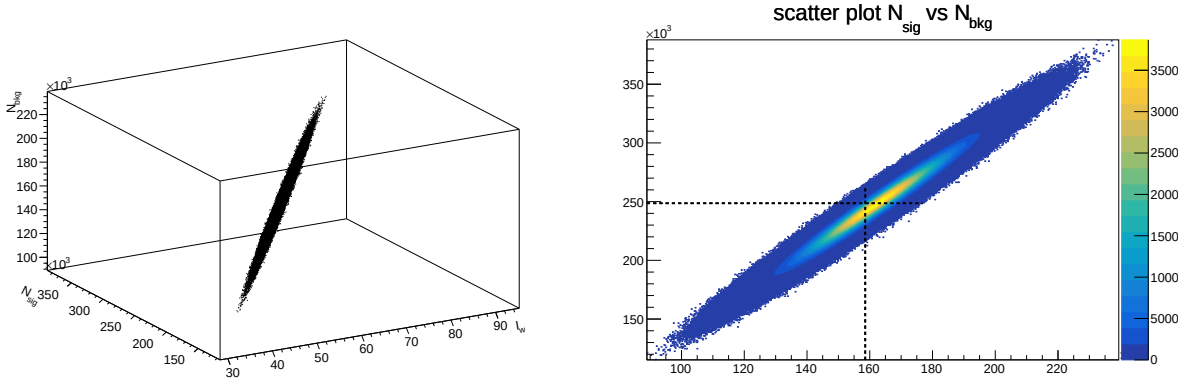

Figure 4.28: (left) 3-dim scatter plot of $N_{\rm sig}$ and $N_{\rm bkg}$ versus I_w. (right) Constraint plot for $N_{\rm sig}$ and $N_{\rm bkg}$ against I_w, whose axis is not visible. The fitted values of signal and background are reported with dashed lines.

$$f(I_w)\, dI_w = \int dN_b \int dN_s \; f(I_w, N_s, N_b)\; dI_w \tag{4.55}$$

In practice, the marginalization can be performed projecting the 3-dim scatter plot in Fig.4.28, left, onto the I_w axis via the method `ProjectionX()` of a `TH3D`. The fit to positron observables provides accurate estimates for the number of signal N_s and background N_b events, with their uncertainties. As a matter of fact, the estimates from the fit represent the actual application of the positron monitoring technique in ENUBET. The post-fit values N_s and N_b are correlated and assumed to be distributed according to a multivariate gaussian p.d.f, as follows:

$$g(\vec{\mu}, \Sigma) \;\equiv\; \text{gauss}(N_s, N_b\,;\, \mu_s,\, \mu_b,\, \sigma_s,\, \sigma_b, \rho)\, dN_s\, dN_b \tag{4.56}$$

where $\mu_s = N_{\rm sig}^{\rm fit}$ and $\mu_b = N_{\rm bkg}^{\rm fit}$ are the estimated values from fit to the observables and $\sigma_s = \sigma_{N_{\rm sig}^{\rm fit}}$ and $\sigma_b = \sigma_{N_{\rm bkg}^{\rm fit}}$ their corresponding uncertainties.
The I_w post-fit p.d.f. can be computed according to the following operating procedure:

1. For each pair of values N_s and N_b, i.e. one bin of the 2-dim scatter plot (N_s, N_b), the conditional p.d.f. $f(I_w \,|\, N_s, N_b) dI_w$ of the integral I_w is computed

$$f(I_w \,|\, N_s, N_b)\, dI_w = \frac{f(I_w, N_s, N_b)}{\int dI_w\, f(I_w, N_s, N_b)}\, dI_w \tag{4.57}$$

   this is done by projecting the intersection of the N_s and N_b slices in the 3-dim plot in Fig. 4.28 onto the I_w axis.

2. The fit constraint is introduced by reweighting the conditional p.d.f. $f(I_w \,|\, N_s, N_b)$ by Eq. (4.56) for each possible value of N_s and N_b

$$f(I_w \,|\, N_s, N_b)\, dI_w \;\cdot\; g(\vec{\mu}, \Sigma) \tag{4.58}$$

   This means that to each possible distribution of I_w, corresponding to fixed values of signal and background, is assigned a different importance based on the actually observed signal and background events, taking into account the errors in the measurement.

3. The post-fit p.d.f. for I_w is computed from Eq. (4.58) by integrating over a confidence interval for N_s and N_b given by the errors from the fit:

$$f_{\text{post-fit}}(I_w)\, dI_w = \int_{\mu_s-\sigma_s}^{\mu_s+\sigma_s} dN_s \int_{\mu_b-\sigma_b}^{\mu_b+\sigma_b} dN_b\, dI_w\ f(I_w \mid N_s, N_b) \cdot g(\vec{\mu}, \Sigma) \qquad (4.59)$$

In essence, the distributions of I_w corresponding to fixed values of signal and background are summed around the best-fit values, within their respective uncertainty ranges.

The resulting pre-fit and post-fit I_w p.d.f.s from the described procedure are shown in Fig. 4.29. Thanks to the constraint from the fit to positron observables, the post-fit I_w p.d.f. has a significantly smaller variance compared to the pre-fit I_w p.d.f., enabling to constrain the hadron production weight maps.

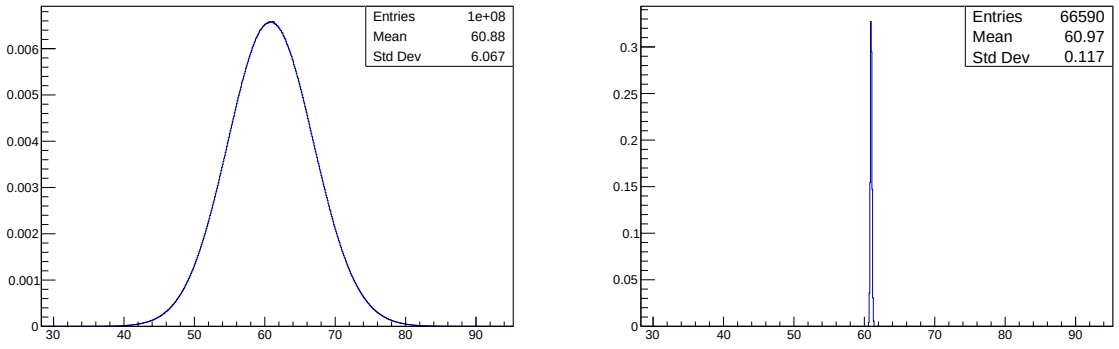

Figure 4.29: I_w p.d.f. pre-fit (left) and I_w p.d.f. post-fit (right).

4.6.3 Generation of post-fit hadroproduction weight maps

In order to reweight the neutrino flux including information from positron monitoring, thus obtaining the neutrino flux post-fit, it is necessary to generate a set of varied hadron production weight maps that satisfy the post-fit constraint on the integral of weights I_w in the ENUBET phase space. It should be remarked that the correlation between N_{sig}, N_{bkg} against the integral of weights I_w has been observed for kaons only, and not for pions or protons, as expected. Therefore, it is possible to set a constraint only on the weights of kaons, whereas the uncertainties of the weights for pions and protons remains the same. In particular, for protons and pions, hadron production weight maps are generated simply by means of the multi-universes method applied using NA20 and NA56/SPY data discussed in Sec. 4.3.1.
In the case of kaons, the multi-universes method is combined with the *rejection sampling technique* [136] in order to generate varied hadroproduction weight maps that satisfy the post-fit constraint. The rejection sampling technique can be implemented in a simple manner from the knowledge of the pre-fit and post-fit p.d.f.s for I_w. Specifically, it allows the generation of multiple hadroproduction weight maps via the multi-universe method, retaining only those whose integral I_w falls within the post-fit I_w distribution. Finally, a set of varied hadron production weight maps for kaons is produced according to the post-fit distribution. These weight maps will be used in Sec. 4.7 to reweight the neutrino flux at the detector, obtaining the post-fit neutrino flux and thereby mitigating hadroproduction-related systematic uncertainties.

4.7 Neutrino flux and interaction rate at detector

In this section, the flux of neutrinos reaching the detector and the corresponding charged-current interaction rate are computed. Results are presented both before (pre-fit) and after (post-fit) introducing the positron monitoring through the fit to the observables, to compare the performance of the ENUBET monitoring technique in reducing the hadroproduction systematics. A 500 ton LAr neutrino detector located at 50 m from the end of the decay tunnel and with a transversal section of $6 \times 6\,\mathrm{m}^2$ has been considered, according to the beamline design proposed in [76]. The total ν_e flux at the detector, before introducing the positron monitoring information (the pre-fit flux), is shown in Fig. 4.30. The mean hadroproduction weight maps are used for reweighting the neutrino events. The contributions are distinguished based on the region of the facility where the parent particle decayed; namely, the instrumented decay tunnel (tagger), the proton-dump, the hadron-dump, the target, the transfer line (TL) or other regions of the facility.

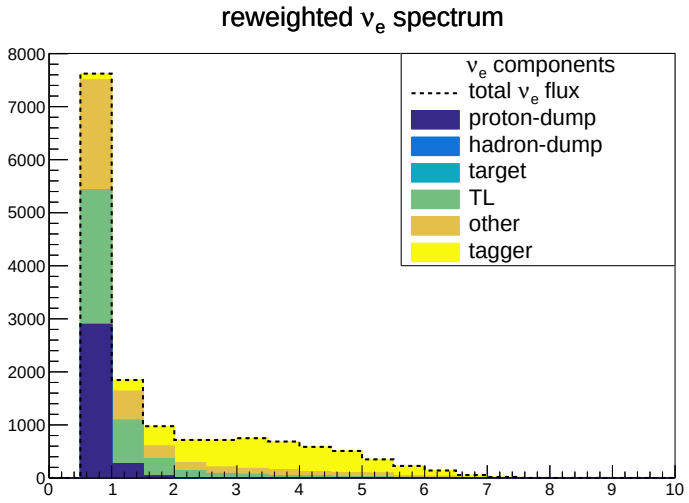

Figure 4.30: Total ν_e flux at detector.

Almost all low energy ν_e are produced outside the tagger, mainly at the proton-dump, in the target region or along the transfer line, due to reinteractions of secondaries with passive elements of the beamline, such as collimators or magnetic elements.
The pre-fit neutrino flux covariance and correlation matrices are obtained by means of the multi-universes technique. The only information exploited at this point is the one available from the hadroproduction data of NA20 and NA56/SPY discussed in Sec. 4.3.1: the full hadroproduction uncertainty is propagated to the neutrino flux. Therefore, a new set of hadroproduction weight maps is generated by varying the hadroproduction parameters according to their covariance matrix. This new set of weight maps is then used to reweight neutrino events in the MC simulation, producing multiple realizations of the ν_e flux. From this set of fluxes $\{\Phi_u\}_{\text{pre-fit}}$, the mean flux $\Phi^{\text{pre-fit}}_{\text{mean}}$ is computed, and subsequently the ν_e flux covariance matrix is calculated as follows:

$$V_{ij} = \frac{1}{N}\sum_{k=1}^{N}\left(\Phi^{i}_{\text{mean}} - \Phi^{i}_{k}\right)\cdot\left(\Phi^{j}_{\text{mean}} - \Phi^{j}_{k}\right) \tag{4.60}$$

where i and j identify a pair of bins in the neutrino flux and k the k-th universe within the N produced. The pre-fit covariance and correlation matrices are shown in Fig. 4.31.

The correlation matrix (Fig. 4.31, right) suggests that the two distinct neutrino populations, the low-energy component and the higher energy one above $\sim 1.5\,\text{GeV}$, are poorly correlated. Moreover, all the bins belonging to the same population are highly correlated among themselves. The presence of poorly correlated low- and high-energy neutrino populations can be explained by their independent sources. High energy neutrinos are mostly produced from decays occurring in the tagger or along the transfer line, whereas low energy neutrinos are produced in various other regions of the facility, e.g. dumps, through re-interaction of particles with the material.

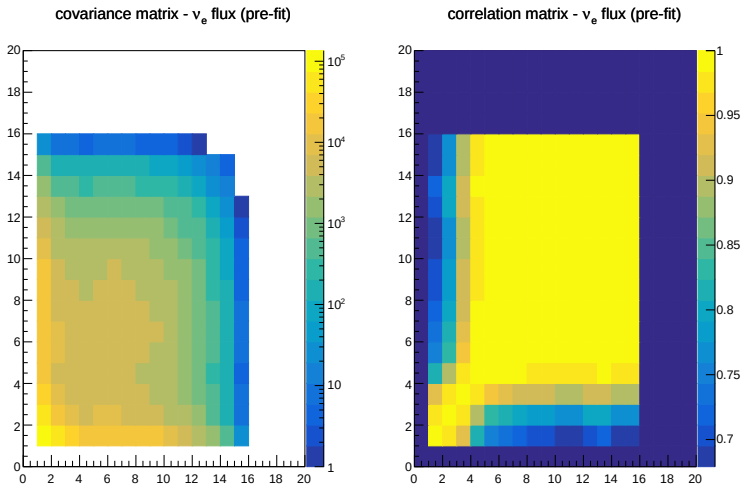

Figure 4.31: Pre-fit covariance (left) and correlation (right) matrices, obtained by means of the multi-universes method. The visualization of the covariance matrix is in logarithmic scale along the z axis.

Positron monitoring information, incorporated through the fit to the measured calorimetric observables, is introduced to reduce the hadroproduction uncertainty in the ν_e flux. This is achieved by using the set of post-fit hadron production weight maps, computed using the procedure described in Sec. 4.6.3, to reweight the ν_e events. As in the pre-fit case, the new set of fluxes $\{\Phi_u\}_{\text{post-fit}}$ is used to compute the mean flux $\Phi^{\text{post-fit}}_{\text{mean}}$, and subsequently, the ν_e flux covariance matrix with Eq. (4.60). Fig. 4.32 shows the post-fit flux covariance and correlation matrices. A qualitative comparison of the covariance matrices in Figs. 4.31 and 4.32 indicates improved precision in the neutrino flux, resulting from the constraints imposed by the fit to the observables. A more quantitative comparison is provided below using the neutrino rates at the detector, which are of greater physical interest with respect to the flux itself. The ν_e CC interaction rates at the detector and corresponding covariance matrices can be estimated from the pre- and post-fit ν_e fluxes $\{\Phi_u\}$ computed above. The rate is computed from the flux as follows:

$$R(E_i) = \sigma_\nu(E_i) \cdot \Phi_\nu(E_i) \cdot N_n \tag{4.61}$$

where $\sigma_\nu(E_i)$ is the ν_e CC cross section as a function of the energy E_i of the i-th bin of the flux histogram. The number of nucleons N_n in the detector can be computed as:

$$N_n = \frac{M_{\text{det}}[\text{g}]}{A_{\text{iso}}[\text{g/mol}]} \cdot A \cdot N_A \tag{4.62}$$

where $M_{\text{det}}[\text{g}] = 0.5 \cdot 10^{19}\,\text{g}$ is the detector mass, $A = 40$ and $A_{\text{iso}}[\text{g/mol}] = 39.948\,\text{g/mol}$ are respectively the number of nucleons and the atomic weight of Ar, whereas N_A is the Avogadro number. To obtain the total neutrino rate expected after the full data-taking

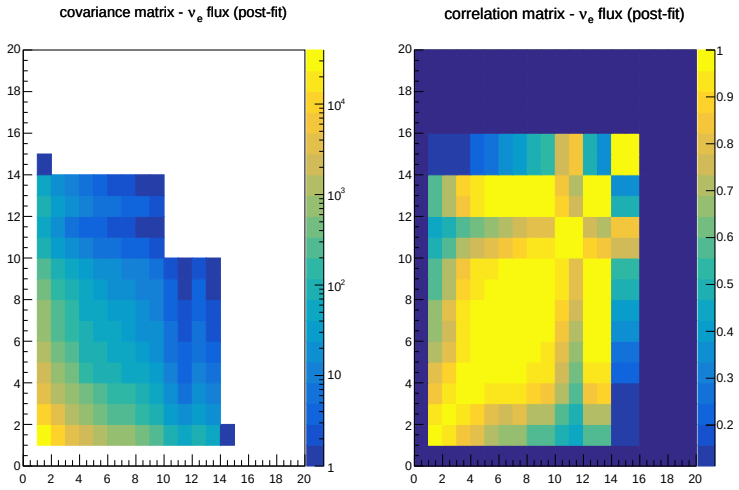

Figure 4.32: Post-fit covariance (left) and correlation (right) matrices, obtained reweighting neutrino events with the post-fit constrained hadron production weight maps, generated combining the multi-universes and rejection sampling technique. The visualization of the covariance matrix is in logarithmic scale along the z axis.

of the ENUBET facility, the neutrino flux is rescaled to the total number of protons-on-target, given by $N_{\text{pot}}^{\text{tot}} = 4.5 \cdot 10^{19}$ pot:

$$\Phi_\nu(E_i) = \frac{N_\nu(E_i)}{S_{\text{det}}} \cdot \frac{N_{\text{pot}}^{\text{tot}}}{N_{\text{pot}}^{\text{sim}}} \tag{4.63}$$

where $N_\nu(E_i)$ is the number of ν_e in the energy bin centered in E_i, $S_{\text{det}} = 6 \times 6 \cdot 10^4\,\text{cm}^2$ is the detector area, whereas $N_{\text{pot}}^{\text{sim}} = 1\,\text{GPOT}$ is the number of protons-on-target in the `FLUKA` simulation.
The pre-fit ν_e CC interaction rate obtained from this computation is shown in Fig. 4.33, with a breakdown of the different components according to the region of the facility where the neutrinos were produced. The error bands for the ν_e rate are computed from the flux covariance matrix, and displayed as a gray shaded area in Fig. 4.33. Considering the total neutrino rate, many neutrinos have origin from particles which cannot be properly reweighted according to the procedure developed in this work. For instance, since the majority of low energy neutrinos are produced from interactions of primary protons in the proton-dump, they cannot be reweighted using the hadron production weight maps of particles at the target exit. Therefore, in the following analysis, the neutrino flux is separated into components due to different types of particles produced at the target exit, rather than considering the total contribution. In particular, emphasis is given to the neutrino flux component originated from charged kaons produced at target, since the current workflow for the assessment of systematics exploits the fitted positron observables to set a constraint on the hadron production weight maps for kaons in the ENUBET phase space. Therefore, in this work the positron monitoring is exploited to set a post-fit constraint on the dominant flux component due to charged kaons produced at target. However, electron neutrinos are produced also from the propagation and decay of particles exiting the target different from charged kaons, mainly pions and K_L^0. These neutrino flux contributions, originated from particles exiting the target different from charged kaons, are not constrained by the procedure developed in this work. The ν_e event rate separated by different particles exiting the target is shown in Fig. 4.34, with the majority of the contribution originated from K^+ and π^+ produced at target.

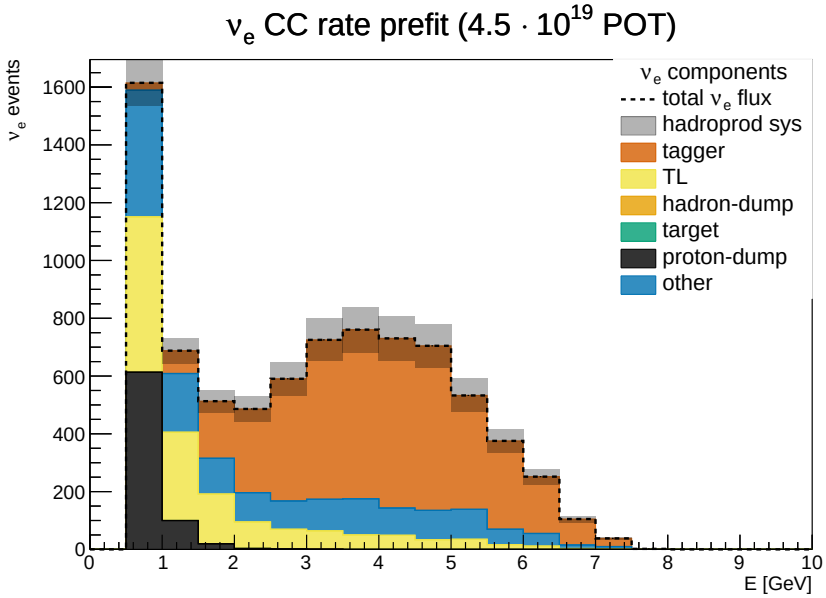

Figure 4.33: Pre-fit ν_e CC interaction rate. The ν_e rate error bands are obtained from the flux covariance matrix and displayed as a gray shaded area.

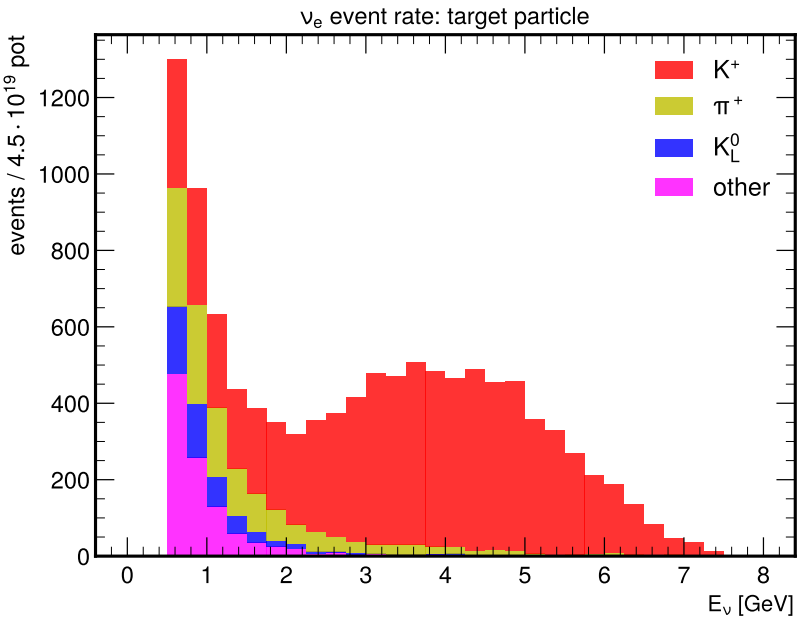

Figure 4.34: The ν_e event rate separated by different particles exiting the target.

The fraction of total ν_e rate - for each bin - originated from K^+, π^+ or other target particles is shown in Fig. 4.35, left. For visualization purposes, the fraction values above 2 GeV for kaons and pions or other particles produced at target are summarized in the histogram shown in Fig. 4.35, center and right, respectively.
The comparison of the pre- and post-fit ν_e rate due to *kaons at target* and their error bands are shown in Fig. 4.36, left. The corresponding pre- and post-fit relative bin errors are shown in Fig. 4.36, right. Since the neutrino energy distribution is reweighted using the weight maps for kaons, the pre-fit relative error has a flat trend, due to the fact that all events are properly reweighted on hadron production data for kaons.

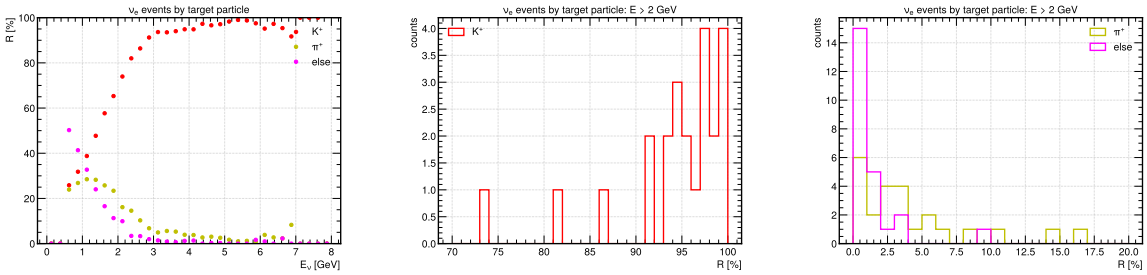

Figure 4.35: (left) Fraction of total ν_e rate - as a function of energy - originated from K^+, π^+ or other target particles. (center) Histogram of fraction values above 2 GeV for kaons produced at target. (right) Histogram of fraction values above 2 GeV for pions or other particles produced at target.

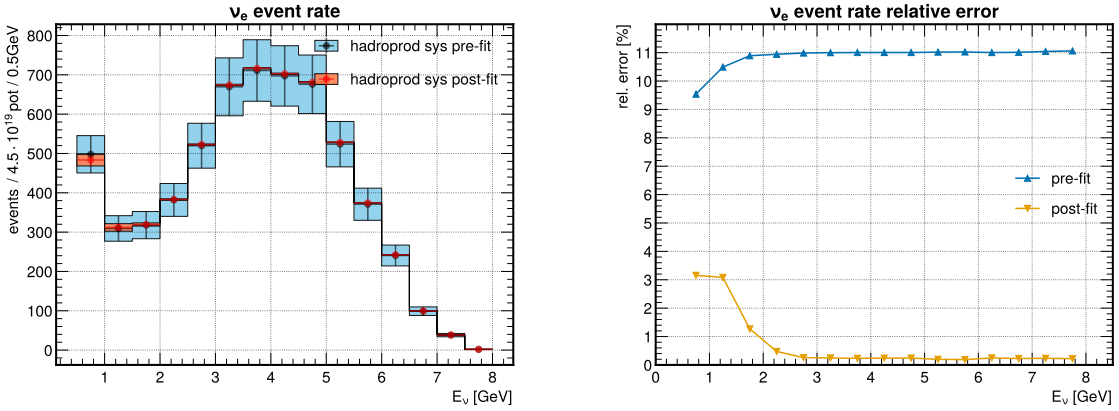

Figure 4.36: (left) Pre- and post-fit total ν_e rate due to *kaons at target* and their error bands, shown as blue and red shaded areas respectively. (right) Energy dependence of the pre-fit and post-fit ν_e rate due to *kaons at target* relative bin errors.

Moreover, reweighting the neutrino flux with the weight maps for kaons - for which the constraint has been set - the precision on the neutrino flux is well below $\sim$ 1% level for energies above $\sim$ 2 GeV. The rise of the post-fit error at lower energies is due to the fact that for energies below $\sim$ 2 GeV many of the neutrinos originate from particles outside the ENUBET phase space. Fig. 4.37 shows a visualization of charged kaons produced at target (purple dots) giving origin to neutrinos at detector, superimposed to the target phase space in the region $(p, \theta) \in [0, 10\,\text{GeV/c}] \times [0, 45\,\text{mrad}]$. Fig. 4.37, left, shows the phase space of kaons producing neutrinos with energies $E_\nu < 2\,\text{GeV}$, whereas the phase space of kaons producing neutrinos with energies $E_\nu \geq 2\,\text{GeV}$ is shown in Fig. 4.37, right. For energies above 2 GeV the kaons fall in the ENUBET phase space defined within the 10% momentum bite around the central momentum $p = 8.5\,\text{GeV/c}$

and within the angular acceptance of 25 mrad, as shown in Fig. 4.37, right. Therefore, kaons producing high energy neutrinos with $E_\nu \geq 2\,\text{GeV}$ are mainly produced in a phase space in which hadron production weight maps are well constrained using the procedure explained in Sec. 4.6.1. Nonetheless, as shown in Fig. 4.37, left, there is a significant number of kaons producing low energy neutrinos with $E_\nu < 2\,\text{GeV}$ that are produced in a scattered phase space distant from the ENUBET phase space. Therefore, in these phase space regions distant from the ENUBET phase space, the weight maps of kaons are not well constrained, resulting in an increase of the post-fit error for energies below $E_\nu < 2\,\text{GeV}$.

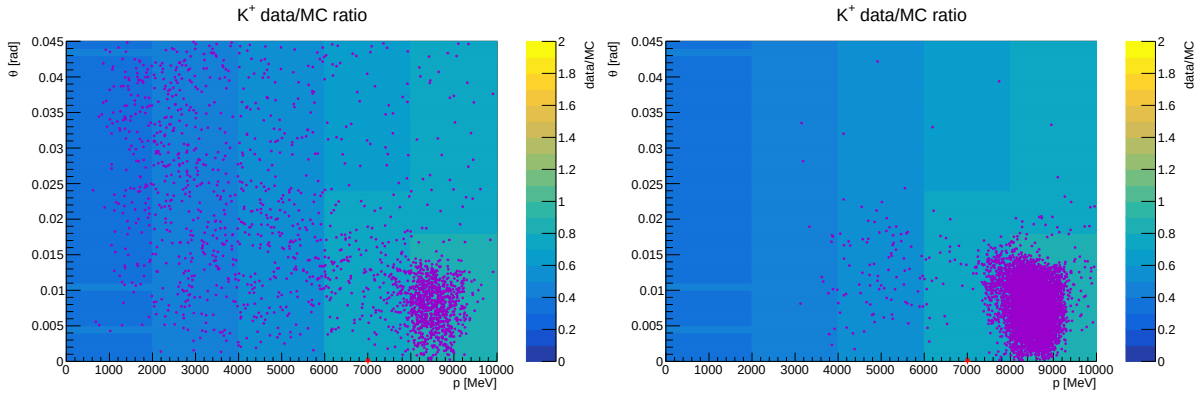

Figure 4.37: Visualization of charged kaons produced at target (purple dots) giving origin to neutrinos at detector with energies $E_\nu < 2\,\text{GeV}$ (left) or energies $E_\nu \geq 2\,\text{GeV}$ (right), superimposed to the target phase space in the region $(p, \theta) \in [0, 10\,\text{GeV/c}] \times [0, 45\,\text{mrad}]$.

After the kaons produced at target, the second most significant contribution to the total ν_e rate comes from pions at target, as shown in Fig. 4.34. For energies $E_\nu > 2\,\text{GeV}$ the core of the neutrino flux can be estimated, at first order, from the flux of neutrinos produced from kaons and pions at target, namely $\Phi_{K+\pi} \simeq \Phi_{tot}$. However, an hadron production constraint for pions produced at target has not been set in the present work, but there exist different handles that can be explored to improve the knowledge of such a flux contribution originated from pions at target. For instance, the ratio K/π from measured hadron production data can be used to set a constraint on the pion yields exploiting the constrained hadron production yields of kaons. Moreover, since electron neutrinos results also from the decay in flight of muons produced from $\pi_{\mu\nu}$ and $K_{\mu\nu}$ decays, the sample of muons recorded in the tunnel walls and in the hadron dump can be exploited to constrain the pions and kaon weight maps, which can be used also to constrain the electron neutrinos from muon decay.

The comparison of pre- and post-fit ν_e rates due to *kaons and pions at target* and their error bands are shown in Fig. 4.38, left. The corresponding pre- and post-fit relative bin errors are shown in Fig. 4.38, right. At energies above 2 GeV the constraint from the fit to positron observables allows to enhance the precision on the neutrino flux at $\mathcal{O}(1\%)$ level, with further possibility of improvement if constraining the pions yields using the muon sample, as discussed above. Fig. 4.33 shows that a fraction of neutrinos in the detector acceptance are not produced from meson decays occurring along the instrumented decay tunnel, but rather from other regions of the facility, and thus they cannot be monitored. The neutrino flux component having origin from the dumps and reaching the detector can be reduced, in principle, with a different location of the dumps. These non-monitored neutrino contributions can also be minimized using other handles, for instance exploiting the longitudinal position of the neutrino interaction vertex reconstructed along the neu-

trino detector depth, e.g. using the directionality of the reconstructed tracks to discard neutrinos crossing the detector but produced at the proton dump with a high angle with respect to the neutrino beam axis.

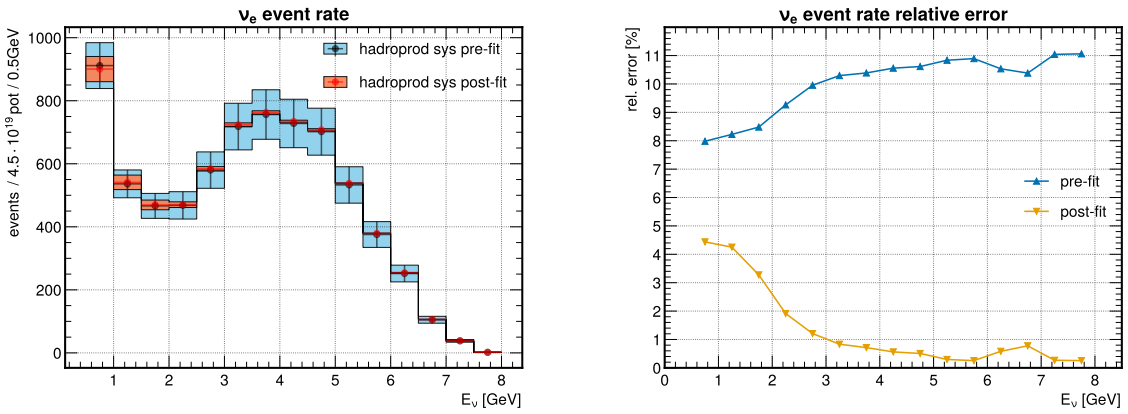

Figure 4.38: (left) Pre- and post-fit total ν_e rate due to *kaons and pions at target* and their error bands, shown as blue and red shaded areas respectively. (right) Energy dependence of the pre-fit and post-fit ν_e rate due to *kaons and pions at target* relative bin errors.

4.8 Treatment of detector systematics

In this section, the systematics related to the instrumentation of the decay tunnel and the method adopted for their assessment are discussed. These are expected to be subleading compared to the hadron production systematics. Three different types of detector effects have been considered:

- calibration uncertainty
- calibration bias
- scintillator ageing (i.e. photo-electron statistics)

These detector effects can impact the neutrino flux systematics budget, as they affect the number of reconstructed positrons in the calorimeter.

4.8.1 Injection workflow

It is important to note that the raw output of the tagger simulation does not account for any detector-related effect. These effects must be applied to the simulation output, and the procedure for doing so is referred to as the *injection workflow*. A schematic for the injection workflow of detector-related systematic uncertainties in the tagger simulation output (`G4TAG`) is shown in Fig. 4.39. In each calorimetric channel, the *true MC energy deposits* are smeared by uncertainties related to detector effects. No new `G4TAG` output files are produced with detector effects included, as the procedure is applied on the fly at the `Middlelayer` level, where the energy deposits are used as input. Therefore, the `Middlelayer` output file including detector systematics are saved on disc, and subsequently used in the reconstruction chain, namely the `Event Builder` reconstruction algorithm and the `ANN selection` PID analysis.

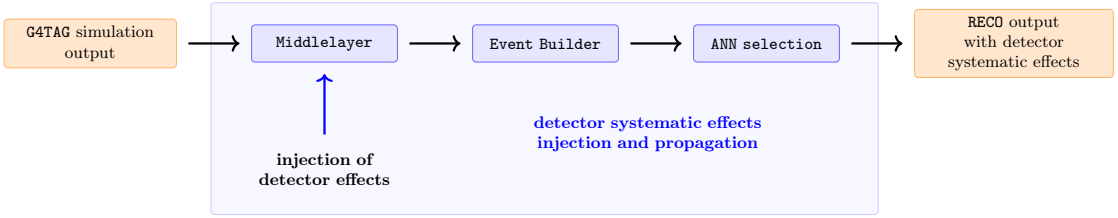

Figure 4.39: Schematics of the workflow for the injection of detector systematic effects into simulated events (`G4TAG` simulation output). The systematics injection and propagation involve the three standard reconstruction steps, namely the `Middlelayer`, `Event Builder` and `ANN selection`, highlighted by the light blue block.

The *ANN weights* used for the PID analysis in the workflow described above are the same one used for the results presented in Sec. 4.1.1, computed from the bare true MC simulation output[13]. This scenario corresponds to what would happen in a real data analysis: the datasets collected by a real experiment would undergo PID analysis using a set of ANN weights computed from the true detector response obtained from MC simulation. In real data, the true values of the energy depositions in the calorimetric channels are not known a priori. We only know how to obtain the calibrated energies and how to apply corrections to account for channel response changes due to ageing. Special auxiliary measurements are used to determine the sets of coefficients for calibration and ageing corrections. However, these coefficients are affected by uncertainties and possible biases, and the true value of the energy depositions depend on the true values of the coefficients within their p.d.f.s. Therefore to assess the detector effects, it is necessary to produce different simulation outputs, each corresponding to a possible realization of the true energy depositions within the uncertainties of these coefficients. In practice, to produce each of these simulation outputs, a set of smearing coefficients $\{S_{ch}\}_i$ for the calorimetric channels is computed to account for the detector effect uncertainty being studied. Each set of smearing coefficients is applied following the workflow depicted in Fig. 4.39, eventually obtaining a set of `RECO` outputs including detector systematic effects, dubbed as *systematic universes*. The generation of a set of systematic universes from the application of many realizations of smearing coefficients is schematically shown in Fig. 4.40. At the end of the injection procedure, a set of n systematic universes - each one with its own realization of detector effects - is produced. The systematic universes are thus a set of `RECO` outputs which implement the detector effects.

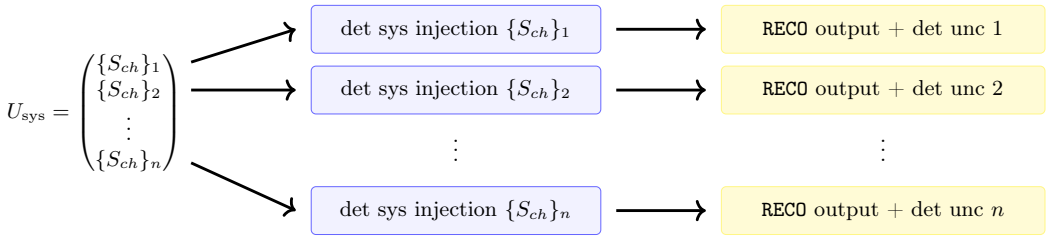

Figure 4.40: Generation of a set of systematic universes from a set of smearing coefficients $\{S_{ch}\}_i$ used to injected detector systematics in the `RECO` output.

4.8.2 Combination of hadroproduction and detector systematics effects

The systematic universes obtained in the previous section are represented in the uppermost block in Fig. 4.41. This set is the building block of the procedure developed to assess the impact of detector-related systematics on the observed charged lepton events in the

[13] In this case the ANN weights are the same one used for the published results in [76].

tagger. Combined with the hadroproduction uncertainties, it is used for both fit model building and pseudo-data generation. Of course, model building relies on information known a priori, before the experiment is performed. Therefore the procedure consists of reweighting the set of systematic universes using the *mean hadroproduction weight maps*, in order to account for the average effects of hadroproduction combined with detector systematics. This new set of *mean hadroproduction reweighted systematic universes* is represented in the leftmost block in Fig. 4.41.

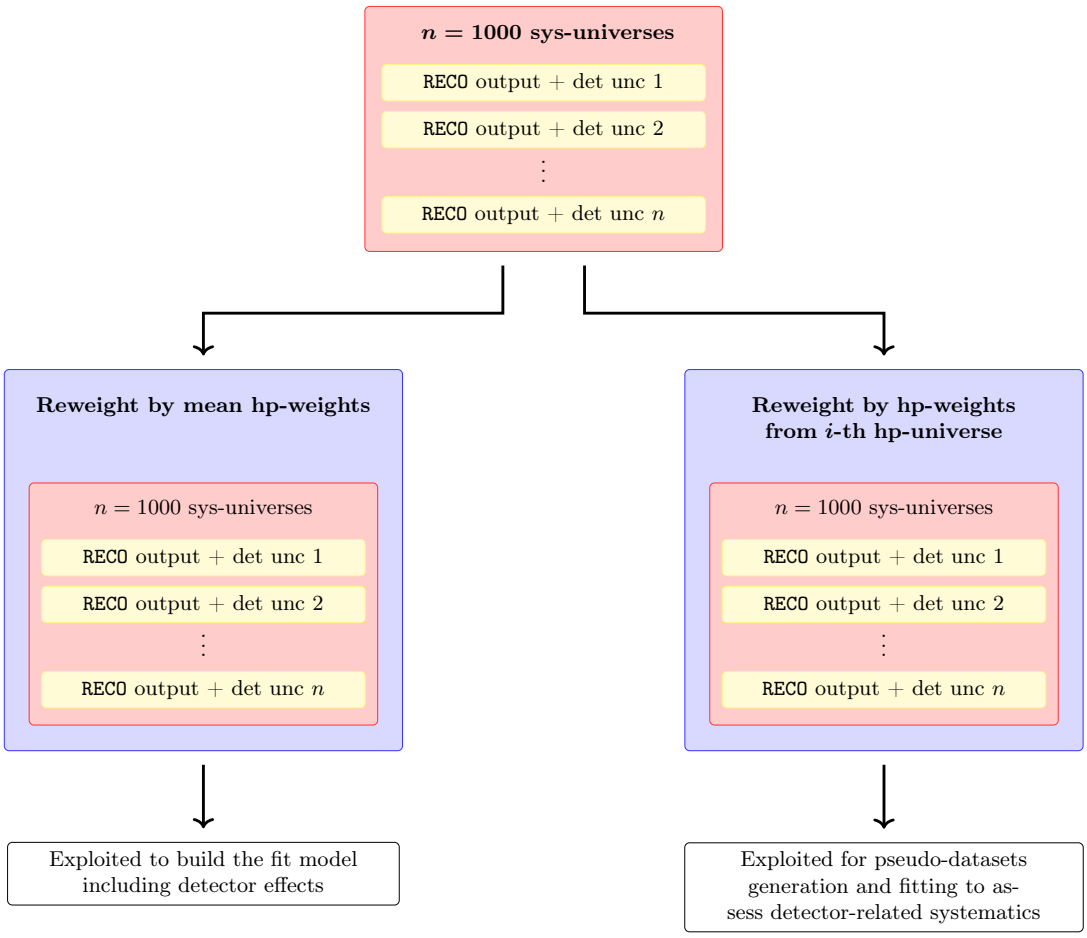

Figure 4.41: Uppermost block: set of RECO outputs each one including a possible realization of a detector effect within the uncertainties. Leftmost block: same as the uppermost set, but includes the reweighting by the mean hadron production weight (hp-weight) maps; this set is used to extract the information needed for building a model p.d.f. including detector effects. Rightmost block: same as the leftmost set, but includes reweighting using the hp-weight maps from a specific hp-universe - specifically, the one assumed to be realized in Nature; this is used to produce the pseudo-datasets to be fitted.

The set is then analyzed to extract the information needed to build the model p.d.f. Specifically, the distributions of the total number of signal, background and total events (from the integrals of observables distributions) are plotted to estimate potential biases induced by detector effects, which are then accounted for in the fit model through scale factor parameters. The covariance matrix induced by detector systematics on the observables bin contents is also computed from the new set of universes, and used to constrain the nuisance parameters introduced in the model to describe the bin-by-bin detector effects. Pseudo-data samples, including detector and hadroproduction effects, are generated from the set of systematic universes reweighted using the hadroproduction weight maps corresponding to a *specific hadroproduction universe*. Therefore the new set, repre-

sented by the rightmost block in Fig. 4.41, includes detector systematics and is rescaled by hadroproduction effects, accounting for the hadroproduction parameter values chosen by Nature as the true ones (see Sec. 4.5.7). The produced pseudo-datasets undergo the fitting procedure using the model including both hadroproduction and detector systematics. The only missing element is a *reference* result without detector effects, against which the results including detector systematics can be compared to assess the impact of the detector uncertainties. Therefore, the reference result includes only the hadroproduction, and can be obtained by analyzing the tagger simulation output reweighted by the specific hadroproduction universe mentioned above (see Fig. 4.42).

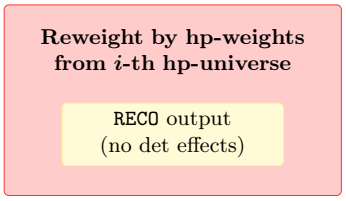

Figure 4.42: `RECO` output reweighted with the hp-weights of a specific hadroproduction universe - specifically, the one assumed to be realized in Nature. The output is used to compute the reference result to be compared with detector systematic results.

4.8.3 Calibration uncertainty

The calibration of the calorimetric LCMs can be performed through m.i.p. particles (high energy muons or pions), as discussed in Sec. 3.5. The signal distribution in each LCM is a Landau distribution, like the ones obtained at the prototypes test-beams and shown in Fig. 3.17. The MPV value of the Landau function is used to determine the response of a channel to a m.i.p. energy deposition. The calibrated response of each channel is given by:

$$E[\mathrm{MeV}]_{\mathrm{ch}} = \frac{\langle \mathrm{MIP} \rangle^{\mathrm{ch}}_{\mathrm{MeV}}}{\mathrm{MPV}^{\mathrm{ch}}_{\mathrm{ADC}}} \cdot \mathrm{PH}^{\mathrm{ch}}_{\mathrm{ADC}} = c_{\mathrm{ch}} \cdot \mathrm{PH}^{\mathrm{ch}}_{\mathrm{ADC}} \tag{4.64}$$

The calibration coefficient c_{ch} is affected by an uncertainty, which affects directly the charged lepton observables measured by the ENUBET calorimeter, and thus the determination of the neutrino flux. The measured value of the calibration coefficient of a channel is distributed according to a gaussian, so that the actual energy measured in a channel is given by:

$$\begin{aligned} E[\mathrm{MeV}]_{\mathrm{ch}} &= \mathrm{Gauss}(\mu_{c_{\mathrm{ch}}}, \sigma_{c_{\mathrm{ch}}}) \cdot \mathrm{PH}^{\mathrm{ch}}_{\mathrm{ADC}} \\ &= \mu_{c_{\mathrm{ch}}} \cdot \mathrm{Gauss}(1, \sigma_{c_{\mathrm{ch}}}/\mu_{c_{\mathrm{ch}}}) \cdot \mathrm{PH}^{\mathrm{ch}}_{\mathrm{ADC}} \\ &= \mathrm{Gauss}(1, \sigma_{c_{\mathrm{ch}}}/\mu_{c_{\mathrm{ch}}}) \cdot \langle E \rangle [\mathrm{MeV}]_{\mathrm{ch}} \end{aligned} \tag{4.65}$$

These considerations allow to define a procedure for the injection of the calibration uncertainty effects in the reconstructed electrons. A new set of smearing coefficients for all calorimetric channels can be obtained by extracting as many values as the calorimetric channels from the gaussian, as follows:

$$\{S_{\mathrm{ch}}\}_u = \{\mathrm{Gauss}(1, \sigma_{c_{\mathrm{ch}}}/\mu_{c_{\mathrm{ch}}})\}_u \tag{4.66}$$

This set can be used to smear the energy deposition of the events produced through the `G4TAG` simulation, as shown in Fig. 4.43, and to obtain a new `G4TAG` output with injected calibration uncertainty effects. This will correspond to one *systematic universe*.

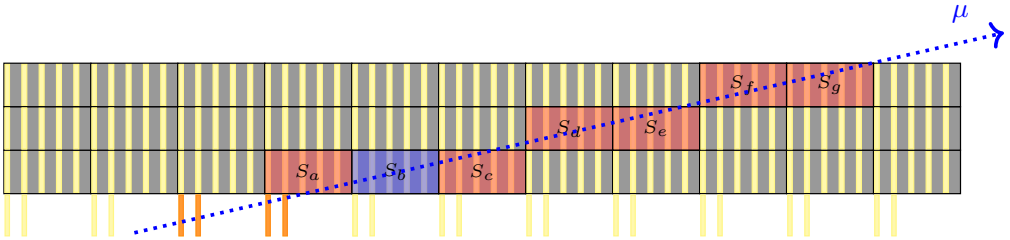

Figure 4.43: In this schematic view, a longitudinal section of the ENUBET calorimeter is shown, together with the energy depositions caused by a crossing muon (channels highlighted in red and light blue). The effect of calibration uncertainty is taken into account by smearing the energy deposits by the corresponding smearing coefficients of the involved channels $S_{\text{ch}}^{a,b,c,d,e,f,g} \in \{S_{\text{ch}}\}_u$. Note that this procedure is performed for each type of energy deposit across all reconstructed events. For illustrative purposes, a muon is used in the schematic to help visualize the involved channels.

The set of smearing coefficients, corresponding to different realizations of the calibration coefficients within their uncertainties, produced by means of Eq. (4.66) are given by:

$$U_{sys} = \{\{S_{\text{ch}}\}_1, \{S_{\text{ch}}\}_2, ..., \{S_{\text{ch}}\}_n\} \tag{4.67}$$

and applied to the `G4TAG` output (see Figs. 4.40 and 4.41). The workflow described in Sec. 4.8.1 and Sec. 4.8.2 is used to extract the information to build the fit model p.d.f. and to produce the pseudo-datasets.
A systematic value of $\sigma_{c_{\text{ch}}}/\mu_{c_{\text{ch}}} = 5\%$ is assumed for calibration uncertainty hereafter, and it represents a conservative choice, supported by preliminary analyses of the test beam data which indicate that the systematic uncertainty lies below this threshold.

4.8.4 Calibration bias

The LCMs can be calibrated according to their m.i.p. response, as discussed in Sec. 4.8.3, as follows:

$$E[\text{MeV}]_{\text{ch}} = \frac{\langle \text{MIP} \rangle_{\text{MeV}}}{\text{MPV}_{\text{ADC}}^{\text{ch}}} \cdot \text{PH}_{\text{ADC}}^{\text{ch}} = c_{\text{ch}} \cdot \text{PH}_{\text{ADC}}^{\text{ch}} \tag{4.68}$$

assuming the m.i.p.s deposit on average an energy $\langle \text{MIP} \rangle_{\text{MeV}}$ equal for all channels. Such a value can be estimated using MC simulation; however, the real experimental setup differs from MC because of material budget, angular and energy distribution of beam particles and other effects. Moreover, the calorimeter response depends on the type and energy of the incoming particle and its shower development. These effects can lead to a systematic mis-measurement of the energy deposited in the channels $E[\text{MeV}]_{\text{ch}}$, i.e. a calibration bias equal to all LCMs. Similarly to the modeling of calibration uncertainties in Sec. 4.8.3, the calibration bias effect is modeled computing smearing coefficients for the deposited energy in the channels. Indeed, the MC energy deposits in the LCMs are scaled with these coefficients to take into account the effect of a calibration bias, according to:

$$E[\text{MeV}]_{\text{ch}} = \text{Gauss}(1, \sigma_{c_{\text{bias}}}/\mu_{c_{\text{bias}}}) \cdot \langle E \rangle [\text{MeV}]_{\text{ch}} \tag{4.69}$$

where the scaling coefficients are modeled through a gaussian with mean 1 and bias uncertainty normalized to the mean value. The set of scaling coefficients for calibration bias are equal for all channels in a given systematic universe, as follows:

$$\{B_{\text{ch}}\}_u = \{\text{Gauss}(1, \sigma_{c_{\text{bias}}}/\mu_{c_{\text{bias}}})\}_u \tag{4.70}$$

$$U_{\text{sys}} = \{b_1, b_2, ..., b_n\} \tag{4.71}$$

Therefore, one coefficient b_u defines one possible realization of the calibration bias on the measured particles, i.e. defines one of the systematic-universes.
A systematic value of $\sigma_{c_{\text{bias}}}/\mu_{c_{\text{bias}}} = 5\%$ is assumed for calibration bias hereafter.

4.8.5 Scintillator ageing

The scintillator ageing mechanisms can be divided into two main categories [137–139]:

- *Unrelated to radiation dose*: e.g. crazes within the material caused by mechanical stressing, fogging of the material caused by water penetration and condensing, yellowing induced by photochemical processes caused by oxidation of the material.
- *Related to radiation dose*: damage of the substrate (PS/PVT) can result in the creation of *color centers* (radicals, carbonyl species etc.) that can absorb light emitted by secondary flour reducing the absorption length of scintillation light.

The effect of the scintillator ageing is a drop in the scintillation light yield from the LCMs over time. A monitoring system in the experimental setup will allow to correct for this effect and get a constant response of the calorimeter for fixed energy depositions. In order to assess the scintillator ageing systematic impact on the neutrino flux it is necessary to introduce two parameters in the simulation: the total drop in light yield after the full data-taking period of NP06/ENUBET and the error on the light yield measurement from the monitoring system. In the following, a conservative value for the light drop $\text{LY}_{\text{red}} = 10\%$ and a 1% error on the light measurement are assumed, as a result of both ageing effects above[14].

The scintillator ageing systematic is thus included in the `G4TAG` simulation output of the calorimeter producing different systematic universes, each one with its own realization of the ageing effect, as outlined in the following. At time T (e.g. at the end of NP06/ENUBET data taking) the scintillator transparency will be reduced, implying a reduction of the light yield of:

$$\varepsilon_T^{-1} = \varepsilon_{T=0}^{-1} \cdot (1 - \text{LY}_{\text{red}}) = 13.5 \text{ p.e./MeV} \tag{4.72}$$

where the value $\varepsilon_{T=0}^{-1} = 15$ p.e./MeV [76] corresponds to the light yield at the beginning of the data taking (i.e. no ageing) and $\text{LY}_{\text{red}} = 10\%$ is the total relative light yield drop. In practice, the calorimetric response due to the light drop is corrected for using the monitoring system, which allows to measure 4.72. Nonetheless, a drop in the produced scintillator light implies a larger statistical fluctuation in the measured energy depositions. Therefore, each energy deposition in the LCMs is varied to account for the larger statistical fluctuations. Given the true MC energy deposit, the mean number of p.e. after a time T can be computed according to:

$$\langle N_{\text{p.e.}} \rangle_T = \varepsilon_T^{-1} \cdot E_{\text{dep}}^{\text{MC}} \tag{4.73}$$

This is used to get a new p.e. value after statistical fluctuations:

$$N_{\text{p.e, T}}^{\text{stat}} \in \text{Poiss}(\langle N_{\text{p.e.}} \rangle_T) \tag{4.74}$$

[14] In the instrumented tunnel, the expected doses estimated with `FLUKA` is between few Gy up to kGy [76]. Considering 10^{20} pot, $0.4 \times 10^{-3} K$/pot and an average energy deposit in the scintillators of 200 MeV, the average dose is $\mathcal{O}(100\,\text{Gy})$. Using as a reference the light yield reduction in CMS experiment [138], the drop is of the order of 5% for doses up to 100 Gy, and of about 10% for doses up to 1 kGy (note that this does not take into account the different dose rates). The light yield drop values are measured with few % errors. For the ageing effect unrelated to the radiation dose, a 6% drop in the light yield can be expected and an error of $\mathcal{O}(1\%)$ in the light yield measurement [137].

and the corresponding new value for the deposited energy:

$$E_{\text{dep}}^{\text{stat}} = \frac{N_{\text{p.e, T}}^{\text{stat}}}{\varepsilon_T^{-1}} \tag{4.75}$$

where the factor 4.72 after the ageing is used in order to get back to the deposited energy. As mentioned before, the monitoring system allows to compute correction coefficients for the calorimetric response, which are applied to the pulse heights measured in the LCMs. The correction coefficients are affected by an error that, as is done for the other detector effects, is propagated to the final measured energy deposition:

$$E_{\text{dep}}^{\text{ageing}} = \text{Gauss}\left(1, \sigma_{\text{LY}}/\mu_{\text{LY}}\right) \cdot E_{\text{dep}}^{\text{stat}} \tag{4.76}$$

obtaining a smearing coefficient which is the same for all LCMs within a given systematic universe. The smearing is modeled through a gaussian with mean 1 and relative monitoring error assumed to be $\sigma_{\text{LY}}/\mu_{\text{LY}} = 1\%$. The set of scaling coefficients for scintillator ageing are equal for all channels in a given systematic universe, as follows:

$$\{B_{\text{ch}}\}_u = \{\text{Gauss}\left(1, \sigma_{\text{LY}}/\mu_{\text{LY}}\right)\}_u \tag{4.77}$$

$$U_{\text{sys}} = \{b_1, b_2, ..., b_n\} \tag{4.78}$$

similar to procedure employed for the calibration bias in Sec. 4.8.4.

4.8.6 Fit model and likelihood for detector systematics

The fit model and likelihood discussed in Sec. 4.5 can be extended to include detector-related systematic uncertainties. Such detector effects can be parametrised by *nuisance parameters*, in addition to the parameters of interest $\vec{p} = (\vec{\alpha}, \vec{\beta})$ related to hadroproduction. In fact, the variation induced by detector effects in each bin of the charged lepton observables is modeled through a set of $\vec{\gamma}$ *bin-by-bin nuisance parameters*, common for signal and background events. The bias induced by detector effects in the total observed events is taken into account by means of *bin-by-bin scaling factors* $\vec{f_s}$. The definition of the fit model may vary depending on both the detector effect and the physical channel considered. For instance, a bin-by-bin scale factors $\vec{f_s}$ is considered for positrons. These nuisance parameters are gathered in a vector $\vec{\nu}$ defined as:

$$\vec{\nu} = (\vec{f_s}, \vec{\gamma}) \tag{4.79}$$

The number of events predicted by the model in each bin i is given by:

$$N_i^{\text{p}}(\vec{p}, \vec{\nu}) = f_{s,i} \cdot [(1 + \alpha_i + \gamma_i) \cdot T_{Si} + (1 + \beta_i + \gamma_i) \cdot T_{Bi}] \tag{4.80}$$

where N_i^{p} is the predicted number of events in a fixed bin i. At present, the scaling factor is fixed in the fitting procedure. The detector systematic uncertainties are then included in the likelihood through a prior p.d.f. for the $\vec{\gamma}$ nuisance parameters, assumed to be a multivariate normal distribution defined as:

$$\pi_{\text{det}}(\vec{\gamma}) = \frac{1}{(2\pi)^{k/2} \cdot |V_{\vec{\gamma}}|^{\frac{1}{2}}} \cdot e^{-\frac{1}{2}\vec{\gamma} \cdot V_{\vec{\gamma}}^{-1} \cdot \vec{\gamma}^T} \tag{4.81}$$

where $V_{\vec{\gamma}}$ is the covariance matrix induced by detector effects. The binned likelihood function is thus extended to include detector systematics, according to:

$$\mathcal{L}(\vec{p},\vec{\nu}) = \pi_{\rm hp}(\vec{p}) \cdot \pi_{\rm det}(\vec{\gamma}) \cdot \prod_{i}^{n} P(N_i|N_i^{\rm p}(\vec{p},\vec{\nu})) \tag{4.82}$$

The $\vec{\gamma}$ nuisance parameters are thus constrained by the covariance matrix $V_{\vec{\gamma}}$ induced by detector effects. The negative log-likelihood ratio for the combined fit of multiple pseudo datasets can be finally extended according to:

$$\chi^2(\vec{p},\vec{\nu}) = -2\ln\lambda(\vec{p},\vec{\nu}) = 2\sum_{d}^{D}\sum_{i}^{n}\left[N_i^{\rm p}(\vec{p},\vec{\nu}) - N_i + N_i\ln\left(\frac{N_i}{N_i^{\rm p}(\vec{p},\vec{\nu})}\right)\right] + \tag{4.83}$$

$$+ \sum_{j,k}^{m} p_j V_{j,k}^{-1} p_k + \sum_{j,k}^{n} \gamma_j V_{\vec{\gamma}_{j,k}}^{-1} \gamma_k \tag{4.84}$$

where the terms (4.84) are the penalty terms on the parameters. The fit model in Eq. (4.80) allows to fit both hadron production and detector systematic effects, therefore it is possible to isolate the interesting contribution represented by $\vec{\alpha}$, $\vec{\beta}$ parameters of interest which directly affect the neutrino flux. In the best case scenario, the detector systematic effect can be completely accounted for: the hadroproduction effect is completely extracted from the fit and thus the $\vec{\alpha}$, $\vec{\beta}$ best fit values and errors are equal to what expected in the absence of any detector effect. The actual behaviour, due to the introduction of $\vec{\gamma}$ nuisance parameters, is that of changing the best fit values for the $\vec{\alpha}$, $\vec{\beta}$ parameters of interest, worsening their errors with respect to the hadroproduction only case. The result is a change of the reweighted neutrino flux due to a detector systematic effect.

4.8.7 Assessment of the impact of detector-related systematics on monitoring

This section describes the general procedure for the assessment of detector-related systematics on the events observed in the tagger and the neutrino rates. The specific applications will be shown in Secs. 4.9.2 and 4.9.3. The starting point is represented by the set of *hadroproduction reweighted systematic universes*, namely the set of `RECO` output files including detector effects reweighted by hadroproduction weight maps from the specific hadroproduction universe. This set, shown in the rightmost block of Fig. 4.41, is used for pseudo-datasets generation and fitting. The full set of $K = 1000$ systematic universes is considered[15], each one used to generate and fit a total of $M = 100$ pseudo-experiments. For each one of the M pseudo-experiments, a set of $D = 50$ datasets (i.e. corresponding to a total statistics of $5 \cdot 10^{12}$ pot) including statistical fluctuations is generated and fitted with the model described in the previous section. From the M fitted values of signal and background events for the k-th systematic universe, with $k \in K$, the mean $\langle N_{\rm sgn/bkg}^{\rm (hp+det\text{-}sys)\text{-}univ}\rangle_{k\text{-th}}$ and standard deviation $\sigma_{\rm sgn/bkg,\ k\text{-th}}^{\rm (hp+det\text{-}sys)\text{-}univ}$ are computed. These values are then compared against the *reference* result. The reference result is obtained from the fit to the set of M pseudo-datasets, with the same $5 \cdot 10^{12}$ pot statistics, generated from the `RECO` output file reweighted by the specific hadroproduction universe, as described in Sec. 4.8.2. The fit is performed with the fit model in Eq. (4.42), including hadroproduction only. From the M fitted values, the reference mean $\langle N_{\rm sgn/bkg}^{\rm hp\text{-}only}\rangle_{\rm ref}$ and standard deviation $\sigma_{\rm sgn/bkg,\ ref}^{\rm hp\text{-}only}$ are computed. From the mean fitted values that include

[15] A subset $K = 100$ of the systematic universes can also be used, without impacting the final result.

both hadroproduction and detector systematics, and the reference mean value that includes only hadroproduction, the detector systematic effect on the signal and background events measured in the calorimeter can be computed according to:

$$\sigma^{\text{up}}_{\text{det-sys}} = \max_i\{\langle N^{\text{(hp+det-sys)-univ}}_{\text{sgn/bkg}}\rangle_i\} \; - \langle N^{\text{hp-only}}_{\text{sgn/bkg}}\rangle_{\text{ref}} \tag{4.85}$$

$$\sigma^{\text{down}}_{\text{det-sys}} = \langle N^{\text{hp-only}}_{\text{sgn/bkg}}\rangle_{\text{ref}} - \; \min_i\{\langle N^{\text{(hp+det-sys)-univ}}_{\text{sgn/bkg}}\rangle_i\} \tag{4.86}$$

The final result on signal and background events can thus be expressed as follows:

$$N_{\text{sgn/bkg}} = \langle N^{\text{hp-only}}_{\text{sgn/bkg}}\rangle_{\text{ref}} \pm \sigma^{\text{hp-only}}_{\text{sgn/bkg,ref}} + \sigma^{\text{up}}_{\text{det-sys}} - \sigma^{\text{down}}_{\text{det-sys}} \tag{4.87}$$

The logic for propagating detector systematics to the neutrino flux and rate at the detector is the following. The fit model used for detector-related systematics is that of Eq. (4.80), where the set of $\vec{\nu}$ *nuisance parameters* takes into account the variation induced by detector effects in each bin of charged lepton observables. The predicted number of events N^{p}_i in a given bin i stated in Eq. (4.80) can be expressed as:

$$N^{\text{p}}_i(\vec{p},\vec{\nu}) = f_{s,i}\cdot[(1+\alpha_i)\cdot T_{Si} + (1+\beta_i)\cdot T_{Bi}] + f_{s,i}\cdot\gamma_i\cdot T_{Si} + f_{s,i}\cdot\gamma_i\cdot T_{Bi} \tag{4.88}$$

which can be rewritten in a more compact form as follows:

$$N^{\text{p}}_i(\vec{p},\vec{\nu}) = f_{s,i}\cdot\left[N^{\text{eff}}_{\text{sgn},i}(\vec{\alpha}) + N^{\text{eff}}_{\text{bkg},i}(\vec{\beta}) + \Delta^{\text{det}}_{\text{sgn},i}(\vec{\gamma}) + \Delta^{\text{det}}_{\text{bkg},i}(\vec{\gamma})\right] \tag{4.89}$$

In each bin i, the *effective* number of signal/background events in Eq. (4.89) are defined as follows:

$$N^{\text{eff}}_{\text{sgn},i}(\vec{\alpha}) = (1+\alpha_i)\cdot T_{Si} \tag{4.90}$$

$$N^{\text{eff}}_{\text{bkg},i}(\vec{\beta}) = (1+\beta_i)\cdot T_{Bi} \tag{4.91}$$

and represent variation induced by hadroproduction only; they are thus function of the set of $\vec{\alpha}$, $\vec{\beta}$ *parameters of interest* only. The *detector correction* terms in Eq. (4.89):

$$\Delta^{\text{det}}_{\text{sgn},i}(\vec{\gamma}) = \gamma_i\cdot T_{Si} \tag{4.92}$$

$$\Delta^{\text{det}}_{\text{bkg},i}(\vec{\gamma}) = \gamma_i\cdot T_{Bi} \tag{4.93}$$

represent the variations induced by detector effects on the shape of the observables; they are thus functions of the set of $\vec{\gamma}$ *nuisance parameters* only. Note that the *bin-by-bin scaling factors* $\vec{f_s}$, taking into account the bias induced by detector effects in the total observed events, is a fixed set of parameters in the fit.

The fit to the observables, performed using the model in Eq. (4.89), provides, for each bin i of the distributions, an estimate of the effective number of signal and background via Eqs. (4.90) and (4.91). By summing these fitted values over all bins, the total effective number of events $N^{\text{eff,tot}}_{\text{sgn}}$ and $N^{\text{eff,tot}}_{\text{bkg}}$ are computed. These represent the best estimates of the signal and background as they would be observed in the calorimeter if only hadroproduction effects were present. By applying the procedure described in Sec. 4.6, and using $N^{\text{eff,tot}}_{\text{sgn}}$ and $N^{\text{eff,tot}}_{\text{bkg}}$ as values provided by the monitoring, a new set of constrained hadroproduction weight maps is obtained for each systematic universe. The constrained hadroproduction weight maps are finally used to reweight the neutrino flux and to compute the expected interaction rate at detector, following the same method

discussed in Sec. 4.7.
From the procedure described above, a set of $k \in K$ different predictions of the reweighted neutrino flux $\{\Phi_\nu\}_k$ is thus obtained, whose small variations are induced by residual detector effects on the effective signal fitted values. From these fluxes, the corresponding set of neutrino rates $\{R_\nu\}_k$ is computed and used to evaluate the impact of detector systematics. This set of neutrino rates is split into two subsets: one corresponding to rates above $\{R_\nu\}_k^{\text{up}}$, and one to rates below $\{R_\nu\}_k^{\text{down}}$, relative to the reference rate distribution $R_\nu^{\text{hp-only}}$, which includes only the hadroproduction effect. For each bin $R_{\nu,b}^{\text{hp-only}}$ of the hadroproduction only rate distribution, the value $R_{\nu,b}^{\text{det-sys,up}}$, corresponding to one standard deviation of the $\{R_{\nu,b}\}_k^{\text{up}}$ distribution, is interpreted as the detector systematic uncertainty on the upper value of the neutrino rate for that bin. Similarly, the value $R_{\nu,b}^{\text{det-sys,down}}$, derived from $\{R_{\nu,b}\}_k^{\text{down}}$, represents the uncertainty on the lower value.
The relative upper and lower systematic variation in the neutrino rate induced by detector effects can be simply computed as follows:

$$\Delta R_\nu^{\text{det-sys,up}}\,[\%] = \frac{R_\nu^{\text{det-sys,up}} - R_\nu^{\text{hp-only}}}{R_\nu^{\text{hp-only}}} \cdot 100 \tag{4.94}$$

$$\Delta R_\nu^{\text{det-sys,down}}\,[\%] = \frac{R_\nu^{\text{hp-only}} - R_\nu^{\text{det-sys,down}}}{R_\nu^{\text{hp-only}}} \cdot 100 \tag{4.95}$$

for both bin-by-bin contents and integral values of the neutrino rate. The procedure described above is applied to each of the detector effects considered in this study, allowing to assess the detector systematic on the neutrino rate for each one of them. The overall systematic effect on the neutrino rate is reported as the quadrature sum of the single systematic contributions. As with the hadroproduction systematic uncertainty, the relative value of the systematic effect is the same for both the neutrino rate and the neutrino flux.

4.9 Assessment of the impact of detector systematics

This section describes the assessment of detector-related systematic uncertainties for positron events measured in the instrumented decay tunnel and electron neutrino rates at the detector. The effect induced by detector-related systematics on signal and background events observed in the calorimeter is assessed in Sec. 4.9.2, which will be eventually propagated to neutrino flux in Sec. 4.9.3.

4.9.1 Building blocks of the model including detector systematics

The building blocks of the fit model, including detector systematics and the mean effect of hadroproduction, are presented in this section. Specifically, they are reported below for the case of calibration uncertainty. The discussion for other detector effects is very similar and therefore omitted. As explained in Sec. 4.8.2, the systematic universes represented in the leftmost box of Fig. 4.41 are used to build the fit model. From these universes, the mean total observable template `TotObsMean_hpsys`, shown in Fig. 4.44, right, and the covariance and correlation matrices for the bin-by-bin nuisance parameters $\vec{\gamma}$, shown in Fig. 4.45, are computed. It should be noted that the covariance and correlation matrices are computed for the total content, signal plus background, of each bin.
As discussed in Sec. 4.8.6, detector effects can induce a bias in the total observed events which can be taken into account by means of *bin-by-bin scaling factors* $\vec{f_s}$. These coefficients $\vec{f_s}$ are computed by comparing the average observable template that includes

both hadroproduction and detector systematics with the one that includes only hadroproduction. Specifically, they are obtained from the ratio of `TotObsMean_hpsys`, Fig. 4.44, right, to the average total observable template `TotObsMean_hp` computed from variations induced by hadroproduction only, Fig. 4.44, left. The obtained normalization coefficients $\vec{f}_s$ for calibration uncertainty are shown in Fig. 4.46.

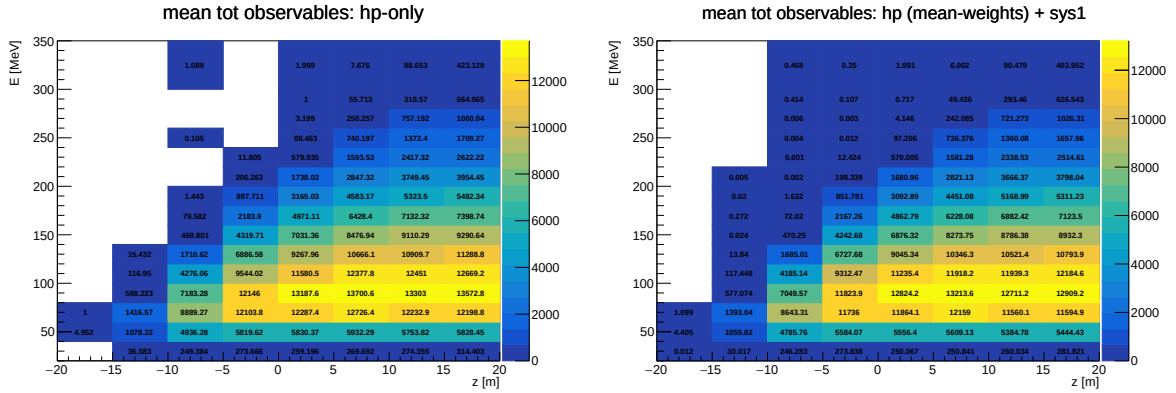

Figure 4.44: (left) Mean total observables template `TotObsMean_hp` due to variations induced by hadron production uncertainties only. (right) Mean total observables template `TotObsMean_hpsys` due to variations induced by calibration uncertainty and rescaled by mean hadroproduction effects.

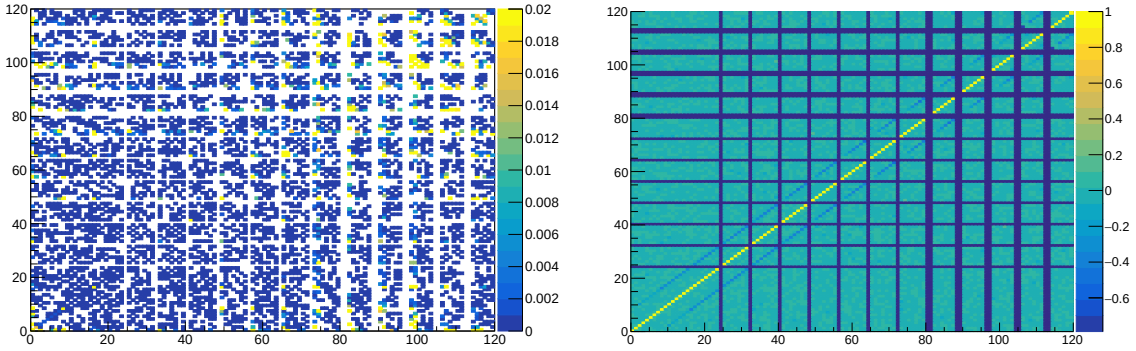

Figure 4.45: Covariance (left) and correlation (right) matrices for total bin contents of total observable templates built from systematic universes with calibration uncertainty.

In summary, the systematic universes in the leftmost box of Fig. 4.41 are used to compute the scaling factors $\vec{f}_s$ and the covariance matrix $V_{\vec{\gamma}}$ for the nuisance parameters $\vec{\gamma}$. These are used in the fit model that includes detector systematics, discussed in Sec. 4.8.6. All other components of the fit model, namely the signal template, T_S, the background template, T_B, and the covariance matrix $V_{\vec{p}}$ for the hadroproduction parameters $\vec{p} = (\vec{\alpha}, \vec{\beta})$, are derived from the analysis performed considering only hadroproduction effect.

4.9.2 Impact on monitored positrons

In this section the detector-related systematic effects on fitted signal and background events are assessed. As outlined in Sec. 4.8.2, pseudo-experiments are generated and fitted from the systematic universes shown in the rightmost plot of Fig. 4.41. The pseudo-experiments are generated for each of the 1000 universes, therefore the choice was to produce 100 of them for each universe, to avoid being limited by time and computing

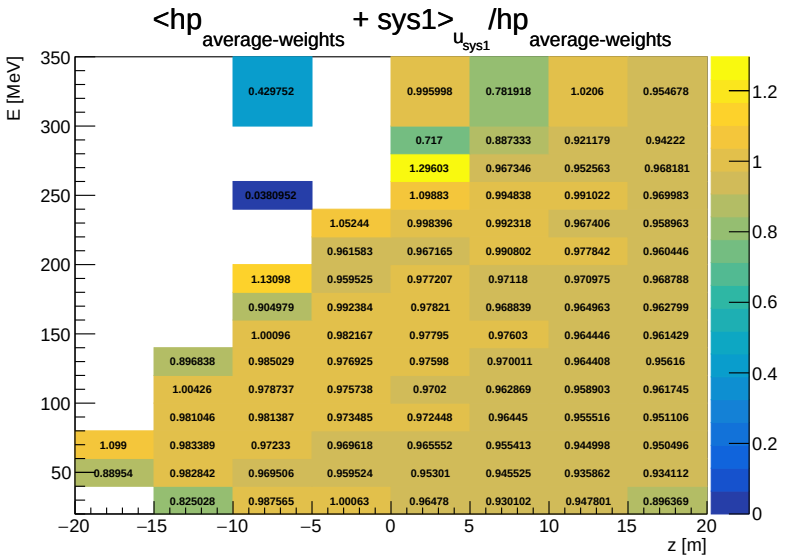

Figure 4.46: Bin-by-bin scaling factors $\vec{f}_s$ to take into account a bias in total observed events induced by calibration uncertainty.

constraints. This does not impact the final result. The total number of datasets produced for each pseudo-experiment must be the same (i.e. 50 datasets, for a total $5 \cdot 10^{12}$ pot statistics). The results from the fits are compared to the reference fit obtained from 100 pseudo-experiments generated from the universe shown in Fig. 4.42, including only the hadroproduction effects. In the following subsections, results for calibration uncertainty, calibration bias and scintillator ageing effects are reported.

Calibration uncertainty

The results of the fits as a function of different occurrences of calibration uncertainties in each generated systematic universe are shown in Fig. 4.47, for signal and background events respectively, considering a subset of 100 systematic universes for visualization purposes.

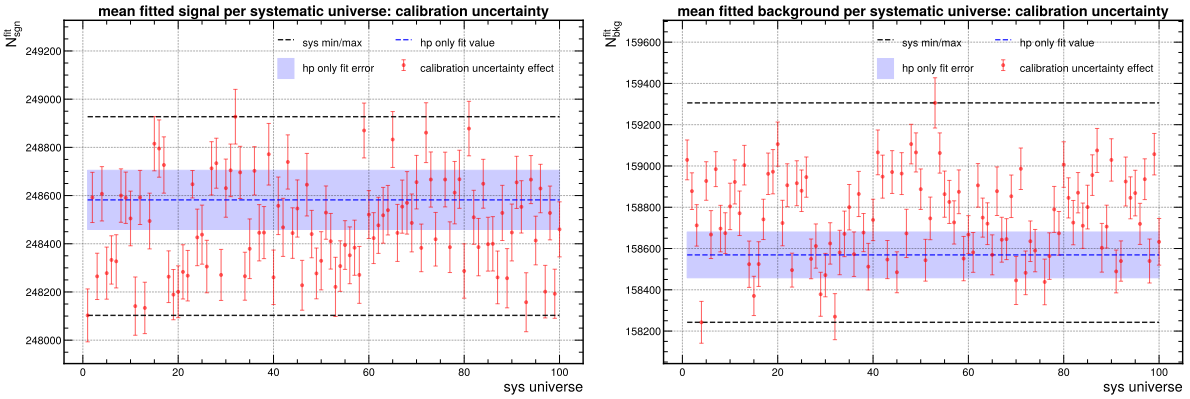

Figure 4.47: Distribution of the mean and standard deviation of fitted signal events, $N_{\text{sgn}}^{\text{fit}}$ (left), and background events, $N_{\text{bkg}}^{\text{fit}}$ (right), obtained by fitting a set of pseudo-experiments from 100 different systematic universes (red points), each corresponding to a different instance of the calibration coefficients within their *calibration uncertainty*. The maximum and minimum values are highlighted through the black dashed lines. The mean and standard deviation of fitted events obtained fitting pseudo-experiments in the hadroproduction only case are shown by the blue dashed line and band.

The red points are the mean values $\langle N^{\text{(hp+det)-univ}}_{\text{sgn/bkg}} \rangle_i$ and the red error bands their corresponding standard deviations $\sigma^{\text{(hp+det)-univ}}_{\text{sgn/bkg},\ i}$. The mean $\langle N^{\text{hp-only}}_{\text{sgn/bkg}} \rangle_{\text{ref}}$ and standard deviation $\sigma^{\text{hp-only}}_{\text{sgn/bkg,ref}}$ from the hadroproduction only case are shown in blue, representing the reference values used for comparison. The definition of the procedure used for computing the mean and standard deviations mentioned here is reported in Sec. 4.8.7. The black dashed lines represent the maximum excursion of fitted events with respect to the hadroproduction only case. The distributions of the $\langle N^{\text{(hp+det)-univ}}_{\text{sgn/bkg}} \rangle_i$ values, computed from the full set of 1000 systematic universes, are shown in Fig. 4.48. The correlation between the fitted signal and background is illustrated in Fig. 4.49, which shows the scatter plot of mean fitted signal versus background.

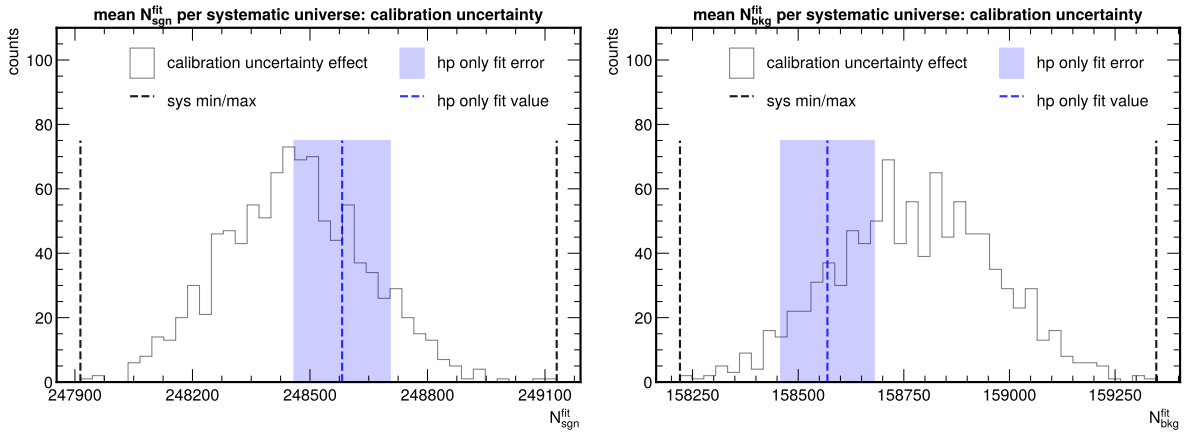

Figure 4.48: Projection of the distributions in Fig. 4.47 along the mean fitted signal and background axes (y-axes).

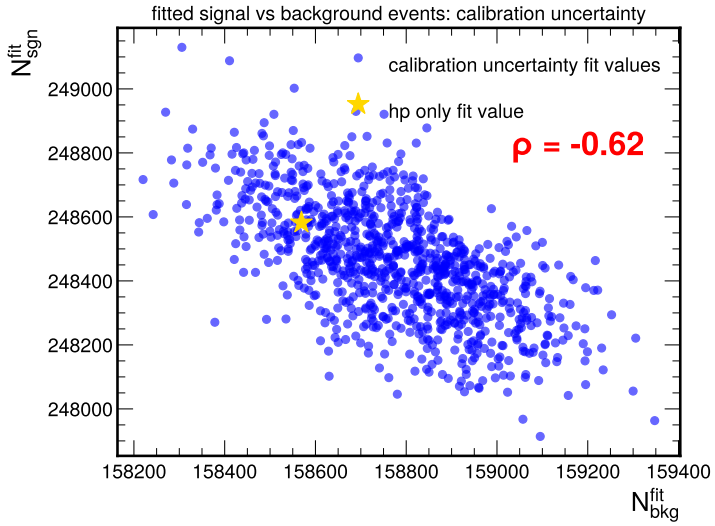

Figure 4.49: Scatter plot of the mean fitted values of signal and background events for 1000 systematic universes (*calibration uncertainty*). The correlation coefficient of the distribution is shown in red. The reference fit value obtained for the hadroproduction only case is shown with the yellow star.

The deviation of the mean fitted values, $\langle N^{\text{(hp+det)-univ}}_{\text{sgn/bkg}} \rangle_i$, with respect to the reference value, $\langle N^{\text{hp-only}}_{\text{sgn/bkg}} \rangle_{\text{ref}}$, in the distributions from Figs. 4.47, 4.48 and 4.49 represents a measure of the calibration uncertainty effect on the reconstructed positrons in the calorimeter.

The actual evaluation of the calibration uncertainty (CU) systematic effect on the fitted signal and background is computed using Eqs. (4.85) and (4.86), and the final result written using Eq. (4.87):

$$N_{\text{sgn}} = 248582 \pm 0.05\% \text{ (hp-only) } {}^{+0.22\%}_{-0.27\%} \text{ (CU-sys)} \tag{4.96}$$

$$N_{\text{bkg}} = 158569 \pm 0.07\% \text{ (hp-only) } {}^{+0.49\%}_{-0.22\%} \text{ (CU-sys)} \tag{4.97}$$

Calibration bias

The results of the fits as a function of different occurrences of calibration bias in each generated systematic universe are shown in Fig. 4.50, for signal and background events respectively, considering a subset of 100 systematic universes for visualization purposes. Fig. 4.51 shows the distributions of the mean fitted signal and background computed from the full set of 1000 systematic universes for the *calibration bias*. The correlation between the fitted signal and background is illustrated in Fig. 4.52.

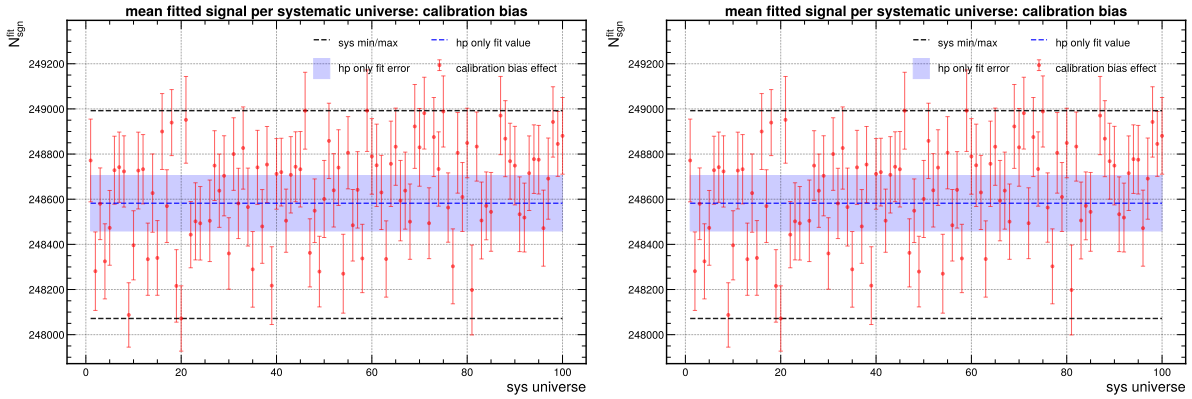

Figure 4.50: Distribution of the mean and standard deviation of fitted signal events, $N_{\text{sgn}}^{\text{fit}}$ (left), and background events, $N_{\text{bkg}}^{\text{fit}}$ (right), obtained by fitting a set of pseudo-experiments from 100 different systematic universes (red points), each corresponding to a different instance of the calibration coefficients within their *calibration bias*. The maximum and minimum values are highlighted through the black dashed lines. The mean and standard deviation of fitted events obtained fitting pseudo-experiments in the hadroproduction only case are shown by the blue dashed line and band.

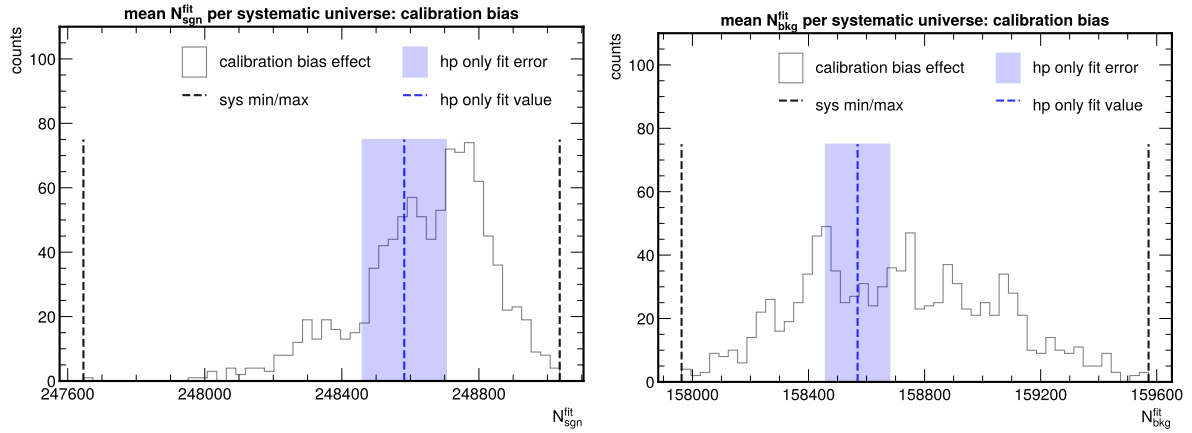

Figure 4.51: Projection of the distributions in Fig. 4.50 along the mean fitted signal and background axes (y-axes).

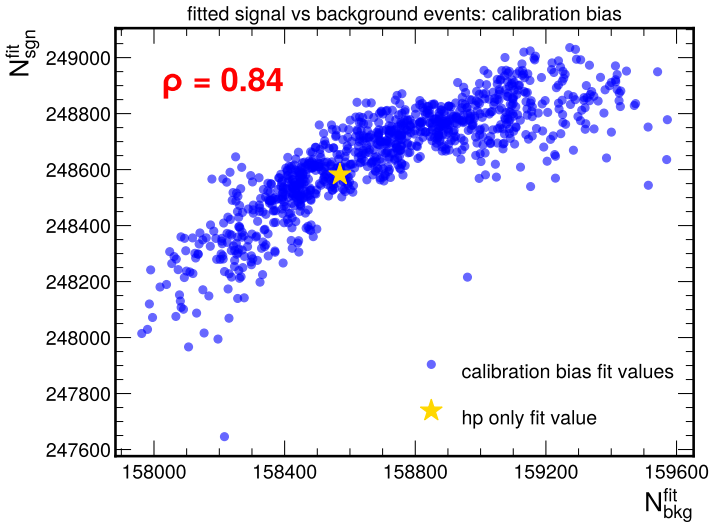

Figure 4.52: Scatter plot of the mean fitted values of signal and background events for 1000 systematic universes (*calibration bias*). The correlation coefficient of the distribution is shown in red. The reference fit value obtained for the hadroproduction only case is shown with the yellow star.

Finally, the effect induced by calibration bias (CB) on the fitted signal and background events is the following:

$$N_{\text{sgn}} = 248582 \pm 0.05\% \text{ (hp-only)} \, ^{+0.18\%}_{-0.38\%} \text{ (CB-sys)} \tag{4.98}$$

$$N_{\text{bkg}} = 158569 \pm 0.07\% \text{ (hp-only)} \, ^{+0.63\%}_{-0.38\%} \text{ (CB-sys)} \tag{4.99}$$

Scintillator ageing

The results of the fits as a function of different occurrences of scintillator ageing in each generated systematic universe are shown in Fig. 4.53, for signal and background events respectively, considering a subset of 100 systematic universes for visualization purposes. Fig. 4.54 shows the distributions of the mean fitted signal and background computed from the full set of 1000 systematic universes for the *scintillator ageing*. The correlation between the fitted signal and background is illustrated in Fig. 4.55.
Finally, the effect induced by scintillator ageing (AG) on fitted events is the following:

$$N_{\text{sgn}} = 248582 \pm 0.05\% \text{ (hp-only)} \, ^{+0.32\%}_{-0.51\%} \text{ (AG-sys)} \tag{4.100}$$

$$N_{\text{bkg}} = 158569 \pm 0.07\% \text{ (hp-only)} \, ^{+0.73\%}_{-0.3\%} \text{ (AG-sys)} \tag{4.101}$$

In summary, for all considered detector systematics, the impact on the estimated signal and background positron events from the monitoring technique is less than 1%. It can be also noted that the impact of the detector systematic is larger than that of hadron production. However, as will be shown in the following section, this is no longer the case when propagating detector systematics to the neutrino rate. This behavior is intrinsic to the propagation procedure.

4.9.3 Impact on neutrino rate

In this section the results of the assessment of detector-related systematics on neutrino rates are reported and discussed. They are obtained according to the procedure outlined

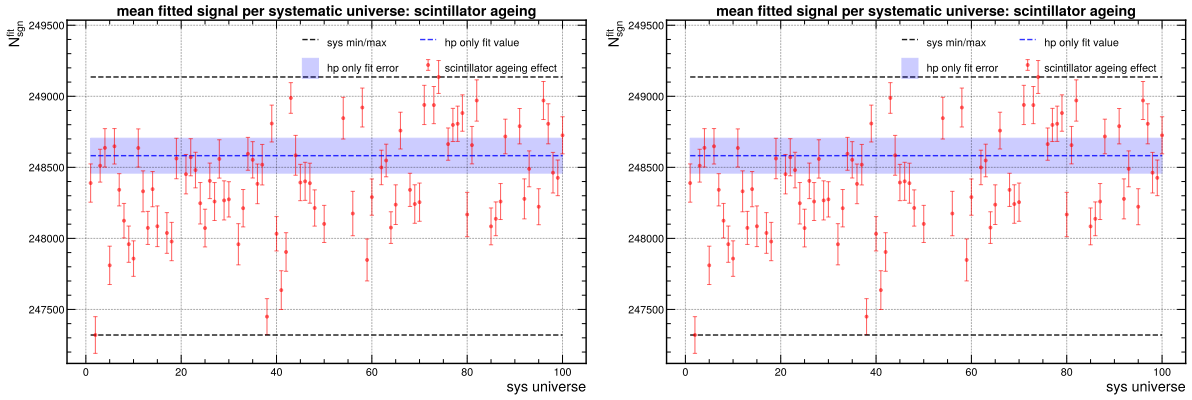

Figure 4.53: Distribution of the mean and standard deviation of fitted signal events, $N_{\text{sgn}}^{\text{fit}}$ (left), and background events, $N_{\text{bkg}}^{\text{fit}}$ (right), obtained by fitting a set of pseudo-experiments from 100 different systematic universes (red points), each corresponding to a different occurrence of *scintillator ageing* systematic. The maximum and minimum values are highlighted through the black dashed lines. The mean and standard deviation of fitted events obtained fitting pseudo-experiments in the hadroproduction only case are shown by the blue dashed line and band.

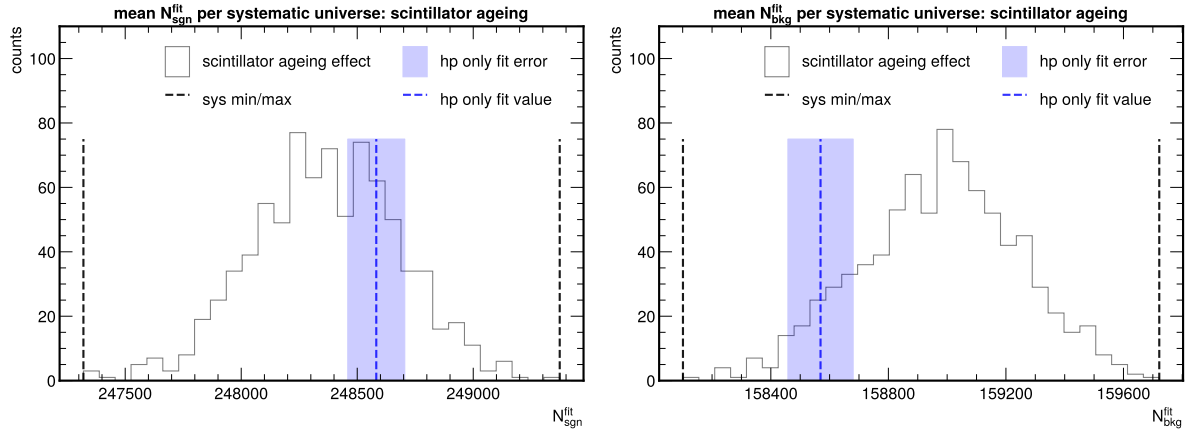

Figure 4.54: Projection of the distributions in Fig. 4.53 along the mean fitted signal and background axes (y-axes).

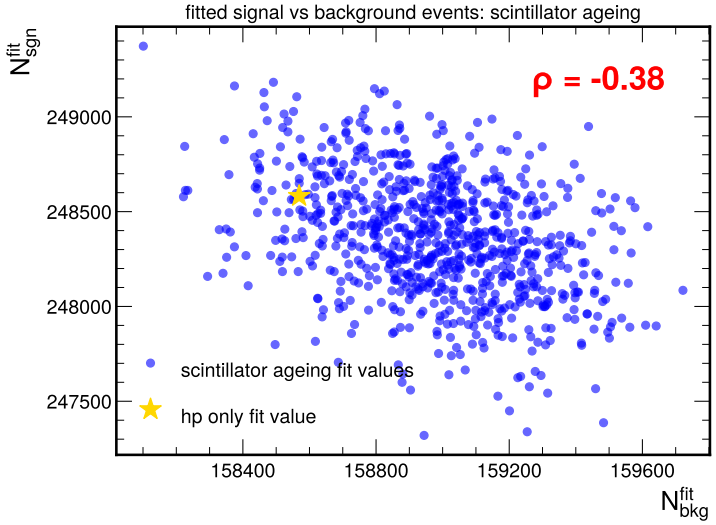

Figure 4.55: Scatter plot of the mean fitted values of signal and background events for 1000 systematic universes (*scintillator ageing*). The correlation coefficient of the distribution is shown in red. The reference fit value obtained for the hadroproduction only case is shown with the yellow star.

in Sec. 4.8.7. In the case of detector-related systematics, the fitted events are *corrected for detector effects* through the nuisance parameters $\vec{\gamma}$ introduced in the fit model, and then used to set a constraint on hadron production weight maps, similarly to the hadron production only case. Therefore, the detector systematic effects are propagated to the ν_e CC interaction rate at detector by reweighting the neutrinos using the new constrained hadroproduction maps. As a reference, the pre- and post-fit ν_e rate with the uncertainty related to the hadron production only systematic are shown in Fig. 4.56. On the left of the Figure is reported the total ν_e rate, whereas on the right only the ν_e rate component from neutrinos produced by *kaons at target* is shown. In the following, the impact of detector systematics is assessed on the ν_e rate component from neutrinos produced by *kaons at target*. In fact, this is the neutrino component directly constrained by the analysis discussed in this thesis.

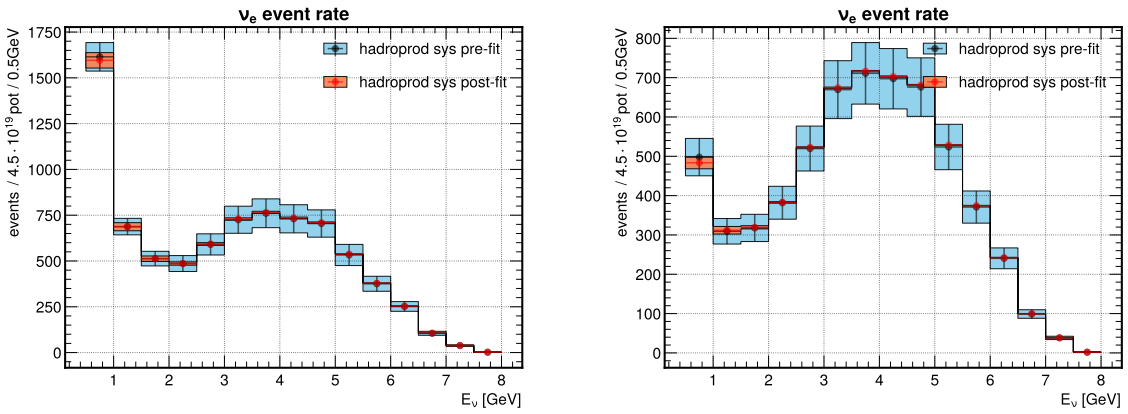

Figure 4.56: (left) Total ν_e rate before (pre-fit, blue) and after (post-fit, red) monitoring of positrons from K_{e3}, with bands representing the neutrino rate uncertainties due to the hadroproduction systematic. (right) Same as the left plot, but for the ν_e rate component from neutrinos produced by *kaons at target*.

The left side of Figs. 4.57, 4.58 and 4.59 report the post-fit ν_e rate together with their hadron production uncertainty (blue band) and the three considered detector systematics (red band). The corresponding relative errors for the hadron production and detector effects are shown on the right side of the same figures. The results indicate that the impact of the detector systematics is subdominant compared to that of hadroproduction, remaining below the 1% level.
To summarize the results, all the post-fit detector-related systematics (calibration uncertainty, calibration bias and scintillator ageing) are shown in Fig. 4.60 and compared to the post-fit hadron production systematic, considering the ν_e rate component from neutrinos produced by *kaons at target*. The total impact of detector systematics on the neutrino rate, shown by the blue line in Fig. 4.60, is evaluated assuming that all the three contributions are uncorrelated, and is therefore obtained by summing them in quadrature. These results show that the impact of detector systematics on the neutrino rate at the detector is subdominant compared to the hadroproduction systematic, with a contribution on the rate uncertainty below $\sim 0.5\%$.

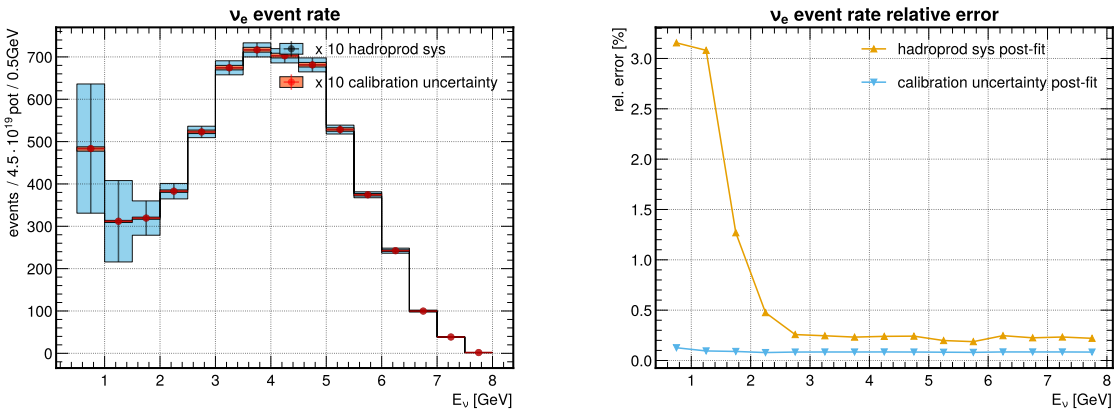

Figure 4.57: **Calibration uncertainty** (left) ν_e rate after monitoring of positrons from K_{e3} (post-fit), with bands representing neutrino rate uncertainties due to the residual hadroproduction systematic (blue) and the impact of calibration uncertainties (red). Only the ν_e rate component from neutrinos produced by kaons at target is shown (see text). Errors have been inflated for visualization purposes. (right) Relative errors on the ν_e rate shown in the left plot. The impact of calibration uncertainty (blue line) is subdominant compared to the hadroproduction systematic (orange line).

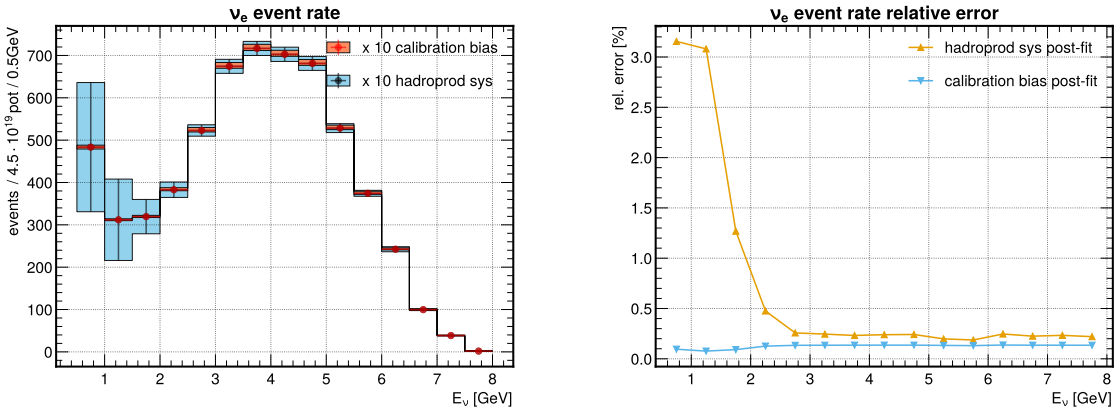

Figure 4.58: **Calibration bias** (left) ν_e rate after monitoring of positrons from K_{e3} (post-fit), with bands representing neutrino rate uncertainties due to the residual hadroproduction systematic (blue) and the impact of calibration bias (red). Only the ν_e rate component from neutrinos produced by kaons at target is shown (see text). Errors have been inflated for visualization purposes. (right) Relative errors on the ν_e rate shown in the left plot. The impact of calibration bias (blue line) is subdominant compared to the hadroproduction systematic (orange line).

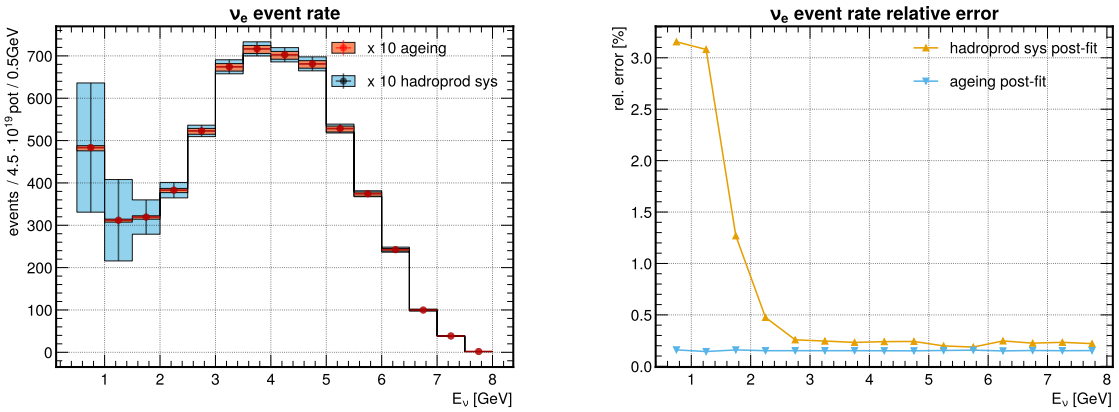

Figure 4.59: **Scintillator ageing** (left) ν_e rate after monitoring of positrons from K_{e3} (post-fit), with bands representing neutrino rate uncertainties due to the residual hadroproduction systematic (blue) and the impact of scintillator ageing (red). Only the ν_e rate component from neutrinos produced by kaons at target is shown (see text). Errors have been inflated for visualization purposes. (right) Relative errors on the ν_e rate shown in the left plot. The impact of scintillator ageing (blue line) is subdominant compared to the hadroproduction systematic (orange line).

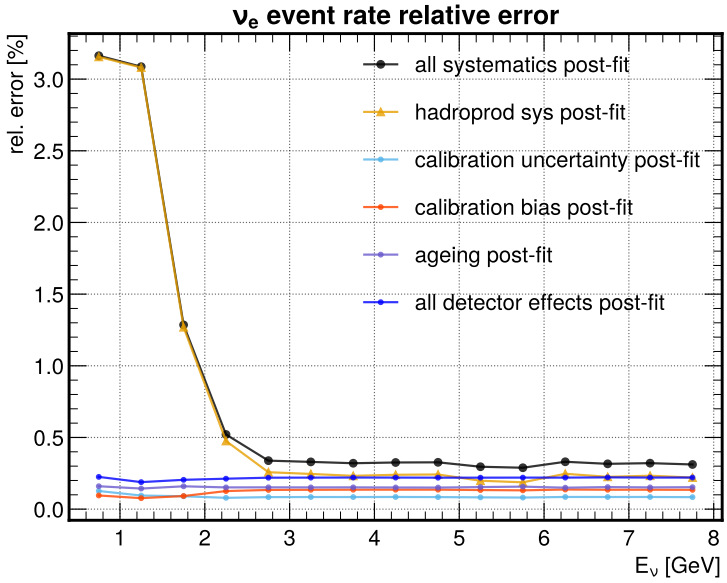

Figure 4.60: Summary plot showing the relative error contributions to the ν_e rate after monitoring of positrons from K_{e3} (post-fit). Only the ν_e rate component from neutrinos produced by kaons at target is shown (see text). The relative error due to the residual hadroproduction systematic (orange) is compared to that from the three considered detector systematics: calibration uncertainty (light blue), calibration bias (red) and scintillator ageing (slate blue). The impact of the total detector systematic, computed as the quadrature sum of the three individual contributions, is also shown (dark blue). The overall systematic uncertainty on the neutrino rate (black), obtained by summing in quadrature the residual hadroproduction and total detector systematics, is below 0.5% above 2.5 GeV.

5 The physics potential of the nuSCOPE monitored and tagged neutrino beam in neutrino cross-section measurements

The nuSCOPE monitored and tagged neutrino beam offers a wide range of unique and powerful cross-section measurements that can be tailored to characterise the physics responsible for the dominant systematic uncertainties in neutrino oscillation analyses. Past and present experiments such as MiniBooNE, T2K, MicroBooNE, NOνA, and MINERνA have provided a wide range of measurements on different targets. This large body of measurements, primarily focused on quasi-elastic-like interactions and in the $\sim 1\,\text{GeV}$ regime, has highlighted important shortcomings in the way in which neutrino-nucleus interactions are modeled. Furthermore, in the run-up to the DUNE experiment, there are no existing or planned high-statistics measurements using an argon target in the energy range relevant for DUNE beam oscillations (i.e., $2-3\,\text{GeV}$ and above). This Chapter provides a non-exhaustive overview of some of the measurements that could be made with nuSCOPE and how they can reduce uncertainties in neutrino oscillation experiments. In particular, their application is focused on supporting the DUNE physics program[1], since the use of the argon-based reference detector described in Sec. 2.4 is assumed. Indeed, the reference neutrino detector is a liquid argon (LAr) detector with 500 ton fiducial mass, positioned 25 m from the end of the decay tunnel. The neutrino detector front face measures $4 \times 4\,\text{m}^2$, for a total length of 22.3 m. The LAr TPC is assumed to have a time resolution improved to 300 ps compared to the current ProtoDUNE, thanks to an enhanced photon detection system as planned for DUNE Phase II upgrades. The physics goals presented in this Chapter are part of a global strategy of cross-section measurements aimed at addressing the main sources of systematic uncertainties for future experiments. They complement past measurements made by the MiniBooNE, T2K, NOνA, MicroBooNE, and MINERνA experiments, and will benefit from the experience we will learn from upcoming measurements at the Fermilab SBN program with ICARUS and SBND. They are also complementary to the measurements that will be performed in situ with the DUNE and Hyper-Kamiokande near detectors. This Chapter focuses on measurements of neutrino cross-sections, but in principle, similar measurements could be made with an antineutrino beam. The work presented in this Chapter constitutes the core of the neutrino cross-section physics studies of the documents submitted in late March 2025 as input to the European Strategy for Particle Physics Update 2026 for the nuSCOPE physics case [70, 106].

Sec. 5.1.1 presents the two methods offered by the nuSCOPE facility to measure the neutrino energy without relying on neutrino interactions: the Narrow Band Off-Axis (NBOA)

[1] Tailored studies assuming a water-based detector and projected cross-section measurements focused on supporting the physics program of Hyper-Kamiokande will be reported in future work.

technique, which achieves a precision of approximately $\mathcal{O}(10\%)$, and the tagging method, which can reach the ultimate precision of $\sim 1\%$. The expected performance of the facility for a range of reference cross-section measurements is detailed in the following sections. In particular, Sec. 5.2 describes the neutrino fluxes and then Sec. 5.3 provides an overview of the simulation to estimate the event rates that can be used for cross-section measurements. Sec. 5.4 focuses on measurements that exploit the NBOA technique and the monitored neutrino beam to first make a ν_μ inclusive energy-dependent cross-section measurement; ν_μ and ν_e differential cross-section measurements are then provided in Sec. 5.5. Sec. 5.6 explains the PRISM technique and how it can be applied using the ν_μ NBOA fluxes to directly measure the ν_e/ν_μ cross-section ratio. Sec. 5.7 explains how the NBOA technique can be used to constrain common backgrounds for neutrino oscillation analyses, in particular the NC π^0 contribution. A set of measurements benefiting from neutrino tagging is then considered in Sec. 5.8, including direct measurements of neutrino energy reconstruction bias that can be used to calibrate DUNE alongside measurements of powerful kinematic quantities to characterise neutrino interactions that are usually only accessible to electron-scattering experiments.

5.1 A priori measurement of the neutrino energy

5.1.1 The Narrow-Band Off-Axis technique

Due to the proximity of the neutrino detector to the neutrino beam (25 m baseline), and to the large size of the detector itself, the detector surface (4×4 m^2) is exposed to a range of incoming neutrino directions. The energy of ν_μ produced in $\pi^+ \to \mu^+\nu_\mu$ and $K^+ \to \mu^+\nu_\mu$ decays is correlated to the emission angle, due to the two-body decay kinematics. As a result, neutrinos interacting at different off-axis angles span different energy ranges. The off-axis technique has already been exploited by a cross-section measurement from the T2K experiment [140], and is essential for the PRISM technique [141], which is planned for use in the DUNE [142] and Hyper-Kamiokande near detectors [143] as well as in the SBND experiment [144]. A key advantage of a narrow-band beam like nuSCOPE is that the off-axis neutrino energy estimation can leverage the parent meson momentum knowledge at $\mathcal{O}(10\%)$, enabling an a priori determination of the neutrino energy without relying on the reconstruction of final-state particles. This is the core concept of the Narrow-Band Off-Axis (NBOA) technique, which can be applied to ν_μ fluxes from $\pi_{\mu\nu}$ and $K_{\mu\nu}$ decays. Neutrinos interacting at different off-axis angles can be identified by defining a set of hollow cylinders within the detector volume, corresponding to different radii where interaction vertices occur. The relationship between the probed neutrino energy E_ν and the radial distance r of the interaction point with respect to the center of the neutrino detector front face is shown in Fig. 5.1. The radial distances covered by the detector surface correspond, in practice, to an angular range of $0 - 4.5°$. By selecting specific radial slices, it is possible to probe a neutrino flux narrower than the total flux. Such a feature is leveraged in the experimental setup by defining 10 radial slices, each spanning a 20 cm window. The contribution of the total ν_μ flux within each radial slice is shown in Fig. 5.2, left. The total flux exhibits the characteristic dichromatic energy spectrum of a narrow-band beam, with a low-energy component from $\pi_{\mu\nu}$ and a high-energy component from $K_{\mu\nu}$. At low energies, there is also a contamination of neutrinos from off-momentum mesons produced in the early stages of the beamline. Notably, this contamination is absent when considering only neutrinos produced in the decay tunnel, as shown in Fig. 5.2, right. As expected, the neutrino energy decreases with increasing radial distances for both $\pi_{\mu\nu}$ and $K_{\mu\nu}$ components. It can be noticed that the sum of the

NBOA fluxes will be slightly lower than the total flux, as only cylindrical sections inside the detector volume are considered, while the exposed face of the detector is square. Therefore, areas near the detector corners are not included in the analysis.

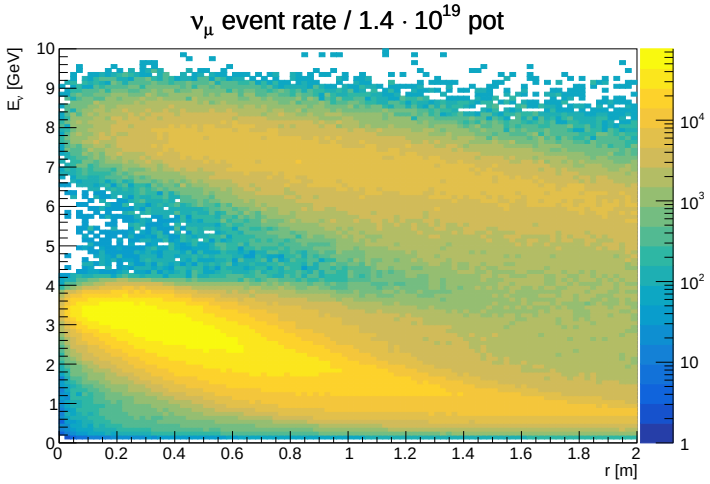

Figure 5.1: Distribution of neutrino energies E_ν from $\pi_{\mu\nu}$ and $K_{\mu\nu}$ decays as a function of the radial distance r of the neutrino interaction vertex on the exposed surface of the detector.

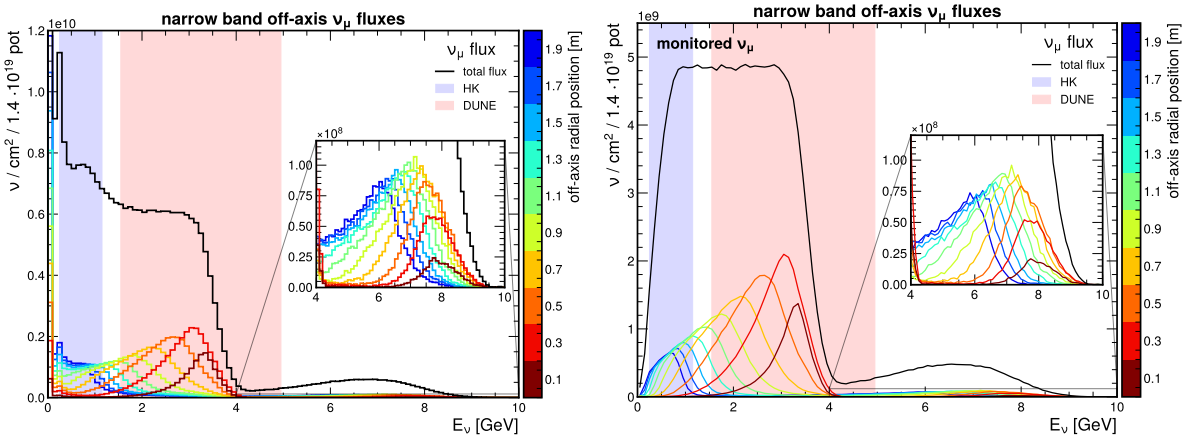

Figure 5.2: ν_μ narrow band off-axis fluxes at different radial distances on the detector surface. The black line shows the total flux (i.e. considering the total squared surface of the exposed detector face) and the colored lines show the fluxes incident on filled discs of 20 cm at different radial positions on the detector surface. The radial position is given by the color scale alongside each plot. (left) Breakdown for all incoming neutrinos. (right) Breakdown only for the monitored neutrinos, i.e. neutrinos produced from decays occurring along the instrumented decay tunnel. An inlay shows a zoom on the contribution of neutrinos from kaon parents in the $4-10$ GeV energy range.

The change in the probed neutrino energy profile with increasing off-axis angles is shown in Fig. 5.3. The $\pi_{\mu\nu}$ and $K_{\mu\nu}$ contributions were separated using an energy cut placed at ~ 4 GeV, depending on the off-axis configuration. Since their shape is not symmetrical, the width of NBOA spectra with asymmetric error bars is reported, representing the 68% percentiles of their distributions with respect to the mean energy. Kaon peaks cover the range from ~ 5 to ~ 8 GeV, whereas pion peaks have energies particularly well-suited for cross-section measurements in the energy domain of next-generation oscillation experiments.

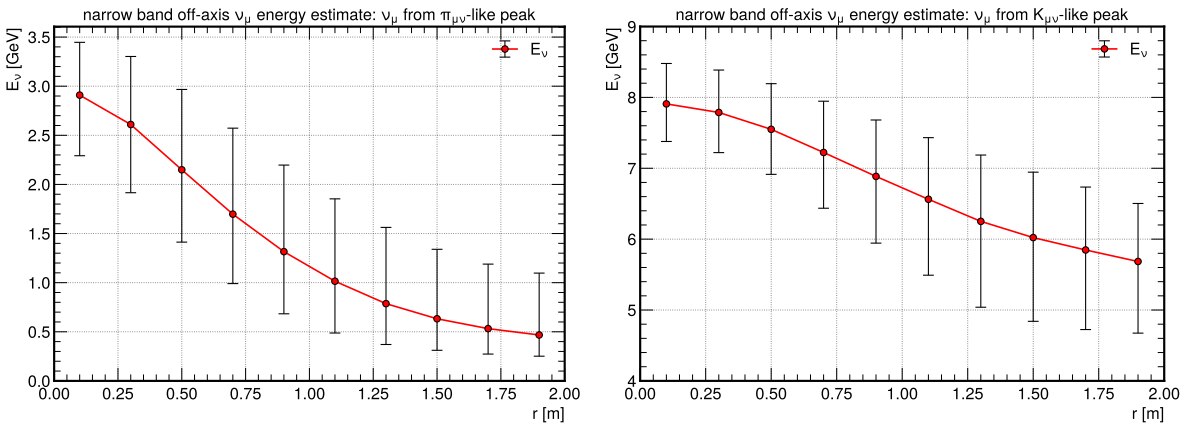

Figure 5.3: Mean neutrino energy $\langle E_\nu \rangle$ as a function of radial distance r for NBOA interaction spectra obtained from $\pi_{\mu\nu}$-like (left) and $K_{\mu\nu}$-like (right) peaks. The asymmetric error bars correspond to regions of E_ν containing 68% of the flux integral on either side of the mean energy (above a threshold of 200 MeV, see Sec. 5.2).

5.1.2 Neutrino energy measurement from tagging

The beam tagging allows for measuring the energy of each tagged neutrino interaction from the kinematics of the associated parent meson decay ($E_{\nu_\mu} = E_{\pi,K} - E_\mu$), independently of the neutrino detector response. The energy resolution is dominated by multiple scattering in the beam and muon spectrometers' tracking planes. The expected energy resolution for tracker planes of 0.5% and 1% radiation length is shown in Fig. 5.4. The neutrino energy resolution lies in the sub-% range, below 0.4% for $E_\nu > 1$ GeV. Such a precise energy resolution allows for measuring muon neutrino cross-sections as a function of energy with a fine-grained binning and negligible smearing between bins. It also gives the opportunity to directly measure the energy smearing and bias in LAr, as needed by the DUNE experiment, by comparing the energy estimated in the LAr detector to that precisely measured by the taggers.

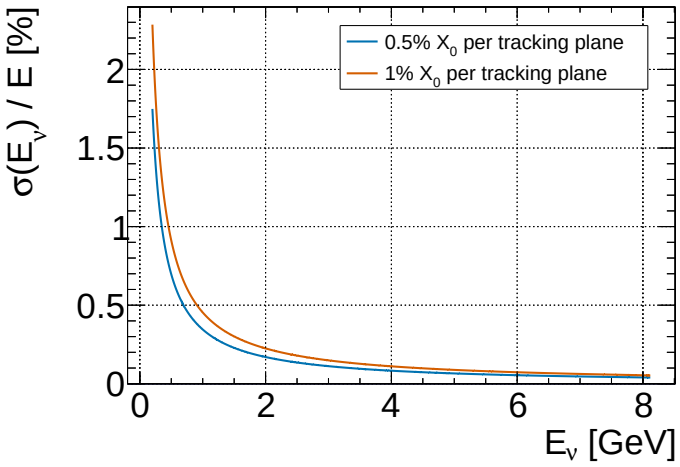

Figure 5.4: Expected energy resolution of tagged neutrino interactions from π and K decays, as a function of the true neutrino energy for a material budget per tracking plane of 0.5% (blue) and 1% (orange) of a radiation length.

5.2 Neutrino fluxes

The total neutrino fluxes are computed as the neutrinos in the detector acceptance and normalized to the neutrino detector 4×4 m^2 front face area and to the total protons on target exposure, which corresponds to $1.4 \cdot 10^{19}$ pot. The total obtained ν_μ and ν_e fluxes are shown in Fig. 5.5. The beamline design is such as to maximize the number of neutrinos produced from meson decays occurring along the instrumented decay tunnel, since these neutrinos can be monitored by measuring the associated charged leptons. The large-angle positrons and muons produced from K_{e3} and $K_{\mu\nu}$ kaon decays can be measured using the instrumented decay tunnel, whereas the forward-going muons produced in $\pi_{\mu\nu}$– outside the decay volume acceptance – can be recorded using an instrumented hadron dump. Nevertheless, a significant fraction of neutrinos in the detector acceptance do not come from meson decays occurring along the instrumented decay tunnel, but rather from other regions of the facility, and thus they cannot be monitored. These neutrinos come from interactions within the graphite target, along the beamline, and in the dumps. In particular, the dominant contribution is below 1 GeV, whereas for higher energies, there are residual contributions due to neutrinos produced along the beamline after the second dipole (early decays before entering the tunnel) and in the hadron dump. For the monitoring technique, these neutrinos represent a source of irreducible background in the energy spectra and, since they cannot be monitored, their contribution to the total flux will have a larger systematic flux uncertainty associated with them. For the tagging technique, their impact is reduced as, in most cases, they won't be matched to a mesonic decay. A breakdown of the neutrino flux into monitored neutrinos and these additional background neutrinos is also shown in Fig. 5.5.

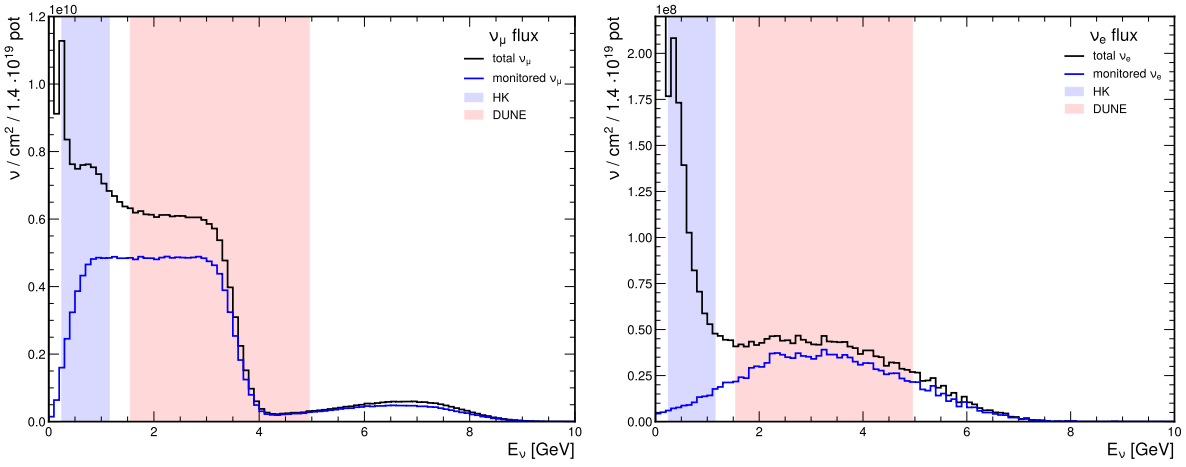

Figure 5.5: Total ν_μ (left) and ν_e (right) fluxes on the surface of the detector. The monitored neutrinos (blue) contributing to the total flux (black) are those produced from decays occurring along the decay volume, i.e. for which the associated charged lepton can be measured using either the instrumented decay tunnel (ν_μ from $K_{\mu\nu}$ and ν_e from K_{e3}) or the instrumented hadron dump (ν_μ from $\pi_{\mu\nu}$). Note that the y-axis range is limited to exclude the large spike at very low energies coming from neutrinos produced in the target region; the spike in the first bin extends to $\sim 8 \cdot 10^{10}$ and $\sim 7 \cdot 10^9$ $\nu\,/\,\text{cm}^2\,/\,1.4 \cdot 10^{19}$ pot for the ν_μ and ν_e fluxes respectively.

In practice, although there is a large contribution from the low-energy unmonitored neutrinos to the total flux, their impact on the observable event rate will be minimal. At $E_\nu \lesssim 200$ MeV, the cross-section for charged current interactions is almost negligible, and it increases with neutrino energy. To improve the readability of the fluxes, we apply a 200 MeV cut to remove this contribution. This cut is applied to both the ν_μ and ν_e

fluxes. As mentioned in Sec. 5.1.1, the monitored ν_μ flux exhibits the typical narrow-band beam dichromatic energy spectrum [59] since two distinct peaks can be identified: a low energy peak at $E_\nu \lesssim 4\,\text{GeV}$ due to neutrinos produced by two-body decay in flight of pions ($\pi^+ \to \mu^+\nu_\mu$) and a high energy peak at $E_\nu \gtrsim 4\,\text{GeV}$ coming from the two-body decay of kaons ($K^+ \to \mu^+\nu_\mu$). On the other hand, since muon decays-in-flight are nearly negligible in nuSCOPE, the ν_e flux is due to neutrinos coming predominantly from the three-body kaon decays ($K^+ \to e^+\pi^0\nu_e$), and a single large peak can be identified.

5.3 Event rates and simulation

5.3.1 Neutrino interaction models and simulation

Neutrino interactions on an argon target are simulated using the GENIE event generator [145, 146] and the total and narrow band off-axis fluxes shown in Fig. 5.5 and Fig. 5.2, respectively. The nominal configuration chosen for the simulation is the `AR23_20i_00_000` comprehensive model configuration (CMC), corresponding to the model chosen by the DUNE Collaboration for upcoming sensitivity studies [147]. The CMC uses a Local Fermi Gas model to describe quasi-elastic (CCQE) interactions [148], with an additional contribution at high nucleon momenta mimicking the impact of short-range correlations (SRCs) [149]. The nucleon axial form factor is described by the z-expansion parametrization, detailed in [150]. Multi-nucleon interactions (mostly two-particle-two-hole interactions, or 2p2h) are simulated with the SuSAv2 model [151, 152]. Resonant interactions (referred to as RES in the following) use the model by Rein and Sehgal [36]. At higher energies, non-resonant hadronization processes are simulated using the custom AGKY model [153] for interactions with an invariant hadronic mass $W < 1.7\,\text{GeV}$, and using the PYTHIA 6 generator [154] for $W > 3\,\text{GeV}$, with a linear interpolation between the two regions. Intra-nuclear transport processes (i.e. final state interactions, or FSI) are described using the GENIE hA2018 model [155]. This model uses tuned parameters according to the work in [156], in which the parameters have been tuned to neutrino-nucleon scattering measurements from bubble chamber experiments. In some studies, this model is compared to an alternative CMC, `G21_11a_00_000`, whose implementation details can be found in [157]. The `G21_11a_00_000` model has two main differences with respect to the `AR23_20i_00_000` model. First, QE and 2p2h interactions are both simulated using the SuSAv2 model, but only using inclusive predictions (i.e., only as a function of lepton kinematics). One of the main consequences of this difference is that the models apply different treatments to the inclusion of long-range correlations inside the nucleus (also known as RPA, or random phase approximations), which will have a significant impact at low energy transfers. Second, the tuned parameters described in [156] are not applied to this CMC, which results in a higher predicted cross-section for inelastic events.

5.3.2 Expected event rates

The GENIE event generator is used to simulate 1 million CC interaction events using the total ν_μ flux, 1 million CC events using the total ν_e flux, and 1 million CC events using each of the ten NBOA total fluxes shown in Fig. 5.2. The NUISANCE framework [158] is then used to facilitate the analysis of these generated events. The total number of expected events is obtained by multiplying the flux integral and the corresponding GENIE cross-section, and scaling this number according to the expected exposure, i.e. $1.4 \cdot 10^{19}$ pot, and the number of argon nucleons in each corresponding detector volume: the whole detector volume for the total fluxes and the volumes of hollow cylinders with

20 cm thick wall at each radial position. As mentioned above, a total fiducial mass of 500 tons of argon in a $4 \times 4 \times 22.3$ m^3 volume located 25 m from the tunnel end is considered. Except for the study detailed in Sec. 5.7, any detector effects, efficiencies, or smearing are not applied. Therefore, for ν_μ and ν_e CC inclusive interactions, it is assumed that the reconstruction efficiency for muons and electrons is 100% and that the smearing on their momenta is much smaller compared to the size of the binning chosen in the studies. This approximation is quite realistic for LAr Time Projection Chambers, given their outstanding granularity and particle identification capabilities. Note, however, that this approximation relies on the assumption that the detector setup can either fully contain muons or it is instrumented with a downstream magnetized spectrometer. The studies presented in the following sections aim to provide an overview of the types of measurements possible with this setup, notably in terms of expected statistics. A complete study will need an estimation of detector effects in the projected measurements, and it is left for future work.
The total CC event rates are shown in Fig. 5.6 and summarised in Tab. 5.1. As expected, the large contribution from the low-energy neutrinos outside of the monitored area in the flux is almost entirely suppressed by the low interaction cross-section. The event rates show that the two-peaked structure of the ν_μ flux and the single peak of the ν_e flux are preserved, and the contributions are enhanced at higher energies due to the larger interaction cross-section. The clear separation between the $\pi_{\mu\nu}$ and $K_{\mu\nu}$ peaks seen in the simulated fluxes is preserved in the event rates. The event rates effectively cover the range of neutrino energies relevant to the DUNE experiment.

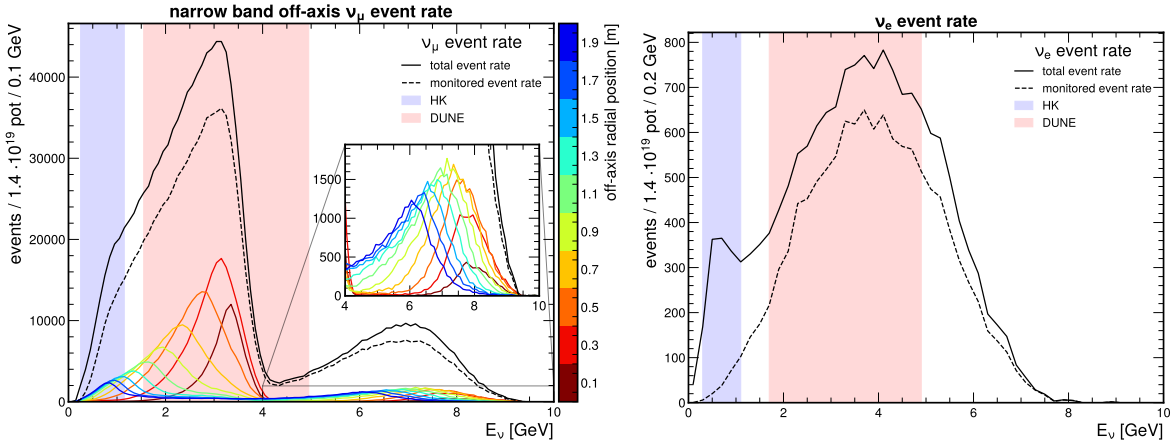

Figure 5.6: Total ν_μ (left) and ν_e (right) charged current event rates. The black solid line shows the total event rate, and the dashed black line the monitored event rate. For the ν_μ case, the NBOA total fluxes are also shown with colored solid lines, where the colors correspond to different radial positions. The HK (blue) and DUNE (red) regions of interest are given by the shaded areas.

5.4 Flux-averaged ν_μ CC-inclusive cross-section measurement

One of the simplest yet most powerful measurements that can be made using a monitored neutrino beam is the measurement of flux-averaged CC cross-sections using different NBOA fluxes. Since the visible event rate for a neutrino experiment results from the convolution of the neutrino flux and the interaction cross-section, it is only possible to measure the total cross-section for a process *averaged* over the range of available energies.

channel	events / $1.4 \cdot 10^{19}$ pot
off-axis ν_μ at $r = 0.1\,\mathrm{m}$	1.0×10^5
off-axis ν_μ at $r = 0.3\,\mathrm{m}$	2.2×10^5
off-axis ν_μ at $r = 0.5\,\mathrm{m}$	2.2×10^5
off-axis ν_μ at $r = 0.7\,\mathrm{m}$	1.8×10^5
off-axis ν_μ at $r = 0.9\,\mathrm{m}$	1.3×10^5
off-axis ν_μ at $r = 1.1\,\mathrm{m}$	1.0×10^5
off-axis ν_μ at $r = 1.3\,\mathrm{m}$	8.3×10^4
off-axis ν_μ at $r = 1.5\,\mathrm{m}$	6.8×10^4
off-axis ν_μ at $r = 1.7\,\mathrm{m}$	5.9×10^4
off-axis ν_μ at $r = 1.9\,\mathrm{m}$	5.2×10^4
total ν_μ	1.3×10^6
total ν_e	1.7×10^4
total monitored ν_μ	1.0×10^6
total monitored ν_e	1.2×10^4
total tagged ν_μ	7.6×10^5

Table 5.1: ν_μ and ν_e event rate integral for `AR23_20i_00_000`. The event rate is given for the total number of events, as well as separated into different radial slices with respect to the center of the exposed detector face.

The flux-averaged cross-section $\langle\sigma\rangle_\Phi$ (in cm^2/nucleon) is defined as follows:

$$\langle\sigma\rangle_\Phi = \frac{N_{\mathrm{events}}}{\Phi N_{\mathrm{tgt}} N_{\mathrm{pot}}} \tag{5.1}$$

where N_{events} is the number of expected events in the detector (as predicted by GENIE), Φ is the neutrino flux integral (expressed in $\nu/\mathrm{cm}^2/\mathrm{pot}$), N_{tgt} is the number of nucleons in the considered volume and N_{pot} is the total exposure in protons on target, i.e. $1.4 \cdot 10^{19}$ pot. This method does not rely on a fine reconstruction of all final-state particles. Indeed, it is equivalent to counting the number of neutrino interactions that have a charged lepton consistent with a muon in the final state, regardless of other products. For wide-band beams, the measurement of the CC inclusive cross-section is intrinsically limited by the range spanned by the neutrino flux, since the neutrino energy is not known on an event-by-event basis. However, by performing a flux-averaged measurement, we avoid building in model dependence into this analysis. To estimate the feasibility and precision of such a measurement, this method can be applied to all the NBOA fluxes. As shown in Fig. 5.2 and Fig. 5.6, the $\pi_{\mu\nu}$-like and $K_{\mu\nu}$-like contributions to both the neutrino flux and the event rate are well separated at $\sim 4\,\mathrm{GeV}$ in true neutrino energy. We therefore apply this $\sim 4\,\mathrm{GeV}$ energy cut, depending on the off-axis configuration, to the obtained event rates[2] and extract two flux-averaged cross-sections for each NBOA flux – once for $\pi_{\mu\nu}$ decays, and once for $K_{\mu\nu}$ decays.
The resulting flux-averaged cross-sections, along with statistical uncertainties, are shown in Fig. 5.7. Several observations can be made:

- Thanks to the large size of the detector assumed in this setup, the statistical errors associated with such a measurement are almost always below 1%. The measurement would therefore be entirely limited by systematic uncertainties. In current high-statistics measurements, the largest source of systematic uncertainty usually stems

[2]Indeed, this cut in true neutrino energy introduces some model dependence in the analysis, as the cut would be made on events as a function of reconstructed neutrino energy. However, due to the small flux in this region and the natural separation between the fluxes, a negligible contribution to the systematic budget of the experiment can be expected.

from the knowledge of the neutrino flux [159, 160]. A systematic uncertainty on the normalization of the flux of 1% has been assumed, coming from the monitored beamline. Still, note that, to complete this study, it is also essential to assign appropriate uncertainties to the unmonitored contributions to the neutrino flux, which will be investigated in future work.

- The energy ranges spanned by the $\pi_{\mu\nu}$ and $K_{\mu\nu}$ peaks cover the vast majority of the DUNE on-axis flux.
- The natural span of the $\pi_{\mu\nu}$ and $K_{\mu\nu}$ fluxes results in a gap in the inclusive cross-section measurements between $3 - 5\,\text{GeV}$. However, this region can be recovered using techniques such as obtaining a virtual flux from the real ν_μ fluxes (the PRISM technique), which will be described in Sec. 5.6.

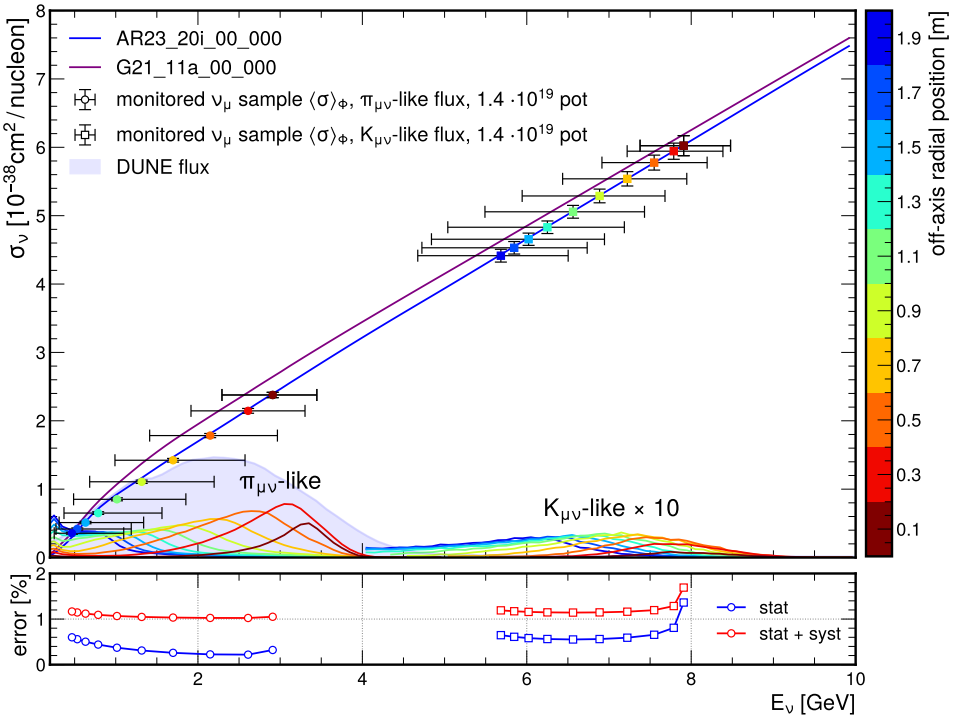

Figure 5.7: Flux-averaged ν_μ CC inclusive cross-section as a function of neutrino energy using the NBOA technique. The colored lines correspond to the NBOA fluxes at different radial distances, given by the colored scale to the right of the figure. The $K_{\mu\nu}$ component of each flux has been artificially inflated by a factor of 10 for illustration purposes. Each NBOA flux has a corresponding predicted measurement point of the same color. Horizontal error bars encase the 68% percentiles with respect to the mean energy for the NBOA fluxes. The underlying figure shows the size of uncertainties due to available statistics (blue) and considering also systematic uncertainties related to the monitored flux prediction, assumed to be ∼1% (red). The measurements are compared to the `AR23_20i_00_000` model (blue) and the `G21_11a_00_000` model (purple). The DUNE near-detector flux is shown for reference using an arbitrary normalization.

It is worth noting that, in principle, other experiments can perform such flux-averaged measurements using off-axis fluxes. This technique is proposed both for DUNE via the DUNE-PRISM [142] setup and by the SBND experiment [144]. However, in the case of DUNE-PRISM, the off-axis fluxes are significantly wider than the NBOA fluxes considered in this work, making a fine-grained analysis of the evolution of the cross-section more difficult. They also cannot easily probe the tail of DUNE neutrino energy distributions. Whilst the SBND-PRISM concept offers exciting possibilities for imminent measurements, it spans only a small range of neutrino energies compared to the NBOA

fluxes in this analysis. More importantly, the measurement proposed in this Chapter will benefit from the percent-level constraint on the integral of the neutrino flux from the monitoring instrumentation, whereas conventional beams are currently limited by flux systematic uncertainties of the order of 10%, which present a bottleneck to precision measurements.

5.5 Flux-averaged ν_μ and ν_e CC double-differential cross-section measurements

Whilst the inclusive cross-section measurement presented in Sec. 5.4 provides a very useful measurement, it only constrains the total CC cross-section, which gets contributions from several channels regulated by different dynamic processes. The relative contribution and the specific underlying physics of each process are fundamental information needed to ensure the success of future experiments. There are a variety of measurements that allow us to probe these individual mechanisms; in this section, only a few examples inspired by measurements made by current neutrino scattering experiments are considered.

5.5.1 ν_μ CC0π differential cross-section

The measurement of differential cross-sections as a function of outgoing lepton kinematics is a notable example. The simplest channel that can be targeted experimentally is the CC quasi-elastic (CCQE) process, also referred to as a one-particle-one-hole (1p1h) process, containing a single lepton and nucleon in the final state. Indeed, it is not possible to measure pure CCQE events, since the interaction takes place inside the nuclear medium and final state interactions result in the same interaction topology from different interaction channels. The closest visible final state in a detector is one with a final state lepton and no pions, known as the CC0π topology. The CC0π topology will have significant contributions from CCQE processes, but also from multi-nucleon interactions (2p2h), resonant pion production where the pion has been absorbed inside the nucleus (RES), or other processes with no pions in the final state. CC0π cross-sections have been extensively measured by neutrino scattering experiments (see e.g. [140, 161, 162]). The interest in measuring the differential cross-section as a function of outgoing lepton kinematics is that the latter maps to the momentum and energy transfer in a neutrino scatter, averaged over the range of available neutrino energies. In addition, inclusive predictions as a function of lepton kinematics are often the only type of predictions available inside neutrino generators from different models. A projected measurement of this double-differential cross-section, using the `AR23_20i_00_000` model, as a function of the muon momentum p_μ and direction with respect to the beam axis $\cos\theta_\mu$ is shown in Fig. 5.8.
The choice of p_μ and $\cos\theta_\mu$ binning was not optimized for the detector setup. Instead, the $\cos\theta_\mu$ binning employed by the T2K experiment in the measurement reported in [140] has been used. The T2K p_μ binning has been refined to have at least 50 expected events in each bin. From Fig. 5.8, it is apparent that the dominant channel across all $\cos\theta_\mu$ ranges is the CCQE process, but we also see contributions from 2p2h, RES, and other processes, as expected for this topology. The muon angle is correlated with the energy transfer ω in the interaction – it is clear that the range of muon momenta increases with increasing values of $\cos\theta_\mu$. Importantly, the projected statistical errors on the cross-section measurement are reported, assuming two different neutrino interaction models. Across all bins, this error is below 10%. In the peak regions, the error is below 1%. It is important to note that this level of statistical uncertainty is comparable to that of conventional cross-section experiments, and at this level of precision, such measurements

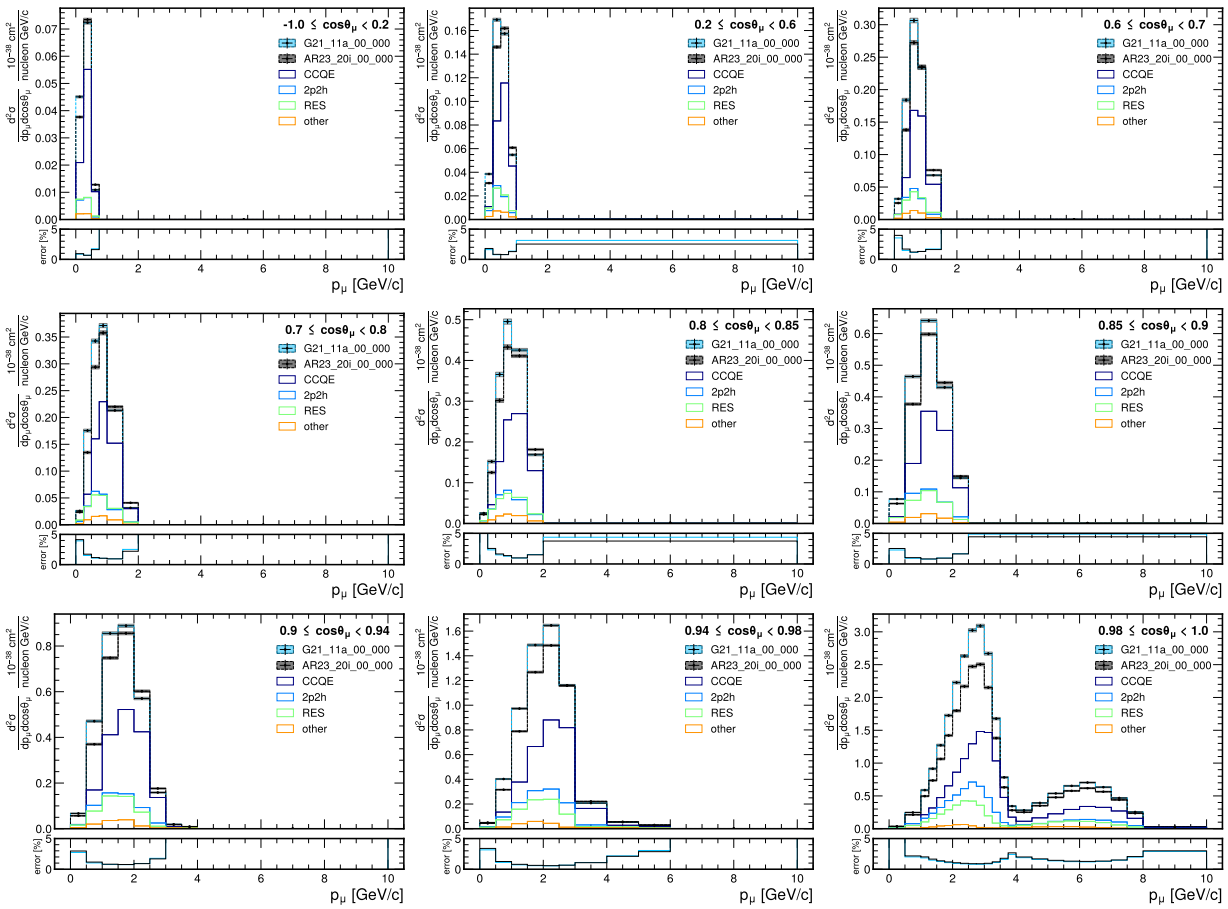

Figure 5.8: Projected measurement of ν_μ flux-averaged cross-section for CC0π events as a function of muon momentum p_μ in bins of $\cos\theta_\mu$, using the `AR23_20i_00_000` model (black line) and the `G21_11a_00_000` model (blue line) with error bars. The `AR23_20i_00_000` prediction is also broken down by true interaction mode, with each mode represented by solid colored lines, as indicated in the legend. The statistical error associated with each measurement is shown beneath each of the main figures

become systematically limited. However, the largest source of systematic uncertainty on conventional measurements comes from the modeling of flux uncertainties, at the level of 10%, whereas the monitored neutrino beam allows this source to be reduced to the level of 1%. The projected measurement is compared with one using a different model, `G21_11a_00_000`. The two models predict different values for the differential cross-section across all angular regions. The statistical power of the projected measurement is enough to discriminate between the two models, and the different kinematic regions are sensitive to distinct aspects of modeling differences. For instance, at high scattering angles and intermediate momenta, the models differ primarily in the strength of the cross-section for resonant pion production processes. At forward scattering angles, the models apply different treatments for the description of collective nuclear effects (such as nuclear screening). The latter, in particular, is one of the dominant sources of systematic uncertainties for neutrino oscillation experiments, whether using beam or atmospheric neutrinos.

5.5.2 ν_e double differential cross-section

Similar to the projected measurement for muon neutrinos, there is also interest in measuring the differential cross-section for electron neutrinos. Fig. 5.9 illustrates a projected measurement as a function of calorimetric observables, E_{avail} and q_3. The available, or recoil, energy E_{avail} is the calorimetric sum of the outgoing hadronic state. Given the low energy transfers of interest for modern accelerator experiments $\mathcal{O}(0.1 - 5\,\text{GeV})$, it is a proxy for the energy seen in a detector with a high tracking threshold, where individual charged pions are not identified, and no neutron energy is measured [163]. The available, or recoil, energy E_{avail} is defined as follows:

$$E_{\text{avail}} = \sum_{i=\pi^{\pm},p} T_i + \sum_{i=\pi^0,\gamma} E_i \tag{5.2}$$

where $\sum_{i=\pi^{\pm},p} T_i$ is the sum of proton and charged pion kinetic energies, and $\sum_{i=\pi^0,\gamma} E_i$ is the sum of total energies deposited by neutral pions and photons. This is equivalent to MINERνA's definition of E_{avail} [164]. This variable is particularly interesting as it provides a proxy for the energy transfer in a neutrino interaction. q_3 is the projection of the momentum transfer vector onto the incoming neutrino direction, which can be computed according to:

$$q_3 = \sqrt{Q^2 + q_0^2} \tag{5.3}$$

where $q_0 = \omega$ is the energy transfer. $Q^2 = -q^2$ is the square of the four-momentum transfer, which can be computed as follows:

$$Q^2 = 2(E_l + q_0)(E_l - |\vec{p}_l| \cos\theta_l) - m_l^2 \tag{5.4}$$

where $E_l, \vec{p}_l, \cos\theta_l$ and m_l are the outgoing lepton energy, momentum vector, direction with respect to the neutrino beam and lepton mass, respectively. For this illustration, the reconstructed q_3 from particle kinematics are assumed to have been unfolded to the true value of q_3 [165]. It is important to notice that this is a model-dependent procedure when using a wide neutrino beam, but the model dependence can be mitigated at nuSCOPE by using tagged neutrinos, whose energy is well-known.

As in the case of the ν_μ differential cross-section measurement, the projected statistical errors are below 5% for the vast majority of analysis bins. As in the ν_μ CC double-differential measurement, the reference model is compared to the alternative

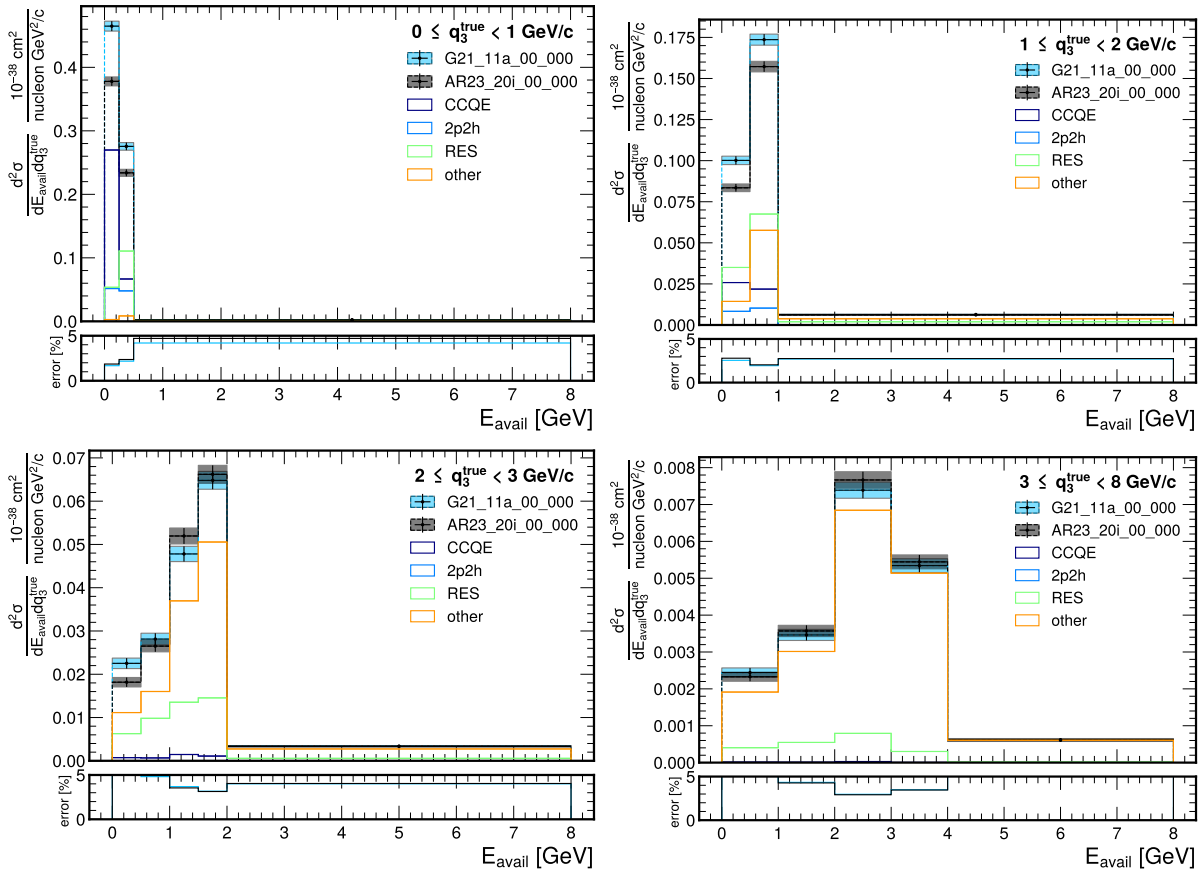

Figure 5.9: ν_e flux-averaged cross-section for CC inclusive events as a function of available energy E_{avail} in true three-momentum transfer q_3^{true} bins, broken down by interaction mode.

`G21_11a_00_000` model. Large differences between the two models can be observed, in particular, at low values of E_{avail} and low q_3. This is a region corresponding to low energy and momentum transfer, where differences between ν_μ and ν_e cross-sections become significant due to the relative contributions of the lepton mass differences. This proof of principle illustrates that this measurement can be achieved with good statistical precision, and, as in the case of the ν_μ CC double differential measurement, with low associated flux uncertainties of $\sim 1\%$.

5.6 Measurement of the ν_e/ν_μ cross-section ratio

One of the largest sources of systematic uncertainty for future oscillation experiments is related to the differences between electron and muon neutrino cross-sections. Long baseline oscillation experiments are in general designed to measure ν_e appearance in a ν_μ beam; nonetheless, they have few direct constraints on the ν_e cross-section – the latter often represent small intrinsic contamination in the neutrino flux probed with the near detector, and they span energies often higher than those of appearance events. The general strategy of oscillation experiments is to extrapolate the constraints obtained at the near detector using primarily muon neutrinos, by relying on models that translate such constraints for the electron neutrino cross-section. If lepton universality is assumed, the only differences between ν_μ and ν_e cross-sections are due to terms in which the lepton mass becomes significant, which become important at relatively low energy transfers [166, 167]. In these regions, nuclear models predict differences of the order of 3% [167] on the $\sigma(\nu_e)/\sigma(\nu_\mu)$ ratio. To be competitive with the differences predicted by theoretical models, a direct measurement of $\sigma(\nu_e)/\sigma(\nu_\mu)$ would require an associated error of less than 3%. Such a direct measurement is challenging to perform, since current artificial beams do not produce similar ν_μ and ν_e fluxes, meaning that cross-section measurements of each are integrated over different fluxes and thus cannot be directly compared. In this section, the prospects of measuring the $\sigma(\nu_e)/\sigma(\nu_\mu)$ ratio with a monitored neutrino beam using the NBOA technique are discussed to obtain a virtual flux of muon neutrinos that matches the shape of the flux of electron neutrinos from three-body decays. Such a measurement employs the PRISM technique [141], which consists of performing linear combinations of real fluxes in order to obtain an arbitrary target flux shape. These fluxes will be used to extract the total flux-averaged cross-section for ν_e and ν_μ interactions, and their associated ratio.

5.6.1 PRISM analysis using narrow band off-axis fluxes

The PRISM technique [141, 168, 169] aims to provide measurements at different off-axis positions with respect to the neutrino beam and to create a virtual flux from a linear combination of the neutrino fluxes measured at different off-axis positions. The PRISM concept can thus be used to create a *virtual flux* φ to reproduce the shape of an arbitrary *target flux* ϕ from a set of linear combinations of the different off-axis fluxes. In nuSCOPE, the ν_μ narrow band off-axis fluxes obtained at different radial positions with respect to the center of the neutrino detector can be linearly combined to create a virtual flux to match the shape of a given target flux.
In principle, an arbitrary target flux $\phi(E_\nu)$ can be reproduced from a proper linear combination of off-axis fluxes $\Phi_j(E_\nu)$ measured at different off-axis positions j according to:

$$\phi(E_\nu) = \sum_j c_j \Phi_j(E_\nu) \tag{5.5}$$

Since the off-axis neutrino fluxes $\Phi_j(E_\nu)$ are binned in neutrino energy, Eq. (5.5) can be written in a more compact form as a set of linear equations to be solved in the coefficient vector $\vec{c}$, as follows:

$$\vec{\phi} = \Phi \cdot \vec{c} \tag{5.6}$$

where Φ is a matrix such that $\Phi_{i,j}$ is the expected flux at energy bin i and off-axis position j, whereas $\vec{\phi}$ is a vector such that ϕ_i is the target flux at energy bin i. Therefore, given the flux matrix Φ and the target flux $\vec{\phi}$, the coefficient vector $\vec{c}$ solving Eq. (5.6) can be used to create the virtual flux $\vec{\varphi}$ according to:

$$\vec{\varphi} = \Phi \cdot \vec{c} \tag{5.7}$$

thus providing an approximation of the target flux $\vec{\phi}$. Moreover, the set of coefficients $\vec{c}$ can be used to linearly combine the event rates measured at each off-axis position, obtaining a virtual event rate $\vec{n}$ corresponding to the virtual flux $\vec{\varphi}$, as follows:

$$\vec{n} = N \cdot \vec{c} \tag{5.8}$$

where N is the event rate matrix corresponding to the flux matrix Φ. In this analysis, the input off-axis fluxes are split into the pion and kaon parent contributions with a cut at $\sim 4\,\text{GeV}$ neutrino energy, as described in Sec. 5.4. The flux matrix Φ and event rate matrix N obtained using narrow band off-axis fluxes and projected event rate are shown in Fig. 5.10, respectively. The units used in the flux matrix are neutrinos in detector acceptance normalized to the $4 \times 4\,\text{m}^2$ front face area of the neutrino detector.

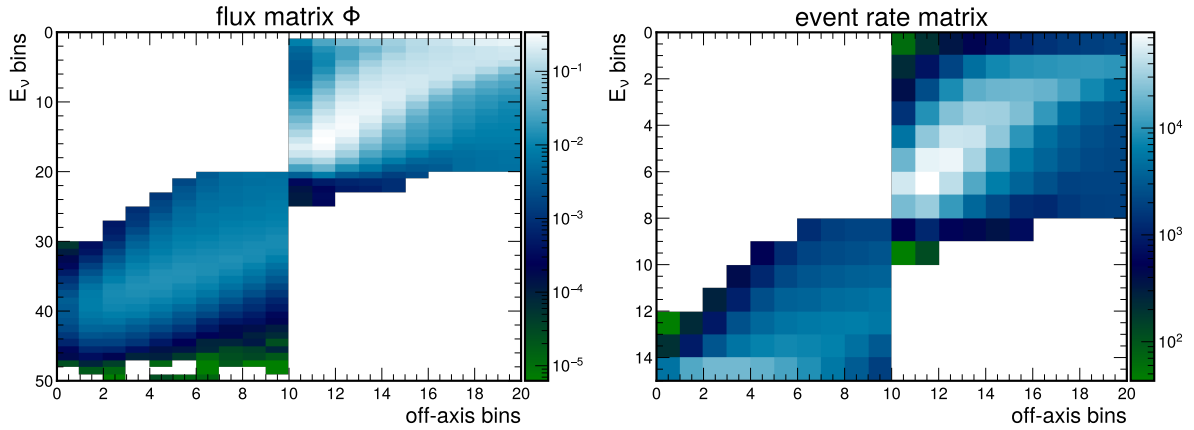

Figure 5.10: Flux matrix Φ $[\nu\,/\,\text{cm}^2]$ (left) and event rate matrix N (right) obtained using narrow band off-axis fluxes. The neutrino fluxes are ordered for increasing values of off-axis angle, i.e. for increasing radial distances. The $K_{\mu\nu}$-like fluxes are shown first and $\pi_{\mu\nu}$-like fluxes follow. Therefore, as the off-axis angle increases, the energy decreases.

Since the virtual event rate bin content is $n_i = \sum_j N_{i,j} \cdot c_j$, using error propagation the bin-by-bin event rate statistical uncertainty can be computed as $\delta n_i^2 = \sum_j \left(c_j \sqrt{N_{i,j}}\right)^2$; therefore the *total event rate statistical uncertainty* can be estimated as follows:

$$\delta n = \left[\sum_i \delta n_i^2\right]^{1/2} = \left[\sum_{i,j} c_j^2 N_{i,j}\right]^{1/2} \tag{5.9}$$

The statistical uncertainty can be estimated in a more accurate way using a numerical method based on the multi-universes approach [130]. For each universe, the event rate bin

contents are varied according to Poisson statistical fluctuations and, for a given $\vec{c}$ solution, an ensemble of N statistically fluctuated virtual event rate histograms is obtained. The event rate covariance matrix can be computed according to:

$$\mathrm{cov}[j,k] = \frac{1}{N-1}\sum_{u}^{\mathrm{histo}}(\nu_j - n_{uj})(\nu_k - n_{uk}) \tag{5.10}$$

where ν is the mean virtual event rate and n_u the virtual event rate of a certain universe u.

It is important to stress that the set of linear equations encoded in Eq. (5.6) does not provide an exact and unique solution, since it is an ill-posed linear algebra problem. If the set of equations were solved by matrix inversion, namely $\vec{c} = \Phi^{-1}\cdot\vec{\phi}$, the statistical fluctuations in the target flux would lead to large variations in a highly degenerate solution [170]. Therefore, any subsequent analysis using the virtual flux would have very large statistical uncertainties stemming from the implicit subtraction of large numbers in Eq. (5.5). The Tikhonov regularization method [171, 172] can be used to find a stable approximated solution with less variance, where the variations between adjacent elements of $\vec{c}$ are reduced. This introduces a bias to reduce the variance, which can be adjusted via a regularization strength. The set of coefficients solution $\vec{c}$ can be obtained by minimizing:

$$\left\|\Phi\cdot\vec{c} - \vec{\phi}\right\|^2 + \|\Gamma\cdot\vec{c}\|^2 \tag{5.11}$$

where Γ is the regularization matrix defined as follows:

$$\Gamma = \tau\cdot A \tag{5.12}$$

where τ is a parameter determining the strength of the regularization and the A regularization matrix has the following form:

$$A = \begin{bmatrix} 1 & -1 & 0 & 0 & \dots & 0 & 0 \\ 0 & 1 & -1 & 0 & \dots & 0 & 0 \\ 0 & 0 & 1 & -1 & \dots & 0 & 0 \\ 0 & 0 & 0 & 1 & \dots & 0 & 0 \\ \vdots & \vdots & \vdots & \vdots & \ddots & \vdots & \vdots \\ 0 & 0 & 0 & 0 & \dots & 1 & -1 \\ 0 & 0 & 0 & 0 & \dots & 0 & 0 \end{bmatrix} \tag{5.13}$$

thus forcing the adjacent elements of $\vec{c}$ to be similar, since the regularization is on the first derivative of the coefficient solution $\vec{c}$. The set of coefficients $\vec{c}$ can be computed using Tikhonov regularization according to the general formula [170]:

$$\vec{c} = \left[\Phi^T P\,\Phi + \Gamma^T\Gamma\right]^{-1}\Phi^T P\vec{\phi} \tag{5.14}$$

where P is a diagonal matrix which can be used to down-weight regions of neutrino energy where it is difficult to achieve a good mapping between the real fluxes and the target one. This can be used, for instance, to prevent the lowest and highest neutrino energies from affecting the coefficients calculation, in order to prioritise the achievement of a good matching between the virtual $\vec{\varphi}$ and the target flux $\vec{\phi}$ in the region of interest. In this analysis, the simplest scenario where $P = \mathbb{1}$ is considered, and Eq. (5.14) reduces to:

$$\vec{c} = \left[\Phi^T\,\Phi + \Gamma^T\Gamma\right]^{-1}\Phi^T\vec{\phi} \tag{5.15}$$

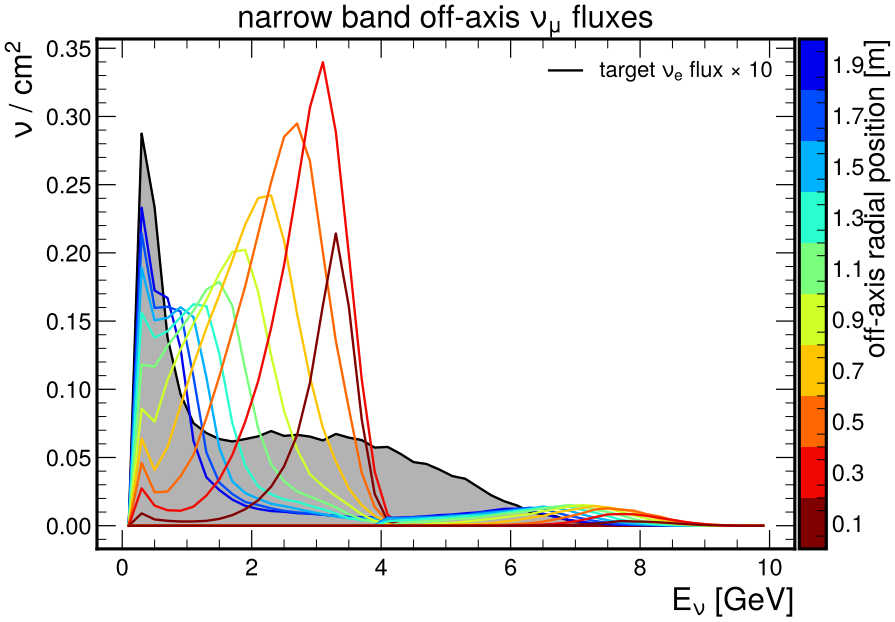

Figure 5.11: ν_e target flux and ν_μ narrow band off-axis fluxes. The ν_e target flux is shown in grey and inflated by a factor of 10 to make it comparable with the ν_μ fluxes. The colored lines represent different NBOA fluxes, and the line color corresponds to the color scale showing the radial position with respect to the center of the exposed detector face.

Since, in principle, the target neutrino flux is arbitrary, an appropriate choice is to use the ν_e flux measured by nuSCOPE as target and then to create a virtual ν_e flux from the ν_μ narrow band off-axis fluxes. This choice makes possible an estimation of $\sigma(\nu_e)/\sigma(\nu_\mu)$ cross section ratio, as will be discussed in the following.
To facilitate a stable solution, a coarse bin width of 0.2 GeV is employed both for the ν_e and ν_μ neutrino flux histograms and a 0.2 GeV energy cut is applied to remove the first bin from the analysis (where the interaction cross-section is negligible). The bin width used for the ν_e and ν_μ event rate histograms is 0.5 GeV (except for the last bin, which is coarser); indeed, a larger bin width is employed to reduce statistical fluctuations in poorly populated bins. The ν_e target flux and ν_μ narrow band off-axis fluxes are shown in Fig. 5.11, with a cut at 0.2 GeV. The ν_e target flux is shown in grey and inflated by a factor 10 to make it comparable with the ν_μ fluxes.
An important observation for the PRISM analysis using the NBOA technique is that, at each off-axis position, the ν_μ flux is dichromatic and two peaks corresponding to $\pi_{\mu\nu}$-like and $K_{\mu\nu}$-like events are present. The $\pi_{\mu\nu}$-like and $K_{\mu\nu}$-like peaks have different amplitudes due to the branching ratio of corresponding decays; therefore, if a two-peaked flux were used for each off-axis configuration, it would be difficult to reproduce an arbitrary target flux, since the virtual reconstructed one would have a preference for a double peak shape, due to their linear combinations. For the proof-of-concept study presented in this Section, the choice was to separate the $\pi_{\mu\nu}$-like and $K_{\mu\nu}$-like using an energy cut at ~ 4 GeV, depending on the off-axis configuration. This assumption is justified by the fact that, when using the NBOA technique, the $\pi_{\mu\nu}$-like and $K_{\mu\nu}$-like populations are generally well separated. As a result, an energy cut can be applied to effectively distinguish between them. In reality, the NBOA fluxes are not well separated for all off-axis configurations (in particular at high off-axis position in the current reference detector setup) because of background neutrinos coming from regions of the facility different from the decay tunnel, and in addition, migrations between the two populations can be expected because of the

reconstructed neutrino energy. The benefit offered by the $\pi_{\mu\nu}$ and $K_{\mu\nu}$ flux separation is that, as long as they can be considered as independent fluxes, the number of off-axis configurations is doubled and, as a result, the same applies for the number of coefficients $\vec{c}$ - i.e. degrees of freedom - exploited to reproduce the shape of the target flux. Note that in Fig. 5.10 the $\pi_{\mu\nu}$-like and $K_{\mu\nu}$-like fluxes measured in the same radial position are reported in different off-axis bins such to create a flux matrix which is more effective in terms of flux matching capabilities. An example of $\vec{c}$ solution according Eq. (5.15) for a non optimized value of the regularization strength $\tau = 10^{-5}$ is shown in Fig. 5.12, and the corresponding virtual flux and event rate computed according to Eqs. (5.7) and (5.8) are shown in Fig. 5.13, respectively. The presence of a dip at $\sim 4\,\text{GeV}$ can be explained by the difficult task of combining off-axis fluxes in an energy region corresponding to $\pi_{\mu\nu}$-like and $K_{\mu\nu}$-like peaks separation, where fluxes are poorly populated and flux matching can be difficult to achieve.

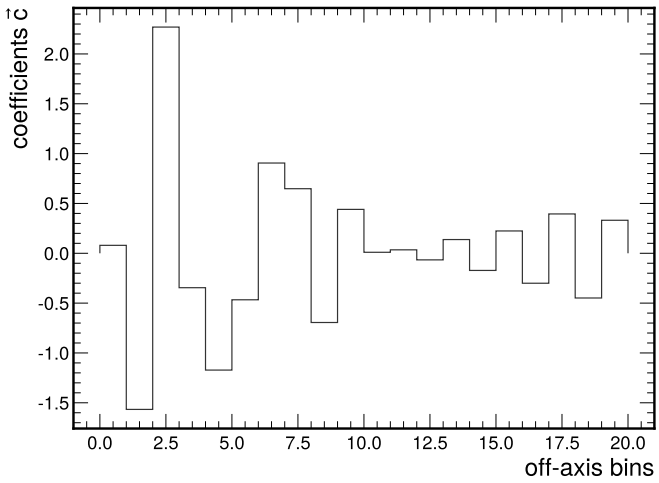

Figure 5.12: Solution coefficients $\vec{c}$ for a non optimized value of the regularization strength $\tau = 10^{-5}$.

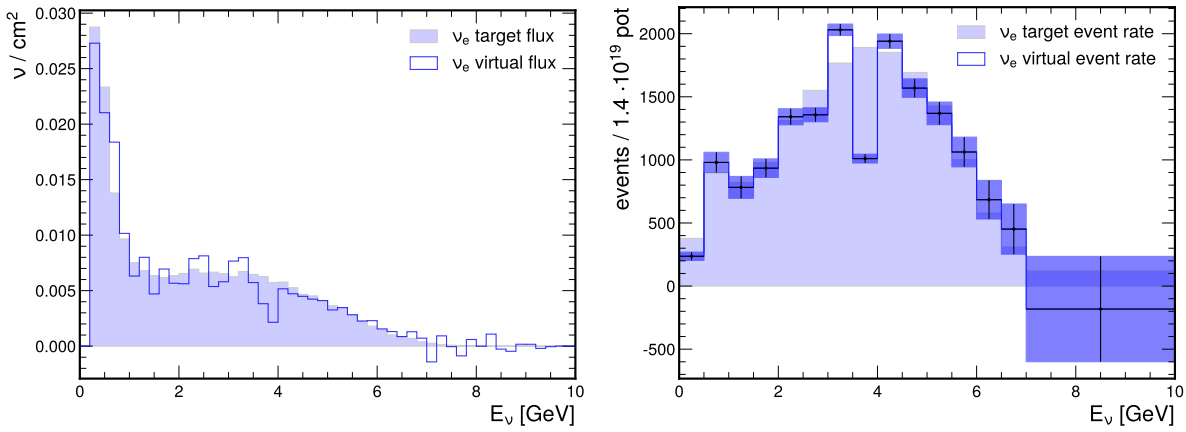

Figure 5.13: Virtual flux (left) and virtual event rate (right) for a not optimized value of the regularization strength $\tau = 10^{-5}$. The virtual ν_μ flux or event rate (blue lines) obtained by applying the PRISM technique are compared with the target ν_e flux or event rate (filled blue area).

The Tikhonov regularization condition in Eq. (5.11) introduces a bias in the result in order the make the coefficients vary smoothly among themselves. The smoothness of the coefficient variations is determined by the regularization parameter τ. Therefore, the

choice of the regularization strength τ is pivotal for a PRISM analysis since the smoothness of the linear combination coefficients controls the size of the statistical uncertainties. The optimization of this sensitive parameter is, in general, performed using an "L-curve scan". The idea of the L-curve scan is to look at the graph of two variables L_x and L_y, defined as follows:

$$\begin{aligned} L_x &= \log \left\| \Phi \cdot \vec{c} - \vec{\phi} \right\| \\ L_y &= \log \left\| A \cdot \vec{c} \right\| \end{aligned} \tag{5.16}$$

and to locate the point where the curvature is maximal [173]. Note that the L_x term measures the agreement of the virtual and target flux (bias term), whereas L_y measures the agreement of $\vec{c}$ with the regularization condition. For $\tau \to 0$ the value of L_x is minimal and L_y is maximal, since $\left\| \Phi \cdot \vec{c} - \vec{\phi} \right\| \to 0$. As τ gets large, L_x increases whereas L_y gets small. In general, the parametric plot of L_y against L_x shows a kink and is L-shaped. The optimum value of τ generally corresponds to the kink location, and its value is chosen to maximize the curvature. The curvature $\mathcal{C}$ of the L-curve is computed according to:

$$\mathcal{C} = \frac{d^2 L_y dL_x - d^2 L_x dL_y}{[(dL_x)^2 + (dL_y)^2]^{\frac{3}{2}}} \tag{5.17}$$

where the first and second derivatives of $L_{x/y}$ with respect to τ are approximated using cubic spline parametrization. The point of maximal curvature $\mathcal{C}$ is determined using a cubic spline parametrization of $\mathcal{C}(\tau)$ [173]. The L-curve scan and the curvature $\mathcal{C}(\tau)$ profile are shown in Fig. 5.14 respectively, with the τ value maximizing the curvature.

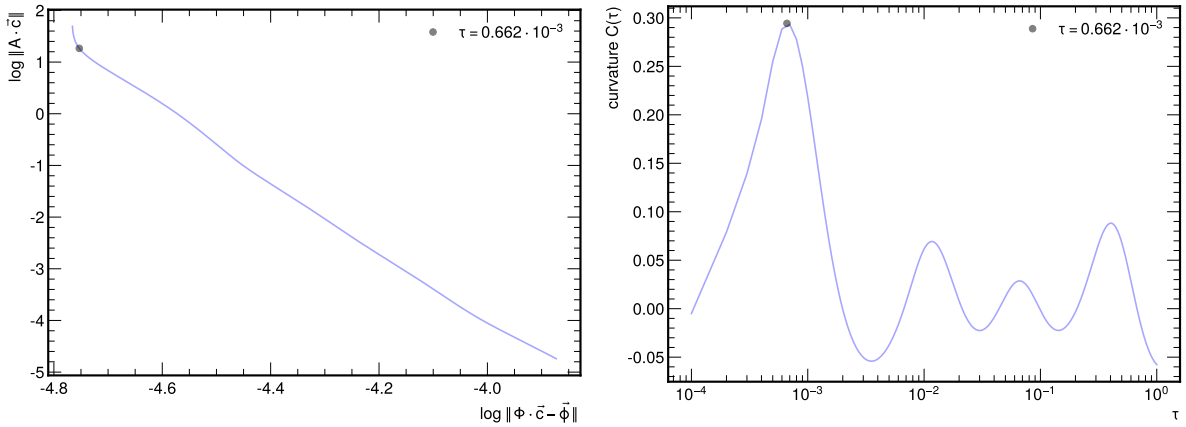

Figure 5.14: L-curve scan (left) and curvature $\mathcal{C}(\tau)$ profile (right), showing an optimized value of the regularization strength τ value maximizing the curvature.

It is also important to note that as $\tau \to 0$ the bias is minimal, but the spikiness of the coefficients $\vec{c}$ is maximal, since the smoothness of the regularized solution is minimal. If no regularization is applied, wild statistical fluctuation dominates in the solution. Therefore, the spikiness/smoothness of the solution $\vec{c}$ and the event rate statistical uncertainty are, in general, anti-correlated and an over-regularized solution is not preferable, since the virtual event rate prediction is dominated by statistical fluctuations.
An alternative method chosen to find the optimum τ value is to scan the trend of the total event rate statistical uncertainty as a function of τ parameter, and to determine the value corresponding to a total statistical uncertainty of 2 or 3%, as shown in Fig. 5.15.
The final choice for the regularization strength τ is to obtain a total statistical uncertainty of 2%, i.e $\tau = 1.25 \cdot 10^{-3}$. The set of coefficients $\vec{c}$ solution is shown in Fig. 5.16, and it

can be noted that the relative variation among adjacent bins is reduced with respect to the non-optimized solution shown in Fig. 5.12. The resulting virtual flux, compared to the target flux, is shown in Fig. 5.17, right. Even if there is room for further optimisation of the regularisation and binning scheme, the fluxes match quite well. The remaining discrepancy could be accounted for using small model-dependent corrections, where the model dependence is further mitigated by neutrino tagging.

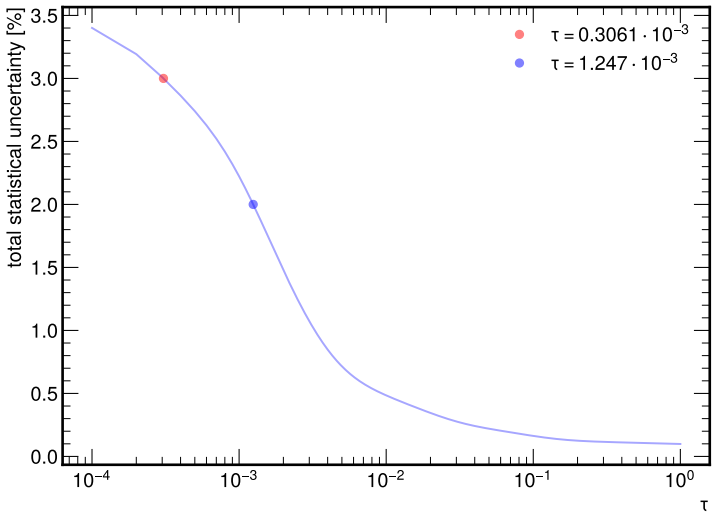

Figure 5.15: Total statistical uncertainty as a function of the regularization parameter τ. The optimum values for τ are chosen as the ones corresponding to a given total statistical uncertainty (2% or 3%).

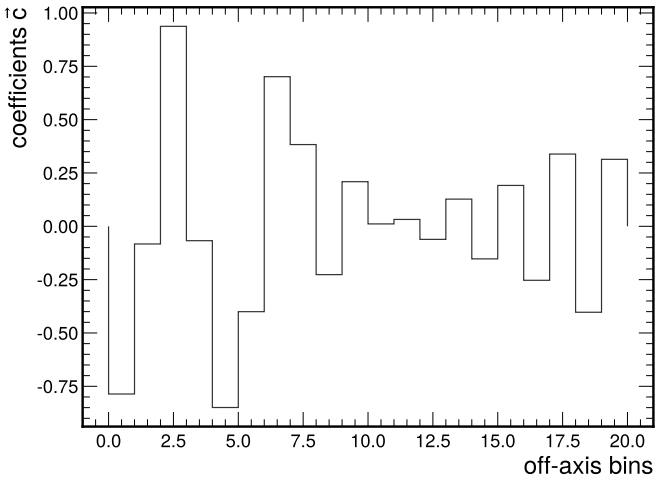

Figure 5.16: Solution coefficients $\vec{c}$ for the optimized value of the regularization strength τ corresponding to a total statistical uncertainty of 2%.

The possibility of creating a virtual flux which matches the target electron neutrino flux from linear combinations of muon neutrino fluxes by means of the PRISM concept makes it possible to access the $\sigma_{\nu_e}/\sigma_{\nu_\mu}$ ratio, according to:

$$\frac{\sigma_{\nu_e}}{\sigma^{\texttt{virt}}_{\nu_\mu}} = \frac{N_{\nu_e}}{N^{\texttt{virt}}_{\nu_\mu}} \cdot \frac{\int \Phi^{\texttt{virt}}_{\nu_\mu}(E_\nu)\, dE_\nu}{\int \Phi_{\nu_e}(E_\nu)\, dE_\nu} \tag{5.18}$$

where Φ_{ν_e} and N_{ν_e} are the genuine ν_e flux and event rate measured by nuSCOPE whereas Φ_{ν_μ} and N_{ν_μ} are the virtual flux and event rate built from linear combinations of ν_μ fluxes

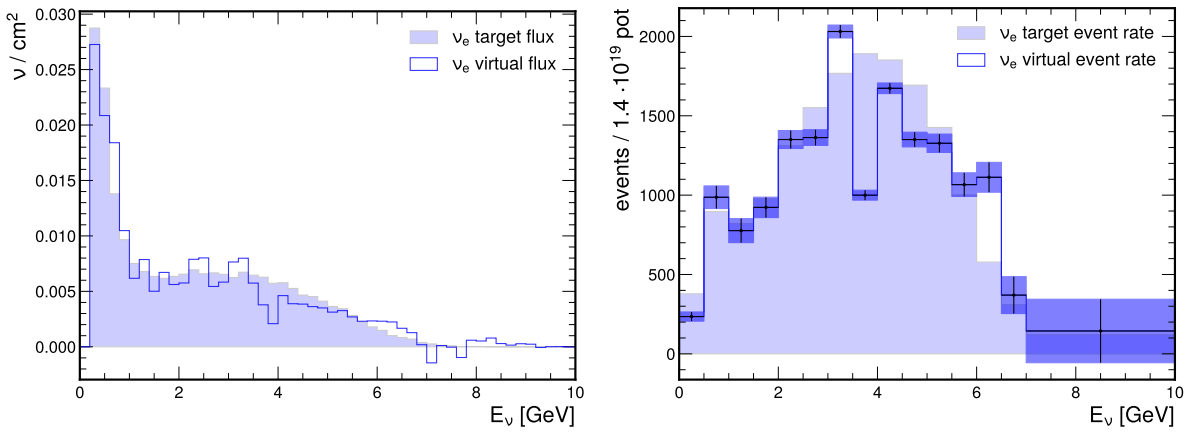

Figure 5.17: Virtual flux (left) and virtual event rate (right) obtained for the optimized value of the regularization strength τ corresponding to a total statistical uncertainty of 2%. The virtual ν_μ flux or event rate (blue lines) obtained by applying the PRISM technique are compared with the target ν_e flux or event rate (filled blue area).

and event rates measured by nuSCOPE using the narrow band off-axis technique. Note that since the virtual event rate is obtained from linear combinations of ν_μ event rates, the knowledge of σ_{ν_μ} is encoded in the measured ν_μ event rates. Therefore, the ratio of real and virtual event rates provides direct access to the $\sigma_{\nu_e}/\sigma_{\nu_\mu}$ cross-section ratio since using the same ν_e and ν_μ fluxes, thus on the same energy range. In Eq. (5.18), N_{ν_e} is the ν_e event rate integral whereas $N^{\texttt{virt}}_{\nu_\mu} = \sum_{i,j} N_{i,j} \cdot c_j$ is the virtual event rate integral. Using the `AR23_20i_00_000` model, a virtual-flux-integrated ν_μ cross-section measurement with a 2% statistical uncertainty is obtained. A ν_e flux-integrated measurement can be made using the ν_e flux directly with an estimated statistical precision of $\sim 1\%$. Using the virtual flux and event rate obtained using the PRISM technique, shown in Fig. 5.17, it is possible to provide a measurement of $\sigma_{\nu_e} \,/\, \sigma_{\nu_\mu}$ as follows:

$$\frac{\sigma_{\nu_e}}{\sigma_{\nu_\mu}} = 1.02 \pm 0.02 \tag{5.19}$$

thus the relative statistical uncertainty is $\sim 2\%$[3]. Therefore, assuming the residual differences in the virtual flux can be accounted for, a projected measurement of the ν_e/ν_μ cross-section ratio averaged over the ν_e flux with a statistical precision of $\sim 2\%$ is obtained. The monitored beam is expected to reduce flux systematic uncertainties at or below this level, and so a direct measurement of the ν_e/ν_μ cross-section ratio at a level of precision that is comparable to theory calculations is achievable. As shown in Fig. 5.11, this would be a measurement within the DUNE region of interest, providing a unique constraint on a source of systematic uncertainty that is currently projected to limit the experiment's sensitivity to constraining CP-violation. A measurement using a water-based target and a lower-energy meson beam may be able to achieve a similar result for Hyper-Kamiokande.

5.7 Flux-averaged ν_μ NC π^0 cross-section measurement

In addition to providing measurements of the CC-inclusive cross-section, nuSCOPE is also well-suited to provide a measurement of neutral current (NC) processes. NC interactions constitute a source of background for neutrino oscillation measurements. Although no charged lepton is produced at the primary vertex, hadrons or photons produced in NC

[3]The flux integral ratio is $\Phi^{\texttt{virt}}_{\nu_\mu}/\Phi_{\nu_e} \sim 0.969$.

interactions can be mis-reconstructed as electrons following photon conversion processes. This causes some NC events to be misattributed to CC events with a final state electron. This is notably one of the main sources of background for neutrino oscillation searches, in which the flavor of the lepton is used to measure electron (anti-)neutrino appearance. The main NC channel that contributes to this background is the production of neutral pions in NC interactions, referred to as the NCπ^0 topology. The neutral pions can be produced via a resonance, coherent scattering off the nucleus, or via neutral pion production during reinteractions inside the nucleus. This process has been measured by several neutrino scattering experiments (see e.g. a measurement performed by the MicroBooNE Collaboration in [174], used as a reference for this study). Still, the measurements are limited to energies below $\sim 1\,\text{GeV}$. In this section, prospects of measuring this process using a monitored neutrino beam and the NBOA technique are presented. The same approach used in Sec. 5.4 is followed. To reduce backgrounds, MicroBooNE separates the NCπ^0 sample into two contributions from events with two photon showers (2γ) and either no tracked protons ($0p$) or one tracked proton ($1p$). The selected events have a single π^0 in the final state and either zero or one proton with momentum above $300\,\text{MeV/c}$ (corresponding approximately to the tracking threshold for a liquid argon detector such as MicroBooNE, quoted as a kinetic energy of $50\,\text{MeV}$). An efficiency correction factor of 10% is applied to the total number of NCπ^0 events to match the efficiencies obtained by MicroBooNE in [174]. The obtained ν_μ NCπ^0 event rate using the NBOA technique is shown in Fig. 5.18a. Despite the reduction in statistics due to the efficiency correction and the lower cross-section for NC processes, the NBOA fluxes are still visible and well separated.

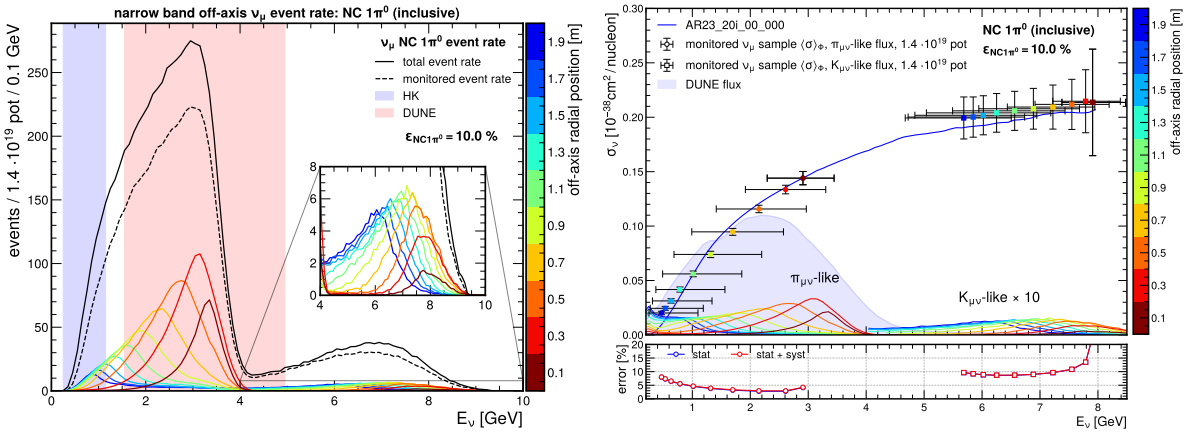

(a) NCπ^0 event rate.

(b) NCπ^0 flux-averaged cross-section.

Figure 5.18: Expected performance of the setup for an NCπ^0 measurement using the NBOA technique. The radial position is given by the associated color scale. The red and blue shaded areas highlight the DUNE and Hyper-Kamiokande regions of interest, respectively. The assumed selection efficiency $\varepsilon_{\text{NC1}\pi^0}$ is of 10%. (left) Expected NCπ^0 event rates using the GENIE `AR23_20i_00_000` model. The black line shows the expected event rate using the total flux and the colored lines show the expected contributions at different radial positions in the detector. (right) Flux-averaged ν_μ NCπ^0 inclusive cross-section as a function of neutrino energy. The $K_{\mu\nu}$ component of each flux has been artificially inflated by a factor of 10 for illustration purposes. Each NBOA flux has a corresponding predicted measurement point of the same color. Horizontal error bars encase the 68% percentiles with respect to the mean energy for the NBOA fluxes. The underlying figure shows the size of the statistic (blue) and the statistic + systematic (red) errors corresponding to each measurement. The measurements are compared to the reference `AR23_20i_00_000` simulation (blue). The DUNE near-detector flux is shown for reference using an arbitrary normalization.

Using each NBOA flux, the flux-averaged inclusive NCπ^0 cross-section[4] as a function of the incoming neutrino energy are extracted, as shown in Fig. 5.18b. The expected size of statistical errors is below 10% across the majority of DUNE energies and below 5% in the peak region. For reference, the statistical error associated with the MicroBooNE measurement is of $\sim 6\%$. However, it is important to note that the latter has an associated systematic error of $\sim 16\%$, of which the dominant contribution comes from neutrino flux uncertainties at the order of $\sim 12\%$. With the NBOA technique, the contribution of the flux uncertainty (assumed to be 1%) becomes subdominant compared to the statistical error. Moreover, the MicroBooNE measurement provides a single flux-averaged cross-section measurement for a mean energy of $\sim 0.8\,\text{GeV}$. Using the NBOA technique, the cross-section for this process can be measured for a multitude of mean neutrino energies, covering the relevant energies for DUNE and Hyper-Kamiokande.

5.8 Cross-section measurements with the tagged neutrino sample

In addition to the measurements using a monitored neutrino beam and the NBOA technique, nuSCOPE provides the unique opportunity to perform measurements using tagged neutrinos. This provides prospects for performing measurements where the neutrino energy is known on an event-by-event basis. In this section, several measurements that can be made by exploiting this new capability are presented and their impact on future generation experiments is discussed. First, the expected event rate from tagged neutrinos using the `AR23_20i_00_000` model is shown in Fig. 5.19, left. Despite the reduction in statistics because tagged neutrinos can only be found in the decay tunnel, and taking into account the tagging efficiency, the total event rate is significant and comparable to that obtained using the NBOA technique discussed in Sec. 5.3.2. The $K_{\mu\nu}$ contribution is smaller than the NBOA case due to the lower tagging efficiency in this region. The $\pi_{\mu\nu}$ contribution is similar to the one obtained with the monitored beam.
In the following sections, a few examples of measurements that can be achieved by exploiting the tagging technique are presented.

5.8.1 ν_μ CC-inclusive cross-section

As a natural extension of the study presented in Sec. 5.4, the total ν_μ CC inclusive cross-section can also be measured with tagged neutrinos. The key advantage of a tagged neutrino beam is that it allows for performing the cross-section measurement directly as a function of neutrino energy, instead of extracting a flux-averaged cross-section for each off-axis position. The projected measurement is shown in Fig. 5.19, right. The neutrino energy binning employed for this measurement is uniform in steps of 200 MeV[5], which is coarser than the neutrino energy resolution shown in Fig. 5.4.
The total statistics at each neutrino energy extracts a cross-section with associated statistical uncertainties of less than 5% across the entire considered energy range. The statistical error on the measurement is below $\sim 1\%$ between $1 - 4\,\text{GeV}$, corresponding to the higher statistics coming from $\pi_{\mu\nu}$ decays. The small increase in statistical error around 4.5 GeV is due to the transition region between the $\pi_{\mu\nu}$ and $K_{\mu\nu}$ populations, and the statistical error stays at the level of $2-3\%$ for the $K_{\mu\nu}$ region. It is important to note

[4]In this measurement, we report the "total" NCπ^0 cross-section as the ratio of the event rates as predicted by GENIE using the `AR23_20i_00_000` model divided by the incoming monitored neutrino flux. Since NCπ^0 is a final state topology rather than an elementary interaction channel, GENIE does not provide a single cross-section for these processes. In these results, any discrepancies between cross-section curves and measurement points are due to statistical fluctuations due to reduced statistics of this topology.

[5]The binning scheme can be further optimized in future studies.

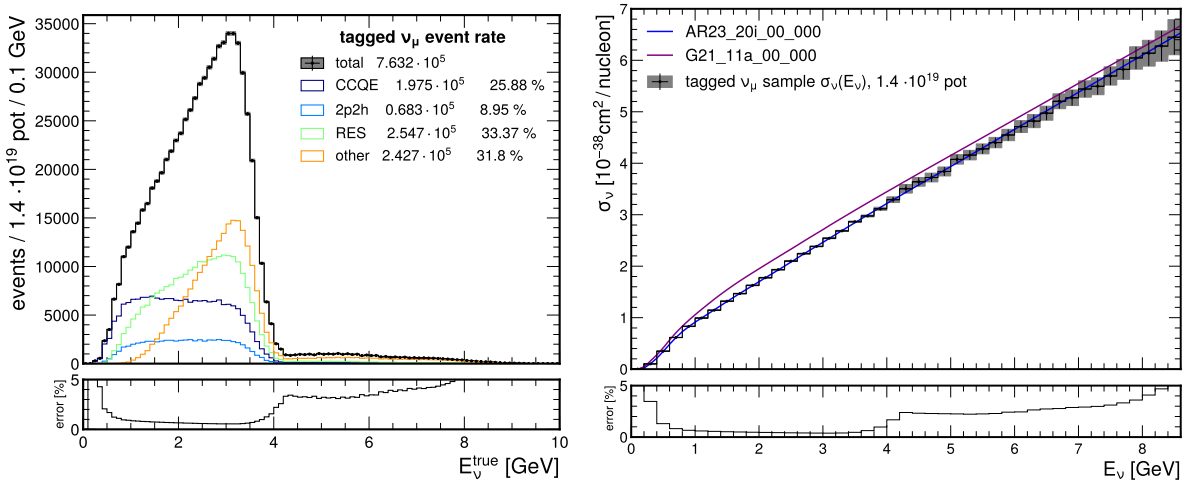

Figure 5.19: (left) Projected measurements of the event rate using tagged neutrinos as a function of the true neutrino energy derived from the tagging procedure. The total event rate (black line) is also broken down by the expected event rates from each interaction mode (colored lines). The total event rates and their percentages with respect to the total are given in the legend. (right) Projected measurement of the ν_μ CC inclusive integrated cross-section as a function of neutrino energy using tagged neutrinos. The reference model `AR23_20i_00_000` (blue) is compared to the alternative model `G21_11a_00_000` (purple). The error bars represent the statistical error expected on the measurement, also shown below the main figure.

that thanks to the tagging technique, this measurement has negligible flux systematic uncertainties.

5.8.2 Measuring the neutrino energy bias

Due to their requirements for high-intensity neutrino beams, future neutrino experiments such as DUNE and Hyper-Kamiokande cannot employ the tagging and monitoring technique in their experimental setups. Therefore, in order to infer the true neutrino energy from the interaction products, they need to rely on neutrino interaction models that relate the amount of visible energy in the detector to the true neutrino energy. There are large uncertainties associated with neutrino interaction models, and this constitutes a large source of systematic uncertainty for oscillation measurements.
Using tagged neutrinos, whose true energy is known on an event-by-event basis, it is possible to directly measure the relationship between the true and reconstructed neutrino energies, as seen by future generation neutrino experiments. The prospects for such a measurement are discussed for a liquid argon detector employing calorimetric energy reconstruction methods[6]. The absolute bias in neutrino energy measurements is defined as the difference between the reconstructed E_ν^{reco} and true neutrino energy E_ν^{true}. In a liquid argon detector, the reconstructed neutrino energy is given by the sum of the visible energy deposited in the detector:

$$E_\nu^{\text{reco}} = E_\mu + \sum_{i=\pi^\pm,p} T_i + \sum_{i=\pi^0,\gamma} E_i, \tag{5.20}$$

where E_μ is the muon energy, $\sum_{i=\pi^\pm,p} T_i$ is the sum of kinetic energies of protons and charged pions and $\sum_{i=\pi^0,\gamma} E_i$ is the sum of total energies of neutral pions and photons. Therefore, under this assumption, the difference between the true and reconstructed neutrino energy will have three main contributions:

[6]For a water Cherenkov detector such as Hyper-Kamiokande a kinematic energy reconstruction method should be used, leading to different sources of bias.

- The missing energy due to the removal energy of nucleons inside the nucleus.
- For each charged pion, a contribution equal to one pion mass (i.e. $m_\pi = 139.6\,\mathrm{MeV/c^2}$), since it is assumed that the number of pions is not determined in the analysis, as they might not always leave an identifiable Michel electron tag and a fraction of their energy is carried away by neutrinos.
- Invisible energy carried by undetected particles, mainly corresponding to neutrons produced primarily through final state interactions inside the nucleus (but some neutrons also come from the elementary interaction processes).

The expected event rates as a function of the absolute and relative neutrino energy bias are shown in Fig. 5.20a and Fig. 5.20b, respectively. From Fig. 5.20a, it is visible that the distribution exhibits sharp peaks spaced by integer multiples of pion masses m_π. The majority of single pions come from RES interactions. At higher energies, the pion peaks are populated by "other" interactions, which mainly correspond to deep or shallow inelastic scattering processes. Each peak has a width of the order of 50 MeV, corresponding to the span in nucleon removal energies associated with the ground state of the nucleus. The absolute bias distributions from pion production and CCQE events sit on top of a slowly decaying contribution, coming from all interaction modes, corresponding to events in which a fraction of the energy is carried away by neutrons. The fraction of neutrino energy carried away by events producing charged pions and neutrons (primarily in the tail of the distribution) is responsible for a fraction of invisible energy ranging between $10\% - 50\%$, as can be seen in Fig. 5.20b,

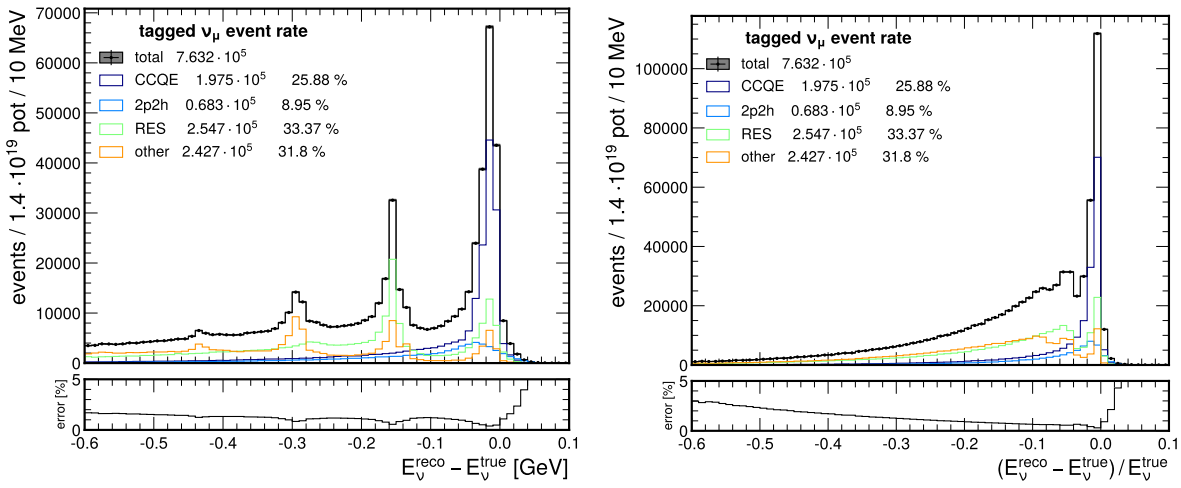

(a) Absolute bias.

(b) Relative bias.

Figure 5.20: Expected event rates using the tagging technique as a function of the absolute and relative neutrino energy bias, using the `AR23_20i_00_000` model. The distributions are split by true interaction mode, indicated in the legend. E_ν^{reco} is defined as in Eq. (5.20), whereas E_ν^{true} is the true neutrino energy derived from the tagging procedure. Error bars are given for the total predictions from the model. The colored lines show the breakdown by interaction channel as predicted by the model. Each figure is accompanied by an underlying plot showing the evolution of the statistical error on the cross-section measurement as a function of each quantity.

Using the a priori knowledge of the energy of tagged neutrinos, the projected measurement of the absolute and relative neutrino energy for different regions of neutrino energy is shown in Fig. 5.21. The energy ranges considered are between $[0, 2]$ GeV (low), $[2, 3]$ GeV (mid) and $[3, 5]$ GeV (high). The choice of energy intervals can be further optimized and was chosen to illustrate how the contributions to the neutrino energy bias change as a function of neutrino energy. This is particularly important for oscillation experiments,

since the constraints obtained with the near detector must be propagated to the far detector, where oscillations change the shape of the neutrino flux.

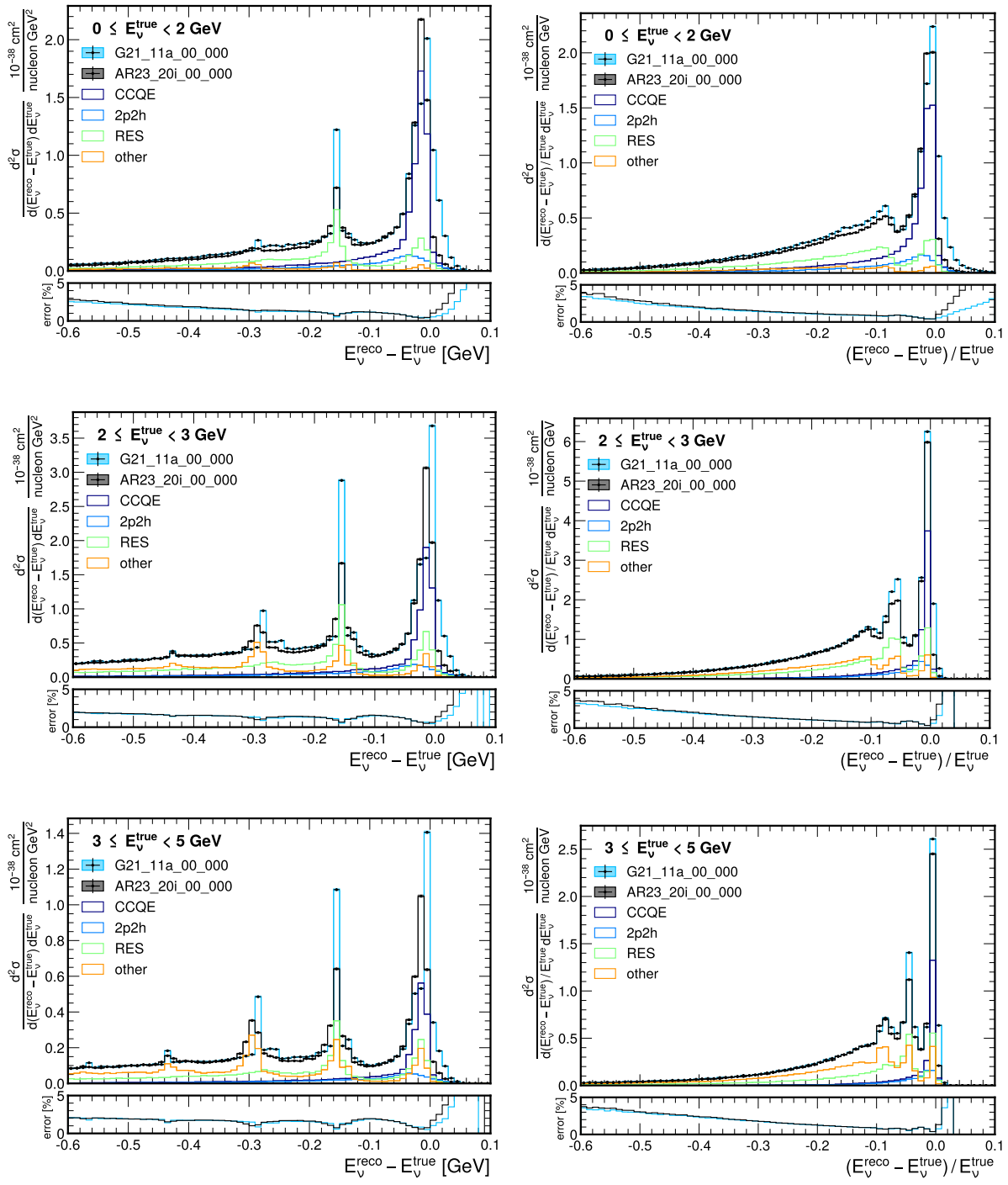

Figure 5.21: Projected measurements of the CC cross-section as a function of the absolute $E_\nu^{\text{reco}} - E_\nu^{\text{true}}$ (left) and relative $(E_\nu^{\text{reco}} - E_\nu^{\text{true}})/E_\nu^{\text{true}}$ (right) neutrino energy bias using tagged neutrinos, for different neutrino energy regions. E_ν^{reco} is defined as in Eq. (5.20), whereas E_ν^{true} is the true neutrino energy derived from the tagging procedure. Error bars are given for the total predictions from the `AR23_20i_00_000` (black) and the `G21_11a_00_000` (light blue) models. The colored lines show the breakdown by interaction channel as predicted by the `AR23_20i_00_000` model. Each figure is accompanied by an underlying plot showing the evolution of the statistical error on the cross-section measurement as a function of each quantity.

Fig. 5.21 highlights that this measurement can be performed using the chosen reference neutrino detector setup with a statistical precision much below 5% across the vast majority of the spectrum. A similar measurement has been performed by the e4nu Collaboration by using electron scattering measurements [175], providing crucial benchmarks for neutrino interaction models. However, this measurement is only able to probe the vector part of the interaction. Using the tagged neutrino beam and within the considered energy ranges, it is possible not only to measure the vector and axial contributions from neutrino interaction models, but also to use such measurements to effectively calibrate the neutrino energy bias of the DUNE experiment far detectors as a function of neutrino energy across the full range of relevant energies.

5.8.3 Electron scattering-like measurements with tagged neutrinos

The measurements described in Secs. 5.8.1 and 5.8.2 provide direct insight into the quantities relevant for future generation neutrino oscillation analyses, but do not attempt to place constraints on individual interaction channels or the dynamics of the underlying processes. Historically, electron-scattering experiments have aimed to characterize the nuclear dynamics in these processes by measuring differential cross-sections as a function of quantities such as the energy transfer ω and momentum transfer q_3, the invariant mass of the hadronic system W, or the Bjorken x and y variables.
However, electron scattering measurements are only sensitive to the vector part of the interaction process, since electrons interact electromagnetically, and are not well suited to probe the axial part of nuclear dynamics. In a tagged neutrino beam, such measurements become accessible using neutrinos as a probe, since their energy is known on an event-by-event basis, allowing for a direct measurement of the aforementioned quantities. Such measurements are essential since they can give targeted insight into the exact processes that govern nuclear effects, currently dominating neutrino oscillation analyses. In this section some selected examples of measurements that can be made with the tagged neutrino sample to refine the nuclear models are presented. A first example is shown in Fig. 5.22, which compares the expected measurement using muon neutrinos coming primarily from $\pi_{\mu\nu}$ decays. The resulting triple differential cross-sections are reported as a function of the energy transfer ω, the muon scattering direction with respect to the neutrino direction $\cos\theta_\mu$ and for neutrino energies in the $[0, 5]$ GeV range. The energy transfer is defined as:

$$\omega = E_\mu - E_\nu \tag{5.21}$$

where E_μ is the muon energy. Such an observable is only accessible thanks to the a priori knowledge of the neutrino energy with the tagging technique and cannot be accessed using conventional broad-band beams. Two angular regions are chosen to highlight differences between the `AR23_20i_00_000` and `G21_11a_00_000` models. The first angular region ($\cos\theta_\mu \in [0.92, 0.93]$) highlights differences at relatively high energy transfer values, which stems from the different parameters related to nucleon-level form factors within the GENIE event generator. The `AR23_20i_00_000` model applies parameters tuned to bubble chamber measurements of neutrino-nucleon scatters [156], which notably reduces the cross-section of RES interactions and deep and shallow inelastic scatters. The second angular region ($\cos\theta_\mu \in [0.99, 1]$) is dominated by very forward scatters and showcases primarily the difference in the treatment of collective nuclear effects (such as the nuclear screening) applied by the different models in the QE region. In both cases, the associated statistical uncertainty is below 5% across the entire spectrum.
The forward-angle, low energy transfer region probes the physics responsible for the main systematic uncertainties for beam and atmospheric oscillation analyses [176]. An

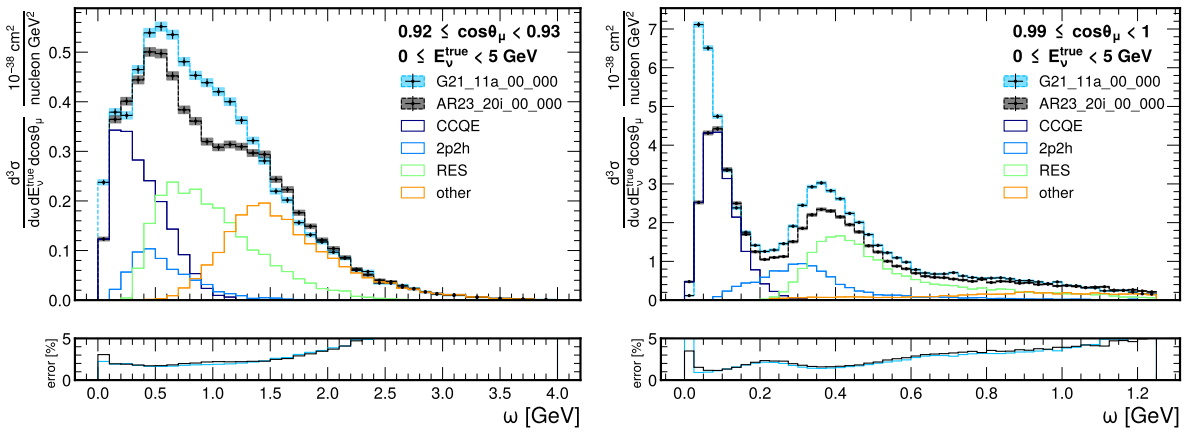

Figure 5.22: CC ν_μ triple differential cross-section as a function of energy transfer ω, for different muon scattering angle $\cos\theta_\mu$ and neutrino energy E_ν^{true} regions. The filled regions show the associated statistical uncertainty for the `AR23_20i_00_000` (black) and `G21_11a_00_000` (light blue) models. The breakdown by interaction mode is given for the `AR23_20i_00_000` model. Each figure is accompanied by the evolution of the associated statistical uncertainty on the measurement, shown underneath.

accurate description of such processes as a function of neutrino energy is essential, as neutrino oscillations modify the fluxes probed with the near and far detectors. The energy dependence of nuclear effects is also particularly important for oscillation analyses involving atmospheric neutrinos, where there are no prior constraints like those obtained with a near detector. This type of measurement can also be achieved with the tagging technique, as illustrated in Fig. 5.23. The size and shape of the differences predicted by the two models change as a function of the neutrino energy range. Across the majority of the spectra, the statistical errors are below 5%, except for low energies (i.e. $E_\nu < 1\,\text{GeV}$) where the measurement in the current binning scheme becomes statistically limited[7].
Finally, another example of an electron scattering-like measurement which can be investigated is the double-differential cross-section as a function of neutrino energy and the invariant mass of the hadronic system W. The invariant mass of the hadronic system W can be computed as follows:

$$W = \sqrt{M_N^2 + 2M_N\omega - Q^2}, \tag{5.22}$$

where M_N is the nucleon mass (i.e. neutron or proton, depending on the interaction channel) and Q^2 is the square of the four-momentum transfer $Q^2 = -q^2$, where $q = (\omega, \vec{q_3})$. This is an inclusive definition of the invariant hadronic mass W, using only the neutrino energy and the four-momentum transfer in the calculation (i.e. it does not add all of the hadronic components, since they are not visible inside the detector) and assumes that the nucleon is at rest. Thanks to the tagging technique such a variable becomes an experimental observable, since E_ν, ω and Q^2 are known on an event-by-event basis, providing valuable insight on the mechanisms for hadron generation in neutrino interactions. The distributions of W exhibit peaks corresponding to the different baryons that are probed during the interaction – first, a nucleon for QE and 2p2h interaction, then a $\Delta(1232)$ resonance for the lightest resonance in pion production processes and then increasingly higher-order resonances. In the DUNE energy range, resonant pion production processes account for roughly $\sim 1/3$ of the available CC interactions. Such a projected measurement is shown in Fig. 5.24, illustrating that as the mean value of neutrino energies increases, the phase space for interaction as a function of W probes increasingly higher

[7]However, there is potential for further optimization of the binning for such a measurement.

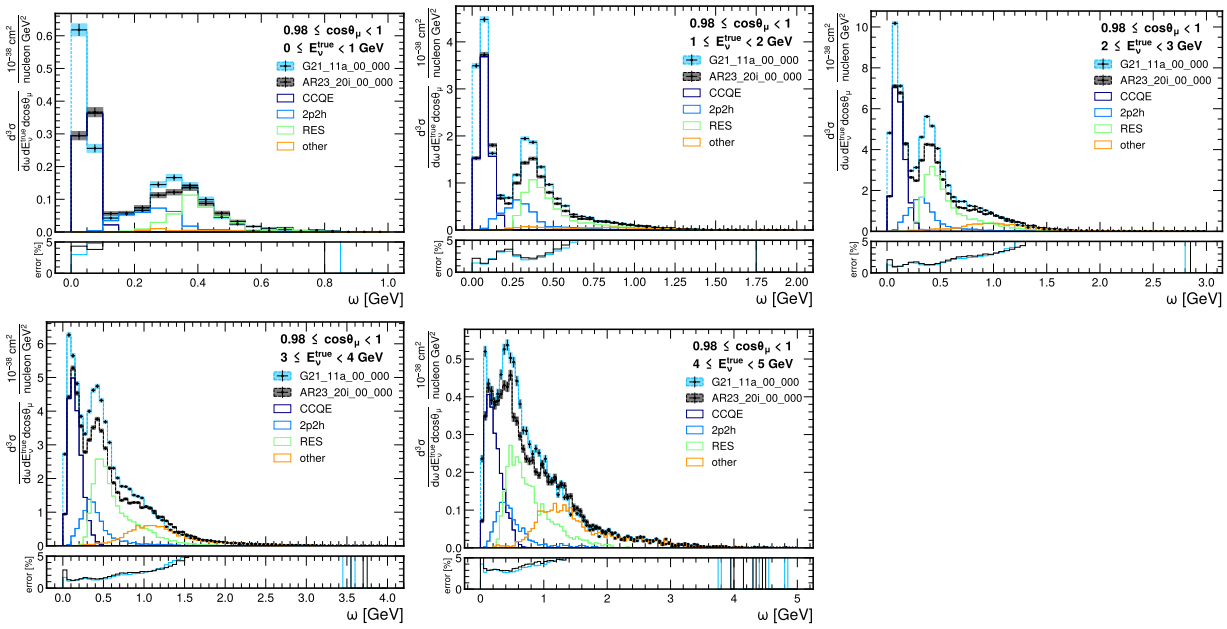

Figure 5.23: CC ν_μ triple differential cross-section as a function of energy transfer ω, for very forward muon scattering directions $\cos\theta_\mu \in [0.98, 1]$ and different neutrino energy E_ν^{true} regions. The filled regions show the associated statistical uncertainty for the `AR23_20i_00_000` (black) and `G21_11a_00_000` (light blue) models. The breakdown by interaction mode is given for the `AR23_20i_00_000` model. Each figure is accompanied by the evolution of the associated statistical uncertainty on the measurement, shown underneath.

mass baryons and the interactions become more inelastic. The associated statistical error on the cross-section is far below 5% (often below 2%) across all regions of interest.

5.8.4 Other measurements with a tagged neutrino beam

The projected measurements illustrated in this section provide a non-exhaustive set of measurements that could be made with a tagged neutrino beam. Indeed, an experiment with event-by-event knowledge of the neutrino energy would represent a paradigm shift for neutrino cross-section measurements, both from the perspective of mitigating systematic uncertainties in neutrino oscillation analyses and of using neutrinos as a weakly-interacting probe of the nucleus. Therefore, there exist several additional possibilities for measurements with a tagged neutrino beam. For instance, the measurement presented in Sec. 5.6 could be repeated without the statistically challenging linear combinations of NBOA fluxes. Instead, an inclusive ν_μ flux-integrated tagging analysis could simply be reweighted on an event-by-event basis to model-independently correct the measurement to the shape of the ν_e flux. The same concept could be applied to directly measure the ν_μ cross-section in the oscillated or unoscillated flux of neutrino oscillation experiments, allowing a precision check of the cross-sections relevant to those experiments. Reconstructing specifically the hadronic energy and momentum imbalance could be used for precision studies of final state interactions (effectively fixing ω and comparing it to the observed hadronic energy) or to construct spectral functions from neutrino scattering measurements in the same way it is done for electron scattering [177], allowing a detailed evaluation of the nuclear initial state. Moreover, the knowledge of the neutrino energy would also allow a detailed exploration of the very poorly understood resonant to deep inelastic transition region, which is of particular importance to experiments operating at the few GeV energy scale such as DUNE. The Bjorken and Nachtmann variables could be precisely reconstructed, and the suppression of the cross-section with respect to

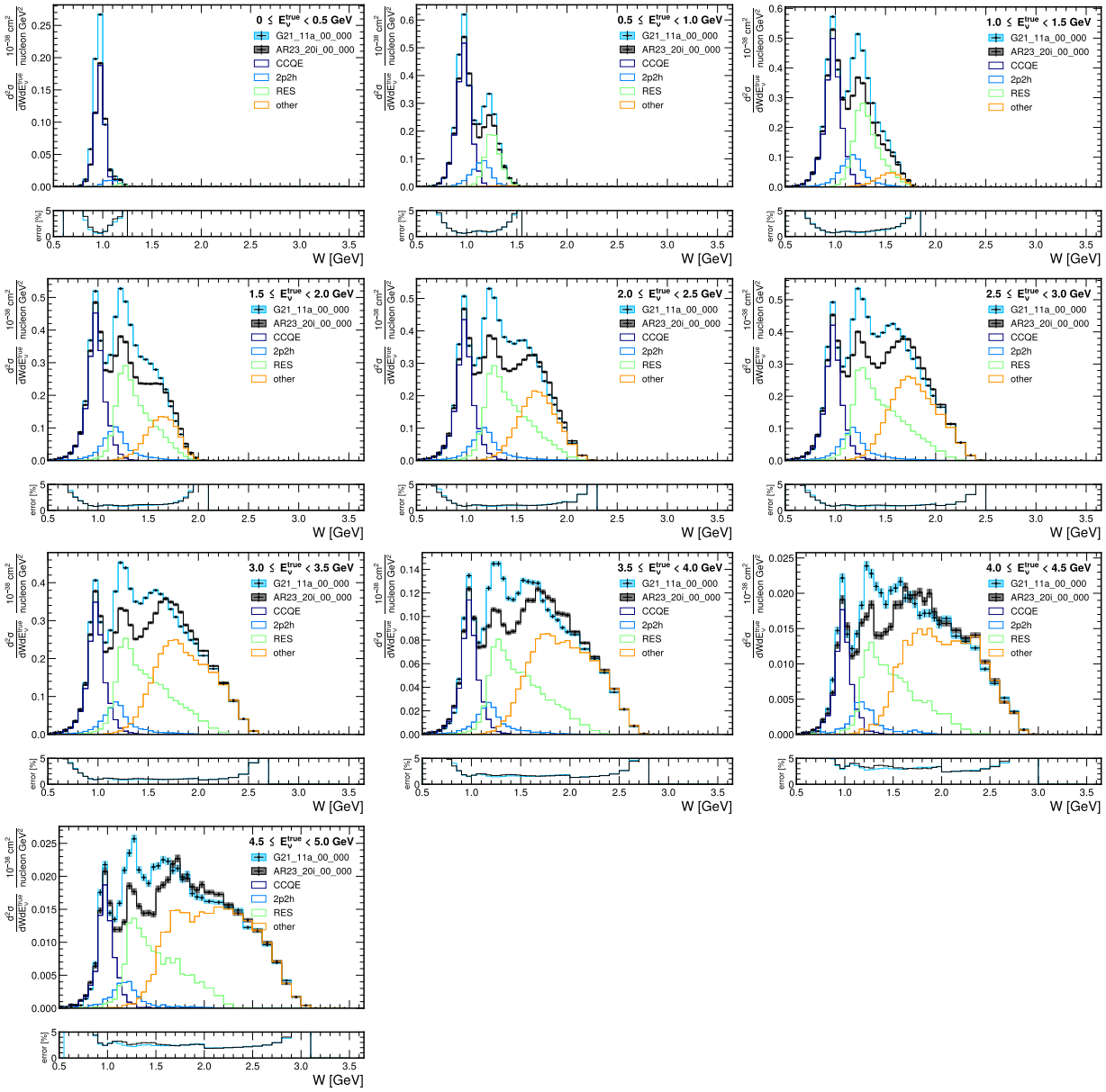

Figure 5.24: CC ν_μ double differential cross-section as a function of the invariant mass of the hadronic system W, and different neutrino energy E_ν^{true} regions. The filled regions show the associated statistical uncertainty for the `AR23_20i_00_000` (black) and `G21_11a_00_000` (light blue) models. The breakdown by interaction mode is given for the `AR23_20i_00_000` model. Each figure is accompanied by the evolution of the associated statistical uncertainty on the measurement, shown underneath.

calculations naively extrapolating standard parton distribution functions into the non-perturbative region could be precisely mapped. The hadronization could also be explored in much more detail, using the precise knowledge of four-momentum transfer allowed using a tagged beam.

Conclusions

This Ph.D. thesis aims to study the physics potential and prospects of a monitored and tagged neutrino beam at CERN. The ENUBET/nuSCOPE experiment is designed to deliver neutrino cross-section measurements at the GeV scale at the percent level, which is crucial in the precision era of oscillation physics and lepton flavor studies. This novel facility enables a wide range of measurements that were previously out of reach and proves essential for next-generation long-baseline neutrino oscillation experiments to achieve their full precision potential.

The research work I carried out within ENUBET/nuSCOPE contributed to achieving relevant results for the experiment and its future implementation.

The ENUBET demonstrator, a large-scale prototype of a section of the instrumented decay tunnel, was exposed at the CERN PS T9 area during dedicated test beam data campaigns in 2022, 2023, and 2024. I contributed to the analysis of test beam data to assess prototype performance, the development of a full and realistic GEANT4 simulation of the demonstrator reproducing test beam conditions, and data/MC agreement studies. By selecting electrons from the beam, I assessed the electromagnetic energy resolution and response linearity of the equalized calorimeter. The energy resolution of the right side of the demonstrator is $\frac{\sigma}{E} = \frac{15.3\%}{\sqrt{E}} \oplus \frac{1.1\%}{E} \oplus 4.4\%$, which is appropriate for the aims of ENUBET ($< 25\%$ at 1 GeV). The discrepancies observed in the data/MC agreement of the energy resolution were explained by including in the simulation some detector effects that can contribute to a degradation of the energy resolution, such as photo-electron statistic fluctuations and geometrical misalignments. In particular, the description of dead regions between scintillator tiles provided a significant improvement in the data/MC agreement for the energy resolution. The results from the test beam data analysis are of great importance for the final validation of the detector performance and as a proof-of-principle of the ENUBET technique. Furthermore, the data/MC comparison is crucial for validating the full simulation of the instrumented decay tunnel, which is used to determine the performance of the charged lepton monitoring technique. Therefore, the assessment of the demonstrator performance complements, on the instrumental side, the studies carried out to evaluate the final systematic budget on the neutrino flux.

The assessment of neutrino flux systematic uncertainties and their mitigation thanks to the monitoring of charged leptons recorded in the instrumented decay tunnel are crucial tasks for a proof-of-concept of the ENUBET technique. In particular, I investigated the leading systematic contribution affecting the neutrino flux: the yields of secondary hadrons produced at the target. The hadron production model considered in this work is drawn from the NA20 and NA56/SPY experiments, from which some semiempirical formulae both for cross sections and hadron yields have been retrieved. The use of such a parameterization should be considered as a proof-of-principle test, aiming to demonstrate that the monitoring of positrons from K_{e3} in the decay volume actually allows to reach a percent-level precision on the electron neutrino flux and, in turn, on its cross section. The hadron yields measured by NA20 and NA56/SPY have been used to reweight both

the positron observables at the instrumented decay tunnel and the neutrino flux at the detector, obtained from a GEANT4 simulation of the entire facility. I developed an algorithm capable of determining the impact of neutrino flux systematic uncertainties before and after using the information provided by the fit to charged lepton observables. The algorithm is based on a fit model where the parameters of interest are related to the hadron production; additional nuisance parameters are then introduced to parametrize the uncertainties related to detector effects (calibration uncertainty and bias, scintillator ageing). The GEANT4 simulation of the instrumented tunnel is used to derive a set of pseudo-experiments including the effects of hadron production and detector-related uncertainties on the charged lepton observables. I used these synthetic datasets to perform an extended maximum likelihood fit on the observables to study the feasibility of the monitoring concept; I used the fit results to set a constraint on the hadron production yields and on the expected neutrino flux. I carried out the propagation of uncertainties to the physical observables and to the neutrino flux at the detector by means of the multi-universe technique, namely a numerical approach to estimate the neutrino flux covariance matrix from multiple simulations (universes) where the parameters affecting the flux estimate are sampled from appropriate probability distributions. The observables considered in my work are the distributions of visible energy and the impact point of positrons along the decay tunnel. I have shown that these observables can be used to constrain the neutrino flux at the percent level. The neutrino flux component originating from the dumps and reaching the detector cannot be monitored, but it can, in principle, be reduced by optimizing the location of the dumps. These non-monitored neutrino contributions can also be minimized using other handles, for instance, by exploiting the longitudinal position of the reconstructed interaction vertex along the neutrino detector length and the directionality of reconstructed tracks. The assessment of neutrino flux systematics has been presented, in particular, considering the contribution to the flux due to neutrinos originating from kaons produced at the target, since in this case all events are properly reweighted on hadron production data for kaons. Considering the neutrino flux produced by kaons at the target —given that the fit constrains the hadron production weight maps for kaons— the post-fit precision is well below $\sim 1\%$ level for energies above $\sim 2\,\mathrm{GeV}$. Kaons originating high-energy neutrinos with $E_\nu \geq 2\,\mathrm{GeV}$ are mainly produced in a phase space in which hadron production weight maps are well constrained using the procedure discussed above. Conversely, for energies below $\sim 2\,\mathrm{GeV}$, many of the neutrinos originate from particles outside the ENUBET phase space. Therefore, the constraint is weaker and the post-fit error is higher than what obtained at higher energies. Following kaons, the next most important contribution to the total ν_e rate comes from pions produced at the target. In this work, no hadron production constraint was applied to pions produced at the target. However, several strategies can be employed to improve the knowledge of this flux component. For instance, one could use the measured K/π ratio from hadron production data, or exploit the sample of muons recorded in the tunnel walls and in the hadron dump. These muon data can be used to further constrain the pion and kaon weight maps that will ultimately be used to reweight the electron-neutrino flux from muon decay. The results obtained demonstrate that charged lepton monitoring in the instrumented decay volume can be used to reduce neutrino flux systematic uncertainties at the percent level for the dominant hadron production systematic and below the percent level for subleading detector-related systematics.

The physics prospects of the nuSCOPE monitored and tagged neutrino beam in terms of neutrino cross-section measurements have been extensively explored. I provided a set of neutrino cross-section measurements that could be made by nuSCOPE to reduce uncertainties in neutrino oscillation experiments, with a focus on their application to support

the DUNE physics program, since the use of an argon-based detector is assumed. I simulated neutrino interactions on an argon target using the GENIE event generator and estimated the expected event rates projected to the total $1.4 \cdot 10^{19}$ pot statistics, considering a proton sharing at the SPS compatible with the physics program of BDF/SHiP. For the case of a monitored neutrino beam, I investigated a set of double differential cross-section measurements for ν_e and ν_μ. The nuSCOPE facility also offers an a priori determination of the neutrino energy without relying on the reconstruction of final state particles in a neutrino interaction, by means of the narrow-band off-axis (NBOA) technique and the tagging method, which can reach the ultimate precision of $\sim 1\%$. I investigated the use of such techniques to perform a ν_μ inclusive energy-dependent cross-section measurement, whose knowledge is essential for neutrino oscillation experiments to extrapolate between near and far detectors. Moreover, the NBOA method has also been exploited to constrain the main backgrounds at the far detectors, such as NCπ^0 events. I investigated the feasibility of a PRISM analysis using a monitored neutrino beam by creating a virtual flux from linear combinations of the ν_μ narrow band off-axis fluxes, in order to reproduce the shape of a target ν_e flux. Such a method can thus be used to constrain the muon to electron neutrino cross-section ratio, which is projected to be a dominant systematic uncertainty for measurements of CP-violation, and can be further improved considering the use of a tagged neutrino beam. A set of measurements with a tagged beam could be leveraged to determine how simulated events for DUNE or Hyper-Kamiokande are expected to look in their near or far detectors, thanks to the event-by-event characterization of neutrino energy. For instance, the direct measurement of neutrino energy offers the unique possibility to measure the smearing and bias in the reconstruction of neutrino energy, which need to be understood to properly interpret far detector event rates as an oscillation probability. Furthermore, a neutrino probe at the GeV-energy scale could also be leveraged to explore nuclear physics in a previously unattainable way. For instance, the unique possibility to provide electron-scattering-like measurements but with tagged neutrinos can definitely provide valuable insights into nuclear physics. The physics case of nuSCOPE should be further expanded with future work, in order to consider a water-based target tailored to support the HyperKamiokande physics program, anti-neutrino beam running, lower energy beam configurations, sensitivity to BSM physics, and a detailed assessment of the detector performance required to realize its full physics program.

Finally, the results obtained in this Ph.D. thesis rigorously motivate the statement that monitored and tagged neutrino beams can be used to provide neutrino cross-section measurements at the GeV scale at the percent level.

Acknowledgments

First and foremost, I would like to express my deepest gratitude to my Tutor, Prof. Francesco Terranova, for guiding me throughout all these years and for supporting me in every step of my academic path. His constant advice, encouragement and invaluable insights have been fundamental to complete this thesis.

Secondly, I am sincerely grateful to my Supervisor, Dr. Antonio Branca, for his constant guidance, patience and invaluable help during the course of my research project. Collaborating closely with him has been truly enriching, both professionally and personally.

I would also like to thank my CERN supervisors Stephen Dolan and Laura Munteanu, for the opportunity to spend a research period at CERN within the EP-NU group and for their availability and constant guidance throughout my work. Working at CERN has been a highly valuable professional experience and a great opportunity for growth in such a truly international environment.

My heartfelt thanks go to all my numerous colleagues of the ENUBET Collaboration, University of Milano-Bicocca group and CERN EP-NU group. In particular, I would like to thank Andrea Longhin, Fabio Pupilli, Daniele Guffanti, Leon Halić, Henrique Vieira De Souza, Federico Galizzi and Ciaran Hasnip for their fruitful suggestions and stimulating discussions.

I am deeply grateful to my lifelong friends, Ruben, Federico, Elena, Flora, Francesco, Cecilia, Beatrice, Riccardo, Michele, who have always stood by me with unwavering support and encouragement.

There are also many other people I would like to thank, whose names are written in my heart.

Finally, my deepest gratitude goes to my family, my parents and my brother. Their love and constant support throughout these years have been the foundation on which I have built this journey. Without them, none of this would have been possible.

Bibliography

[1] S. Navas et al. Review of particle physics. *Phys. Rev. D*, 110(3):030001, 2024.

[2] M.C. Gonzalez-Garcia and Michele Maltoni. Phenomenology with massive neutrinos. *Physics Reports*, 460(1):1–129, 2008.

[3] M. C. Gonzalez-Garcia and Yosef Nir. Neutrino masses and mixing: evidence and implications. *Rev. Mod. Phys.*, 75:345–402, Mar 2003.

[4] Francesco Terranova. *A Modern Primer in Particle and Nuclear Physics*. Oxford University Press, 11 2021.

[5] Surender Verma. Theoretical and Phenomenological Status of Neutrino Physics: A Brief Review. *Advances in High Energy Physics*, 2015(1):385968, 2015.

[6] C. Giganti, S. Lavignac, and M. Zito. Neutrino oscillations: The rise of the PMNS paradigm. *Progress in Particle and Nuclear Physics*, 98:1–54, 2018.

[7] Carlo Giunti and Chung W. Kim. *Fundamentals of Neutrino Physics and Astrophysics*. 2007.

[8] Ivan Esteban, M. C. Gonzalez-Garcia, Michele Maltoni, Ivan Martinez-Soler, João Paulo Pinheiro, and Thomas Schwetz. NuFit-6.0: updated global analysis of three-flavor neutrino oscillations. *Journal of High Energy Physics*, 2024(12), December 2024.

[9] All Things Neutrino, Which neutrino is the lightest? `https://neutrinos.fnal.gov/mysteries/mass-ordering/#moreinfo`.

[10] Francesco Terranova. Future Long-Baseline Neutrino Experiments. *Universe*, 10(5), 2024.

[11] K. Abe et al. Indication of Electron Neutrino Appearance from an Accelerator-produced Off-axis Muon Neutrino Beam. *Phys. Rev. Lett.*, 107:041801, 2011.

[12] P. Adamson et al. Measurement of the Neutrino Mixing Angle θ_{23} in NOνA. *Physical Review Letters*, 118, 04 2017.

[13] B. Abi et al. Volume I. Introduction to DUNE. *Journal of Instrumentation*, 15(08):T08008, August 2020.

[14] R.B. Patterson. Prospects for Measurement of the Neutrino Mass Hierarchy. *Annual Review of Nuclear and Particle Science*, 65(1):177–192, October 2015.

[15] F. P. An et al. Observation of Electron-Antineutrino Disappearance at Daya Bay. *Phys. Rev. Lett.*, 108:171803, Apr 2012.

[16] J. K. Ahn et al. Observation of Reactor Electron Antineutrinos Disappearance in the RENO Experiment. *Phys. Rev. Lett.*, 108:191802, May 2012.

[17] Y. Abe et al. Improved measurements of the neutrino mixing angle 13 with the Double Chooz detector. *Journal of High Energy Physics*, 2014(10), October 2014.

[18] K. Abe et al. Hyper-Kamiokande Design Report, 2018.

[19] K. Abe et al. Constraint on the matter–antimatter symmetry-violating phase in neutrino oscillations. *Nature*, 580(7803):339–344, April 2020.

[20] M. Sajjad Athar and S. K. Singh. *The Physics of Neutrino Interactions*. Cambridge University Press, 5 2020.

[21] M. Sajjad Athar, A. Fatima, and S. K. Singh. Neutrinos and their interactions with matter, 2022.

[22] J. A. Formaggio and G. P. Zeller. From eV to EeV: Neutrino cross sections across energy scales. *Reviews of Modern Physics*, 84(3):1307–1341, September 2012.

[23] R. Bradford, A. Bodek, H. Budd, and J. Arrington. A new parameterization of the nucleon elastic form factors. *Nuclear Physics B - Proceedings Supplements*, 159:127–132, September 2006.

[24] J. J. Kelly. Simple parametrization of nucleon form factors. *Phys. Rev. C*, 70:068202, 2004.

[25] V. Punjabi, C. F. Perdrisat, M. K. Jones, E. J. Brash, and C. E. Carlson. The Structure of the Nucleon: Elastic Electromagnetic Form Factors, 2015.

[26] Rajan Gupta, Yong-Chull Jang, Huey-Wen Lin, Boram Yoon, and Tanmoy Bhattacharya. Axial-vector form factors of the nucleon from lattice QCD. *Physical Review D*, 96(11), December 2017.

[27] Aaron S. Meyer, Minerba Betancourt, Richard Gran, and Richard J. Hill. Deuterium target data for precision neutrino-nucleus cross sections. *Physical Review D*, 93(11), June 2016.

[28] A. Branca, G. Brunetti, A. Longhin, M. Martini, F. Pupilli, and F. Terranova. A new generation of neutrino cross section experiments: Challenges and opportunities, 2021.

[29] Véronique Bernard, Latifa Elouadrhiri, and Ulf-G Meißner. Axial structure of the nucleon. *Journal of Physics G: Nuclear and Particle Physics*, 28(1):R1, nov 2001.

[30] V. Lyubushkin et al. A study of quasi-elastic muon neutrino and antineutrino scattering in the NOMAD experiment. *The European Physical Journal C*, 63(3):355–381, August 2009.

[31] R. Gran et al. Measurement of the quasielastic axial vector mass in neutrino interactions on oxygen. *Physical Review D*, 74(5), September 2006.

[32] Y. Nakajima et al. Measurement of inclusive charged current interactions on carbon in a few-GeV neutrino beam. *Physical Review D*, 83(1), January 2011.

[33] A. A. Aguilar-Arevalo et al. First measurement of the muon neutrino charged current quasielastic double differential cross section. *Physical Review D*, 81(9), May 2010.

[34] M. Martini, M. Ericson, G. Chanfray, and J. Marteau. Unified approach for nucleon knock-out and coherent and incoherent pion production in neutrino interactions with nuclei. *Physical Review C*, 80(6), December 2009.

[35] C. H. Llewellyn Smith. Neutrino Reactions at Accelerator Energies. *Phys. Rept.*, 3:261–379, 1972.

[36] Dieter Rein and Lalit M. Sehgal. Neutrino Excitation of Baryon Resonances and Single Pion Production. *Annals Phys.*, 133:79–153, 1981.

[37] Janet M. Conrad, Michael H. Shaevitz, and Tim Bolton. Precision measurements with high-energy neutrino beams. *Reviews of Modern Physics*, 70(4):1341–1392, October 1998.

[38] L. Alvarez-Ruso et al. NuSTEC White Paper: Status and challenges of neutrino–nucleus scattering. *Prog. Part. Nucl. Phys.*, 100:1–68, 2018.

[39] R.A. Smith and E.J. Moniz. Neutrino reactions on nuclear targets. *Nuclear Physics B*, 43:605–622, 1972.

[40] J. Nieves, I. Ruiz Simo, and M. J. Vicente Vacas. Inclusive charged-current neutrino-nucleus reactions. *Phys. Rev. C*, 83:045501, Apr 2011.

[41] Omar Benhar, Adelchi Fabrocini, and Stefano Fantoni. The nucleon spectral function in nuclear matter. *Nuclear Physics A*, 505(2):267–299, 1989.

[42] J Nieves, I Ruiz Simo, and M J Vicente Vacas. The nucleon axial mass and the MiniBooNE CCQE neutrino-nucleus data. *Journal of Physics: Conference Series*, 408(1):012040, feb 2013.

[43] I Ruiz Simo, J E Amaro, M B Barbaro, A De Pace, J A Caballero, and T W Donnelly. Relativistic model of 2p-2h meson exchange currents in (anti)neutrino scattering. *Journal of Physics G: Nuclear and Particle Physics*, 44(6):065105, April 2017.

[44] R. Gran, J. Nieves, F. Sanchez, and M. J. Vicente Vacas. Neutrino-nucleus quasi-elastic and 2p2h interactions up to 10 GeV. *Phys. Rev. D*, 88:113007, Dec 2013.

[45] R. González-Jiménez, G. D. Megias, M. B. Barbaro, J. A. Caballero, and T. W. Donnelly. Extensions of superscaling from relativistic mean field theory: The SuSAv2 model. *Physical Review C*, 90(3), September 2014.

[46] W.M. Alberico, M. Ericson, and A. Molinari. The role of two particle-two hole excitations in the spin-isospin nuclear response. *Annals of Physics*, 154(2):356–395, 1984.

[47] Keigo Nakamura. The T2K cross-section results and prospects from the oscillation perspective. *PoS*, NuFact2017:046, 2018.

[48] Costas Andreopoulos, Christopher Barry, Steve Dytman, Hugh Gallagher, Tomasz Golan, Robert Hatcher, Gabriel Perdue, and Julia Yarba. The GENIE Neutrino Monte Carlo Generator: Physics and User Manual, 2015.

[49] Yoshinari Hayato and Luke Pickering. The NEUT neutrino interaction simulation program library. *The European Physical Journal Special Topics*, 230(24):4469–4481, October 2021.

[50] T. Golan, J.T. Sobczyk, and J. Zmuda. NuWro: the Wrocław Monte Carlo Generator of Neutrino Interactions. *Nuclear Physics B - Proceedings Supplements*, 229-232:499, 2012. Neutrino 2010.

[51] O. Buss, T. Gaitanos, K. Gallmeister, H. van Hees, M. Kaskulov, O. Lalakulich, A.B. Larionov, T. Leitner, J. Weil, and U. Mosel. Transport-theoretical description of nuclear reactions. *Physics Reports*, 512(1–2):1–124, March 2012.

[52] L. Alvarez-Ruso et al. NuSTEC White Paper: Status and challenges of neutrino–nucleus scattering. *Progress in Particle and Nuclear Physics*, 100:1–68, May 2018.

[53] K. Abe et al. Measurement of double-differential muon neutrino charged-current interactions on C_8H_8 without pions in the final state using the T2K off-axis beam. *Phys. Rev. D*, 93:112012, Jun 2016.

[54] M. Martini, M. Ericson, G. Chanfray, and J. Marteau. Neutrino and antineutrino quasielastic interactions with nuclei. *Phys. Rev. C*, 81:045502, Apr 2010.

[55] J. Nieves, F. Sánchez, I. Ruiz Simo, and M. J. Vicente Vacas. Neutrino energy reconstruction and the shape of the charged current quasielastic-like total cross section. *Phys. Rev. D*, 85:113008, Jun 2012.

[56] K. Abe et al. Measurement of the inclusive ν_μ charged current cross section on carbon in the near detector of the T2K experiment. *Physical Review D*, 87(9), May 2013.

[57] S. Henry et al. Measurement of electron neutrino and antineutrino cross sections at low momentum transfer. *Phys. Rev. D*, 109:092008, May 2024.

[58] Mauro Mezzetto and Francesco Terranova. Three-Flavor Oscillations with Accelerator Neutrino Beams. *Universe*, 6(2), 2020.

[59] Nikolaos Charitonidis, Andrea Longhin, Michelangelo Pari, Elisabetta Giulia Parozzi, and Francesco Terranova. Design and Diagnostics of High-Precision Accelerator Neutrino Beams. *Applied Sciences*, 11(4):1644, February 2021.

[60] Sara Bolognesi. Neutrino Physics with Particle Beams. *PoS*, EPS-HEP2021:042, 2022.

[61] B. Abi et al. Deep Underground Neutrino Experiment (DUNE), Far Detector Technical Design Report, Volume II: DUNE Physics, 2020.

[62] Artur M Ankowski and Camillo Mariani. Systematic uncertainties in long-baseline neutrino-oscillation experiments. *Journal of Physics G: Nuclear and Particle Physics*, 44(5):054001, March 2017.

[63] L. Aliaga et al. Neutrino flux predictions for the NuMI beam. *Physical Review D*, 94(9), November 2016.

[64] S. Agostinelli et al. Geant4-a simulation toolkit. *Nuclear Instruments and Methods in Physics Research Section A: Accelerators, Spectrometers, Detectors and Associated Equipment*, 506(3):250–303, 2003.

[65] Alfredo Ferrari, Paola R. Sala, Alberto Fasso, and Johannes Ranft. FLUKA: A multi-particle transport code (Program version 2005). 10 2005.

[66] K. Abe et al. Results from the T2K experiment on neutrino mixing including a new far detector μ-like sample, 2025.

[67] N. Abgrall et al. Measurements of $\pi^{\pm}$, $K^{\pm}$ and proton double differential yields from the surface of the T2K replica target for incoming 31 GeV/c protons with the NA61/SHINE spectrometer at the CERN SPS. *The European Physical Journal C*, 79(2), January 2019.

[68] K. Abe et al. T2K neutrino flux prediction. *Physical Review D*, 87(1), January 2013.

[69] K. Abe et al. Measurements of neutrino oscillation parameters from the T2K experiment using 3.6×10^{21} protons on target. *The European Physical Journal C*, 83(9), September 2023.

[70] F. Acerbi et al. nuSCOPE: A short-baseline neutrino beam at CERN for high-precision cross-section measurements. 2025.

[71] L.N. Hand. A study of 40-90 GeV neutrino interactions using a tagged neutrino beam. In *Proceedings. Second NAL Summer Study, Jun 9 - Aug 3*, 1969.

[72] B. Pontecorvo. Tagging direct neutrinos. A first step to neutrino tagging. *Lett. Nuovo Cim.*, 25:257–259, 1979.

[73] V. V. Ammosov et al. Neutrino investigations at the UNK using tagged neutrino beam facility. 10 1990.

[74] D. Beavis et al. P889: Long Baseline Neutrino Oscillation Experiment at the AGS, April 1995. Report No. BNL-52459.

[75] S. Kopp. Accelerator neutrino beams. *Physics Reports*, 439(3):101–159, February 2007.

[76] F. Acerbi et al. Design and performance of the ENUBET monitored neutrino beam. *Eur. Phys. J. C*, 83(10):964, 2023.

[77] The European Strategy Group. Deliberation document on the 2020 Update of the European Strategy for Particle Physics. Technical report, Geneva, 2020.

[78] A. Longhin, L. Ludovici, and F. Terranova. A novel technique for the measurement of the electron neutrino cross section. *The European Physical Journal C*, 75(4), April 2015.

[79] ENUBET: Enhanced Neutrino Beams from Kaon Tagging, 2016. ERC-CoG-2015 (PI A. Longhin), grant agreement n. 681647 `https://www.pd.infn.it/eng/enubet/` .

[80] F Acerbi et al. The ENUBET project. Technical report, CERN, Geneva, 2018.

[81] A Longhin and F Terranova. The NP06/ENUBET SPSC annual report (2023). Technical report, CERN, Geneva, 2023. co-spokesperson: Francesco Terranova (University Milano Bicocca and INFN).

[82] F Acerbi et al. NP06/ENUBET Annual Report for the SPSC (2021). Technical report, CERN, Geneva, 2021.

[83] F Acerbi et al. NP06/ENUBET annual report 2022 for the SPSC. Technical report, CERN, Geneva, 2022. co-spokesperson F. Terranova.

[84] A Longhin and F Terranova. NP06/ENUBET annual report for the CERN-SPSC. Technical report, CERN, Geneva, 2020.

[85] F Terranova and A Longhin. NP06/ENUBET annual report 2024 for the SPSC. Technical report, CERN, Geneva, 2024.

[86] Michelangelo Pari. Study and development of SPS slow extraction schemes and focusing of secondary particles for the ENUBET monitored neutrino beam , February 2023.

[87] M. Pari, F. M. Velotti, M. A. Fraser, V. Kain, and O. Michels. Characterization of the slow extraction frequency response. *Phys. Rev. Accel. Beams*, 24:083501, Aug 2021.

[88] Karl L Brown, David C Carey, F Christoph Iselin, and F Rothacker. *TRANSPORT*. CERN Yellow Reports: Monographs. CERN, Geneva, 1973. Also publ. as SLAC and FERMILAB.

[89] The MAD-X Project.

[90] Thomas J. Roberts and Daniel M. Kaplan. G4Beamline Simulation Program for Matter dominated Beamlines. *Conf. Proc. C*, 070625:3468, 2007.

[91] Thomas Papaevangelou. Développement d'un détecteur PICOSEC-Micromegas pour ENUBET – PIMENT, 2022. Available at `https://anr.fr/Projet-ANR-21-CE31-0027` .

[92] B. Abi et al. First results on ProtoDUNE-SP liquid argon time projection chamber performance from a beam test at the CERN Neutrino Platform. *Journal of Instrumentation*, 15(12):P12004–P12004, December 2020.

[93] F. Acerbi et al. The ENUBET positron tagger prototype: construction and test-beam performance. *Journal of Instrumentation*, 15(08):P08001–P08001, August 2020.

[94] A. Berra et al. A compact light readout system for longitudinally segmented shashlik calorimeters. *Nuclear Instruments and Methods in Physics Research Section A: Accelerators, Spectrometers, Detectors and Associated Equipment*, 830:345–354, 2016.

[95] A. Berra et al. Shashlik Calorimeters With Embedded SiPMs for Longitudinal Segmentation. *IEEE Transactions on Nuclear Science*, 64(4):1056–1061, 2017.

[96] G. Ballerini et al. Testbeam performance of a shashlik calorimeter with fine-grained longitudinal segmentation. *Journal of Instrumentation*, 13(01):P01028–P01028, January 2018.

[97] F. Acerbi et al. Irradiation and performance of RGB-HD Silicon Photomultipliers for calorimetric applications. *Journal of Instrumentation*, 14(02):P02029–P02029, February 2019.

[98] F. Acerbi et al. Polysiloxane-based scintillators for shashlik calorimeters. *Nuclear Instruments and Methods in Physics Research Section A: Accelerators, Spectrometers, Detectors and Associated Equipment*, 956:163379, March 2020.

[99] R. H. Bernstein, F. Borcherding, D. Jovanovic, M. J. Lamm, and F. Vannucci. A Proposal for a Neutrino Oscillation Experiment in a Tagged Neutrino Line. 9 1988.

[100] Mathieu Perrin-Terrin. Neutrino tagging: a new tool for accelerator based neutrino experiments. *Eur. Phys. J. C*, 82(5):465, 2022.

[101] Anna Baratto-Roldán, Mathieu Perrin-Terrin, Elisabetta Giulia Parozzi, Marc Andre Jebramcik, and Nikolaos Charitonidis. NuTag: a proof-of-concept study for a long-baseline neutrino beam. *Eur. Phys. J. C*, 84(10):1024, 2024.

[102] G. Aglieri Rinella et al. The NA62 GigaTracKer: a low mass high intensity beam 4D tracker with 65 ps time resolution on tracks. *JINST*, 14:P07010, 2019.

[103] Sandro Cadeddu, Gian Matteo Cossu, Luca Frontini, Adriano Lai, Valentino Liberali, Lorenzo Piccolo, and Alberto Stabile. Recent developments in the IGNITE project on front-end design in CMOS 28-nm technology. *JINST*, 19(01):C01040, 2024.

[104] Eduardo Cortina Gil et al. First detection of a tagged neutrino in the NA62 experiment. *Phys. Lett. B*, 863:139345, 2025.

[105] Physics Beyond Collider, Annual Workshop, 2024. https://indico.cern.ch/event/1369776/.

[106] Input to the European Strategy for Particle Physics - 2026 update, SBN@CERN: A short-baseline neutrino beam at CERN for high-precision cross-section measurements, 2025. https://indico.cern.ch/event/1439855/contributions/6461501/.

[107] Elisabetta Giulia Parozzi. Design and optimisation of a variable momentum secondary beamline for the NP06/ENUBET project, 2023. Presented 2023.

[108] F Hahn, F Ambrosino, A Ceccucci, H Danielsson, N Doble, F Fantechi, A Kluge, C Lazzeroni, M Lenti, G Ruggiero, M Sozzi, P Valente, and R Wanke. NA62: Technical Design Document. Technical report, CERN, Geneva, 2010.

[109] Laurence J. Nevay et al. BDSIM: An accelerator tracking code with particle–matter interactions. *Comput. Phys. Commun.*, 252:107200, 2020.

[110] Sergey Alekhin et al. A facility to Search for Hidden Particles at the CERN SPS: the SHiP physics case. *Rept. Prog. Phys.*, 79(12):124201, 2016.

[111] LHCb. Framework TDR for the LHCb Upgrade II. `http://cds.cern.ch/record/2776420`, 2021.

[112] G. Termo et al. Radiation response of 28 nm CMOS transistors at high proton and neutron fluences for high energy physics applications. *Nucl. Instrum. Meth. A*, 1065:169497, 2024.

[113] S. Cadeddu et al. Timespot1: a 28 nm CMOS Pixel Read-Out ASIC for 4D Tracking at High Rates. *JINST*, 18(03):P03034, 2023.

[114] Lau Gatignon. East area documentation. CERN SBA website, November 2013. `https://sba.web.cern.ch/sba/beamsandareas/east/east.htm`.

[115] M. Prest, G. Barbiellini, G. Bordignon, G. Fedel, F. Liello, F. Longo, C. Pontoni, and E. Vallazza. The AGILE silicon tracker: An innovative gamma-ray instrument for space. *Nucl. Instrum. Meth. A*, 501:280–287, 2003.

[116] Johannes Bernhard et al. CERN Proton Synchrotron East Area Facility: Upgrades and renovation during Long Shutdown 2. CERN Yellow Reports: Monographs, CERN-2021-004 (CERN, Geneva, 2021).

[117] Mukund Gupta. Calculation of radiation length in materials. Technical report, CERN, Geneva, 2010.

[118] Claus Grupen and Boris Schwartz. *Particle Detectors, Second Edition.* Cambridge University Press, 2008.

[119] Christian W. Fabjan and Fabiola Gianotti. Calorimetry for particle physics. *Rev. Mod. Phys.*, 75:1243–1286, Oct 2003.

[120] W J Metzger. *Statistical methods in data analysis.* Nijmegen Univ. Fys. Lab., Nijmegen, 2002.

[121] M. Bonesini, A. Marchionni, F. Pietropaolo, and T. Tabarelli de Fatis. On particle production for high energy neutrino beams. *The European Physical Journal C*, 20(1):13–27, April 2001.

[122] G. Ambrosini et al. Measurement of charged particle production from 450-GeV/c protons on beryllium. *Eur. Phys. J. C*, 10:605–627, 1999.

[123] Henry W Atherton, Claude Bovet, Niels T Doble, L Piemontese, Alfredo Placci, Massimo Placidi, David E Plane, Max Reinharz, Edouard Rossa, and G Von Holtey. *Precise measurements of particle production by 400 GeV/c protons on beryllium targets.* CERN Yellow Reports: Monographs. CERN, Geneva, 1980.

[124] A. Hoecker et al. TMVA - Toolkit for Multivariate Data Analysis, 2009.

[125] A. S. Carroll, I. H. Chiang, T. F. Kycia, K. K. Li, M. D. Marx, D. C. Rahm, W. F. Baker, D. P. Earty, G. Giacomelli, A. M. Jonckheere, P. F. M. Koehler, P. O. Mazur, R. Rubinstein, and O. Fackler. Absorption cross section of $\pi^{+/-}$, $K^{+/-}$, p and p on nuclei between 60 and 280 GeV/c. *Physics Letters B*, 80(3):319–322, January 1979.

[126] Joanna Stepaniak and Damian Pszczel. On the relation between K^0_s and charged kaon yields in proton–proton collisions. *Eur. Phys. J. C*, 83(10):928, 2023.

[127] Holly Parkinson. Understanding the off-axis flux of neutrinos from neutral kaons.

[128] M. Kordowsky. Error bands from the many universes method. Minerva note, n.7433.

[129] Ben Messerly et al. An Error Analysis Toolkit for Binned Counting Experiments. *EPJ Web Conf.*, 251:03046, 2021.

[130] Steven Gardiner. Mathematical methods for neutrino cross-section extraction, 2024.

[131] William H. Press, Saul A. Teukolsky, William T. Vetterling, and B. P. Flannery. *Numerical Recipes: The Art of Scientific Computing (Third Edition)*. Cambridge University Press, 2007.

[132] UNU.RAN – Universal Non-Uniform RANdom number generators. `https://statmath.wu.ac.at/unuran/`.

[133] Mohamed Afzal Norat. Automatic Nonuniform Random Variate Generation. *Journal of the Royal Statistical Society Series A: Statistics in Society*, 168(1):253–254, 12 2004.

[134] Sarah Joanne Ives. *Study of the kaon contribution to the T2K neutrino beam using neutrino interactions in the Near Detector*. PhD thesis, Imperial Coll., London, 2012.

[135] S. S. Wilks. The Large-Sample Distribution of the Likelihood Ratio for Testing Composite Hypotheses. *Annals Math. Statist.*, 9(1):60–62, 1938.

[136] George Casella, Christian Robert, and Martin Wells. Generalized Accept-Reject sampling schemes. *Lecture Notes-Monograph Series*, 45, 01 2004.

[137] K. Abe et al. Scintillator ageing of the T2K near detectors from 2010 to 2021. *Journal of Instrumentation*, 17(10):P10028, oct 2022.

[138] A.M. Sirunyan et al. Measurements with silicon photomultipliers of dose-rate effects in the radiation damage of plastic scintillator tiles in the CMS hadron endcap calorimeter. *Journal of Instrumentation*, 15(06):P06009, jun 2020.

[139] C. Papageorgakis et al. Dose rate effects in radiation-induced changes to phenyl-based polymeric scintillators. *Nuclear Instruments and Methods in Physics Research Section A: Accelerators, Spectrometers, Detectors and Associated Equipment*, 1042:167445, November 2022.

[140] K. Abe et al. First measurement of muon neutrino charged-current interactions on hydrocarbon without pions in the final state using multiple detectors with correlated energy spectra at T2K. *Phys. Rev. D*, 108(11):112009, 2023.

[141] S. Bhadra et al. Letter of Intent to Construct a nuPRISM Detector in the J-PARC Neutrino Beamline, 12 2014. arXiv:1412.3086.

[142] A. Abed Abud et al. Deep Underground Neutrino Experiment (DUNE) Near Detector Conceptual Design Report. *Instruments*, 5(4):31, 2021.

[143] K. Abe et al. Hyper-Kamiokande Design Report, 5 2018. arXiv:1805.04163.

[144] Marco Del Tutto. SBND-PRISM: Sampling Multiple Off-Axis Neutrino Fluxes with the Same Detector. In *APS April Meeting 2021, Vol. 66, n. 5*, 2021. Presentation at APS April Meeting 2021.

[145] Costas Andreopoulos et al. The GENIE Neutrino Monte Carlo Generator: Physics and User Manual, 2015. arXiv:1510.05494, FERMILAB-FN-1004-CD.

[146] Luis Alvarez-Ruso et al. Recent highlights from GENIE v3. *Eur. Phys. J. ST*, 230(24):4449–4467, 2021.

[147] https://github.com/GENIE-MC/Generator/releases/tag/R-3_04_00. Accessed: 10/07/2024.

[148] J. Nieves, I. Ruiz Simo, and M. J. Vicente Vacas. Inclusive Charged–Current Neutrino–Nucleus Reactions. *Phys. Rev.*, C83:045501, 2011.

[149] S. Dytman, S. Gardiner, A. Papadopoulou, and M. Roda. Generator R-3 00 04 bug-fix release. Technical report, 05 2019. https://genie-docdb.pp.rl.ac.uk/cgi-bin/ShowDocument?docid=113.

[150] Aaron S. Meyer, Minerba Betancourt, Richard Gran, and Richard J. Hill. Deuterium target data for precision neutrino-nucleus cross sections. *Phys. Rev. D*, 93(11):113015, 2016.

[151] I. Ruiz Simo, J. E. Amaro, M. B. Barbaro, A. De Pace, J. A. Caballero, and T. W. Donnelly. Relativistic model of 2p-2h meson exchange currents in (anti)neutrino scattering. *J. Phys. G*, 44(6):065105, 2017.

[152] G. D. Megias, J. E. Amaro, M. B. Barbaro, J. A. Caballero, T. W. Donnelly, and I. Ruiz Simo. Charged-current neutrino-nucleus reactions within the superscaling meson-exchange current approach. *Phys. Rev.*, D94(9):093004, 2016.

[153] T. Yang, C. Andreopoulos, H. Gallagher, K. Hoffmann, and P. Kehayias. A Hadronization Model for Few-GeV Neutrino Interactions. *Eur. Phys. J. C*, 63:1–10, 2009.

[154] Torbjorn Sjostrand, Stephen Mrenna, and Peter Z. Skands. PYTHIA 6.4 Physics and Manual. *JHEP*, 05:026, 2006.

[155] Steven Dytman, Yoshinari Hayato, Roland Raboanary, J. T. Sobczyk, Julia Tena Vidal, and Narisoa Vololoniaina. Comparison of validation methods of simulations for final state interactions in hadron production experiments. *Phys. Rev. D*, 104(5):053006, 2021.

[156] Júlia Tena-Vidal et al. Neutrino-nucleon cross-section model tuning in GENIE v3. *Phys. Rev. D*, 104(7):072009, 2021.

[157] S. Dolan, G. D. Megias, and S. Bolognesi. Implementation of the SuSAv2-MEC 1p1h and 2p2h models in GENIE and analysis of nuclear effects in T2K measurements. *Phys. Rev.*, D101:033003, 2020.

[158] P. Stowell et al. NUISANCE: a neutrino cross-section generator tuning and comparison framework. *JINST*, 12(01):P01016, 2017.

[159] P. Abratenko et al. Inclusive cross section measurements in final states with and without protons for charged-current ν_μ-Ar scattering in MicroBooNE. *Phys. Rev. D*, 110(1):013006, 2024.

[160] A. Bashyal et al. High-Statistics Measurement of Antineutrino Quasielastic-like scattering at $E_\nu \sim 6\,\text{GeV}$ on a Hydrocarbon Target. *Phys. Rev. D*, 108(3):032018, 2023.

[161] C. E. Patrick et al. Measurement of the Muon Antineutrino Double-Differential Cross Section for Quasielastic-like Scattering on Hydrocarbon at $E_\nu \sim 3.5\text{GeV}$. *Phys. Rev. D*, 97(5):052002, 2018.

[162] P. Abratenko et al. First Simultaneous Measurement of Differential Muon-Neutrino Charged-Current Cross Sections on Argon for Final States with and Without Protons Using MicroBooNE Data. *Phys. Rev. Lett.*, 133(4):041801, 2024.

[163] C. Wilkinson, S. Dolan, L. Pickering, and C. Wret. A substandard candle: the low-ν method at few-GeV neutrino energies. *The European Physical Journal C*, 82(9), September 2022.

[164] S. Henry et al. Measurement of electron neutrino and antineutrino cross sections at low momentum transfer. *Phys. Rev. D*, 109(9):092008, 2024.

[165] P. A. Rodrigues et al. Identification of nuclear effects in neutrino-carbon interactions at low three-momentum transfer. *Phys. Rev. Lett.*, 116:071802, 2016. [Addendum: Phys.Rev.Lett. 121, 209902 (2018)].

[166] Alexis Nikolakopoulos, Natalie Jachowicz, Nils Van Dessel, Kajetan Niewczas, Raúl González-Jiménez, José Manuel Udías, and Vishvas Pandey. Electron versus Muon Neutrino Induced Cross Sections in Charged Current Quasielastic Processes. *Phys. Rev. Lett.*, 123(5):052501, 2019.

[167] T. Dieminger, S. Dolan, D. Sgalaberna, A. Nikolakopoulos, T. Dealtry, S. Bolognesi, L. Pickering, and A. Rubbia. Uncertainties on the ν_μ/ν_e, $\bar{\nu}_\mu/\bar{\nu}_e$ and $\nu_e/\bar{\nu}_e$ cross-section ratio from the modelling of nuclear effects and their impact on neutrino oscillation experiments. *Phys. Rev. D*, 108:L031301, 2023.

[168] Amir Gruber. *Neutrino-Nucleus Cross Section Analysis with DUNE- PRISM: Proof-of-Concept*, August 2022.

[169] S. Abbaslu et al. Towards mono-energetic virtual beam cross-section measurements: A feasibility study of ν-Ar interaction analysis with DUNE-PRISM. 9 2025.

[170] C. Hasnip. *DUNE-PRISM - a new method to measure neutrino oscillations*. PhD thesis, Oxford University, Oxford U., 2023.

[171] David L. Phillips. A Technique for the Numerical Solution of Certain Integral Equations of the First Kind. *J. ACM*, 9(1):84–97, January 1962.

[172] Andrey N. Tikhonov and Vasiliy Y. Arsenin. *Solutions of ill-posed problems*. V. H. Winston & Sons, Washington, D.C.: John Wiley & Sons, New York, 1977. Translated from the Russian, Preface by translation editor Fritz John, Scripta Series in Mathematics.

[173] Stefan Schmitt. TUnfold: an algorithm for correcting migration effects in high energy physics. *JINST*, 7:T10003, 2012.

[174] P. Abratenko et al. Measurement of neutral current single $\pi 0$ production on argon with the MicroBooNE detector. *Phys. Rev. D*, 107(1):012004, 2023.

[175] M. Khachatryan et al. Electron-beam energy reconstruction for neutrino oscillation measurements. *Nature*, 599(7886):565–570, 2021.

[176] K. Abe et al. First Joint Oscillation Analysis of Super-Kamiokande Atmospheric and T2K Accelerator Neutrino Data. *Phys. Rev. Lett.*, 134(1):011801, 2025.

[177] L. Jiang et al. Determination of the argon spectral function from (e,e'p) data. *Phys. Rev. D*, 105(11):112002, 2022.